Numerical Investigations of Single Bunch Collective Instabilities in Synchrotron Storage Ring

Jatuporn Puntree
St Catherine's College
University of Oxford

Thesis submitted in fulfilment of the requirements for the degree of Master of Science by Research at the University of Oxford

Trinity Term, 2016

Numerical Investigations of Single Bunch Collective Instabilities in Synchrotron Storage Ring

Jatuporn Puntree

St Catherine's College, University of Oxford

Thesis submitted in fulfilment of the requirements for the degree of Master of Science by Research at the University of Oxford

Trinity Term, 2016

Abstract

Electron beam traversing in vacuum chamber can be severely affected by collective instabilities generated from an interaction of beam with its surrounding, geometric wakefield, and the synchrotron radiation emitted, radiation wakefield. The beam dynamics is significantly influenced by such beam-wakefield interactions eventually limiting the maximum stored current. Especially in short bunch consideration which is a primary criterion for the generation of coherent synchrotron radiation (CSR), the beam instability is strongly amplified by an enhanced wakefield. The understanding of beam intensity limitation mechanism has still been underdeveloped. Therefore, the dynamical development of a bunch with a presence of collective instability needs to be scrutinized.

A numerical evaluation tool, sbtrack, is developed to be able to calculate the collective effects due to both radiation and geometric wakefields. The impedance characterization with Haissinski equation is also proposed and evidently shows that a broad-band impedance model is able to reproduce most features of intensity dependent bunch development under particular wakefield. Evaluation of longitudinal beam dynamic verifies that each kind of wakefield contributes characteristic effect to the bunch development and essentially influences resulting CSR bursting behaviour. In positive alpha, the bunch transforms from a confined barred-spiral shape to sawtooth behaviour while in negative alpha, spur-like local fluctuation is induced on the bunch phase space and enhancing the semi-chaotic fluctuation of the entire bunch when the chaotic threshold is exceeded. Beyond the chaotic threshold, bunch profile of both alpha cases are found to evolve with similar systematic development. However, such mechanism in negative alpha seems to be able to consistently occurred at higher current than positive alpha. Unexpectedly, the temporal occurrence of chaotic-harmonic evolution of a bunch is numerically discovered in negative alpha. The bunch appears to be recovered to the state of steady CSR bursting even when it has already exceeded the chaotic threshold. This phenomenon is likely suggesting a novel technique on the generation of THz CSR at much higher current than any conventional methods.

Acknowledgements

This thesis could not have been accomplished without valuable contributions from many people. First of all, I would like to thank the Development and Promotion of Science and Technology Talents Project (DPST) and Ministry of Science and Technology, The Royal Thai Government for their long-term support and encouraging me to an exciting world of science that allows me to enjoyably live and learn while having an opportunity to contribute to the wellbeing of others.

I would like to thank my supervisor, Prof Riccardo Bartolini, for support, guidance and patience during my graduate work. He taught me many lessons on how to work progressively and largely contributed to my professional growth. I also really appreciate the help from Accelerator Physics and Beam Diagnostic divisions of Diamond Light Source, especially Dr Ian Martin and Dr Guenther Rehm for many valuable advice, suggestion, discussion and all the measurements presented in this thesis.

I would also like to acknowledge my gratitude to Dr Prapong Klysubun, Prof Prayoon Songsiriritthigul of the Synchrotron Light Research Institute (SLRI) and Prof Emmanuel Tsesmelis of CERN for providing me an opportunity to have invaluable experience in Oxford.

I would like to admit my gratitude to Prof Nara Chirapatpimol, the first teacher who introduced me to get to know accelerator when I was a high school student. I would also like to thank Prof Chitrlada Thongbai and Prof Somsorn Singkarat of the Fast Neutron Research Facility (FNRF), Chiang Mai University and Prof Helmut Wiedemann of SLAC and Stanford University for motivating and promoting me to move on to a fascinating subject of accelerator physics.

I would like to express my deepest gratitude to the help from Prof Amanda Cooper-Sarkar and Ms Sue Geddes during the toughest time of my student life. In the middle of gloomy depression and bitter disappointment, their help shed the light of hope on me. Without their help I would have given up and gone back home defeated with great sorrow.

Above all, I have always gained indispensable and unconditional support from my family. Their endless love, patience and unaltered faith and confidence on me always motivate and endorse me to walk over any obstacles coming to my life.

Contents

List of Figures

List of Tables

Chapter 1

Introduction

Accelerator physics has been continuously progressing throughout many decades and endeavouring to push the beam intensity to the limit for the sake of achieving highest luminosity in collider machine as well as highest brightness of ‘light’ for accelerator-based light source in order to expand the capability to scrutinizing more profound details of atomic and molecular interactions for photon science applications.

Particularly for light source accelerator, generation of short and intense pulse of photon is the figure of merit that most synchrotron facilities desire to achieve. The light pulse with short duration compared to the dynamical interaction of the system being studied enable us the capability to resolve and track the evolution of ongoing process at atomic or molecular resolution imaging level. Furthermore, it can reduce exposure time that the sample will be affected by radiation damage which consequently leads to its degradation.

Electron beam with the bunch length short compared to the radiation wavelength is experimentally approved that it is able to generate considerably short photon pulse and radiate coherently with exponential raised of radiation power output.

However, such a bunch which is highly charged and packed within considerably short length is not easy and straight forward to be produced. There have been evidenced that the higher beam current is pushed, the more beam-induced electromagnetic fields produced from the interaction between vacuum chamber and the beam itself. Moreover, the coherent radiation which is enhanced with decreasing bunch length will be further amplified. The beam dynamics can be significantly influenced by such self-induced field and strongly disturbed by the coherent radiation eventually limiting the maximum stored current and restraint the accelerator performance accordingly. This interaction is stronger as the number of particle per bunch increases, hence the name ‘collective effects’ or ‘collective instabilities’.

Significance of the collective instability due to the self-induced field and the coherent synchrotron radiation is subjected to how do they ‘wake’ ensemble of particles in the bunch. The self-induced field is originated from the interaction between inducing particle and its surrounding. Its resulting field wakes the trailing particle. The coherent synchrotron radiation (CSR) wake is accorded to the synchrotron radiation which always travels at speed of light. At proper circumstance, such radiation catches up with leading particles. Therefore, the investigation of both beam instability sources is, in other words, a comprehensive study of collective phenomena that almost synchrotron facilities are being experienced.

Nevertheless, the beam dynamic near the current limiting threshold attains the evolution complexity due to collective instabilities, there appears to be a couple of promising beam phenomenology emerged among the dynamical complexation which is highly potent for the revolution of short and intense radiation pulse production. Many experiments have demonstrated that at proper controlled beam parameter, pushing the beam current near the threshold might induce microstructure on the longitudinal density distribution. These ‘microbunches’ behave much similar to several smaller bunches with relatively shorter length and able to emit the coherent radiation. This phenomenon has been defined as the ‘microbunching effect’ or ‘microbunching instability’.

Another distinctive beam dynamic complexation near the threshold was suggested that at proper circumstances the evolution of a bunch distribution in longitudinal phase space is apparently broken into two sub-bunches. These binary bunches periodically orbit around each other and fused together within a few synchrotron periods. There have been demonstrations that the bunch is able to sustainably oscillate between fusion and separation phase. Hence the name ‘sawtooth instability’ was coined because of its saw-tooth liked bunch length curve plotted in time domain. It is anticipated that during the separation phase both sub-bunches might behave like a couple of smaller bunches with sufficiently short length to emit the coherent radiation.

Many further experiments have been performed and evidently affirmed that these characteristic beam behaviours near the current threshold are of high potential to be practically applied to the synchrotron facilities and able to implement a capability to provide extremely powerful radiation in THz frequency range. In practice, this wavelength is ideally matched for filling the terahertz radiation gap which has been being struggled to find sufficiently intense source for many applications. However, such proper beam conditions that initiate these characteristic beam instabilities appear to be somewhat ambiguous and particularly sensitive to the beam parameter variations. Therefore, the study of such beam evolution complexity near the threshold is vital for fundamental understanding of dynamical constraints that electron bunch would be affected. Furthermore, it might be able to contribute suggestions on beam quality improvement techniques that would be allowed new measurement options to light source facilities, especially existing synchrotron storage rings.

Apart from these characteristic beam instabilities near the current threshold, the comprehensions of beam dynamics at the threshold and beyond have still been under development due to the fact that devastating beam break up would have been triggered since the threshold is reached. Therefore, machine experiment investigating these turbulent beam dynamics is subsequently impossible. The numerical investigation might be better approach to study the beam dynamics during the threshold and would be able to reveal the evolution of the bunch beyond the threshold where practical experiment is difficult.

This thesis presents the numerical investigation of the longitudinal beam dynamical evolution influenced by collective instabilities varied from sub-threshold intensity and beyond which essentially resulting the coherent radiation behaviour of the bunch. Ultimately, a bunch shortening mechanism initiated by the beam instabilities is numerically revealed. The development of a numerical tracking tool that specifically engages with the beam dynamics evolution influenced by the collective instabilities particularly at short bunch regime is reported. In addition, a new technique of impedance model characterization is also proposed.

1.1 Historical review of collective effects and beam instabilities

The subject of collective instabilities in high energy accelerator has been studied since late 1950s [1]. The summary of beam instabilities study in the first decade has been given by Richter *et al.* since 1965 [2]. Over the years, the beam instabilities research field has been significantly progressing. Many kinds of instabilities have been observed roughly around one instability mechanism every 3 years [3]. Accelerator physicists have attempted many techniques to explain and cure these instabilities, most of them had been accomplished but some of them have yet been succeeded.

Of those, the beam instabilities could be categorized into two types depending on where the electromagnetic force that cause the instability are from [4]. There are the beam instabilities developed from ‘internal force’ caused by inter-particle interaction within ensemble of particles and another one developed from ‘external force’ caused by beam-induced electromagnetic and radiation fields such as resistive wall, sawtooth and microbunching instabilities. In general, the inter-particle force exerted within the bunch is significant on the proton and ion beams but negligible on the case of electron and positron beams [5]. Therefore, most considerable instabilities occurred on electron beam are originated from the beam-induced and radiation-induced electromagnetic fields. Such fields are generated from the bunch self-radiated and self-induced when it electromagnetically interacts with beam environment. The strength of these fields are usually proportional to or, in other word, ‘collectively’ increased with the number of particles in the bunch.

When charged particle traverses inside the vacuum chamber of accelerator it interacts with the metallic surroundings. Due to discontinuities and/or finite conductivity of structure components, this interaction generates electromagnetic radiation which interacts back upon the trailing particles. Such radiation is referred to as 'wakefield'. This kind of wakefield can also be specified as 'geometric wakefield' due to its characteristic generation from the interaction of the bunch with surrounding structure. The name 'wake' of 'wakefield' was initiated from the nature of this beam-induced electromagnetic field as it only 'wakes' the trailing particles while being vanished in forward direction.

Instabilities mechanism	**Year of discovery**
Negative mass instability	1959
Resistive wall instability	1960
Beam break up instability	1966
Head-tail instability	1969
Microwave instability	1969
Beam-beam limit in colliders	1971
Potential well distortion	1971
Anomalous bunch lengthening	1974
Transverse mode coupling instability	1980
Coherent synchrotron radiation instability	1990
Sawtooth instability	1993
Electron beam-ion instability	1996
Electron cloud instability	1997
Microbunching instability	2005

Table 1.1: Beam instabilities mechanism and the year of discovery concluded by Chao, The 6th Overseas Chinese Physics Association Accelerator School, 2010 [3]

According to the position of affected particles with respect to an inducing particle, there existed two longitudinal directions of affected areas, one on forward and another one on backward directions. The definition of wakefield is literally referred to the wake force that interacts on backward direction respected to exciting particle. Nevertheless, there is also a ‘radiation wakefield’ generated from the synchrotron radiation of an exciting particle when it moves in curve trajectory. This radiation always travels at speed of light and makes the shortest displacement through the chord of curvature and encounters with other particles in the bunch on its forward direction. It behaves substantially similar to geometric wakefield in disturbing the beam dynamics.

Still the name ‘wakefield’ has already been commonly referred to any kind of self-induced or self-excited electromagnetic fields influencing the beam dynamic in accelerator.

Considering the beam instabilities near and beyond the current threshold that play the important role on dynamical development of longitudinal bunch distribution which consequently affected the coherent radiation behaviour. There are geometric wakefield and coherent synchrotron radiation (CSR) wakefield that can be accounted as major sources of beam instability. Combination of their contributions is depended on particular circumstance of machine and specific parameter setup [6].

In early 90s, Baartman and D’yachkov [7] proposed another unconventional mechanism of a newly observed beam instability emerged beyond the threshold. It was observed at the SLAC Linear Collider (SLC) damping ring [8] and also at SURF-II storage ring [9]. Experimental results show that at sufficiently high beam intensity, the bunch length signals start oscillating in saw-tooth fashion over time. They also investigated the causes of such beam turbulence and reported that it is contributed by the vacuum chamber impedance due to discontinuities of accelerator components.

The numerical studied by Baartman and D’Yachkov suggested that this ‘sawtooth’ instability is strongly relevant to a present of short bunch. They also demonstrated that the dynamical progressing of sawtooth fluctuation can be described with only an influencing geometric wakefield simply characterized with broad-band resonator model.

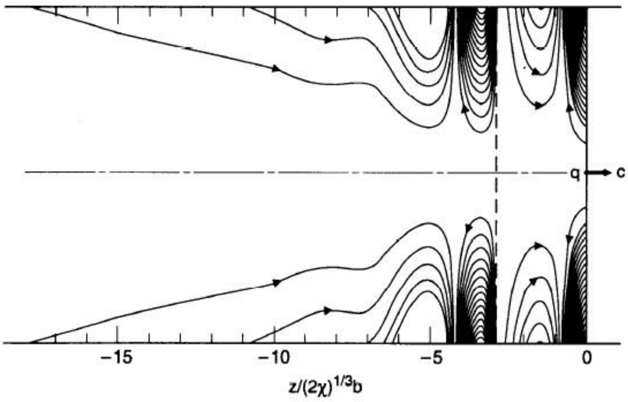

Figure 1.1: Wakefield lines in resistive wall vacuum pipe generated by a relativistic point charge q propagating in perfectly smoothed chamber. [10]

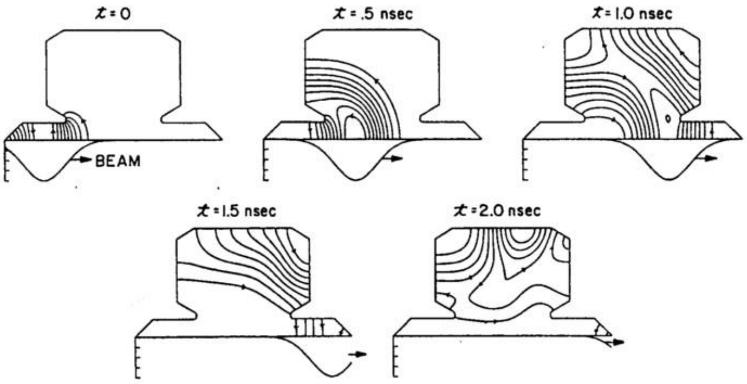

Figure 1.2: Electric field lines from a bunch when traversing an accelerator component and induced wakefields pattern [11].

Their study also affirmed an emergence of critical effect due to broad-band resonator wakefield to the bunch deformation beyond the threshold. It is much more severe than the effect due to potential well distortion which is also caused by geometric wakefield at sub-threshold intensity.

In term of the influence on resulted coherent radiation of the beam, at the separation phase, the bunch behaves as same as two identical bunches. The bunch length of each sub-bunch is relatively shorter than the initial bunch. At this characteristic length, each sub-bunch might be sufficiently short to emit the coherent radiation. Although this kind of beam dynamic scheme is interesting to be comprehended, the practical description of parameter setup that would triggers such a fluctuation has still been unknown.

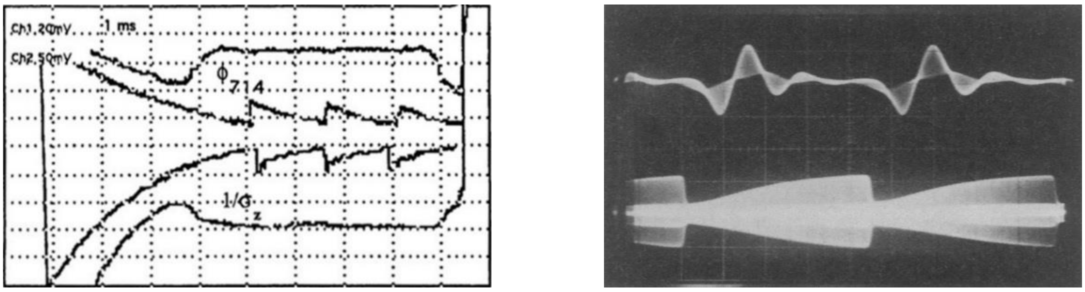

(a)

(b)

Figure 1.3: (a) The inverse bunch length signals detected at SLC damping ring exhibits sawtooth oscillation [8]. (b) Bunch length signals detected at SURF-II electron ring. Upper curve exhibits two bunches repetitive sweep signals with 2 ns/div. Lower trace monitors bunch oscillation envelope with 20 ms/div [9].

In synchrotron storage ring, the CSR instability is occurred due to the nature of accelerated charged particles that normally emit synchrotron radiation in forward direction. When the bunch length is getting shorter, the radiation will interfere constructively and turns out to be the coherent radiation. The total power output of the bunch with N particles is given by [5], [12], [13]

$$P = NP_n + N(N-1)P_n f_n \tag{1.1}$$

where P_n is the incoherent radiation power emitted by each particle and the form factor f_n is given by

$$f_n(\upsilon) = \left| \int_{-\infty}^{\infty} \lambda(z) e^{-i2\pi\upsilon z} dz \right|^2 \tag{1.2}$$

for normalization $\int_{-\infty}^{\infty} \lambda(z)dz = 1$ where $\lambda(z)$ is a longitudinal density distribution of a bunch. The first term in equation 1.1 represents the incoherent radiation which is proportional to the number of particles in the bunch. The second term stands for the coherent radiation which is proportional to the square of the number of particle. Due to all practical machine parameter, the number of particle per bunch is normally at the order of $10^9 - 10^{11}$. At such a considerably high value, the coherent radiation is therefore much more intense than the incoherent radiation at many order of magnitude.

The synchrotron radiation from electron is emitted in forward direction and travels through the chord of circular trajectory at speed of light. The radiation will catch up with the bunch and interacts with the particle ensembles. According to extremely intense power of coherent radiation, the beam dynamics of electron bunch will be enormously disturbed. This interference is fundamentally referred to as the 'free space wakefield'. Its theoretical verification was already given by Murphy *et al.* [14] and will be reviewed in the next chapter.

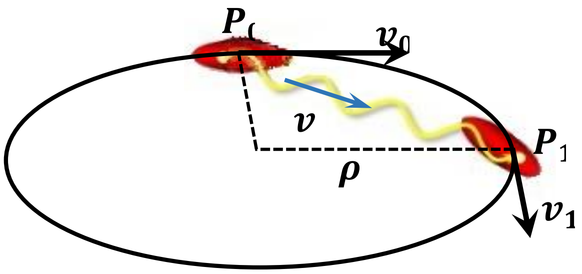

Figure 1.4: A diagram illustrates the synchrotron radiation emitted from a bunch at position P_0 and traveling at speed of light through the curvature chord. While a bunch travels along circumference from point P_0 to P_1 the radiation catches up with the bunch at position P_1.

Due to the fact that the vacuum chamber is generally made from metallic material, hence it electromagnetically interacts with the synchrotron radiation emitted from the bunch. In principle, the radiation wavelength larger than the 'shielding cut-off', λ_c, is exponentially suppressed by the vacuum chamber [12], [15]–[18]. The shielding cut-off wavelength of the vacuum chamber is defined as

$$\lambda_c = 2h\sqrt{\frac{h}{\rho}} \tag{1.3}$$

where h is the chamber cross section size and ρ is the bending radius. Since the ratio $^h/_\rho \ll 1$ and h is usually much shorter than 1 metre, it is obvious that the radiation wavelength which are able to propagate inside the chamber and influence the beam behaviour are usually smaller than or comparable to the transverse size of vacuum chamber. With these conditions the metallic wall chamber can therefore significantly influences the radiation behaviour of the particles. This phenomenon is defined as the ‘radiation shielding’.

The free space wakefield is the source of CSR instability while the radiation shielding limits the maximum radiation wavelength that involve in such instability. They have also been verified to be the induction sources of the microbunching effect on the bunch which leads to an enhancement of coherent radiation behaviour. However, increasing the beam current near the threshold is risky for beam break up and losing. Moreover, the characteristic beam condition that is able to activate such instabilities and consequent coherent radiation have still been underdeveloped. Investigating the effects of geometric and coherent synchrotron radiation wakefields as well as their combined interference on the longitudinal beam dynamics would be able to depict the significant development of the bunch due to each kind of instability source. Revealing an interference mechanism of instability sources that ‘wake’ other particles in forward and backward directions simultaneously might also contributes to the better understanding of mechanism of an emergence of beam intensity threshold.

1.2 Historical review of Coherent Synchrotron Radiation and its production schemes in storage ring based light source

Electron beam which the bunch length is short compared to the radiation wavelength has been a matter of great interest in the last decade because of its high potential to be the revolutionary of photon science. There was theoretical suggestion by Nodvick and Saxon sixty years ago [12] that the coherent synchrotron radiation (CSR) of electron bunch is increased with decreasing bunch length which the radiated power is proportional to the square of number of particles per bunch. At that time the coherent radiation had still been accounted as a ‘threat’ to the machine operation and limiting accelerator performance. It was thirty years later that the coherent radiation was reconsidered by Michel [19] to be a high potential source of intense synchrotron radiation in submillimeter wavelength. A few years later, experimental confirmation was demonstrated when Nakazato *et al.* [20] observed the coherent radiation from 180 MeV short electron bunch with 2.5 mm length from linac.

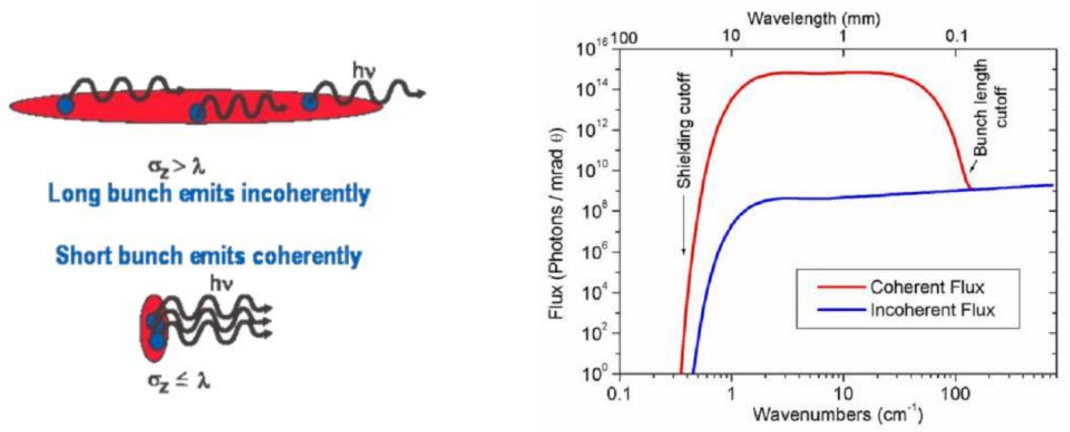

Figure 1.5: A diagram on the left compares radiation behaviour of a long bunch which radiate incoherently and a short bunch that can radiate coherently. Plot of radiation flux with wave number is shown on the right. It exhibits that the coherent radiation flux is much larger than the incoherent flux at many order of magnitude.

During the last decade of 20th century to early of 21st century, several synchrotron facilities reported their observations of the coherent emission [21]–[23]. Of which, their observations are the milestones of the generation of CSR from synchrotron storage ring although there were the bursting of CSR which had still been being impractical for light source users.

In 2002, the generation of steady state coherent synchrotron radiation from synchrotron storage ring was demonstrated by Abo-Bakr *et al.* experiment at BESSY II [24]. Their work was not only reported the detection of coherent radiation bursting but also demonstrated that the CSR in far-infrared (FIR) frequency range can be steadily generated from a controlled steady-state conditions of storage ring. The dedicated ‘low alpha mode’ optic was tuned in order to reduce the momentum compaction factor, α, which leads to bunch shortening and ultimately keeps the beam below the instability threshold.

Their results exhibited that with the low alpha optic the bunch length was shorten down to a record at approximately 2 mm from 5 mm in nominal user optic. The steady state coherent synchrotron radiation was observed at 15 mA with alpha ranging between $1.5 \times 10^{-5} - 7.3 \times 10^{-4}$ and synchrotron frequency, f_s, 1 – 3.5 kHz.

The pioneering work by Abo-Bakr *et al.* suggests that the production of steady state CSR that can practically enable new type of measurements to the user is possible by tuning appropriate beam parameters using existing storage ring. Since then the generation of coherent synchrotron radiation from storage ring has become a progressive field in synchrotron light source development. Most facilities have been attempting to develop their own CSR production scheme both by refining beam parameter or advancing to several unconventional techniques.

In principle, a bunch radiates coherently if its characteristic distance σ_c is shorter than half of the radiated wavelength [5].

$$\sigma_c \leq \frac{\lambda}{2} \tag{1.5}$$

Considering the cut-off wavelength of vacuum chamber following equation 1.3, it can be claimed that the bunch length that starts coherently radiation has to be smaller than half the size of vacuum pipe. For the current practical parameter this value would likely be scaled down to a few millimeter lengths. At such a length, both the microbunches induced by CSR instability and twin sub-bunches induced by sawtooth instability are sufficiently short to be accounted as a short bunch.

Apart from tuning up a proper beam parameter to activate the microbunching effect, several techniques have also been invented for storage ring based light source to achieve sufficiently short bunch length for CSR production. The most practical and effective technique is the beam modulation with laser pulse. Zholents and Zolotorev [25] successfully produced femtosecond pulses of synchrotron radiation by inventing the bunch slicing technique which modulates a femtosecond laser pulse with an electron beam in storage ring. The bunch is sliced into many thin bunches after the interaction with laser pulse. These thin bunches will radiate coherently with the duration of light pulse.

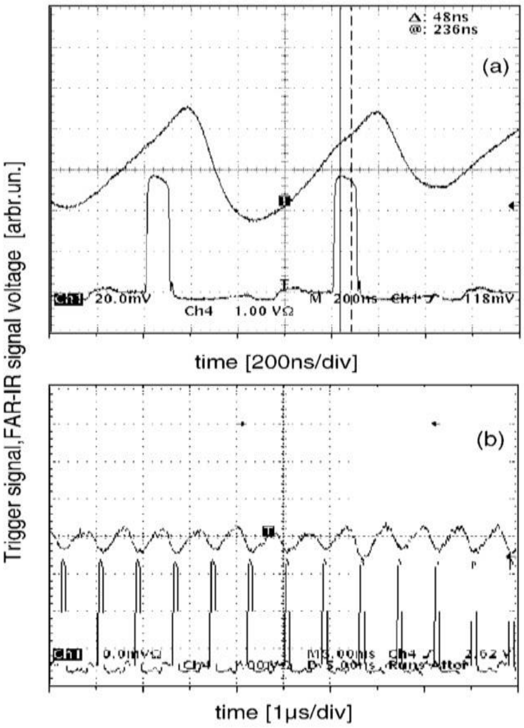

Figure1.6: Time resolved detected signals of repetitive triggering bunch and corresponding sine-like far-infrared radiation of (a) CSR bursting mode at I = 15 mA and (b) steady-state CSR mode at I = 15 mA, f_s = 1.1 kHz, α = -1.5 $\times 10^{-5}$.

Bunch deflection technique is also introduced by Zholents *et al.* [26]. This technique can be easily explained as an electron bunch is tilted vertically correlated to the longitudinal motion. During the bunch is being vertically oriented as seen in figure 1.7, the longitudinal length is temporary short enough to radiate coherently. They used two rf cavities to excited the E110 mode to create vertical displacement correlated to the longitudinal position which vertically tilts the bunch. The bunch during vertical orientation is sufficiently short to generate sub-picosecond X-ray pulse.

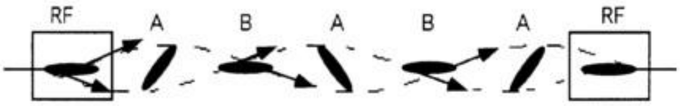

Figure 1.7: An electron bunch is vertically tilted correlated to longitudinal motion by E110 mode using two rf cavities. The longitudinal bunch length is temporary shorter during vertical orientation between two cavity and emits the CSR accordingly [26].

Another technique is the bunch compression suggested by Pellegrini and Robin [27], [28]. This technique attempts to compress the bunch by finely tune up machine parameter particularly the momentum compaction factor and rf voltage in order to achieve the quasi-isochronous condition. They proposed that at this condition the bunch length can be shortened down to a few picoseconds.

The bunch compression by elaborately adjusting beam parameter to approach the status of quasi-isochronous storage ring is a notable technique to be able to apply to existing storage ring. There is no need of installing any new hardware which is the most prominent advantage for practical machine upgrade. However, shorter bunch is being more susceptible to be interfered by the CSR wakefield. The beam dynamic influenced by collective instabilities would has to be carefully considered for practical application.

1.3 Scope and layout of thesis

This thesis concentrates both on the development of numerical tool and investigation of beam dynamics of short and intense bunch that influenced by instabilities due to geometric and coherent synchrotron radiation wakefields. The tracking code is subsequently brought into the numerical investigation of longitudinal beam dynamics affected by wakefields with beam intensity near the threshold as well as the beam dynamics evolution during threshold crossing and beyond. The resulting coherent synchrotron radiation is also revealed and compared with experimental results at each stage of instability.

In chapter 2, necessary theoretical background of longitudinal dynamic of single bunch in storage ring is reviewed. Then, chapter 3 reports the development of numerical tool and results on comparison with the experiments at BESSY II and SOLEIL storage ring. Chapter 4 proposes a new semi-numerical technique for impedance model characterization by figuring out stable Haissinski solution. Then the numerical programme and the impedance models obtained from chapter 4 are brought into the simulation with various beam parameter. The numerical results are compared with experimental detection from Diamond storage ring. The evolution of the bunch in longitudinal phase space is analyzed to examine characteristic effects of coherent synchrotron radiation and geometric wakefields at each stages of beam instability. The resulting coherent radiation behaviour under instability constraint will also be compared with experiment. All of these are reported in chapter 5. Finally, the conclusion depicts the notable phenomenology of longitudinal dynamic evolution of the beam with short bunch regime affected by collective effects. As well as the future outlook on further investigation that might significantly contributes to the study of instability threshold and CSR generation scheme applicable to existing storage ring.

Chapter 2

Single Bunch Longitudinal Dynamics in Synchrotron Storage Ring

2.1 Single particle motion

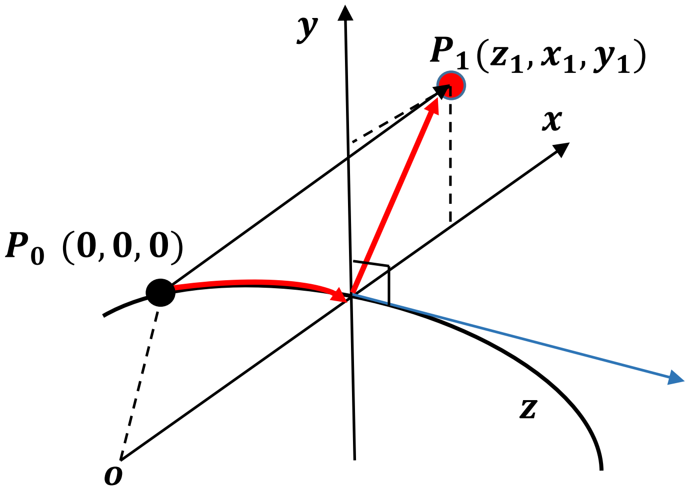

Figure 2.1: Coordinate system for longitudinal motion of particle in synchrotron and circular accelerator.

In general, synchrotron storage ring and circular accelerator denotes a particle moving in the system with the distance along its longitudinal reference trajectory from a reference point. A particle coordinate can be addressed with a position on an ideal longitudinal trajectory, z, and its position transversely deviated from the ideal path, (x, y). The transverse deviation is consisted of the horizontal distance, x, defined by its transverse deviation on the orbit plane and the vertical distance, y, defined by its deviation on the plane perpendicular to the orbit plane. Thus the particle coordinate can be referred to with a position on transverse plane, (x, y), which is perpendicular to and moving along the ideal longitudinal trajectory at the distance z from a reference point.

A particle that always traverses on the ideal longitudinal trajectory, $(z, 0, 0)$, and exactly catches up with the designed synchronous phase, ϕ_s, on arrival at the rf cavity is defined as the synchronous particle. Its coordinate is $(0, 0, 0)$ and always used as a reference point.

Considering synchrotron motion in free space and neglecting radiation damping and quantum excitation, particle losses energy by the synchrotron radiation when its trajectory is deviated which is typically on horizontal plane. An average energy lost per turn, U_0, is compensated by rf accelerating voltage. According to the facts that there is always a dispersion on the longitudinal distribution of particles in the bunch and the accelerating voltage produced in rf cavity is the time-dependent oscillation (neglecting its nonlinearity for now). Thus, this particle acceleration scheme by the rf cavity constitutes characteristic feature of particle motion in longitudinal phase space.

The synchronous phase, ϕ_s, has to be carefully designed to sustain longitudinal phase stability depending on the particle energy being considered as below or above the transition energy. The synchronous particle is designed to possess nominal beam energy, E_0, and always arrives the rf waveform exactly at the designed synchronous phase where it is compensated with energy equal amount of U_0. At the same time, other particles are off-energy and being compensated with energy deviated from the nominal value depending on its arrival phase with respect to the rf wave form.

Below transition energy, $\gamma < \gamma_t$, particle velocity has still been an energy dependent parameter and its changing due to energy deviation, $\delta = \frac{E-E_0}{E_0} = \frac{\Delta E}{E_0}$, is more significant than changing on path length, L, $\left(\frac{\Delta v/v_0}{\delta} > \frac{\Delta L/L_0}{\delta}\right)$. Higher energy particle orbits with higher velocity and arrives the cavity earlier than the synchronous one. Contrary to lower energy particle which traversing with lower velocity and arrives at the cavity later than the synchronous one. In order to establish phase stability, the higher energy particle has to be compensated with lower energy in the next turn (position B on rf voltage displayed in figure 2.2) in order to extend its arrival phase while the lower energy particle has to be compensated with higher energy (position C on rf voltage displayed in figure 2.2) in order to shorten its arrival phase at the cavity. These conditions require $0 < \phi_s < {}^{\pi}/_{2}$.

When a particle is being above transition, $\gamma > \gamma_t$, its velocity is approximately at speed of light, $v \approx c$. The changing on path length due to given energy deviation is much more significant than changing on its velocity $\left(\frac{\Delta v/v_0}{\delta} \ll \frac{\Delta L/L_0}{\delta}\right)$. Only path length has been being an energy dependent value. Higher energy particle executes longer path length and arrives at cavity with later phase than the synchronous particle (position C' on rf voltage displayed in figure 2.2) while lower energy particle executes shorter path length and arrives at earlier phase than the synchronous particle (position B' on rf voltage displayed in figure 2.2). In order to sustain phase stability, the higher energy particle has to gain less energy to reduce its path length while the lower energy has to be compensated with higher energy in order to extend its arrival phase in the next turn. Due to these requirements, synchronous phase has to be ${}^{\pi}/_{2} < \phi_s < \pi$.

Obviously, there are two parameters competing each other which leads to a synchronous phase outlining; a velocity deviation, $\frac{\Delta v}{v_0} = \frac{v - v_0}{v_0}$, and path length deviation, $\frac{\Delta L}{L_0} = \frac{L - L_0}{L_0}$, where v_0 and L_0 are velocity and path length of a synchronous particle. A quantity concerning the relationship between both parameters is a phase slip factor, η, which is related to transition energy as

$$\eta \equiv \frac{(T - T_0)/T_0}{\delta} = \frac{\Delta T/T_0}{\delta} = \frac{\Delta\phi/2\pi}{\delta} \equiv \frac{1}{\gamma_t^2} - \frac{1}{\gamma^2} \equiv \alpha - \frac{1}{\gamma^2} \tag{2.1}$$

where phase arrival, ϕ, can be related to revolution time, T, by $\phi = \frac{2\pi T}{T_0}$. Therefore $\Delta\phi = \phi - \phi_s$ is a phase difference with respect to the synchronous particle and T_0 is the revolution time of a synchronous particle. α is the momentum compaction factor which is a parameter that describes how much the path length executed by particle changes with respect to the path length of synchronous particle for a given energy deviation or, in other words, how much particle is 'packed' in aspect of energy deviation.

$$\alpha = \frac{(L - L_0)/L_0}{\delta} = \frac{\Delta L/L_0}{\delta} \tag{2.2}$$

Equation 2.1 shows that at below transition, $\eta < 0$ and ${}^{\Delta\phi}/_{\delta} < 0$ which implies that higher energy particle arrives earlier than synchronous particle. At above transition, $\eta > 0$ and ${}^{\Delta\phi}/_{\delta} > 0$ which implies that higher energy particle executes longer path length hence arriving later than synchronous particle.

Consequently, particles deviated from the synchronous phase experience a restoring force and are bounded within certain maximum oscillation amplitude. The dynamical motion of particle constitutes the 'synchrotron oscillation' in which off-energy particles oscillate about the synchronous phase. Considering linear approximation of the rf voltage seen by particle at arrival phase ϕ and assuming small oscillation amplitude, the differential equation of phase deviation, $\psi = \Delta\phi = \phi - \phi_s$, can be written as a damped oscillation as [4], [29]

$$\ddot{\psi} + 2\alpha_E\dot{\psi} + f_s^2\psi = 0 \tag{2.3}$$

where f_s is the synchrotron frequency given by

$$f_s = f_{rev}\sqrt{\frac{\alpha h e V_{rf}\sin\phi_s}{2\pi E_0}} \tag{2.4}$$

with h the harmonic number given by $h = \frac{f_{rf}}{f_{rev}}$, V_{rf} the rf voltage, f_{rf} the rf frequency, f_{rev} the revolution frequency and α_E the damping decrement defined by

$$\alpha_E = \frac{1}{2T_0}\frac{dU}{dE} \tag{2.5}$$

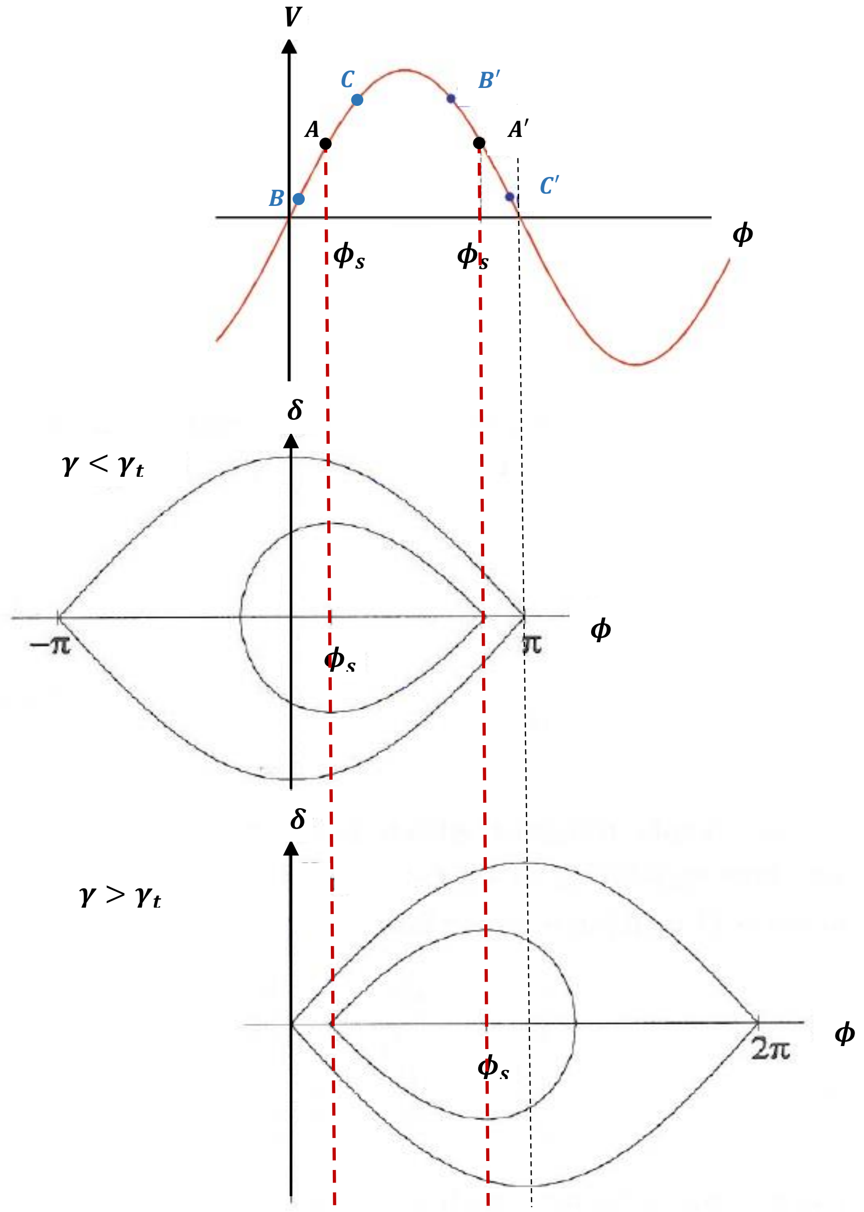

Figure 2.2: Diagrams illustrate the rf voltage (top) together with rf buckets below the transition (middle) and above the transition (bottom). A and A' represent the synchronous particles in the case of below and above transition respectively. B and B' represent the leading particles while C and C' refer to the trailing particles in the case of below and above transition respectively. The symmetric buckets depict the stationary rf buckets where there is no particle acceleration. The fish-like buckets illustrate accelerating rf buckets which face to opposite direction depending on their phase stability requirement.

In absent of the damping term, equation 2.3 becomes

$$\ddot{\psi} + f_s^2\psi = 0 \tag{2.6}$$

Therefore, longitudinal displacement, τ, or phase arrival respected to synchronous phase, $\psi = \phi - \phi_s$, and energy deviation, δ, of all particles in a bunch can be plotted as longitudinal phase space. The motion of each particle in longitudinal phase space evolves as a closed smooth elliptical orbit (due to the fact that radiation damping, quantum excitation and collective effects are being neglected) around the reference point where the synchronous particle is situated. At below transition, $\eta < 0$, bunch distribution in phase space rotates counter-clockwise whereas rotating clockwise when being above transition, $\eta > 0$. At the transition energy, $\eta = 0$, the longitudinal beam dynamic achieves the 'isochronous' condition. Bunch distribution in phase space is frozen and the accelerating bucket is also flipped to another side.

The time dependent rf voltage and the designed synchronous phase essentially form stable region in longitudinal phase space called 'rf bucket' where the particle lying inside the separatrix is stably orbiting while the particle located outside is unstable and eventually lost.

In practice, there is always the radiation damping due to the fact that the particle evolving within positive energy deviation region (upper half of phase space ellipse) its energy lost is greater than that compensated by the rf cavity then the energy deviation tends to decrease. Consecutively, when it evolves into negative energy deviation region (lower half of phase space ellipse), its energy lost is smaller than amount it receives from rf cavity then the energy deviation also tends to decrease. Therefore, when the radiation damping is taken into account the particle trajectory spirals down to a stable fixed point.

Nevertheless, there is also the quantum excitation effect that competes with the contraction of energy deviation and results on an equilibrium spread of particles energy.

Considering both the radiation damping and quantum excitation of synchrotron radiation, the equilibrium energy spread in storage ring with isomagnetic guiding field of curvature radius ρ_0 can be obtained from [30]

$$\left(\frac{\sigma_E}{E}\right)^2 = \frac{C_q\gamma^2}{J_\epsilon\rho_0} \tag{2.7}$$

where J_ϵ is the damping partition number and C_q is given by

$$C_q = \frac{55}{32\sqrt{3}}\frac{\hbar c}{mc^2} = 3.8319 \times 10^{-13}\ m$$

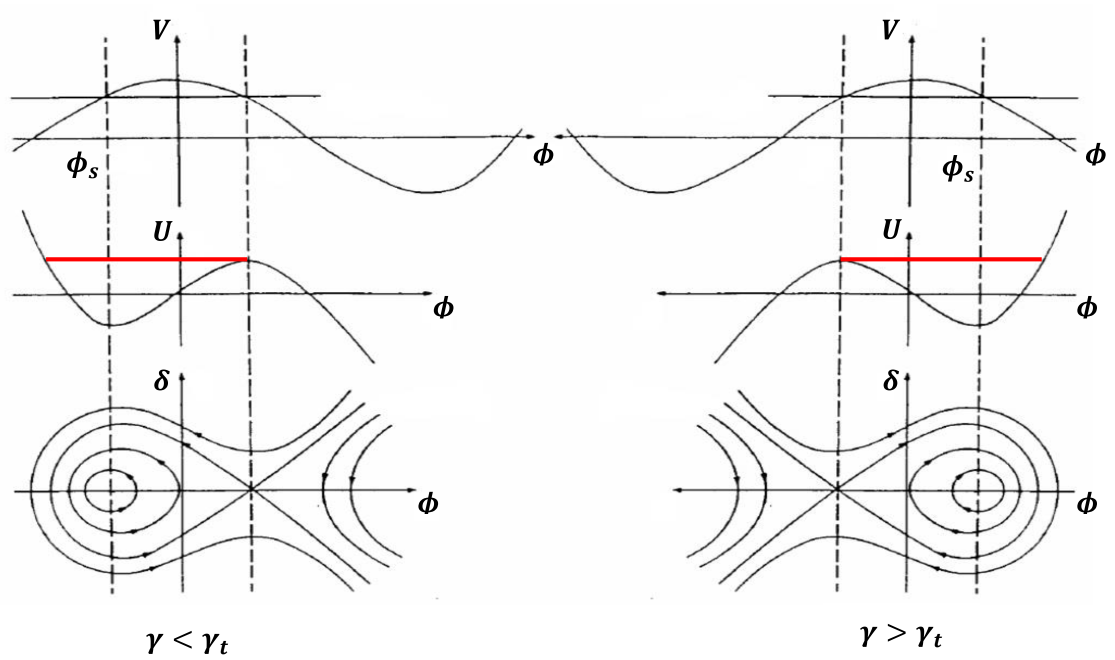

Figure 2.3: Accelerating voltage, potential and rf buckets of particle below (left column) and above (right column) transition. The particles located within the closed separatrix stably execute a completed orbit around storage ring. The plot of accelerating potential also depicts stable region between the curve and the red line. The stable and unstable fixed points are accordingly created from this regime.

The natural bunch length, σ_L, can be determined from energy spread by a formula

$$\sigma_L = \frac{c\alpha}{2\pi f_s}\sigma_E \tag{2.8}$$

According to an expression of synchrotron frequency in equation 2.4 and equations 2.8, it can be concluded that

$$\sigma_L \propto \sqrt{\alpha} \tag{2.9}$$

which obviously implies that the bunch length can be reduced by decreasing the momentum compaction factor.

2.2 Kinetic theory of longitudinal beam dynamics

The evolution of longitudinal phase space of particle in synchrotron machine is generally characterized by time derivative of longitudinal displacement, τ', or phase deviation, ψ', and time derivative of energy deviation, δ'. Ignoring the radiation damping and quantum excitation, the equation of motion can be written as [4], [27], [31]–[33].

$$\psi' = 2\pi\alpha(\delta)\delta \qquad (2.10a)$$

$$\delta' = \frac{eV_{rf}}{2\pi E_0}(\sin(\psi + \phi_s) - \sin\phi_s) \qquad (2.10b)$$

with $\psi = \phi - \phi_s$. Longitudinal equation of motion can also be rigorously described by the Hamiltonian. Deducting from equation 2.10a and b, the Hamiltonian can be written as

$$H = \frac{2\pi\alpha\delta^2}{2} + \frac{eV_{rf}}{2\pi E_0}[\cos(\psi + \phi_s) - \cos\phi_s + \psi\sin\phi_s] \qquad (2.11)$$

where ψ and δ are canonical conjugates which satisfy relations

$$\frac{\partial H}{\partial \delta} = \frac{d\psi}{dt} \ and \ \frac{\partial H}{\partial \psi} = -\frac{d\delta}{dt}$$

2.2.1 Vlasov equation

According to Liouville’s theorem which states that phase space density of particles is conserved for non-dissipative system. The particle distribution in phase space evolves over time similarly to an incompressible liquid. Hence the occupied area is constant.

Let phase space density is $\Psi(q,p,t)$, it can be written as

$$\frac{d\Psi(q,p,t)}{dt} = 0 \tag{2.12}$$

where q is normally related to physical displacement coordinate and p is usually connected to momentum or energy coordinate. Then the absolute partial differential equation with respect to q, p and t can be written as

$$\frac{d\Psi(q,p,t)}{dt} = \frac{\partial\Psi(q,p,t)}{\partial t} + \frac{\partial\Psi(q,p)}{\partial q}\frac{dq}{dt} + \frac{\partial\Psi(q,p)}{\partial p}\frac{dp}{dt} = 0$$

or

$$\frac{d\Psi(q,p,t)}{dt} = \frac{\partial\Psi(q,p,t)}{\partial t} + \dot{q}\frac{\partial\Psi(q,p)}{\partial q} + \dot{p}\frac{\partial\Psi(q,p)}{\partial p} = 0 \tag{2.13}$$

This is an expression of Vlasov equation that exhibits the conservation of phase space density according to Liouville’s theorem. Due to its implication, the evolution of longitudinal bunch distribution over time can be subsequently calculated from Vlasov equation. For stationary case

$$\frac{\partial\Psi(q,p,t)}{\partial t} = 0$$

then Vlasov equation is transformed to

$$\dot{q}\frac{\partial\Psi(q,p)}{\partial q} + \dot{p}\frac{\partial\Psi(q,p)}{\partial p} = 0 \tag{2.14}$$

Substitutes the expressions of canonical conjugates

$$\dot{q} = \frac{\partial H(q,p)}{\partial p} \quad , \quad \dot{p} = -\frac{\partial H(q,p)}{\partial q} \tag{2.15}$$

then it becomes

$$\frac{\partial\Psi}{\partial q}\frac{\partial H}{\partial p} - \frac{\partial\Psi}{\partial p}\frac{\partial H}{\partial q} = \{\Psi, H\} = 0 \tag{2.16}$$

This expression is the Poisson bracket which specifies that for a particular system of a function of variable pair (p, q), its stationary distribution can be defined as a function of Hamiltonian only. Therefore, the corresponding stationary distribution of particles in the bunch can be obtained from Hamiltonian by solving Vlasov equation.

On the other hand, considering the dissipation of system consequently modifies r.h.s. of Vlasov equation in 2.13 with non-zero damping terms. The radiation damping and random forces are appeared and transform Vlasov equation to an expression [33]

$$\frac{d\Psi(q,p,t)}{dt} = \frac{\partial\Psi(q,p,t)}{\partial t} + \dot{q}\frac{\partial\Psi(q,p)}{\partial q} + \dot{p}\frac{\partial\Psi(q,p)}{\partial p} = 2\alpha_E\Psi(q,p) + D\frac{\partial^2\Psi(q,p)}{\partial E^2} \quad (2.17)$$

where the first and the second terms of the r.h.s. represent the radiation damping and random fluctuation due to quantum excitation respectively. This is an expression of Vlasov-Fokker-Planck (VFP) equation that extends the explanation by Vlasov equation to include the dissipative damping and stochastic fluctuation effects.

The VFP equation was brought into the study of beam stability by linearizing the equation about particular distribution, λ_i, and figure out the post-evolving distribution, λ_f, whether it would have still been bounded or broken. Considering the case of longitudinal motion of electron beam influenced by wakefield, the equilibrium solution of the VFP equation is nonlinear integral equation suggested by Haissinski [34]–[37]

$$\lambda_0 = \frac{\exp\left[-\frac{q^2}{2} + I\int_q^\infty V_{ind}(q')dq'\right]}{\int_{-\infty}^{\infty}\exp\left[-\frac{q^2}{2} + I\int_q^\infty V_{ind}(q')dq'\right]dq} \quad (2.18)$$

The parameter I is the normalized current defined by [36]

$$I = \frac{2Nr_e}{\gamma c Z_0 \nu_s \sigma_\varepsilon} \quad (2.19)$$

where $N, r_e, \gamma, c, \nu_s, Z_0$ and σ_ε are number of particles in the bunch, the classical electron radius, the Lorentz relativistic factor, the speed of light, the synchrotron tune, the vacuum impedance and the natural relative energy spread respectively. And $V_{ind}(q)$ is an induced voltage according to a bunch with distribution $\lambda(q)$ which is given by

$$V_{ind}(q) = \int_{q}^{\infty} \lambda(q) W(q' - q) dq \tag{2.20}$$

where q is relative longitudinal position normalized with bunch length, σ_z, given by $q = {}^{z}/_{\sigma_z}$ and $W(q)$ is the wake function.

This expression is widely used to estimate equilibrium distribution of longitudinal density of the bunch under particular wakefield.

2.2.2 Application of Vlasov-Fokker-Planck equation on collective instability

Oide and Yokoya solved Vlasov equation to obtain the equilibrium longitudinal bunch density of electron beam influenced by self-induced wakefield [36]. The longitudinal motion of a single bunch electron beam influenced by collective wakefield is described by

$$\frac{\partial\Psi}{\partial\theta} + p\frac{\partial\Psi}{\partial q} - q\frac{\partial\Psi}{\partial p} - I\frac{\partial\Psi}{\partial p}\int_{-\infty}^{\infty} \lambda(q', \theta)\, W(q' - q) dq' = 2\alpha_E \frac{\partial}{\partial p}\left(p\Psi + \frac{\partial\Psi}{\partial p}\right) \tag{2.21}$$

where $\lambda(q, \theta)$ is the longitudinal density defined by

$$\lambda(q, \theta) = \int_{-\infty}^{\infty} \Psi(q, p, \theta)\, dp \tag{2.22}$$

and normalized as

$$\int_{-\infty}^{\infty} \lambda(q, \theta)\, dq = 1 \tag{2.23}$$

The variables p, q and θ are given by

$$p = \frac{E - E_0}{E_0 \sigma_\varepsilon} = \frac{\delta}{\sigma_\varepsilon} \quad , \quad q = \frac{z}{\sigma_z} \quad , \quad \theta = \omega_s t$$

where $\delta, \sigma_\varepsilon, z, \sigma_z, \omega_s$ and t are the energy deviation, the natural relative energy spread, the longitudinal position, the natural bunch length, the phase of synchrotron motion and the evolving time respectively.

The VFP equation in 2.17 can be solved with perturbation method by separating $\Psi(q,p,\theta)$ into stationary part, $\Psi_0(q,p)$, and oscillating perturbation, $\Psi_1(q,p,\theta)$

$$\Psi(q,p,\theta) = \Psi_0(q,p) + \Psi_1(q,p,\theta)$$

According to [34], the static solution is

$$\Psi_0(q,p) = \frac{\lambda_0(q)}{\sqrt{2\pi}} \exp\left[-\frac{p^2}{2}\right] \tag{2.24}$$

Since $\Psi_0(q,p)$ is deducted from a Gaussian distribution of p and λ_0, the Fokker-Planck term (r.h.s of equation 2.17) is vanished. Therefore, the Haissinski integral equation is eliminated to

$$\lambda_0(q) = \frac{1}{\kappa} \exp\left[-\frac{q^2}{2} + I \int_q^\infty \int_{q'}^\infty \lambda_0(q'') W(q'' - q') dq'' dq'\right] \tag{2.25}$$

with the limit of low current and weak collective effects applied. A constant κ can be obtained from normalization condition shown in formula 2.23.

2.3 Synchrotron radiations

The synchrotron radiation from storage ring appears to the observer as periodic flash of light with frequency governed by harmonics of the revolution frequency, $h\omega_0$, of electron bunch in storage ring. This frequency spans from the revolution frequency (or the cut-off frequency which defined by transverse size of vacuum chamber) to the critical photon frequency, ω_c. Beyond the critical frequency, the photon flux is significantly fall off. The cut-off or ‘shielding cut-off’ frequency is given by the fact that the synchrotron radiation with wavelength longer than the cut-off wavelength given in equation 1.3 is greatly suppressed by the chamber wall.

Thus the lowest synchrotron radiation frequency is limited by either the cut-off frequency or revolution frequency depending on which one is higher.

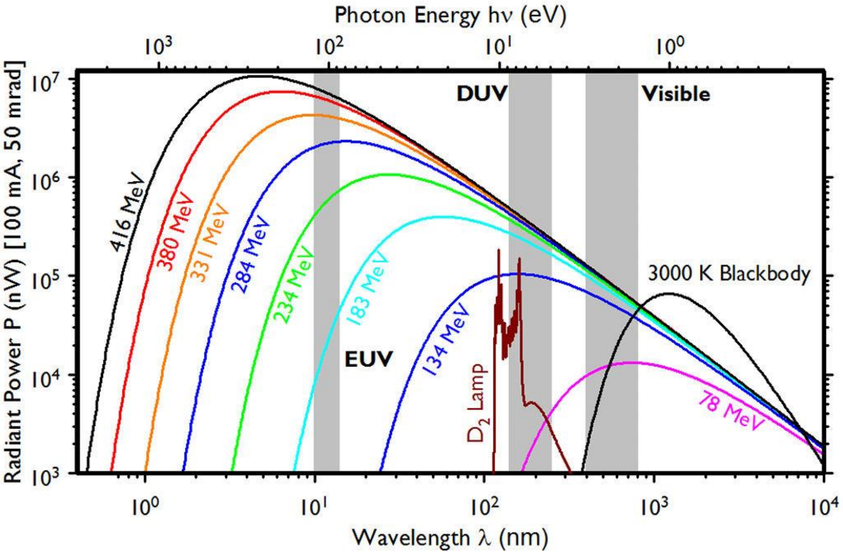

Figure 2.4: Synchrotron radiation spectrum emitted from Synchrotron Ultraviolet Radiation Facility (SURF) storage ring at various photon energy compared to radiation from a 3000 K black body and deuterium lamp. [38] The maximum wavelength is typically determined by the cut-off wavelength, λ_c, defined by equation 1.3 while the minimum wavelength is corresponded to the critical photon frequency, ω_c.

The critical photon frequency is principally defined by the duration of photon emitted by a bunch detected at the observer. By manipulating with some practical units, the critical photon frequency for electron is given by [4]

$$\omega_c = C_c \frac{E^3}{\rho} \tag{2.26}$$

where

$$C_c = \frac{3c}{2(mc^2)^3} = 3.37 \times 10^{18} \qquad \left[\frac{m}{s \cdot GeV^3}\right] \tag{2.27}$$

Then the critical photon energy can be defined by

$$\epsilon_c = 2.218 \frac{E^3[GeV^3]}{\rho[m]} = 0.0665 E^2 B \quad [GeV^2 \cdot kG] \tag{2.28}$$

where E is the beam energy and ρ is a radius of curvature (not a radius of storage ring).

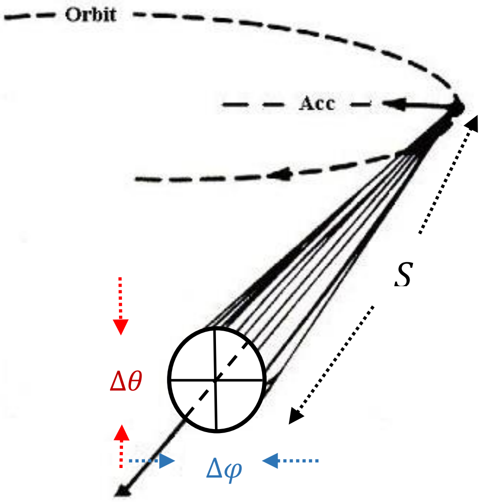

Figure 2.5: Synchrotron radiation cone at distance S from a radiated point. The deflection on orbit plane is defined to parameter φ and the deflection on the plane perpendicular to orbit plane is defined to parameter θ.

In order to characterize the photon intensity of synchrotron radiation, a parameter 'photon flux per unit solid angle per unit bandwidth' from a circulating beam current I_b is defined by

$$\frac{d^2\Phi_{ph}}{d\theta d\varphi} = C_\Omega E^2 I_b \frac{\Delta\omega}{\omega}\left(\frac{\omega}{\omega_c}\right)^2 K^2_{2/3}(\xi)F(\xi,\theta) \tag{2.29}$$

where φ is a deflecting angle on electron orbit plane and θ is a deflecting angle perpendicular to the orbit plane demonstrated in figure 2.5.

$$C_\Omega = \frac{3\alpha}{4\pi^2 e(mc^2)^2} = 1.3273 \times 10^{16} \quad \left[\frac{photons}{s \cdot mrad^2 \cdot GeV^2 \cdot A}\right] \tag{2.30}$$

with α is the fine structure constant and

$$F(\xi,\theta) = \begin{cases} 1 & ,\theta = 0 \\ (1+(\gamma\theta)^2)^2\left(1+\dfrac{(\gamma\theta)^2}{1+(\gamma\theta)^2}\dfrac{K^2_{1/3}(\xi)}{K^2_{2/3}(\xi)}\right) & otherwise \end{cases} \tag{2.31}$$

where $K_{1/3}$ and $K_{2/3}$ are the modified Bessel's functions with argument ξ defined by

$$\xi = \frac{1}{2}\frac{\omega}{\omega_c}(1 + (\gamma\theta)^2)^{\frac{3}{2}} \tag{2.32}$$

The prominent advantage of synchrotron radiation is its highly polarization in both the orbit plane which also called 'σ-mode' and a plane perpendicular to the orbit plane which also called 'π-mode'. The terms in the second parenthesis of equation 2.31 prescribe the photon flux related to each mode. The first term which is equal to unity determines the photon flux in σ-mode while π-mode is defined by the second term.

Equation 2.29 describes the photon flux in both σ and π modes. In practical usage of synchrotron radiation, the beam lines usually make use of the σ-mode and align their experiment stations along the ring circumference. Accordingly, the photon flux deviation with respect to the deflecting angle on electron orbit plane is important to be verified. Then equation 2.29 can be integrated over all vertical angle, θ, and becomes

$$\frac{d\Phi_{ph}}{d\varphi} = \frac{4\alpha}{9}\gamma\frac{I}{e}\frac{\Delta\omega}{\omega}S\left(\frac{\omega}{\omega_c}\right) \tag{2.33}$$

where α in the fine structure constant, γ is the Lorentz relativistic factor, φ is the deflecting angle of the beam on the orbit plane and function $S\left({}^{\omega}/_{\omega_c}\right)$ is given by

$$S\left(\frac{\omega}{\omega_c}\right) = \frac{9\sqrt{3}}{8\pi}\frac{\omega}{\omega_c}\int_{\omega/\omega_c}^{\infty} K_{5/3}(\zeta)d\zeta \tag{2.34}$$

which $K_{5/3}(\zeta)$ is a modified Bessel's function. Equation 2.33 can be manipulated with practical units and reconsidered to

$$\frac{d\Phi_{ph}}{d\varphi} = C_\varphi EI\frac{\Delta\omega}{\omega}S\left(\frac{\omega}{\omega_c}\right) \tag{2.35}$$

where

$$C_\varphi = \frac{4\alpha}{9emc^2} = 3.967 \times 10^{19} \qquad \left[\frac{photons}{s \cdot rad \cdot A \cdot GeV}\right] \tag{2.36}$$

2.4 Coherent Synchrotron Radiation

According to the radiation flux plotted with wave number in figure 1.5, it demonstrates that the synchrotron radiation is emitted with broad spectrum. The lowest frequency (wave number) is equal to the revolution (or shielding cut-off) frequency of electron bunch in storage ring and the highest frequency typically falls just beyond the critical photon frequency.

Fundamentally, when electron bunch length is comparable to or shorter than the radiated wavelength the synchrotron radiation from electron ensembles is constructively interfered. The bunch emits radiation in similar aspect to a single electron with equal charge of the whole bunch. The radiated power is extremely enhanced due to this ‘coherent synchrotron radiation’ (CSR) scheme.

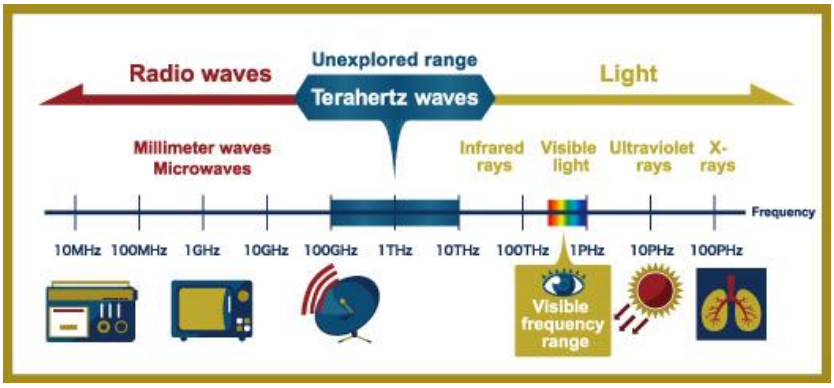

Figure 2.6: A diagram illustrating the terahertz (THz) and sub-terahertz region that bridges the electronics and optics worlds. Spectroscopy at this frequency range has just been approachable in the last decade with moderate intensity radiation produced from an interaction of laser and nonlinear crystals [39], [40]. The production of CSR from short and intense pulses of electrons in storage ring demonstrates possible revolutionary to THz spectroscopy.

The bunch length sufficiently short to generate the CSR and practicable to be produced from synchrotron storage ring is typically in the scale of a few millimetres length or picoseconds duration which corresponds to the terahertz radiation frequency. Therefore, due to extremely high radiation flux of the CSR together with the frequency range produced, the generation of intense pulse of terahertz radiation by storage ring light source is very high potential technique to fill the terahertz gap.

The coherent synchrotron radiation can be distinguished into two types, the temporal coherence and spatial coherence. The temporal coherent radiation is occurred when the bunch length is comparable to or shorter than the radiation wavelength. The production of temporal coherence can be fundamentally performed by shortening electron bunch as much as possible. In contrast, the spatial coherence can be occurred from longer bunch with transverse beam emittance smaller than the radiation wavelength though it is far more difficult to achieve in practical manner.

2.4.1 Temporal coherence

Considering the radiation field at frequency ω with phase φ_k from a single electron is

$$\varepsilon_k \propto e^{i(\omega t+\varphi_k)} \tag{2.37}$$

where

$$\varphi_k = \frac{2\pi}{\lambda} z_k \tag{2.38}$$

with z_k is a longitudinal position of a single electron and λ is the radiation wavelength.

The radiation power is proportional to the square of radiation field, then summing over all N electrons in a bunch consequently yields

$$P(\omega) \propto \sum_{k,j}^{N} e^{i(\omega t+\varphi_k)} e^{-i(\omega t+\varphi_j)} = N_e + \sum_{k\neq j}^{N} e^{i(\varphi_k-\varphi_j)} \tag{2.39}$$

Assuming a bunch with Gaussian distribution with the standard length σ

$$\Psi_g(z) = \frac{N}{\sqrt{2\pi}\sigma} exp\left(-\frac{z^2}{2\sigma^2}\right) \tag{2.40}$$

According to equation 2.38 and 2.39, with considering the Gaussian density distribution in equation 2.40 and integrating over all phase, the radiation power can be written as

$$P(\omega) \propto N + \frac{N(N-1)}{2\pi\sigma^2} I_1 I_2 \tag{2.41}$$

where the integrals I_1 and I_2 are defined as the radiation integrals [4]

$$I_1 = \int_{-\infty}^{\infty} exp\left(-\frac{z^2}{2\sigma^2} + i2\pi\frac{z}{\lambda}\right) dz$$

$$I_2 = \int_{-\infty}^{\infty} exp\left(-\frac{s^2}{2\sigma^2} + i2\pi\frac{s}{\lambda}\right) ds$$

with $z = {}^{\lambda\varphi_k}/_{2\pi}$ and $s = {}^{\lambda\varphi_j}/_{2\pi}$. Therefore the total radiation power at frequency $\omega = {}^{2\pi c}/_{\lambda}$ can be written as

$$P(\omega) = P_n(\omega)N + N(N-1)P_n(\omega)f(\omega) \tag{2.42}$$

where $P_n(\omega)$ is the radiation from a single electron and $f(\omega)$ is the form factor given by the square of Fourier transform of the bunch density distribution

$$f(\omega) = \left| \int_{-\infty}^{\infty} \lambda(z) e^{-i2\pi\omega z} dz \right|^2 \tag{2.43}$$

for

$$\int_{-\infty}^{\infty} \lambda(z) dz = 1$$

where $\lambda(z)$ is a longitudinal density distribution of a bunch.

According to equation 2.42, the first term refers to the incoherent radiation which the radiated power is directly proportional to the number of electron in a bunch. The second term is the coherent radiation power which the radiation power is depended on the square of number of electron per bunch.

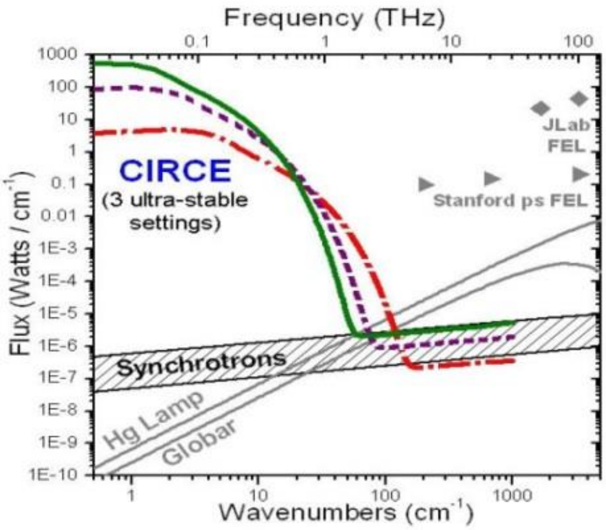

Figure 2.7: Calculated photon flux for Coherent InfraRed CEnter (CIRCE), a proposed storage ring dedicated for coherent synchrotron radiation production at Advanced Light Source, compared among three modes of stable CSR production, incoherent synchrotron radiation and thermal far-IR sources [41]. CSR flux is obviously higher than incoherent radiation at many order of magnitude.

In principle and practical aspects, linear accelerator can typically push the bunch length down to femtosecond duration. Furthermore, the bunch length can also be further shortened with the bunch compressor. As a result, the CSR was firstly observed from 180 MeV short electron bunches of 2.5 mm at the Tohoku 300-MeV linac of Tohoku University [20]. More or less ten years later, the first CSR from storage ring were observed at several facilities [21]–[23]. Since then the generation of CSR has become the matter of great interest for most synchrotron facilities because it would potentially enable them a new measurement technique provided for user.

Several techniques have been invented to produce extremely short electron bunch in storage ring in order to enable the coherent radiation production scheme. The energy modulation with laser pulse technique, femtoslicing, was proposed and firstly demonstrated by Schoenlein *et al.* [42]. Then experimental demonstration to generating femtosecond x-ray pulse was presented by BESSY team [43]. Generation of subpicosecond x-ray pulse using rf orbit deflection was also proposed in 1999 [26]. As well as tilting a bunch with dipole kicker was also demonstrated to be able to generate a few picosecond x-ray pulse [44].

2.4.2 Spatial coherence

Basically, reducing transverse beam emittance also reduces the source size of photon beam. However, this procedure only takes effect until the 'diffraction limit' is occurred. Considering the Fraunhofer diffraction integral with the case of Gaussian particle beam instead of conventional light source yields the 'diffraction limited photon emittance' which can be written as

$$\epsilon_{ph,x,y} = \frac{1}{2}\sigma_r\sigma_{r'} = \frac{\lambda}{4\pi} \tag{2.44}$$

Reducing the electron beam emittance below this value would not results further reduction of photon beam emittance, nevertheless it would rather produce the spatial coherent radiation. The transverse beam emittance must be met the condition

$$\epsilon_{x,y} \leq \frac{\lambda}{4\pi} \tag{2.45}$$

in order to emits the spatial coherent photon beam.

The degree of spatial coherence is increased as the transverse beam emittance decreased. Consequently, the spatial coherent radiation is more difficult to achieve at higher radiation frequency due to an increasing difficulty to reach lower emittance.

2.5 Geometric wakefield and impedance

As mentioned in previous chapter, the wakefield is usually categorized into two types, the geometric and the radiation wakefields. While the radiation wakefield is occurred due to an influence of the synchrotron radiation emitted from particle in the same bunch, the geometric wakefield is emerged from the interaction between an induced charge particle and its surroundings.

Because of the accelerator structure is normally consisted of numerous components which each of them has its own characteristic properties such as physical shape and finite electrical conductivity. The deviation of characteristic properties of entire accelerator structure leads to complicated differentiation in electromagnetic interactions with the induced particle.

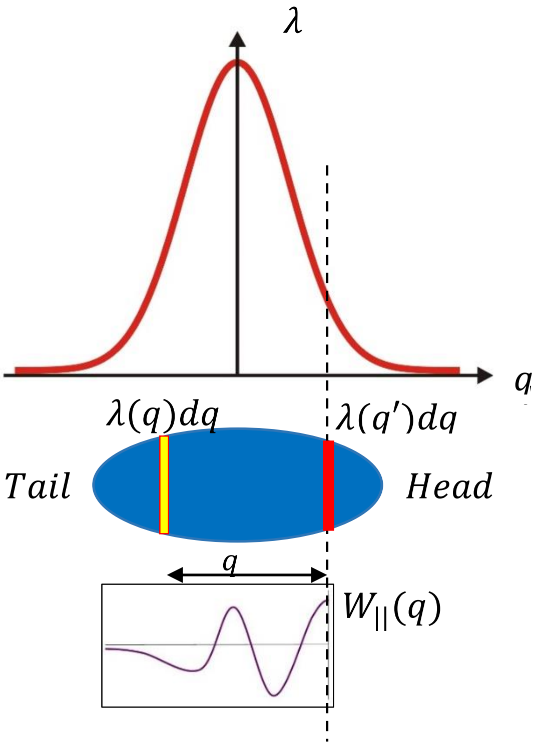

Figure 2.8: Diagram exhibits Gaussian bunch distribution with short range geometric wakefield. An exciting element denoted by $\lambda(q')dq$ induces the wake potential that subsequently affects all the trailing elements. The total wake influences on the element $\lambda(q)dq$ can be obtained from an integration of the wake induced by all particles ahead.

Noticeably, this kind of wakefield is initiated from an induced charged and the imperfections of environment that the particle surpassed. Thus an idea of simulating the imperfections of beam environment as a function of longitudinal charged distribution was arisen. Such function is defined as a ‘beam impedance’.

The wakefield is generally represented with an induced force formulated as a function of longitudinal displacement between induced charge and affected element. This function is called ‘wake function’. Due to the fact that the wakefield is composed of contributions from numerous accelerator components, the more practical way to analyst wakefield and its effects on the beam dynamics is investigating the system in frequency domain. Corresponding wakefield in frequency domain can be generated by Fourier transformation of the wake function which is consequently called ‘impedance’.

The idea of representing accelerator environment with the impedance was firstly introduced by Sessler and Vaccaro in 1967 [45]. Since then, the methods of impedance calculation have been developed by many accelerator physicists. Novokhatski *et al.* [46] developed a calculation for cylindrically symmetric structures in 1998, seven years later Zagorodnov and Weiland overcame difficulty on structure symmetry by developing a calculation for 3D structure [47].

The advancement of high performance computing facilities has made enormous encouragement to the impedance identification. The 3D electromagnetic field simulator GdfidL [48] and the finite-element-method-based electromagnetic field solver, MAFIA [49], were brought into the impedance configuration of individual device as well as a commercial class electromagnetics simulation software from CST Studio [50] has also been developed to tackle this complicated task. Even though these analytical impedance calculation softwares are able to provide sensible results on solving impedance of an individual device, calculating impedance of the whole storage ring has still been being too difficult to be accomplished in practice.

According to this difficulty, the idea of depicting impedance of the whole accelerator structure with a single impedance model characterized by equivalent simple resonator circuit was proposed. Nevertheless, the real vacuum chamber is normally assembled with huge number of discontinuities. Its impedance is very complicated and contains many resonances covering wide range of frequency.

In general, only the short range wakefield is applicable to the consideration of single bunch dynamics. It is quickly dissolved within short distance behind an inducing particle. Accordingly, it implies that the single bunch only ‘senses’ the wakefield that is excited within a short duration compared to the bunch length. Such a short duration of excitation corresponds to broad-band impedance in frequency domain.

The most practical model is the broad-band resonator or usually called ‘LRC resonator’ which a resistor, an inductor and a capacitor are connected. This model was firstly introduced to be used in machine impedance characterization by Hofmann [51]. Alongside, individual model of purely resistive, inductive and/or capacitive impedance are usually applied in order to specifically characterize explicit property on beam retardation of impedance model. They are also frequently used in implementing the LRC resonator to make appropriate model tune up to accompany with experimental results. The serial connected resistive and inductive impedances model was also brought to engage with the Accelerator Test Facility (ATF) damping ring impedance modelisation and well fitted with experimental result [35].

In general, the effects of wakefield are apparently indicated by bunch lengthening and energy spreading with respect to an increasing bunch current. An appropriate impedance model would have to be able to simulate these intensity dependent potential well distortion behaviours observed in experiment.

2.5.1 Broad-band resonator impedance model

In time domain, due to short duration of a single bunch, only the short range wakefield affects the beam dynamic. Transforming the system of interest into frequency domain, it can be subsequently figured out that only the wakefield with broader frequency bandwidth compared to the bunch spectrum is able to be resolved by the bunch. Such a smoothed impedance can be characterized by a broad-band resonator with low quality factor. The broad-band resonator generates longitudinal wakefield given by [10]

$$W_m(z) = \begin{cases} 0 & ,z > 0, \\ \alpha R_s & ,z = 0, \\ 2\alpha R_s e^{\alpha z/c}\left(cos\frac{\overline{\omega} z}{c} + \frac{\alpha}{\overline{\omega}} sin\frac{\overline{\omega} z}{c}\right) & ,z < 0, \end{cases} \tag{2.46}$$

where $\alpha = \omega_R/2Q$, $\overline{\omega} = \sqrt{\omega_R^2 - \alpha^2}$, $Q = R_s\sqrt{C/L}$ is a quality factor and $\omega_R = 1/\sqrt{CL}$ is a resonance frequency. According to equation 2.46, $z = 0$ is the head of the bunch and the wakefield is zero for the point farther beyond, $z > 0$, so that only the trailing particles are influenced by the broad-band resonator wakefield. The corresponding Fourier transformation, i.e. the longitudinal impedance is given by

$$Z_m^{\parallel} = \frac{R_s}{1 + iQ\left(\frac{\omega_R}{\omega} - \frac{\omega}{\omega_R}\right)} \tag{2.47}$$

A shunt impedance R_s, quality factor Q and resonance frequency ω_R are arbitrary parameter that can be adjusted for a proper impedance resulting on acceptable approximation of the bunch length growth and energy spread increasing with bunch current.

2.5.2 Resistive, inductive and capacitive impedance models

A resistor, an inductor and a capacitor can be used to characterize an impedance of accelerator element due to their characteristic features on electrical retardations. Moreover, it can also be used to implement the broad-band resonator model when specific impedance feature is needed [52]. Additionally, the impedance model constructed by serially connecting a resistor with an inductor, R + L, was employed and demonstrated to be well engaged with the ATF damping ring impedance [35]. Characteristic beam retarding features and impedances of each circuit element are described by Bane [35], [53] and Holtzapple [29].

In principle, the wake potential or induced voltage, $V_{ind}(z)$, according to a bunch with distribution $\lambda_0(z)$ where z is longitudinal length in time domain can be equated following an equation 2.20

$$V_{ind}(z) = \int_{z}^{\infty} \lambda_0(z) W(z' - z) dz$$

where $W(z)$ is the wake function. According to equation 2.18 it can be reformulated to a form [53]

$$\frac{\dot{\lambda}}{\lambda} = -\frac{t}{\sigma_0^2} + \frac{V_{ind}}{\dot{V}_{rf}\sigma_0^2} \tag{2.48}$$

Characteristic beam retardation feature of each circuit element depends on their induced voltage that consequently make particular modification described below.

Resistive impedance

An induced voltage due to a resistive impedance model, V_R, is given by

$$V_R(z) = -IR \tag{2.49}$$

where R is a resistance. It has a little effect on bunch lengthening but contributes to the shifting of the bunch centroid when the bunch current is increased due to energy compensation with an increasing of higher mode losses. Such effect is due to the fact that its effects is not restricted to physical retarding. Since the beam is assumed to be moving with speed of light, an induced voltage would therefore lag behind exciting charge.

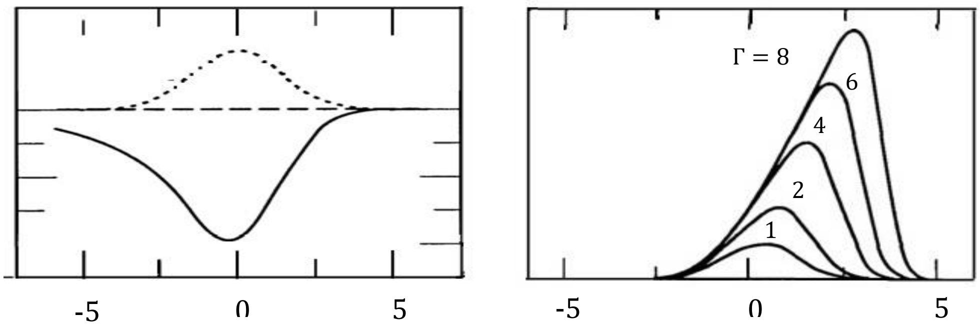

(a) (b)

Figure 2.9: (a) Curves of a bunch longitudinal distribution (dashed) and corresponding wake due to resistive impedance (bold). (b) Effect of resistive impedance to the bunch centroid shifting. Γ is a normalized bunch distribution at various intensity. (Head is to the right) [53]

Accompanying with a resistive impedance model, equation 2.48 can be modified to

$$\lambda' = -(q + \lambda)\lambda \tag{2.50}$$

where $q = {}^{z}/_{\sigma_0}$ is a longitudinal independent variable with σ_0 zero current bunch length. Longitudinal bunch distribution, λ, is defined as $\lambda = {}^{RI}/_{\dot{V}_{\sigma_0}}$ with prime denoting the derivative with respect to q.

Inductive impedance

An inductive impedance is normally responsible for the lengthening effect of bunch distribution but does not involve in energy losses. Its induced voltage is given by

$$V_L(z) = -L\frac{dI}{dt} \tag{2.51}$$

where L is an inductance. Considering an inductive impedance, equation 2.48 can be modified to

$$\lambda' = -\frac{q\lambda}{1 + \lambda} \tag{2.52}$$

with the longitudinal bunch distribution, λ, is given by $\lambda = {}^{LI}/_{\dot{V}_{\sigma_0}^{2}}$.

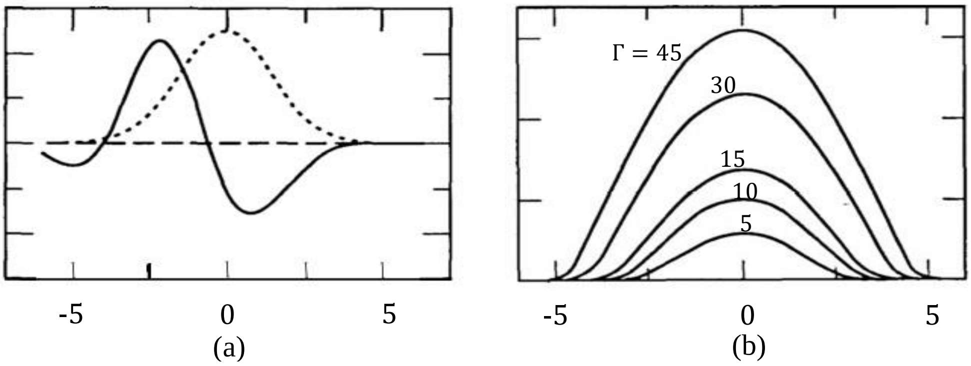

(a) (b)

Figure 2.10: (a) Curves of a bunch longitudinal distribution (dashed) and corresponding wake due to inductive impedance (bold). (b) Effect of inductive impedance to the bunch lengthening. Γ is a normalized bunch distribution at various intensity. (Head is to the right) [53]

Capacitive impedance

A capacitive impedance typically tends to shorten the bunch. Its induced voltage is proportional to an integral of the current

$$V_C(z) = \frac{1}{C}\int_z^{\infty} I(z')dz' \tag{2.53}$$

where C is a capacitance. Equation 2.48 can then be rewritten as

$$\lambda' = -\lambda\left[q + \int_{-\infty}^{q} \lambda(q')dq'\right] \tag{2.54}$$

with the longitudinal bunch distribution, λ, is given by $\lambda = {I}/{\dot{V}_{rf}C}$.

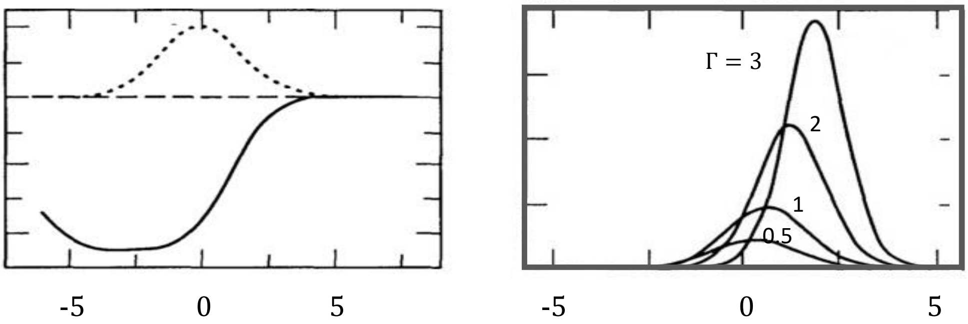

(a) (b)

Figure 2.11: (a) Curves of a bunch longitudinal distribution (dashed) and corresponding wake due to capacitive impedance (bold). (b) Effects of capacitive impedance to the bunch shortening and centroid shifting. Γ is a normalized bunch distribution at various intensity. (Head is to the right) [53]

In order to determine the total wakefield of the ring precisely we can use a combination of these impedance models as well.

2.6 Radiation wakefield

Pioneering work by Schott [54] at the beginning of twentieth century suggested an analytical viewpoint of the radiation field emitted from an electron moving on circular orbit. The effect of such radiation was later recognized to be one of the wakefield source that lengthens electron bunch in storage ring. Murphy *et al.* [14] derived analytic expression of short range wakefield due to a highly relativistic electron in free space. They also determined the effect of radiation suppression by vacuum chamber using a model of an electron travelling in circular trajectory between infinite parallel plates with infinite conductivity.

Relating with the case of short electron bunch moving in synchrotron storage ring, the consideration of longitudinal wakefield associated with synchrotron radiation would essentially have to account both the effects of free space wake and radiation shielding together.

2.6.1 Free space wakefield

According to the deduction by Murphy *et al.* [14], the tangential electric field due to a single electron, E_φ, for $q > 0$ can be written as

$$E_\varphi = -\frac{4}{3}\frac{e\gamma^4}{\rho^2}w(q) \tag{2.55}$$

where q is a dimensionless longitudinal parameter obtained by

$$q = \frac{3s\gamma^3}{2\rho} \tag{2.56}$$

with s is the arc length between a radiated charged particle and the observation point. γ the Lorentz relativistic factor and ρ a radius of circular trajectory. From a relation between wake function and wake potential

$$w(q) = \frac{dv(q)}{dq}$$

where longitudinal wake potential as a function of longitudinal distance is given by

$$v(q) = \frac{9}{4}\frac{cosh\left[\frac{5}{3}sinh^{-1}q\right] - cosh[sinh^{-1}q]}{sinh[2sinh^{-1}q]} \tag{2.57}$$

Thus the wake function in free space is expressed by

$$w(q) = \begin{cases} 0 & ,q < 0 \\ \frac{1}{2} & ,q = 0 \\ 1 - \frac{14}{9}q^2 + \cdots & ,q^2 \ll 1 \\ -\frac{3}{4 \cdot 2^{1/3}} \frac{1}{q^{4/3}} + \cdots & ,q^2 \gg 1 \end{cases} \tag{2.58}$$

where it obeys the condition

$$\int_0^\infty w(q)dq = 0$$

Equation 2.58 clearly expresses that the longitudinal wake function due to synchrotron radiation in free space is directed to forward direction and vanished behind the exciting charge.

Considering the bunch with Gaussian density distribution

$$\lambda(s) = \frac{N}{\sqrt{2\pi}\sigma} e^{-s^2/2\sigma^2} \tag{2.59}$$

The wakefield of a bunch can be defined as

$$W(s) = -\int_{-\infty}^{\infty} \lambda(s')E_\varphi(s - s')ds' \tag{2.60}$$

From equation 2.56, 2.59 and 2.60, it can be deducted to

$$W(x\sigma) = \frac{Ne}{(3\rho^2)^{\frac{1}{3}}} \frac{1}{\sigma^{\frac{4}{3}}} \sqrt{\frac{2}{\pi}} \frac{\partial}{\partial x} \int_0^\infty y^{-\frac{1}{3}} e^{-\frac{1}{2}(x-y)^2} dy \tag{2.61}$$

2.6.2 Radiation shielding

An electron moving with uniform velocity in the middle of vacuum chamber can be simply imagined as it is moving in between two infinitely long parallel plates with infinite conductivity. The presence of conducting parallel plates can substantially modify the radiation of the bunch. Using the method of image charges, Murphy *et al.* suggested that the tangential electric field on electron orbit can be obtained from

$$E_{\varphi} = \frac{e}{4\rho^2\gamma^2}\left[\frac{cos\xi}{sin^2\xi} + \frac{1}{\Delta^3}G_1\left({\xi}/{\Delta^{3/2}}\right)\right] - \frac{4}{3}\frac{e\gamma^4}{\rho^2}\left[W(3\gamma^3\xi) - \frac{3}{8}\frac{1}{\Delta^2\gamma^4}G_2\left({\xi}/{\Delta^{3/2}}\right)\right] \tag{2.62}$$

where

$$G_1\left({\xi}/{\Delta^{3/2}}\right) = 2\sum_{k=1}^{\infty}\frac{(-1)^{k+1}}{k^3}\left[\frac{4Y_k^2(1-3Y_k^4)}{(1+Y_k^4)^3} - \frac{32Y_k^6(5-7Y_k^4)}{(1+Y_k^4)^5}\right] \tag{2.63}$$

and

$$G_2\left({\xi}/{\Delta^{3/2}}\right) = 2\sum_{k=1}^{\infty}\frac{(-1)^{k+1}}{k^2}\left[\frac{4Y_k^4\left(3-Y_k^4\right)}{(1+Y_k^4)^3}\right] \tag{2.64}$$

ξ is an angle on the orbit plane defined by $\xi = \pi - \psi$ where 2ψ is an angle between radiated point and observation point. Δ is a ratio of the distance between parallel plates and the radius of circular trajectory. Scaling functions G_1 and G_2 are plotted in figure 2.12.

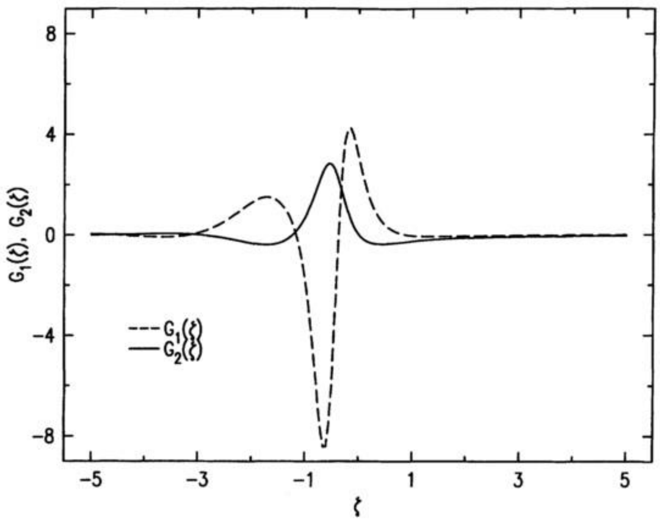

Figure 2.12: Plots of scaling functions G_1 and G_2 [14].

By approximating ${1}/{\gamma^2} \ll \Delta \ll 1$ equation 2.62 is well satisfied

$$E_{\varphi}(s) = -\frac{4}{3}\frac{e\gamma^4}{\rho^2}\left[\frac{dv(q)}{dq} - \frac{3}{8}\frac{1}{\Delta^2\gamma^4}G_2\left(\frac{s}{2\rho\Delta^{3/2}}\right)\right] \tag{2.65}$$

Considering equation 2.60, the wakefield of the bunch due to parallel plates model can be obtained by

$$W(x\sigma) = \frac{Ne}{(3\rho^2\sigma^4)^{\frac{1}{3}}}\sqrt{\frac{2}{\pi}}\left[\Phi(x) - \left(\frac{3}{4}\right)^{1/3}\Sigma^{4/3}\int_{-\infty}^{\infty} dy G_2(\Sigma y)e^{-\frac{1}{2}(x-y)^2}\right] \tag{2.66}$$

where

$$\Sigma = \frac{\sigma}{2h}\sqrt{\frac{\rho}{h}} \tag{2.67}$$

and

$$\Phi(x) = \Gamma\left({}^{2}\!/_{3}\right)e^{-x^2/4}D_{1/3}(-x)$$

with $D_{1/3}$ is the parabolic cylinder function. Equation 2.66 clearly indicates that the wakefield due to parallel plates also effects the trailing particles.

Combining equations 2.61 with 2.66 will construct an analytical expression of radiation wake function. Due to a relation between wake function and wake potential, the radiation wake potential can be obtain by an integration of wake function which yields [13]

$$V_{\omega f}(z) = -\frac{2\pi\rho_0}{4\pi\epsilon_0}eN_e\left(\int_0^{\infty}\frac{2}{(3{\rho_0}^2)^{\frac{1}{3}}}\frac{d\lambda(z-z')}{dz}\frac{1}{(z')^{\frac{1}{3}}}dz'\right.$$

$$\left.-\frac{1}{2h^2}\int_{-\infty}^{\infty}\lambda(z-z')G_2\left[\frac{1}{2h}\left(\frac{\rho_0}{h}\right)^{\frac{1}{2}}z'\right]dz'\right) \tag{2.68}$$

The first term of the r.h.s. represents a wake potential due to free space wake and the second term refers to the wake potential due to radiation shielding.

2.7 Quasi-isochronous storage ring

Isochronicity of the ring is fundamentally defined by an independency of the time particles take to execute a full revolution turn from the energy deviation. The revolution times are subsequently the same for all particles in a bunch. In order to achieve such situation, the deviations on path length have to be zero and all particle have to be traveling at speed of light. These conditions imply that the momentum compaction factor, α, has to be vanished accordingly.

In practice, there has always been a deviation on path length of particles in the bunch due to finite dispersion of the beam even though they are presumable to be traveling at speed of light. Nevertheless, the 'quasi-isochronous' storage ring which α is being approached zero is practically possible and has also been proposed to be a potential technique to reduce bunch length in electron machine [27], [28]. Experiments enquiring quasi-isochronous mode were demonstrated to be able to considerably reduce electron bunch length in UVSOR ring [55] and Super ACO [56].

According to the definition of momentum compaction factor, reducing α consequently implies the reduction of path length deviated from that of synchronous particle. Thus the bunch length is reduced accordingly. At the quasi-isochronous condition, the linear momentum compaction factor is considerably low. Then the nonlinear terms become significant since the momentum compaction factor can be expanded as a function of energy deviation, δ;

$$\alpha(\delta) = \alpha_1 + \alpha_2\delta + \alpha_3\delta^2 + O(\delta^3) \tag{2.69}$$

where expanded α coefficients can be obtained from [57]

$$\alpha_1 = \frac{1}{L_0}\oint \frac{\eta_1}{\rho} ds$$

$$\alpha_2 = \frac{1}{L_0}\int \left(\frac{\eta_1'^2}{2} + \frac{\eta_2}{\rho}\right) ds$$

$$\alpha_3 = \frac{1}{L_0}\int \left(\eta_1'\eta_2' - \frac{\eta_1\eta_1'^2}{2\rho} + \frac{\eta_3}{\rho}\right) ds$$

where η is the slippage factor with subscriptions 1, 2 and 3 refer to the order of expansion terms with respect to energy deviation. Since the slippage factor is given by

$$\eta = \frac{\Delta T / T_0}{\delta} \tag{2.70}$$

where η can also be expanded as a function of energy deviation as

$$\eta = \eta_1 + \eta_2\delta + \eta_3\delta^2 + O(\delta^3) \tag{2.71}$$

Then it can be deducted to

$$\frac{\Delta T}{T_0} = \eta\delta = \eta_1\delta + \eta_2\delta^2 + O(\delta^3) \tag{2.72}$$

According to equation 2.1, when path length, L, equals to the close orbit length, C, then it can be expanded as a power series of momentum compaction factor written in a function of energy deviation, δ; [58]

$$C = C_0\big(1 + \alpha_1\delta + \alpha_2\delta^2 + O(\delta^3)\big) \tag{2.73}$$

where C_0 is the designed close orbit length executed by a synchronous particle. Then it would be easily obtained

$$\eta_1 = \alpha_1 - \frac{1}{\gamma^2} \tag{2.74}$$

$$\eta_2 = \alpha_2 - \frac{\eta_1}{\gamma^2} + \frac{3\beta^2}{2\gamma^2} \tag{2.75}$$

where β and γ are the Lorentz relativistic parameters. For highly relativistic electron beam, $\gamma^2 \gg 1$. It can then be assumed that $\eta_1 \approx \alpha_1$ and $\eta_2 \approx \alpha_2$.

On accounting for higher order slippage factor, the Hamiltonian of longitudinal phase space in equation 2.11 is modified to

$$H = 2\pi\left(\frac{\eta_1\delta^2}{2} + \frac{\eta_2\delta^3}{3}\right) + \frac{eV_{rf}}{2\pi E_0}[\cos(\psi + \phi_s) - \cos\phi_s + \psi sin\phi_s] \tag{2.76}$$

where δ is an energy deviation, e an electron charge, V_{rf} the rf voltage, E_0 the nominal beam energy, ψ the phase deviation of particle given by $\psi = \phi - \phi_s$ and ϕ_s a synchronous phase.

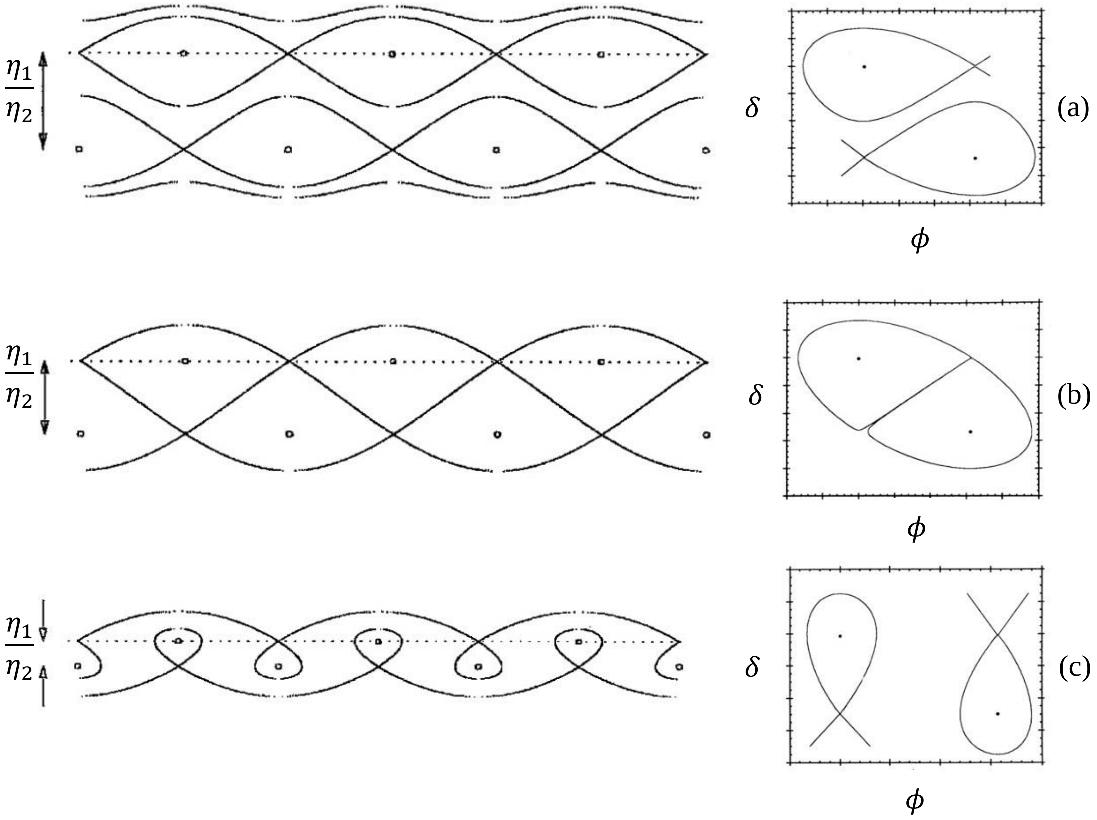

stationary buckets *accelerating buckets*

Figure 2.13: Stationary and accelerating buckets at the transition of rf to alpha bucket schemes occurred when the system is approaching quasi-isochronicity are illustrated. (a) rf buckets with additional buckets at $-\frac{\eta_1}{\eta_2}$ lower than the original ones (b) separatrix of the upper and lower buckets is merging (c) alpha buckets are developed when the system is succeeded to quasi-isochronous state [28], [58].

Apparently, additional stable fixed point is emerged at $\left(\pi - 2\phi_s, {}^{-\eta_1}/_{\eta_2}\right)$ as well as a new unstable fixed point at $\left(0, {}^{-\eta_1}/_{\eta_2}\right)$. With significance of η_2 the rf bucket in longitudinal phase space is therefore transformed to an alpha bucket scheme.

Figure 2.13 exhibits the transition of longitudinal phase space from rf bucket to alpha bucket. Figure 2.13(a) demonstrates additional buckets at lower energy deviation due to η_2 that has become significant when η_1 is approaching zero. The rf bucket scheme transforms to alpha bucket scheme as shown in figure 2.13(c) when the quasi-isochronicity is achieved. Electron can be stored within both bucket. A demonstration of simultaneous electron store in alpha bucket was presented by Murphy and Kramer [59].

In general, the slippage factor can also be defined with respect to the transition energy, γ_t, following a relation

$$\eta \equiv \frac{1}{\gamma_t^2} - \frac{1}{\gamma^2} \tag{2.77}$$

where γ_t is the transition energy given by

$$\gamma_t \equiv \frac{1}{\sqrt{\alpha}} \tag{2.78}$$

Substitutes into expression 2.77, it is modified to

$$\eta \equiv \alpha - \frac{1}{\gamma^2} \tag{2.79}$$

which is identical to linear approximation of η expressed in equation 2.74.

Nonetheless, operation below the transition was found to be better maintain stability of the beam. Fang *et al.* suggested a progressive method to operate with negative momentum compaction factor [60] and predicted that the microwave instability threshold would has been increased as well as presented that the bunch distribution were less deformed. This method keeps the beam being operated well below the transition. Due to negative dependent of orbit time with respect to energy deviation according to negative momentum compaction factor. Therefore, most of particles in the bunch are concentrated at the tail according to energy compensation by rf cavity. The collective geometric wakefield is then being active at the region beyond the bunch tail. Consequently, the particle ensembles are less affected by the wakefield. Thus the longitudinal bunch shape is less distorted than with positive momentum compaction factor.

Negative momentum compaction factor has been demonstrated to be an effective adoption to reduce the bunch length while maintaining the bunch profile less deformed [56], [61]. An experiment at Super ACO [56] also exposed that the bunch lengthening with increasing current of negative momentum compaction factor is noticeably slower than the positive one. The microwave instability threshold was also higher than the case with positive momentum compaction factor.

Hence, negative low momentum compaction factor is really interesting for operating the quasi-isochronous mode in synchrotron storage ring both on an aspect of bunch shortening and reducing the beam vulnerability to collective wakefield.

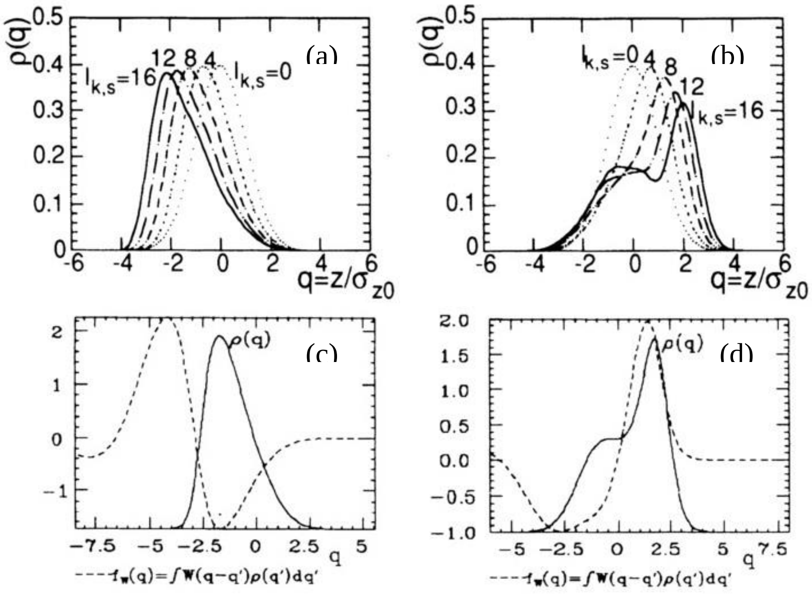

$\alpha < 0$ $\alpha > 0$

Figure 2.14: Plots of longitudinal bunch distribution in the case of negative (left column) and positive (right column) momentum compaction factor. (a) and (b) illustrate the longitudinal bunch distribution at different intensity. (c) and (d) compare the longitudinal bunch distribution with its corresponding wake function [60].

2.8 Sub-threshold phenomena

In general, the instability threshold normally refers to the beam current where the onset of microwave instability is occurred. At this point, the energy spread is suddenly increased.

According to the fact that the equilibrium energy spread is determined by the balancing between radiation damping effect that causes contraction of energy spread and quantum excitation of synchrotron radiation that results in opposite way, it could be consequently anticipated that there must be particular mechanism emerged at the threshold that aggressively increases the energy spread independently of particle number (because there is no particle lost). This phenomenon is often accompanied by high frequency signals, hence the name microwave instability.

Collective effects influence the bunch deformation in two aspects. The stationary perturbation that results in the distortion of bunch density distribution and the time-dependent perturbation that initiates beam instability. Thus, it can be concluded that sub-threshold phenomena is typically developed from the time-independent static perturbation while beyond-threshold phenomena is accompanied by the time-dependent term of perturbation.

Sub-threshold phenomena are concentrated on the distortion of bunch longitudinal stationary distribution due to an alteration of longitudinal potential produced by the bunch distribution itself and implemented by wake potential. Thus the distortion of stationary bunch distribution is called the potential well distortion.

Regarding the bunch distribution in longitudinal phase space which can be described by Vlasov equation written in formula 2.13

$$\frac{\partial\Psi(q,p)}{\partial t}+\dot{q}\frac{\partial\Psi(q,p)}{\partial q}+\dot{p}\frac{\partial\Psi(q,p)}{\partial p}=0$$

For stationary case the time-dependent term is vanished and Vlasov equation is subsequently satisfied a relation

$$\{\Psi,H\}=0$$

which is previously identified by formula 2.16. It then implies that the distribution in longitudinal phase space is only a function of Hamiltonian, $\Psi=\Psi(H)$.

Recall that the Hamiltonian of longitudinal motion of electron influenced by collective effect induced from bunch distribution $\lambda(q)$ is written in general form as

$$H = \frac{p^2}{2} + \frac{q^2}{2} + I\int_q^\infty V(q',p)dq' \tag{2.80}$$

with the longitudinal wake potential,

$$V(q,p) = \int_{-\infty}^{\infty} W(q-q')\lambda(q')\,dq'$$

Consequently, the potential well that bounds the particle motion can be equated as

$$U(q) = \frac{q^2}{2} + I\int_q^\infty \int_{-\infty}^{\infty} W(q-q')\lambda(q')\,dq'dq \tag{2.81}$$

Since q is normalized longitudinal displacement, $q = {}^{z}/_{\sigma_{z0}}$, it is obviously seen that there is no alteration on energy deviation. Thus during the deformation of longitudinal distribution due to potential well distortion, the energy spread is being constant at a natural energy spread. Equation 2.81 also shows that without wake potential the potential well becomes ordinary parabolic shape as a function of longitudinal displacement.

As shown in section 2.5.2, the wake potential that tends to be inductive or capacitive coupling impedance affects the bunch distribution in the way that parabolic potential layout has still been maintained in good symmetry. On the other hand, the wake potential that tends to be resistive disturbs the bunch distribution by shifting the centroid and even substantially breaks the bunch distribution symmetry. Though parabolic distortion is not as severe as causing particle lost, it can deviate the bunch length both shortening and lengthening or shifting its centroid when current is increased. The effect of bunch lengthening due to potential well distortion has still been relatively small compared to the effect of instability beyond the threshold.

Referring to the derivation of Haissinski solution, it is easily realized that the bunch distribution influenced by potential well distortion can be estimated by Haissinski integral solution. However due to an approximation of wakefield over one revolution turn during the derivation of Haissinski solution, it is restricted to be able to engage with the bunch at very low current. Numerical calculation is needed to solve VFP equation at higher current within sub-threshold region.

During mid-90s, Fang *et al.* [60] introduced a novel technique on the operation of electron beam by demonstrating the negative momentum compaction factor, $\alpha < 0$. They revealed that under the potential well distortion regime, the bunch distribution is less distorted than the beam with positive momentum compaction factor at the same intensity.

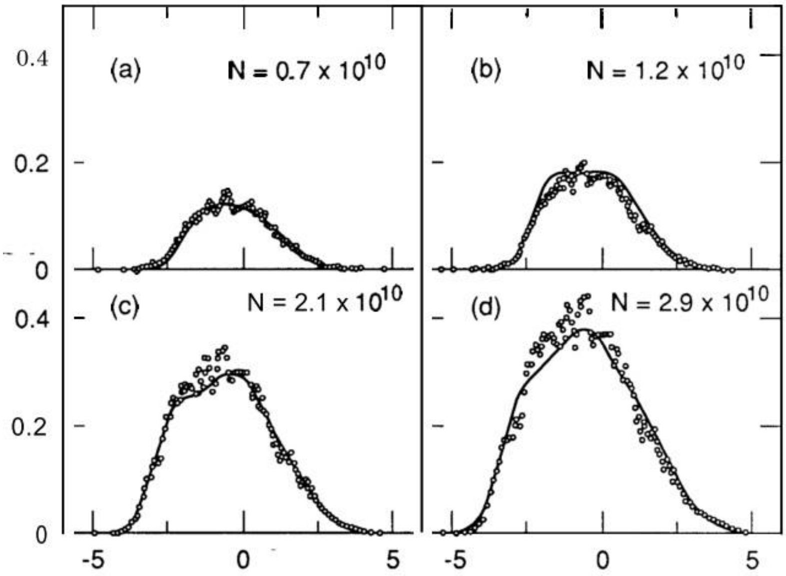

Figure: 2.15: Comparison of the longitudinal bunch distribution detected in experiment at SLC damping ring at several current values fitted with the bunch shape calculated with Haissinski equation [53].

During the energy compensation, with positive momentum compaction factor, $\alpha > 0$, the energy gradient of rf accelerating field where the leading particles (lower energy particles) arrived is smaller than the gradient at the trailing particles (higher energy particles), $\left|\frac{d\delta}{d\phi}\right|_{leading} < \left|\frac{d\delta}{d\phi}\right|_{trailing}$. Then at the next turn, an increasing of path length executed by leading/lower energy particles is smaller than a decreasing of path length executed by trailing/higher energy particles. This regime consequently results on an accumulation of particles at the bunch head. The bunch distribution appears to be leaning forward accordingly.

Contrary to negative momentum compaction factor, $\alpha < 0$, the accelerating rf gradient at the leading particles (higher energy particles) is larger than the gradient where the trailing particles (lower energy particles) arrived, $\left|\frac{d\delta}{d\phi}\right|_{leading} > \left|\frac{d\delta}{d\phi}\right|_{trailing}$. When a bunch revolves to the next turn, an increasing of revolution time performed by leading/higher energy particles is larger than a decreasing of revolution time performed by trailing/lower energy particles. Therefore, this regime apparently propels particles ensembles to be accumulated at the bunch tail. Then the bunch distribution appears leaning backward.

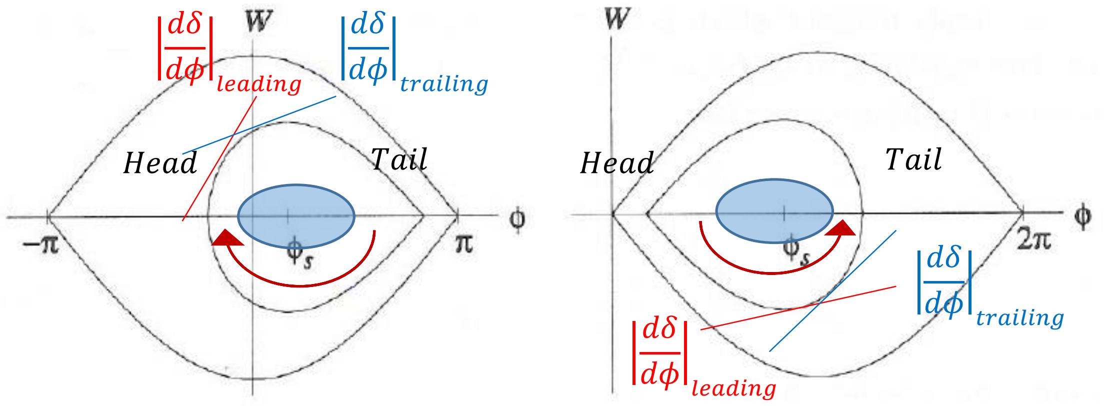

$\alpha < 0$ $\alpha > 0$

Figure 2.16: Diagrams demonstrating the energy compensation in negative (left) and positive (right) momentum compaction factors. Fundamentally, the bunch distribution of negative alpha case rotates clockwise in longitudinal phase space. Particle energy is compensated during it evolving in the head region. The leading particles arrive on the region where an accelerating gradient is greater than the region where trailing particles are located. Then with a given deviation of phase arrival, the decreasing of energy gained by leading particles is greater than the increasing of energy gained by trailing particles. The revolution time of leading particle will be extended more than a contraction of trailing particle revolution time. Consequently, the increasing of arrival phase of leading particles at the next turn is larger than the decreasing of arrival phase of trailing particles. This scheme leads to characteristic feature of negative alpha that the bunch appears leaning backward. For positive alpha, a bunch distribution rotates counter-clockwise in longitudinal phase space. Particle energy is compensated during evolving

in the tail region. The leading particles arrive on the region where an accelerating gradient is smaller than arrival region of trailing particles. With a given deviation of phase arrival, the increasing of energy gained by leading particles is smaller than the decreasing of energy gained by trailing particles. The path length executed by leading particles will be extended smaller than a shortening of path length executed by trailing particles. Therefore, the increasing of arrival phase of leading particles at the next turn is smaller than the decreasing of arrival phase of trailing particles. This scheme leads to characteristic feature of positive alpha that the bunch appears leaning forward.

Explanation of phenomena that the bunch with negative momentum compaction factor is revealed to be less distorted than in positive momentum compaction factor was also suggested by Fang *et al* as follow. Due to the fact that the bunch distribution of positive α case tends to lean forward, the wakefield induced by particles at the head is more immense and seriously disturbing the trailing particles on the tail. On the other hand, the bunch distribution of negative α case tends to lean backward. Although the wakefield induced by particles at the tail is immense, the affected area is farther beyond the bunch distribution. Therefore, the bunch with negative momentum compaction factor is less disturbed by the self-induced geometric wakefield.

2.9 Beyond threshold phenomena

When the onset of instability is occurred the energy spread suddenly risen. According to a relation between energy spread and bunch length, the blowing up of bunch length growth rate is therefore clearly observable when the threshold is reached as well. An abruptly increasing of the growth rates of bunch length and energy spread are characteristic phenomena that would be occurred when the microwave instability threshold is reached. These effects are more severe than the potential well distortion according to an influence of time-dependent perturbation.

It can basically be anticipated that the instability requires an effective triggering time shorter than the synchrotron period and the frequency that the wavelength short compared to the bunch length. With long bunch consideration, Boussard [62] described the threshold by suggesting a modification of Keil-Schnell criterion [63] that was used to define stability condition of the coasting beam by replacing the particle density distribution of a single bunch to the distribution of an unbunched beam.

Considering a short bunch, the wakefields accompanying in the turbulent bunch lengthening are even higher frequency. A thorough explanation was given by Sacherer [64] who suggested that the microwave instability is arisen due to a colliding of turbulent oscillation modes when the beam intensity is increased to the threshold.

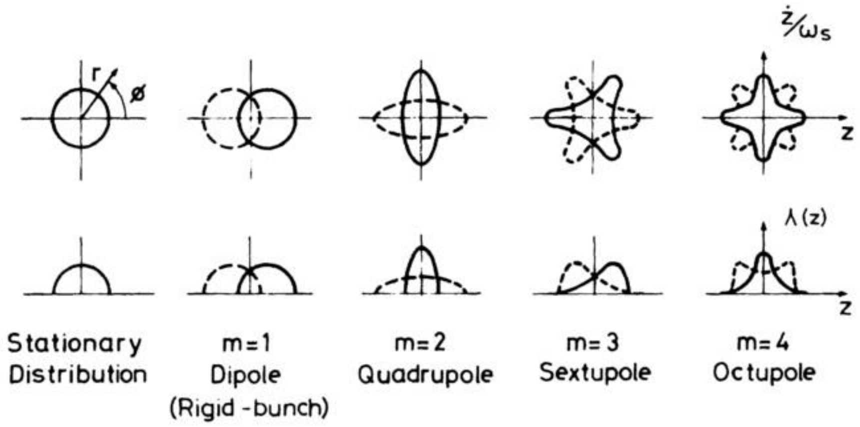

Figure 2.17: Bunch oscillation modes suggested by Sacherer [65].

Low intensity bunch oscillation due to wake force is consisted of several fluctuation modes as exemplified in figure 2.17. Typically, the colliding of mode $m = 1$ with $m = 2$ is of the most possibility to trigger the instability. Due to the fact that the higher fluctuation mode $m > 1$ tend to have resonant frequencies decreased with beam intensity according to the effect of synchrotron frequency shift caused by energy dissipated to resistive impedance. The rigid bunch oscillation mode $m = 1$ is the whole bunch oscillation where the wake force concentrates at the bunch centroid. This kind of motion is not affected by the wake force that is a function of the gradient of longitudinal density distribution. Therefore, the oscillation mode $m = 2$ is expectable to collide with mode $m = 1$ when the intensity is increased as shown in figure 2.18.

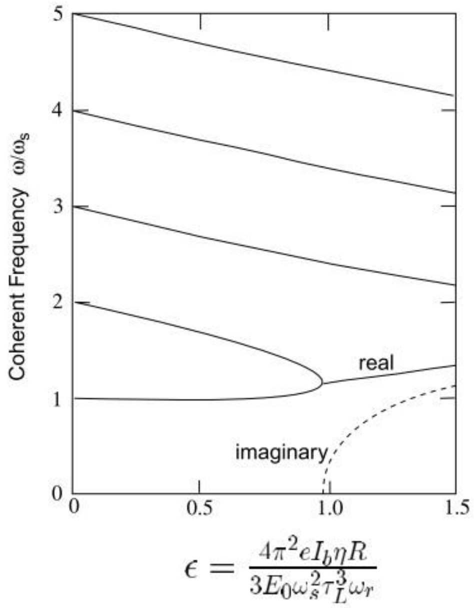

Figure 2.18: A plot illustrates multiple mode instability of parabolic bunch with derived intensity dependent parameter. The bunch with full length τ_L is influenced by broad-band resonator impedance with shunt impedance R and resonance frequency $\omega_r/2\pi$. The higher oscillation modes shift downward except mode $m = 1$. The colliding point of mode $m = 1$ with $m = 2$ typically indicates the threshold intensity [66].

When the beam intensity is further increased, there existed several characteristic phenomena apart from the blowup of energy spread and bunch distribution length. Certainly, their emergences are due to the collective instabilities developed from the time-dependent turbulent on the longitudinal distribution. The oscillation of phase space relaxation that later defined as ‘sawtooth’ instability is apparently revealed at some point beyond the threshold but in rare case with specifically controlled conditions. As well as the development of micro-structure on the longitudinal density distribution which is defined as the microbunching instability is also exposed under short bunch consideration. Both of them are of great interest in the study of longitudinal beam dynamics beyond threshold and the production of extremely intense synchrotron radiation from either existing or newly constructed storage rings.

2.9.1 Microbunching phenomena

Considering the situation that bunch length is shortened to be comparable to the radiation wavelength emitted. The bunch itself becomes susceptible to be disturbed by the radiation from particles within the bunch. Simultaneously, the bunch can radiate coherently at such short bunch length due to the in-phase radiation from most particles within.

In general, the coherent radiation is suppressed by the conducting vacuum chamber wall as described in section 2.6. Therefore, the maximum wavelength involving in the bunch self-disturbance are limited by the shielding cut-off, λ_c, shown in equation 1.3 or the bunch length if it is smaller than λ_c. The radiation wavelengths smaller than or equal to this maximum limitation can trigger density fluctuation in the bunch. Nevertheless, the minimum wavelength influencing in this regime is also determined by the energy spread via the wave number, $k = {}^{1}/_{\lambda_m}$ where λ_m is the characteristic wavelength of modulated microbunch, with a relation [67]

$$k\rho < 2.0\Lambda^{3/2} \tag{2.82}$$

where ρ is the bending radius and Λ is defined by

$$\Lambda = \frac{n_b r_e}{|\eta|\gamma\delta_0^2} \tag{2.83}$$

where n_b is the equilibrium beam density obtained by $n_b = \int \lambda_0(\delta)\, d\delta$, r_e the classical electron radius, η a slippage factor, γ the Lorentz relativistic factor and δ_0 the rms relative energy spread.

At particular condition the density fluctuation with characteristic length short compared to the bunch length can radiates coherently and results in an enhancement of density fluctuation. This phenomena leads to the microbunching instability which many local microstructures are spontaneously arisen on the longitudinal distribution in phase space [67]. Furthermore, these microbunches also radiate coherently and amplify the radiation power of the bunch to be quadratically dependent of the number of particles as shown in equation 1.1.

$$P = NP_n + N(N-1)P_n f_n$$

where the form factor, f_n is given by

$$f_n(\upsilon) = \left| \int_{-\infty}^{\infty} \lambda(z) e^{-i2\pi\upsilon z} dz \right|^2$$

and P_n is the incoherent radiation power emitted by each particle.

Since this instability is initiated by the coherent synchrotron radiation, the name ‘CSR wakefield’ or ‘CSR instability’ have also been widely recognized for this phenomenon.

Stupakov and Heifets also proposed a method to determine the microbunching instability criterion by solving a one dimensional Vlasov equation for the bunch distribution function, λ, [10], [67] assuming the instability yielding time much shorter than the damping time;

$$\frac{\partial \lambda}{\partial s} - \eta \delta \frac{\partial \lambda}{\partial z} - \frac{r_e}{\gamma} \frac{\partial \lambda}{\partial \delta} \int_{-\infty}^{\infty} dz' \, d\delta' W(z - z') \lambda(z', \delta', s) = 0 \qquad (2.84)$$

where z is the longitudinal coordinate with respect to a reference particle, δ is the energy deviation, $s = ct$ and $W(z - z')$ is the CSR wake function which assuming an ultrarelativistic electron and neglecting the shielding effect [14], [68];

$$W(z) = \begin{cases} \dfrac{2}{(3\rho^2)^{1/3}} \dfrac{\partial z^{-1/3}}{\partial z} & for\ z > 0 \\ 0 & for\ z \leq 0 \end{cases} \qquad (2.85)$$

This equation obviously indicates that the wake according to CSR is directed in forward direction of the exciting particle. The bunch distribution function, λ, is represented as a summation of an equilibrium distribution function, λ_0, which is typically Gaussian and the perturbation λ_1;

$$\lambda = \lambda_0(\delta) + \lambda_1(z, \delta, s) \qquad (2.86)$$

with an approximation of $\lambda_0 \gg \lambda_1$. If the modulated wavelength, λ_m, is much shorter than the bunch length and satisfied the criterion on equation 2.82, the microbunches will be developed if the bunch length satisfied

$$\sigma_z \gtrsim 0.5\rho\Lambda^{-3/2} \tag{2.87}$$

Let consider the suppression effect by vacuum chamber. Assuming smooth vacuum pipe with perfect conductivity, the CSR is suppressed at the harmonics [69]

$$k\rho \lesssim \left(\frac{\pi\rho}{2b}\right)^{\frac{3}{2}} \tag{2.88}$$

where b is the diameter or vertical size of the chamber. Combining equations 2.82 and 2.88 yields the range of k value that the microbunches can be developed which is written as;

$$2.0\Lambda^{3/2} > k\rho \gtrsim \left(\frac{\pi\rho}{2b}\right)^{\frac{3}{2}} \tag{2.89}$$

According to the lower and upper limits of $k\rho$, another important instability condition can be expressed as

$$\frac{\rho}{b} \lesssim \Lambda \tag{2.90}$$

The criterions 2.89 and 2.90 have to be satisfied in order for an emergence of microbunching instability unless the finite energy spread of the bunch suppresses the density fluctuation. According to the machine parameter that have typically been applied in most synchrotron facilities, the coherent radiation detected are mostly in the range of sub-millimeter or far-infrared wavelength [21]–[23], [70], [71].

Bursting of the coherent synchrotron radiation is consequently exposed at the time microbunches are developed. These microstructures behave similar to a plenty of small bunches with (modulated) bunch length very short compared to the nominal bunch length. Byrd *et al.* [70] gave experimental evidence to elucidate the mechanism of the coherent synchrotron radiation directly related to the microbunching instability. This will be reviewed in the next sub-section.

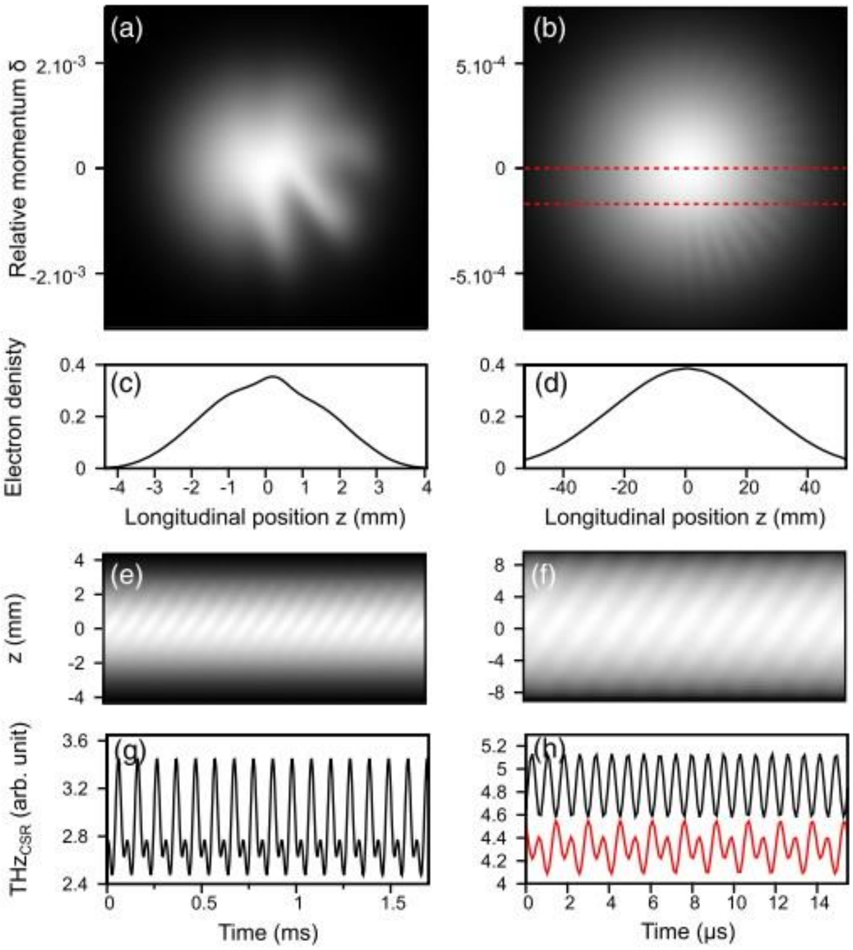

Figure 2.19: (a), (c), (e) and (g) are numerical results of SOLEIL and (b), (d), (f) and (h) are numerical results of UVSOR II. (a) and (b) are the bunch distribution in longitudinal phase space. Microbunches are obviously exhibited. (c) and (d) are the bunch longitudinal distribution. (e) and (f) are the evolution of longitudinal distribution with time. (g) and (h) are associated THz radiation power [72].

2.9.2 Coherent synchrotron radiation bursting

According to the experimental observation performed at Advanced Light Source (ALS) by Byrd *et al.* [70], a new instability regime, microbunching instability, has been elucidated for its mechanism and responsible for the induction of coherent synchrotron radiation burst.

The characteristic features of CSR can be concluded into two points; (1) the coherent radiation wavelength is short compared to the nominal bunch length and (2) the temporal recurrenting of the bursting signal is much shorter than the damping time but the time interval between consecutive bursting is equal to a fraction of damping time. Venturini and Warnock [6] derived a dynamical model for the bursting of CSR including radiation damping and quantum excitation of emitted photon of synchrotron radiation. The nonlinear interplay between CSR wakefield and bunch dynamics was accounted based on longitudinal phase space to figure out the dynamical model. Noticeably, the influence of geometric wakefield has still been excluded from their theoretical consideration.

The numerical evaluation from their work described a dynamical model of above system as follow.

1. Starting at the condition where the microbunches amplitude is very small which subsequently resulting on unnoticeable wavelength of bursting signal component.
2. When the microbunching threshold is reached the impedance due to radiation wake becomes stronger and leads to an exponential growth of microbunches. Then the CSR bursting is exposed.
3. The intrinsic property on stochastic self-consistent of particle ensembles will quickly dissolves the microbunches and prevents them to continue developing. Then the CSR bursting is put down and the overall bunch length is increased within a few synchrotron periods.
4. Within the time shorter than damping time, radiation damping and incoherent synchrotron radiation result phase space diffusion and accordingly cause the bunch shortening and energy spread reduction.
5. The coherent radiation condition is restored again. The CSR instability is set off which consequently triggers another CSR bursting.

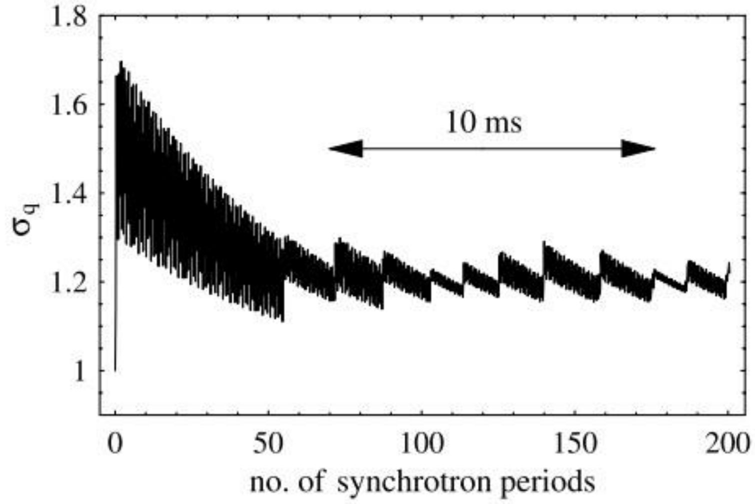

Figure 2.20: Saw-tooth shape oscillation of the bunch length due to CSR instability [6].

These recurrenting process is carried on with a period equal to a fraction of damping time. Plot of bunch length with revolution time is subsequently exhibited as an oscillation with saw-tooth shape similar to the oscillation of relaxation phase space due to sawtooth instability.

Detection of the bursting of CSR has revealed high promising radiation source in far-infrared or THz range due to its extremely high peak radiation power. However, it is a stochastic process which the theoretical explanation and practical consideration have still been unknown. These are the drawbacks for practical usage and application to the synchrotron facilities.

In 2002 Abo-Bakr *et al.* [24] presented a milestone of stable CSR development by demonstrating the generation of steady-state CSR from BESSY II storage ring by applying a low alpha optic tuning. According to their proposed technique the momentum compaction factor is reduced by 1 - 2 orders of magnitude from the nominal value. An enhancement of CSR at 3000 times above background was detected in far-infrared region. The successful production of steady-state-CSR by BESSY team raises much attention among synchrotron facilities because of their tangible approve on practically generating stable THz light with extremely high peak power. Nevertheless, the practical explanation of the production mechanism had yet been known at that time.

Sannibale *et al.* [73] suggested a practical model describing steady-state CSR phenomenology observed at BESSY II. They also proposed practical consideration that is able to be applied to existing electron storage ring in order to optimize for stable CSR production scheme. The key issue is emphasized for the bunch length and current tuning that have to be considerably small enough to make the bunch radiate coherently while maintaining the system below the radiation induced instability threshold for the sake of stability and preventing the burst.

The experiment performed at BESSY II storage ring was analyzed that the beam had been affected by only the radiation wake and shielding effect while the geometric wakefield and lattice nonlinearity effect were neglected. The bunch distribution profile was found to be distorted to leaning forward which yields much more form factor, f_n, than the Gaussian bunch. According to the formula of synchrotron radiation spectrum deducted from equation 1.1

$$\frac{dP}{d\lambda} = \frac{dP_n}{d\lambda}[N + N(N-1)f_n] \tag{2.91}$$

This regime effectively yields considerably coherent radiation rate while still being able to remain below the bursting threshold.

Further suggestion on a practical technique to maximize the CSR emission while remaining below the radiation instability threshold has also been introduced. The important idea is to make the beam only affected by the free space radiation. The negligibility of geometric wakefield and radiation shielding are needed first. In order to suppress the effect of radiation shielding, equation 2.67 needed to satisfy the criterion

$$\Sigma \lesssim 0.2 \tag{2.92}$$

At the coherent radiation condition, the wavelength is shorter than the nominal one but has to be much larger than the critical synchrotron radiation wavelength. The radiated power spectrum can be modified to [74]

$$\frac{dP}{d\lambda} = \frac{CN_b}{L}\left(f_{rf}V_{rf}\right)^2\left(\frac{B}{E}\right)^{1/3}\left(\frac{\sigma_{z0}^2}{\lambda}\right)^{7/3} F(\kappa)^2 f_n(\lambda) \tag{2.93}$$

where $C = 2.642 \times 10^{-21}$ in SI unit. $F(\kappa)$ is the solution of integral equation of equilibrium bunch distribution affected by free space radiation wakefield calculated with Haissinski equation

$$F(\kappa) = \int \lambda(q)\, dq$$

where

$$\lambda(q) = \kappa \exp\left[-\frac{q^2}{2} + sgn(\alpha) \int_0^{\infty} \lambda(q - q')(q')^{-1/3} dq'\right] \qquad (2.94)$$

with $q = \frac{z}{\sigma_{z0}}$ and $sgn(\alpha)$ is the sign of the momentum compaction factor.

The bunch population firstly has to be remained below the threshold which can be written as [67], [70]

$$N \le D \left(\frac{B}{E}\right)^{1/3} f_{rf} V_{rf} \sigma_{z0}^{3} \lambda^{-2/3} \qquad (2.95)$$

where $D = 4.528 \times 10^{-3}$ in SI unit. Assuming criterion 2.92 is satisfied, the bunch population influenced by free space radiation can be expressed as [75]

$$N = A \left(\frac{B}{E}\right)^{1/3} f_{rf} V_{rf} \sigma_{z0}^{7/3} F(\kappa) \qquad (2.96)$$

Combining with a criterion on equation 2.95, the stability criterion can be equated as

$$F \le F_{max} = G \left(\frac{\sigma_{z0}}{\lambda}\right)^{2/3} \qquad (2.97)$$

where $G = 7.463$. Noticeably, if above criterion is satisfied the reduction of natural bunch length, σ_{z0}, leads to as extension of spectral band width which is highly preferable. However, it can also significantly reduce the radiated intensity according to ${\sigma_{z0}}^{14/3}$ dependent on equation 2.93. Therefore, the natural bunch length has to be compromised via its dependent on momentum compaction factor, α. Criterions 2.96 and 2.97 estimate the maximum limit of the current that can be stored in a single bunch without affected by the radiation wake instability.

Incorporating with a strong dependence of instability threshold to the bunch length, it is then implied that only low current limit can satisfy these criteria in a short bunch regime.

2.9.3 Sawtooth instability

The significance of sawtooth instability is given to its affected element. The study by D'Yachkov [76] clarified that an involving wake force is due to the geometric wakefield which affected particles are only the trailing ones.

Although such a dynamics complexity has been defined as a rare case to be detected and its practical description has still been unknown, there have been reported on experimental observation in some circular machines [8], [9]. Certainly, it has also been revealed numerically in the study at Diamond Light Source storage ring being presented in this thesis.

The cycle of sawtooth instability can be depicted as the bunch oscillation between fusion and separation in longitudinal phase space as shown in figure 2.21.

Explanation by D'Yachkov was given as follow:

$a \rightarrow b$: The trailing bunch that was thrown away from the head bunch damps down.

$b \rightarrow c$: Particles from the head bunch diffuse to the trailing bunch. Within approximately 30 synchrotron oscillations the density of both sub-bunches is equal. Then they move to each other and simultaneously throw some amount of particles tending to form the third bunch.

$c \rightarrow d$: The two head bunches collapse together within approximately $1/3$ of synchrotron period.

$d \rightarrow a$: The coalesced bunch throws out large amount of particles while it is executing a large synchrotron oscillation which is less than the synchrotron period.

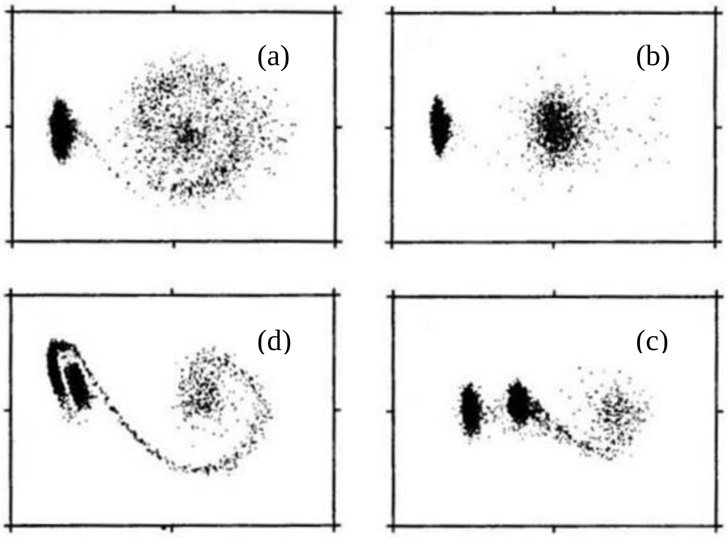

Figure 2.21: Cycle of sawtooth behaviour in longitudinal phase space (head is to the left) [77].

He also noticed that the sawtooth behaviour was clearly observed within the region $0.4 < k_0 < 0.6$ where k_0 is the normalized resonance frequency firstly introduced by Oide and Yokoya [36] defined by $k_0 = \omega_0 \sigma_z / c$.

An explanation of sawtooth instability was also given as a crossover of rf accelerating potential and wake potential as follow. According to figure 2.22, a plot on top frame illustrates the wake voltage (represented as curved line) together with the rf voltage (represented as straight lines due to linear approximation of accelerating waveform seen by particles). In order to compensate energy lost by the wakefield, the rf voltage is needed to cross the wake at its half maximum. At low intensity the wake voltage is still small compared to rf waveform as shown with line (a). Therefore, the particles are concealed within a conventional separatrix and rotate about a stable fixed point. When the beam intensity is increased the wakefield becomes stronger which implies that the wake voltage is amplified and becomes larger than at low intensity. At this situation, the wake voltage is large compared to the rf waveform which relatively effects in the same way as reducing the rf slope. At the threshold, the crossing between wake and rf voltages as shown with line (b) creates an extra unstable fixed point at the tail. When the intensity is further increased the bunch enters to the sawtooth scheme. The wake voltage becomes even larger compared to the rf voltage and accordingly crossover with three points as exhibited with line (c). Therefore, another stable fixed point is created far away at the bunch tail while an extra unstable fixed point previously created at the threshold is slightly shifted forward.

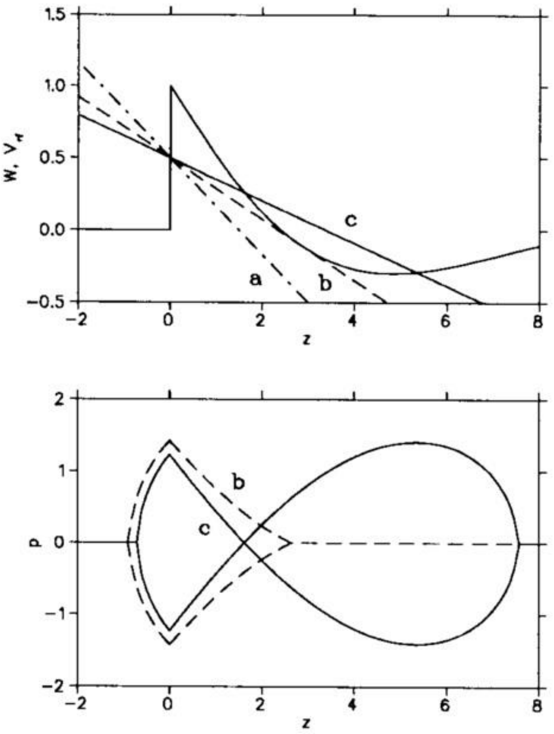

Figure 2.22: Upper diagram is a plot of wake function (displayed with curved line) together with three crossing rf waveforms representing three different situations; (a) below the threshold, (b) at the threshold and (c) above the threshold. Lower diagram is a plot of separatrix in longitudinal phase space illustrating distorted separatrixes exactly at the threshold (b) and beyond the threshold (c) which show additional unstable fixed point and stable fixed point at the tail (head is to the left) [77].

After threshold is exceeded, stochastic excitation and synchrotron radiation cause the energy lost. Then particles diffuse backward through the unstable fixed point and settle down at a newly created stable fixed point on the tail. After that a new sub-bunch at the tail creates its own wake voltage which results some of particles diffuse backward through unstable fixed point due to losing energy by its own wake downstream to another stable fixed point. At the same time potential barrier between two sub-bunches on the head becomes small enough to consequently cause the diffusion and coalescence of them. The resulting bunch appears to be overdense and situated at a wrong phase, so they start executing a large synchrotron oscillation. Concurrently, the backward diffusion is started again which causes a large particle cloud tending to form a trailing sub-bunch.

During the particles is diffusing to a newly created stable fixed point where the large cloud is created, the blowup of bunch length and energy spread are occurred. Consecutively, when an overdense bunch cloud is developing, the bunch length and energy spread are contracted. These behaviours lead to a sawtooth growing of bunch length and energy spread.

D'Yachkov also included that if the growth rate of instability is slower, the damping time will become significant for the sawtooth behaviour. The numerical consideration of wakefield with slower developing time demonstrated that the bunch will be separated into two identical sub-bunches which orbiting about each other in phase space. Hence the name binary star instability [78].

Both the sawtooth and binary star phenomena are at most promptly occurred when the bunch length is comparable to the length of wakefield. Especially with short bunch regime, the bunch is as high possibility to be affected by either sawtooth or binary star instability.

An interesting issue to be emphasized is that during the separation phase the length of each sub-bunch is fairly smaller than the initial bunch length. It is speculated that this characteristic length might be sufficiently short to radiate coherently. Furthermore, if the sawtooth behaviour is occurred in the short bunch regime, each sub-bunch will be created with even shorter than an ordinary bunch consideration. The phenomenology may lead to an enhancement of extremely high peak power radiated due to coherent synchrotron radiation, nevertheless it possibly induces even more severe turbulent on the bunch distribution in phase space.

Chapter 3

Development of Multiparticle Tracking Code: sbtrack

3.1 Code algorithm

Sbtrack is a single bunch multiparticle tracking code with wakefields implementation in 6-dimentional phase space, $[\tau, \delta, x, x', y, y']$, where τ, δ, x, x', y and y' are longitudinal displacement, energy deviation, horizontal displacement, horizontal divergence, vertical displacement and vertical divergence respectively. A flow chart in figure 3.1 briefly describes an algorithm of sbtrack. The code receives machine parameters from an input file and generates the wake function following equations derived from selected impedance model [10]. Concurrently, the code generates the initial 6-dimentional particle distribution and passes on to the one turn map. This one turn map is a virtual storage ring environment representing electromagnetic interaction due to accelerator components configuration where the revolution of the bunch along the accelerator in one turn will be simulated.

The total pre-computing wake function is then convoluted with the 6-dimentional particle distribution by slicing the bunch longitudinally and calculating the effect of wakefield as a sudden variation of energy (energy kick). Newly modified 6-dimentional particle distribution will finally be generated and passed on to the next turn as an input bunch distribution. The simulated particle distribution will be revolved around the (virtual) storage ring and continuously experiences energy kick from wakefield on each turn. After finishing the last turn, an assessed simulated bunch will be saved to the output structure which contains mean value and standard deviation of each element of 6-D phase space and turn-by-turn power radiated from the bunch. This output data will be analyzed and compared with the measurements later.

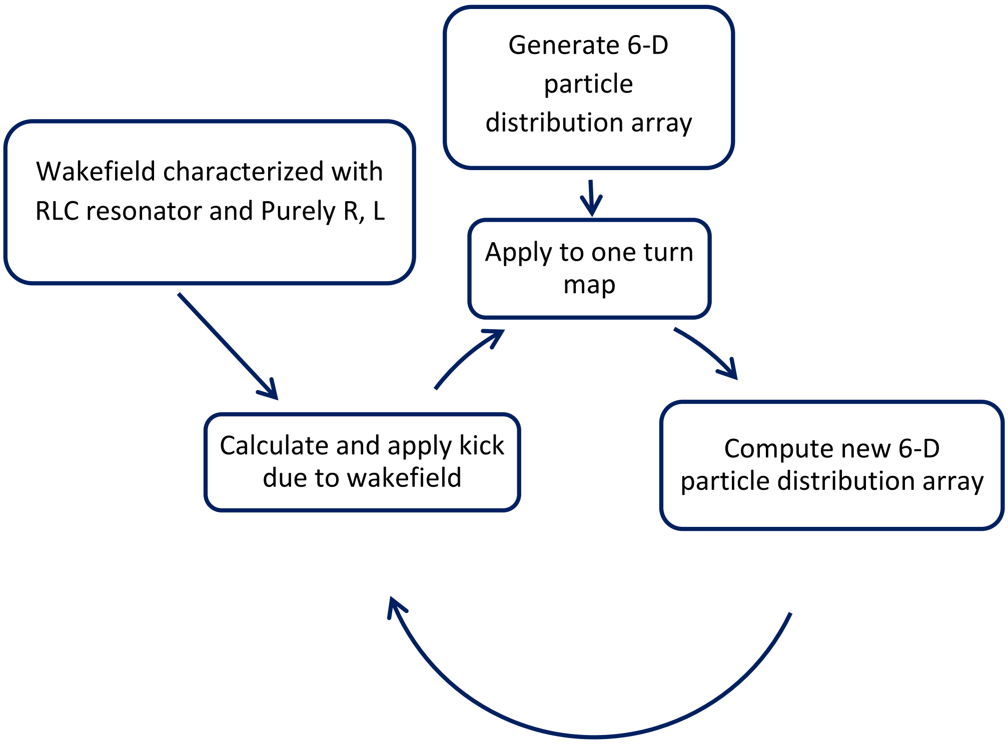

Figure 3.1: A flow chart describing the structure of sbtrack.

3.1.1 Calculation of wakefields

The wakefield is usually described as a function of distance or time delay between the inducing δ-function charge (leading particle) to the point of interest on the beam (trailing particle). It would be worth noting that the wakefield being considered here is geometric wakefield.

In order to investigate the influence of wakefield to beam dynamics, it is more practical to analyst the problem in frequency domain. This scheme introduces a concept of ‘impedance’ [45] which is the Fourier Transformation of wake function. Fundamentally, wakefield is consisted of electromagnetic fields with many resonances. Therefore, it is sensible to apply the resonator model as wakefield source in numerical investigation despite only a single or few resonances can be generated from such model. Several resonator models have been applied to the numerical studies in order to generate corresponding longitudinal wake function, W_m, and impedance, Z_m.

A broad-band resonator (BBR) denoted by [10] is one of the most frequently used model on simulating geometric wakefield. It generates the longitudinal wake function given by

$$W_m^{||}(z) = \begin{cases} 0 & for\, z > 0, \\ \alpha R_s & for\, z = 0, \\ 2\alpha R_s e^{\alpha z/c}\left(cos\frac{\overline{\omega} z}{c} + \frac{\alpha}{\overline{\omega}} sin\frac{\overline{\omega} z}{c}\right) & for\, z < 0, \end{cases} \tag{3.1}$$

$z > 0$ is the distance in time domain beyond the head of the bunch where the wakefield is vanished. Consequently, only the trailing particles are being influenced. The corresponding Fourier transformation, the longitudinal broad-band resonator impedance, is given by

$$Z_m^{\parallel}(\omega) = \frac{R_s}{1 + iQ\left(\frac{\omega_R}{\omega} - \frac{\omega}{\omega_R}\right)} \tag{3.2}$$

where the resonance angular frequency $\omega_R = 2\pi F_{res}$, $\alpha = \omega_R/2Q$ and $\overline{\omega} = \sqrt{\omega_R^2 - \alpha^2}$. Parameters R_s shunt resistance, Q quality factor and F_{res} resonance frequency are arbitrary parameters that can be adjusted to get the most appropriate model providing acceptable prediction of the bunch profiles development with increasing beam intensity.

Purely inductive and purely resistive impedances have also been used to implement the broad-band resonator model to finely adjusting the impedance model that better reproduces bunch lengthening behaviour [52]. According to sub-section 2.5.2, the expressions of wake functions and impedance due to resistive and inductive model can be deducted following the relations [29],

Resistive impedance;

$$Z^{||}(\omega) = R \tag{3.3}$$

which generates a corresponding wake function

$$W_R^{||}(z) = \frac{Rc}{\sigma_{\tau 0}}\lambda(z) \tag{3.4}$$

Inductive impedance;

$$Z^{||}(\omega) = -i\omega L \tag{3.5}$$

which generates a corresponding wake function

$$W_L^{||}(z) = -\frac{L}{\sigma_{\tau 0}}\frac{\partial\lambda(z)}{\partial z} \tag{3.6}$$

As well as the broad-band impedance model, the inductance L and the resistance R are arbitrary parameters that can be attuned. A constant $\sigma_{\tau 0}$ is the zero current bunch length and $\lambda(z)$ is a longitudinal bunch profile. In order to determine the total wakefield of the ring precisely, a combination of these impedance models can be applied.

3.1.2 Programme structure and simulation process

Sbtrack is a collection of programme comprised of several sub-programmes assigned for specific function in the numerical calculation. There are ten sub-programmes in the pre-modified sbtrack. Their names and specific tasks are briefly described in the grey box below.

Beam parameters and other essential constants are all contained within the input file, `sbrack_input.m`, as well as initial beam conditions, numerical calculation conditions, sources of wakefield to be accounted in the calculation and all impedance arbitrary parameters.

The commanding programme, `sbtrack_run.m`, works as the central commanding unit as well as generating the numerical results after the simulation is finished. Numerical simulation by sbtrack is practically started here by executing this commanding routine. The routine will call up the input file, `sbrack_input.m`, to define all initial parameters for the simulation to processing memory and save them to a parameter structure `‘S’` with a saving command assigned by `save_struct.m`.

Next, the commanding programme will call up the main programme, `sbtrack.m`, to start simulation then loads the structure `‘S’` using a loading programme, `load_struct.m`, and enters to the core simulation code.

`sbtrack.m`	main programme
`sbrack_input.m`	input parameter setting up
`sbtrack_run.m`	programme command
`load_struct.m`	input loading command
`save_struct.m`	post-processing saving command
`maptrack.m`	constructing non-linear one turn map
`bbr_longitudinal.m`	longitudinal BBR wake function calculation
`bbr_transverse.m`	transverse BBR wake function calculation
`rw_longitudinal.m`	longitudinal resistive wall wake function calculation
`rw_transverse.m`	transverse resistive wall wake function calculation

At the main processing code of sbtrack, it firstly asks whether the non-linear tracking is requested. If this tracking option (which has already been defined in the input file) is declared ‘yes’, the programme will loads the non-linear one turn map file which had preliminary been prepared by a sub-programme `maptrack.m` that was constructed following the method introduced by Rowland *et al.* [79]. If it is declared ‘no’, the simulation will be carried on with linear tracking simulation.

Next step, the time lagging evaluation grid will be particularly created for wake function calculation conformed to a pre-identified evaluation window determined in an input file. This evaluation grid will be redirected to sub-programme `bbr_longitudinal.m` in order to calculate the longitudinal wake function due to BBR impedance following equation 3.1. As well as redirecting to a sub-programme `bbr_transverse.m` for calculating wake function in transverse plane if the transverse instability was considered.

The calculated wake function due to BBR impedance will be sent back to the core sbtrack programme as a Green function assigned to parameter `Gl` and `Gt` for longitudinal and transverse BBR wake functions respectively. Then they will be executed by the Fast Fourier Transformation (FFT) to obtain the effective impedance which are consequently assigned to parameter `Zl` and `Zt` for longitudinal and transverse plane respectively. After that, they will be sent to numerical calculation started with the first value of bunch current from an array `Ib` which was already given in an input file. The parameter `Ib` can be defined with multiple values of bunch currents.

When entering to the main loop, the code firstly generates the initial values assigned to all particles with 6-dimentional phase space by constructing a $[6 \times N]$ matrix where N is the total number of particles following the Gaussian distribution with standard sigma parameters $\sigma_{\tau 0}, \sigma_{\varepsilon 0}, \sigma_{x0}, \sigma_{xp0}, \sigma_{y0}$ and σ_{yp0} corresponding to the theoretical natural length of each dimension in 6-D phase space analytically calculated from the input parameter. Additionally, there is also another option for manually constructing the initial particle distribution by loading the input distribution via parameters; `Hdistribution0`, `Vdistribution0` and `Ldistribution0` which refer to horizontal, vertical and longitudinal distributions respectively to the core programme.

Then the initial bunch is passed on to the numerical execution loop to start the first revolution turn. First of all, the whole evaluation window (which has already been reserved for at least 14 times longer than the natural bunch length, $\sigma_{\tau 0}$) will be binned longitudinally into discrete set of longitudinal blocks where the number of blocks can be pre-defined with parameter `BINS` in an input file. All particles are then distributed into each block depending on their respected value. After this process the current distribution in 6-D phase space especially the longitudinal current distribution, λ_0, will be completely constructed and ready to be advanced to further numerical calculation process.

The initial bunch distribution will be executed by the FFT and allocated to parameter `fl` which will be convoluted with the impedance parameter `Zl`.

Then the bunch-wakefield convolution product in frequency domain is executed with the inverse Fast Fourier Transformation (iFFT) and assigned to a parameter array `kl` which is later operated with the pre-computed macro charge to generate an energy increment or ‘kick’ due to the wakefield. This energy kick will implement the initial energy spread and delivered to the net energy calculation together with the energy gain from rf cavity and energy lost due to synchrotron radiation in one turn. The radiation damping and quantum fluctuation effects are also included in the calculation. The energy recalculation of the bunch follows a dynamic relation

$$\delta_i(n+1) = \left[\delta_i(n) + \frac{V_{rf}}{E_0} sin\left(2\pi f_{rf}\tau_i(n) + \phi_s\right) - \frac{U_0}{E_0} - k_l \frac{T_0 I_b}{NE_0}\right] \times (1 - D_\varepsilon) + 2\sigma_{\varepsilon 0} R_n \sqrt{\frac{T_0}{\tau_s}} \tag{3.7}$$

where δ_i the energy of particle ensemble i, n the turn number, V_{rf} the rf voltage, E_0 the nominal beam energy, f_{rf} the rf frequency, c the speed of light, ϕ_s the synchronous phase, U_0 the energy lost per turn, T_0 the revolution period, I_b the bunch current, N the number of particle and τ_i the longitudinal position of particles element i.

The second and third term in square bracket are the energy gain from rf cavity and an energy loss due to synchrotron radiation respectively. A term D_ε is the radiation damping obtained from

$$D_\varepsilon = \frac{2}{\tau_s} T_0 \tag{3.8}$$

where τ_s is the longitudinal damping time deducted from

$$\tau_s = \frac{2CE_0}{cU_0 J_s} \tag{3.9}$$

where the longitudinal damping partition number $J_s = 2 + \mathcal{D}$ and quantity $\mathcal{D}$ is given by [80]

$$\mathcal{D} = \frac{1}{2\pi}\int_{mag} D(s)(b_1(s)^2 - 2b_2(s))\, ds$$

According to the practical guideline for lattice design [80], $D(s)$ is dispersion function and b_n is a pure regular multipole defined by

$$b_n = \frac{1}{B\rho}\frac{1}{(n-1)!}\frac{\partial^{(n-1)}B_y(x,y)}{\partial x^{n-1}}\bigg|_{y=0}$$

The last term in equation 3.7 is the effect of quantum fluctuation where R_n is a random distribution.

The values of particle ensemble energy will be passed on to the recalculation of longitudinal positions following

$$\tau_i(n+1) = \tau_i(n) - \alpha T_0 \delta_i(n+1) \tag{3.10}$$

where α the momentum compaction factor. Finally, the post-processing longitudinal array $[\tau, \delta]$ of all N particles will be passed on to the next revolution loop as an initial bunch distribution and the whole process will be repeated until the last revolution turn is successfully succeeded.

At the end of each revolution turn the 6-dimentional distribution will be handed to the calculation of mean value and standard deviation of the particle ensemble in a bunch and saved into corresponding sequence in resulting arrays `means` and `stds` respectively. Both resulting arrays will be stand by in the processing memory unit in order to save the result from next consecutive turns. The arrays would have been continuously accumulated throughout all the simulated revolution until the last revolution loop is finalized. Each of the completed accumulating array comes out as a $[6 \times N_{turn}]$ matrix where N_{turn} is a number of revolution turns and saved into their corresponding sequential bunch current in the resulting structure `‘X’` with saving routine `save_struct.m`.

After finishing all revolution turns of recent bunch current, the code will be set back to start the next current value and repeating all the simulation process again until finishing the last assigned bunch current. The resulting structure 'X' will accordingly appears as a $[6 \times N_{I_b} \times N_{turn}]$ matrix where N_{I_b} is the number of simulated bunch currents and able to be brought into further analysis for the beam dynamical behaviour as well as the radiation properties with a presence of collective wakefields.

3.2 Simulation testing on CSR bursting investigation

Energy $(\boldsymbol{E_0})$	$\mathbf{1.7\ GeV}$
Natural energy spread $(\boldsymbol{\sigma_\varepsilon/E})$	7×10^{-4}
Longitudinal damping time $(\boldsymbol{\tau_s})$	8.0 ms
Momentum compaction factor $(\boldsymbol{\alpha})$	7.3×10^{-4}
Bunch length $(\boldsymbol{\sigma_{\tau 0}})$	10.53 ps
Accelerating voltage $(\boldsymbol{V_{rf}})$	1.4 MV
RF-frequency $(\boldsymbol{\omega_{rf}})$	500 × 2π MHz
Gradient of RF-Voltage $(\boldsymbol{\partial V_{rf}/\partial t})$	4.63 kV/ps
Circumference $(\boldsymbol{C})$	240 m
Revolution time $(\boldsymbol{T_0})$	800 ns

Table 3.1: Nominal beam parameters of BESSY II storage ring.

The preliminary investigation on the CSR bursting behaviour with sbtrack was performed by comparing with experiment performed at BESSY II storage ring. This task is intended to examine the capability of the code in inspecting characteristic behaviour of the temporal transition of stable and unstable motion due to beam instability. This behaviour of the bunch is also directly related to characteristic coherent synchrotron radiation (CSR) bursting. It could be expected that such a mechanism would likely be occurred if the temporal behaviour is exposed.

BESSY II is the third generation synchrotron facility located in Berlin, Germany. They have also been conducting a programme on the CSR generation in THz range. The observation of the CSR bursting was conducted in 2009 [81]. Example of the detected bursting signal is demonstrated in figure 3.2. Theoretical evaluation were also performed later in 2010 [82]. The Vlasov-Fokker-Planck solver verified a simple BBR impedance model that is able to explain many features of the CSR emission.

The sbtrack is brought into numerical examination with BESSY II environment by simulating with the beam parameters listed in table 3.1. The code is executed with 5,000 particles and revolving for 80,000 turns. The evaluation window width is $21\sigma_\tau$ which separated into 512 bins.

Then sbtrack passed on the result to the beam profiles analysis. The longitudinal centroid signal can be obtained from the first coordinate of parameter array `means` which refers to an average longitudinal particle position, $\bar{\tau}$, at each corresponding turn. It is plotted with turn number and bunch current as a colour map illustrated in figure 3.3(Left).

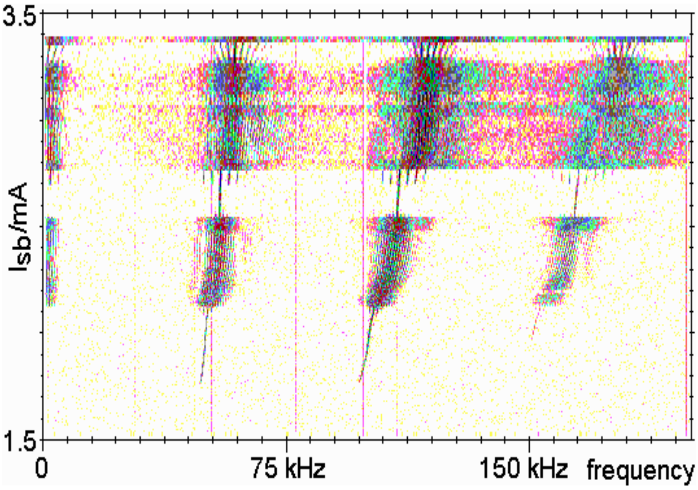

Figure 3.2: The temporal structure of CSR bursting in frequency domain observed without superconducting insertion devices at BESSY II [81].

The bunch length signal can be obtained from the first coordinate of array `stds` which refers to a deviation of longitudinal position of all particles in the bunch. This value is accordingly a bunch length at particular turn. It is plotted with turn number and bunch current as a colour map illustrated in figure 3.3(Right).

Both the signals of bunch centroid and bunch length illustrated in figure 3.3 suggest that the temporal unstable motion of the bunch in time domain is occurred at a current more or less than the bursting signal observed at BESSY II storage ring indicated in figure 3.2. The sudden change between stable and unstable motions in longitudinal plane is an indication of the onset of microwave instability.

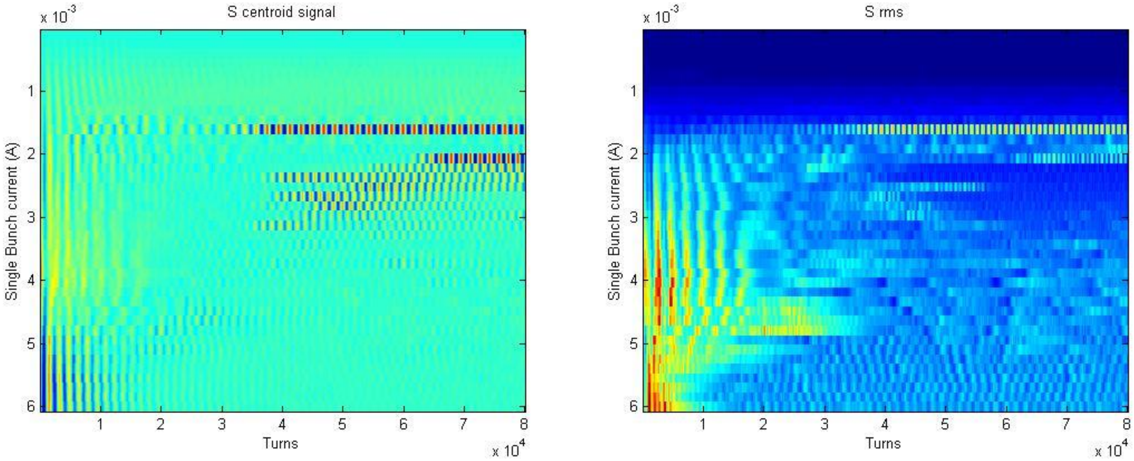

Figure 3.3: Sbtrack simulated longitudinal bunch centroid signal (Left) and bunch length signal (Right) of the simulation with BESSY II parameter.

Figure 3.3 also illustrates that at the instability stage both the bunch centroid and bunch length are periodically oscillating which indicates that the bunch development is repetitively evolved with particular frequency. This behaviour is in agreement with finite CSR bursting frequencies detected in experiment.

3.3 Code implementations

Despite that the sbtrack tryout has demonstrated a programme capabilities to expose an indication of CSR bursting in BESSY II, the geometric wakefield is, in fact, not the only contributor to the beam instability.

As stated, the impedance model is particularly intended to simulate the beam coupling impedance accounting for electromagnetic field excited by the interaction of the bunch and its surrounding structure. Another considerable source of beam instability needed to be considered is the interaction between particle bunch and the synchrotron radiation emitted from particles within the same bunch or the so called ‘radiation wakefield’.

In general, the composition of contributions due to geometric and radiation wakefields on the beam instability are varied upon circumstances of each machine and parameter setup. Both instability contributors are always presented and influenced the beam dynamics in all accelerators, so that it is essential for the numerical simulation to be able to encounter with both majority instability sources. Apart from the geometric collective effect that has already been accounted by the sbtrack, a capability of simulating the beam instability due to the radiation wakefield has to be implemented to the code as well.

In addition to the implementation with calculation of radiation wakefield, sbtrack has also been implemented with others calculation options. Further descriptions of all implementations will be described in this section.

3.3.1 Radiation wakefield implementation

As previously demonstrated in chapter 2, an ensemble of particles moving on curved trajectory emits the radiation traveling at speed of light on a chord and catches up with a bunch. Consequently, the interaction of particles with the radiated electromagnetic field is restricted only to the leading particles. This phenomena leads to the radiation wakefield which has already been asserted to be composed of free space wake and shielding effects [83].

Specifically, in the study of short bunch regime where the radiated wavelength is comparable to the bunch length, the synchrotron radiation from each particle will interfere constructively and result the coherent synchrotron radiation (CSR) which its power is proportional to the square of the number of particles. Since the practical number of particle per bunch is usually in an order of $10^8 – 10^{11}$ [4], the power of the coherent radiation is extremely higher than the conventional incoherent radiation.

Due to the fact that the maximum wavelength of synchrotron radiation from storage ring is generally defined by the bunch length or suppression effect following the shielding cut-off wavelength, λ_c, given by equation 1.3 [17]

$$\lambda_c = 2h\sqrt{\frac{h}{\rho}}$$

where ρ is a radius of curvature of the particles trajectory and h is a transverse size of the chamber or distance between guiding magnet poles. In short bunch regime, the bunch length is usually shorter than the chamber size. Thus the radiated wavelength that is able to propagate in the vacuum chamber and involve in the radiation wakefield is generally the coherent synchrotron radiation. Hence, the radiation wakefield is commonly referred to as the CSR wakefield as well. Furthermore, by characteristic condition of short bunch, the CSR wakefield is further enhanced and resulting on an increasing of bunch vulnerability to be substantially affected by such wakefield.

Both the free space and shielded radiation wakefields can be summed up and represented as the CSR wake potential, $V_{\omega f}$, following formula 2.68 [13], [14]:

$$V_{\omega f}(z) = -\frac{2\pi\rho_0}{4\pi\epsilon_0}eN_e\left(\int_0^{\infty}\frac{2}{(3{\rho_0}^2)^{\frac{1}{3}}}\frac{d\lambda(z-z')}{dz}\frac{1}{(z')^{\frac{1}{3}}}dz'\right.$$
$$\left.-\frac{1}{2h^2}\int_{-\infty}^{\infty}\lambda(z-z')G_2\left[\frac{1}{2h}\left(\frac{\rho_0}{h}\right)^{\frac{1}{2}}z'\right]dz'\right)$$

where ρ_0 is the bending radius, N_e the number of electrons in a bunch, ϵ_0 the vacuum permittivity, λ the bunch distribution, h the half-height of vacuum chamber and G_2 is the parallel plate wakefield scaling function following the formula 2.64 [14]

$$G_2\left(\xi/\Delta^{3/2}\right) = 2\sum_{k=1}^{\infty}\frac{(-1)^{k+1}}{k^2}\left[\frac{4Y_k^4\left(3-Y_k^4\right)}{(1+Y_k^4)^3}\right]$$

The first term on right hand side of equation 2.68 is the free space radiation wake potential and the second term is the shielding effect according to parallel plates. The equation 2.68 can be rewritten into two separated term as follow

$$V_{\omega f}(z) = -\frac{\rho_0^{\frac{1}{3}}eN_e}{3^{\frac{1}{3}}\epsilon_0}\int_0^{\infty}\frac{d\lambda(z-z')}{dz}\frac{1}{(z')^{\frac{1}{3}}}dz' + \frac{\rho_0^{\frac{3}{2}}eN_e}{8h^4\epsilon_0}\int_{-\infty}^{\infty}\lambda(z-z')G_2 z' dz' \quad (3.11)$$

Then the energy of particle ensemble in equation 3.7 is needed to include an effect of radiation wakefield and has to be modified as

$$\delta_i(n+1) = \left[\delta_i(n) + \frac{V_{rf}}{E_0}cos\left(2\pi f_{rf}\tau_i(n) - \phi_s + \frac{\pi}{2}\right) - \frac{U_0}{E_0} - k_l\frac{T_0 I_b}{NE_0} + \frac{V_{\omega f}\left(\tau_i(n)\right)}{E_0}\right]$$
$$\times (1 - D_\varepsilon) + 2\sigma_{\varepsilon 0}R_n\sqrt{\frac{T_0}{\tau_s}} \qquad (3.12)$$

which the rf voltage has also been changed to cosine function in order to prepare for the calculation of negative momentum compaction factor. Details of this modification will be described later in sub-section of higher order alpha implementation.

In order to calculate the CSR wake potential in 3.11, Martin [84] developed a routine to calculate wake potential due to free space and shielding effects. The programme `‘csrwakefield.m’` was developed to particularly calculate the wake potential, $V_{\omega f}$, following equation 3.11 and another programme `‘csrshielding.m’` was also specifically developed to calculate the parallel plate wakefield scaling function, G_2, following equation 2.64.

After implementing an option of CSR wake potential calculation to sbtrack, the core programme has to be modified to passed on all necessary parameters to `‘csrwakefield.m’` at the early stage after entering to the virtual electron revolution loop. The CSR wake calculation sub-programme will return the wake potential to the main programme by assigning to parameter

`‘Vcsr’` which is then brought into the convolution process with the bunch distribution to attach energy increment due to CSR wake potential to the particle ensemble energy, δ_i, with MATLAB function ‘spline’ and ‘ppval’.

For further evaluation on the longitudinal dynamics of a bunch which subsequently be able to examine the resulting synchrotron radiation, the longitudinal position and energy deviation parameters, τ_i and δ_i, of every particle in a bunch are separately saved together with other characteristic parameters such as the longitudinal distribution profile, form factor, evaluation grids, induced voltage with respect to longitudinal bunch profile and radiated power.

3.3.2 Bunch initialization implementation

The initial longitudinal bunch distribution of sbtrack is normally created with the Gaussian distribution with standard sigma dimensions $[\sigma_{\tau 0}, \sigma_{\varepsilon 0}]$. Nevertheless, this initial bunch distribution has demonstrated acceptable tracking results on the numerical tryout in previous session, an electron bunch traversing vacuum chamber is, in fact, normally distributed with a distribution deviated from the Gaussian due to an influent of collective effects.

In chapter 2, a stable solution for the Vlasov-Fokker-Planck equation, the Haissinski equation, has shown that within a limit of low bunch current and weak wakefield, it is able to give an accurate estimation of the bunch distribution with a presence of collective effects. Consequently, the initial bunch distribution that would be advanced to the tracking programme as a starting bunch might be better constructed with a distribution analogous to the bunch in real accelerator. Hence, the bunch distribution constructed by semi-numerical solving of the Haissinski equation might be able to simulate the initial bunch distribution with more accuracy.

The sbtrack has been modified to be able to choose the bunch initialization scheme among three options; an original sbtrack Gaussian initialization or manually input via `Ldistribution0` parameter and newly applied option by constructing with a pre-calculated distribution obtain from Haissinski solution.

Previous studies demonstrated that tracking results can be benchmarked in particular condition with numerical solution of Haissinski equation [36], [85]. Recall that the Haissinski solution is an integral equation that describes the longitudinal current distribution, λ_0, in the limit of low current and weak collective effects. According to the work done by Oide and Yokoya [36], the Haissinski integral equation can be written as formula 2.25

$$\lambda_0(q) = \frac{1}{\kappa}\exp\left[-\frac{q^2}{2} + I\int_q^{\infty}\int_{q'}^{\infty}\lambda_0(q'')W(q''-q')dq''dq'\right]$$

where κ is a constant, W is the wake function, the normalized longitudinal displacement $q = \tau/\sigma_\tau$, parameter $I = \frac{2Nr_e}{\gamma c Z_0 \nu_s \sigma_\varepsilon}$ while $N, r_e, \gamma, c, \nu_s, \sigma_\varepsilon$ and Z_0 are the number of particles in the bunch, the classical electron radius, Lorentz relativistic factor, the speed of light, the synchrotron tune, the energy deviation of particles and the vacuum impedance respectively.

The solution of Haissinski equation can be found analytically in just a few simplified impedance cases, however it can be solved numerically within low current limit. If the low current limit has not been satisfied anymore the bunch distribution will be extremely deviated from the solution given by the Haissinski equation and multiparticle tracking is necessary.

In our case, it is obvious that the equation 2.25 can be solved numerically. Therefore, a separated sub-programme has been specifically created to solve the Haissinski integral equation. The programme `haissinski.m` is created and will be called up by the main programme `sbtrack.m` when the bunch initialization with the solution of Haissinski equation is selected.

This sub-programme will be input with all necessary parameters then passed on to construct a Gaussian distribution as an initial guessing for the first try. Then the programme calculates longitudinal current distribution following equation 2.25 with wakefield obtained by calling up the BBR and CSR wake calculations. The distribution product will be compared with initial distribution and being examined the difference. If the difference is not exceeding the tolerance, it will be passed on to start the next loop as a new input distribution. The process will be carried on until the tolerance is exceeded. The finalized bunch profile will be the distribution that satisfied Haissinski integral solution and then passed on to the main sbtrack programme for further simulation.

3.3.3 Higher order alpha implementation

As stated in chapter 2, in order to achieve the quasi-isochronous condition, a momentum compaction factor has to be reduced to approach zero. At this circumstance, the nonlinear terms of momentum compaction factor become significant. Equation 2.69 shows that the momentum compaction factor can be expanded as a power series of energy deviation, δ, as follow

$$\alpha = \alpha_1 + \alpha_2\delta + \alpha_3\delta^2 + O(\delta^3)$$

where $O(\delta^3)$ is presumably an error due to higher order terms.

Sbtrack was originally intended to perform the multiparticle tracking with average momentum compaction factor which only the linear term is considered. So that the code has to be modified to be able to perform tracking with low alpha lattices which the nonlinearity of higher order alpha becomes significant to the beam dynamics.

The code is implemented with the second and third order alphas. The equation of motion in 3.10 is modified to

$$\tau_i(n+1) = \tau_i(n) - [\alpha_1 + \alpha_2\delta_i(n+1) + \alpha_3\delta_i^2(n+1)]T_0\delta_i(n+1) \quad (3.13)$$

Apart from a low alpha scheme that sbtrack has been provisioned to engage, the negative alpha scheme has also been deliberately scrutinized as well. In principle, the momentum compaction factor is an essential parameter in obtaining the synchronous phase, ϕ_s, and synchrotron frequency, f_s, which can be calculated from relations

$$\phi_s = \arcsin\left(\frac{U_0}{V_{rf}}\right) \quad (3.14)$$

$$f_s = f_{rev}\sqrt{\frac{\alpha heV_{rf}\sin\phi_s}{2\pi E_0}} \tag{3.15}$$

From a formula 3.15, it is obvious that if the alpha becomes negative, the synchrotron frequency will subsequently be imaginary. Therefore, sbtrack is modified with a conditional coding in which the synchrotron frequency will be redefined as

$$\phi_s = \begin{cases} \pi - \arcsin\left(\frac{U_0}{V_{rf}}\right) & for\ \alpha_1 > 0 \\ \arcsin\left(\frac{U_0}{V_{rf}}\right) & for\ \alpha_1 \leq 0 \end{cases} \tag{3.16}$$

which is then passed on to calculate the synchrotron frequency that is also modified to

$$f_s = f_{rev}\sqrt{-\frac{\alpha heV_{rf}cos\phi_s}{2\pi E_0}} \tag{3.17}$$

These modifications consequently modify the sinusoidal function used to obtain the energy compensation from rf cavity. According to an energy compensation term in equation 3.7, the energy compensation, δ_{rf}, has to be modified to

$$\delta_{rf} = \frac{V_{rf}}{E_0}cos\left(2\pi f_{rf}\tau_i(n) - \phi_s + \frac{\pi}{2}\right)$$

as illustrated in equation 3.12. These modifications enable sbtrack to accept the negative momentum compaction factor as well as the higher order terms to the third.

3.3.4 Frequency noise reduction

Bunch density distribution deposited in saved file typically contains inherent noise. Fast Fourier Transformation directly executed from this ‘raw’ bunch distribution consequently appears with lots of unwanted noise which has to be eliminated before passing through to further signal processing evaluations. In order to filter out these frequency noise, the signal filtering window is essentially implemented to sbtrack.

The Hann window function is attached to the sbtrack main code in order to filter out the unwanted noise on top of the longitudinal density distribution of a bunch.

Hanning window function is given by

$$w(n) = 0.5\left(1 - cos\left(2\pi\frac{n}{N}\right)\right) \qquad ,0 \leq n \leq N \tag{3.18}$$

where n is an arbitrary discrete element and N is the overall range of discrete elements.

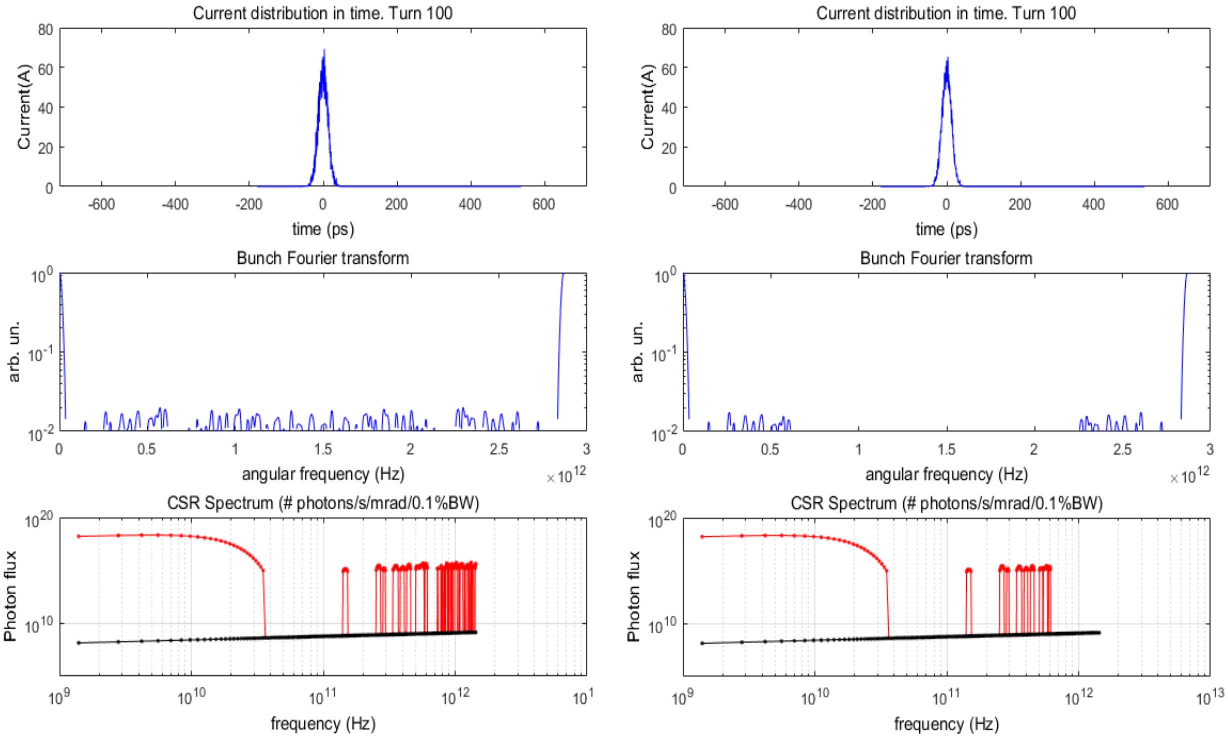

Figure 3.4: Comparison between pre-filtering (left column) and post-filtering (right column) bunch distribution, corresponding FFT and the coherent radiation flux (red) compared to incoherent radiation flux (black).

A raw bunch longitudinal distribution profile will be applied with the Hanning window function in order to get rid of the frequency noise before being passed on to an execution with FFT to get an instant form factor of the bunch. This smoothed form factor will then be passed on to the calculation of coherent radiation power corresponding to equation 2.42. Figure 3.4 demonstrates a comparison of bunch longitudinal distribution, the corresponding post-processed FFT and the photon flux coherently radiated from a corresponding bunch. It also illustrates that a raw bunch with unwanted noise is consequently transformed to high frequency noise on the plot of coherent radiation flux. These noise are significantly eliminated by the Hanning window.

Nevertheless the window function is able to significantly filter out unwanted noise on top of the bunch profile, its further processing result, for example the radiation flux, has still shown the radiation noise at high frequency range. The post-processing demonstration of the programme might need to be implemented with further noise reduction process to be able to eliminate frequency noise at more aggressive level. A MATLAB smoothing function called 'cubic smoothing spline function' (csaps) is then implemented to the post-processing process in sbtrack. A detailed description about this implementation will be explained in the post-processing demonstration sub-section.

3.3.5 Post-processing demonstration

In order to handling sbtrack on the investigation of CSR bursting behaviour, the evaluation of radiation spectra and the bunch dynamical development are critically important to be depicted and compared with the experimental observations.

3.3.5.1 Radiation spectrum showcase

Longitudinal bunch profile saved in the post-processing file will be brought into the coherent radiation and longitudinal dynamics development analysis. Another dedicated sub-programme is constructed to specifically executing raw data deposited in a saved file and prepare the visualized representation in various customizable demonstrations. According to figure 3.5, the longitudinal bunch density distribution will be passed on to the FFT analysis to obtain the bunch distribution in frequency domain which is displayed on the second row. Then it is brought into the calculation of coherent radiation flux following equation 2.42 and illustrated on the third row of figure 3.5 with red dotted line. The plot of CSR flux is also compared with the incoherent radiation displayed in black dotted line.

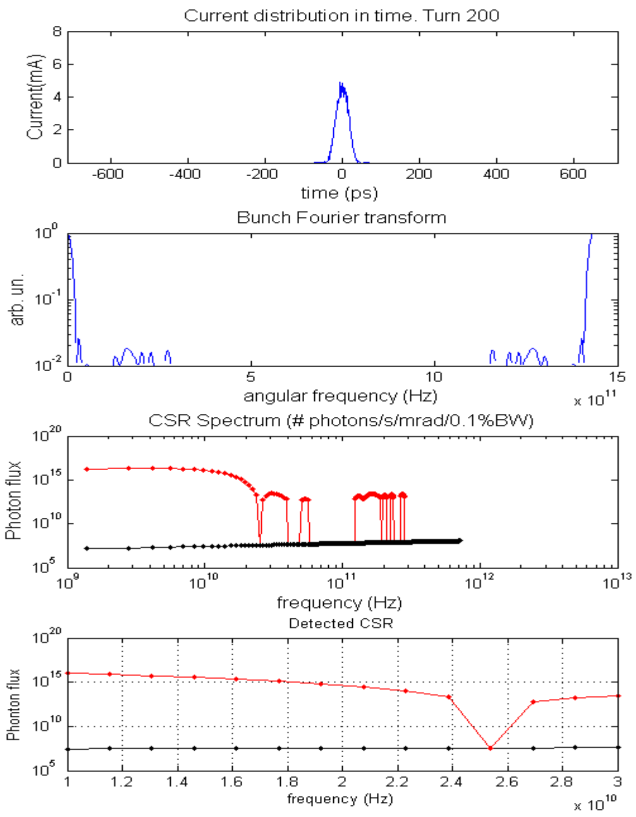

Figure 3.5: Plots of longitudinal bunch profile, its post-processed FFT, coherent radiation flux in all frequency range and in specified simulating range.

The comparison between coherent and incoherent radiation flux in figure 3.5 demonstrates that the coherent flux is much larger than the incoherent radiation at approximately ten order of magnitude.

Sbtrack is also enabled an option to define the simulated detecting frequency range in order to replicate the frequency range of photon detector employed in experiment. This option is able to provide predicted result and easily to compare with the results obtained from machine experiment.

At the same time, the plot of radiation bursting in frequency domain similar to figure 3.2 is also important on the investigation of CSR emission behaviour under particular beam instability.

Such a plot can be generated by obtaining a form factor first. The form factor can be constructed by executing the square of FFT of longitudinal bunch profile following equation 2.43. This form factor will be brought into the integration within pre-defined frequency range to get the radiation power of corresponding frequencies. The radiated power will then be represented in time domain as a function of turn number as illustrated in figure 3.6.

The power radiated in time domain will be redirected to FFT analysis in order to obtain the frequency component of the radiation bursting. This plot will be able to demonstrate the characteristic bursting behaviour of the radiating bunch affected by collective instabilities. An example of this 'bursting pattern' at particular bunch current is demonstrated in figure 3.7.

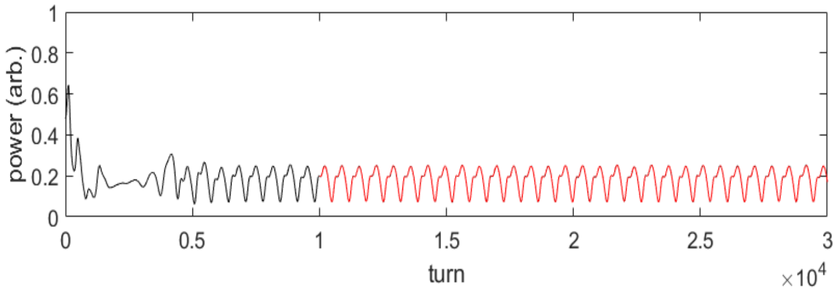

Figure 3.6: Plot of radiation power of frequency range 75 GHz – 1.5 THz with turn number of a bunch with α_1 = 1.0 x 10^{-5} and V_{rf} = 3.4 MV at 20.35 μA. The bunch is influenced by both the broad-band resonator and the CSR wakefields.

The bursting frequency corresponding to several bunch currents can be stacked together to construct a radiation bursting pattern of specified range of current. Figure 3.8 illustrates the bursting pattern of a bunch with α_1 = 1.0 x 10^{-5} and V_{rf} = 3.4 MV at bunch current 0 - 100 μA. The plot is comprised of 50 plots of radiation frequency within range 75 GHz – 1.5 THz.

When the radiation bursting pattern is depicted, it is apparent that the onset of beam instability can be easily inspected by an emerging of bursting lines, for example at 13.90 μA on figure 3.8. Furthermore the characteristic radiation bursting behaviour can also be inspected through this colour map according to the features of CSR introduced by Venturini and Warnock [6].

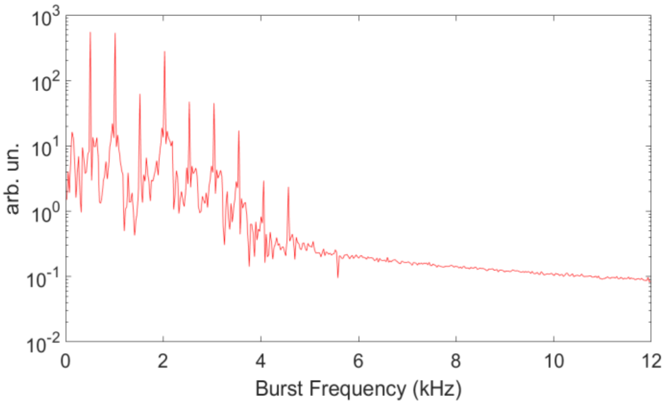

Figure 3.7: Plot of radiation bursting frequencies within range 75 GHz – 1.5 THz of a bunch with α_1 = 1.0 x 10^{-5} with V_{rf} = 3.4 MV at bunch current 30.02 μA.

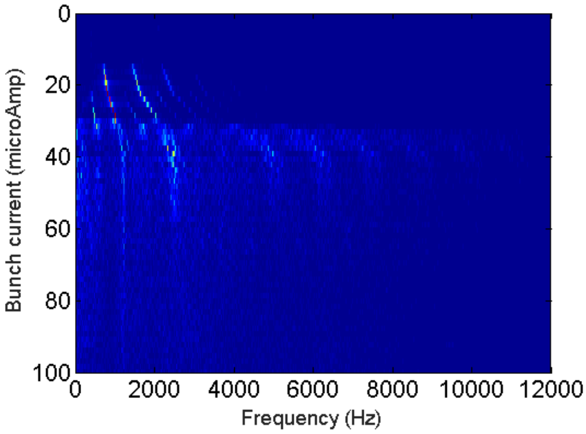

Figure 3.8: The radiation bursting pattern colour map of a bunch with α_1 = 1.0 x 10^{-5} and V_{rf} = 3.4 MV of current 0 - 100 μA. The bunch is influenced by both the broad-band resonator and the CSR wakefields. This colour map is plotted as same as the plot in figure 3.2 but with inverse order of bunch current.

3.3.5.2 Longitudinal beam dynamic showcase

Apart from the radiation pattern that illustrates characteristic feature of the radiation bursting of particular beam parameter, the longitudinal phase space evolution of a bunch is mandatory in exhibiting distinctive feature on dynamical evolution due to beam instabilities.

In order to illustrate the evolution of longitudinal phase space over time, average particle positions and standard deviation of particles in a bunch that are saved in the post-processing structure `‘X’` is insufficient. Because of that a specific routine has to be implemented to the main sbtrack code in order to save the position of all particles in 2-D longitudinal phase space. Then the dedicated phase space imaging programme, `sbrack_read.m`, is created to process a saved array of 2-D phase space to generate time evolution longitudinal phase space of a bunch. An example is demonstrated in figure 3.9.

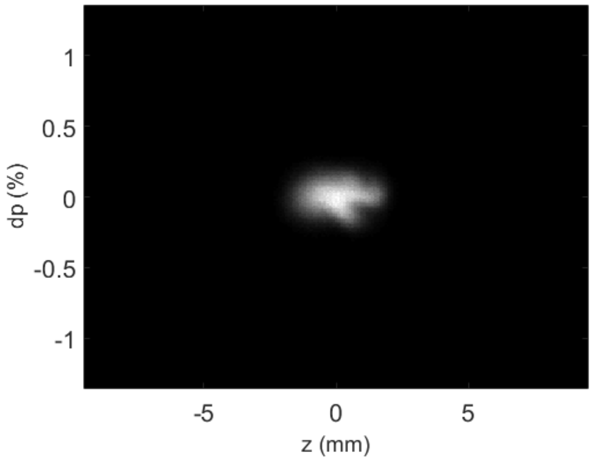

Figure 3.9: The longitudinal phase space of a bunch affected by CSR wakefield with beam parameter α_1 = 1.0 x 10^{-5} and V_{rf} = 3.4 MV at bunch current 44.53 μA revolving at 14000 turn.

3.4 Code testing with SOLEIL parameter

The Synchrotron SOLEIL has also motivated on a short bunch production scheme in order to optimize facility performance to the generation of coherent synchrotron radiation. Machine experiment for the CSR generation has been performed as well as numerical simulation that was also developed and evaluated concurrently. According to the report presented by Evain *et al.* [13], the simulation programme is able to expose the bursting features detected in experiment, even though there has still been discrepancy between bursting threshold predicted by numerical simulation and that occurred in experiment. They also indicated that the numerical programme was developed only a consideration of CSR wakefield while neglecting the geometric wakefield. The experimental detection of the THz bursting signal compared to the bursting pattern rendered from numerical simulation is demonstrated in figure 3.10.

The threshold predicted by the numerical programme has considerably overestimated the experimental result. As well as most of the bursting frequencies revealed by numerical evaluation have still underestimated the detection in experiment.

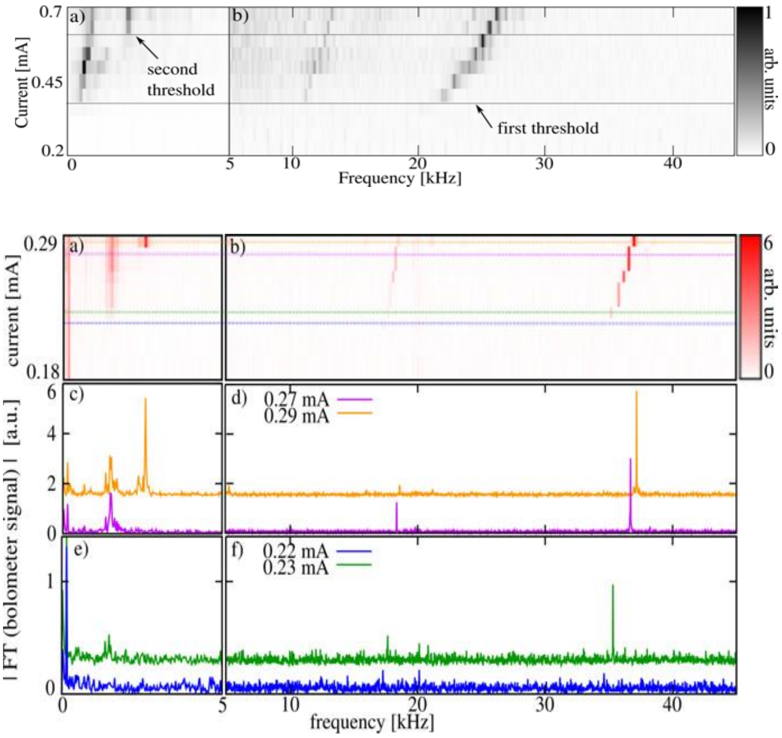

Figure 3.10: (Top) The numerical simulated spectrum performed at SOLEIL with the same condition as experiment. (Bottom) The CSR bursting spectrum detected in experiment at SOLEIL storage ring. [13]

According to an underestimation of the bursting frequencies by numerical programme, it has already been figured out by Bane *et al.* [86] that this phenomena is due to an insufficient number of particles in the simulation. Regarding practical beam parameter of the most synchrotron machines, the number of particles per bunch in experiment is approximately 10^8 – 10^{11}. While the number of particles in numerical evaluation has generally been unable to reach such number because of constraint on the computing capacity and necessity to compromise with running time.

Sbtrack is brought into the investigation with SOLEIL parameter on the generation of coherent synchrotron radiation scheme. Figure 3.11 illustrates a comparison of numerical results performed by SOLEIL and by sbtrack. It demonstrates that sbtrack is able to simulate all the bursting features exposed in the simulation performed at SOLEIL.

In terms of the comparison with experimental results as shown in figure 3.12, sbtrack exhibits its capability to simulate all the bursting features detected in experiment. Despite it has still underestimated the bursting frequencies as well as slightly overestimated the onset of beam instability, the sbtrack result is apparently able to provide a better simulation results than the numerical programme developed at SOLEIL.

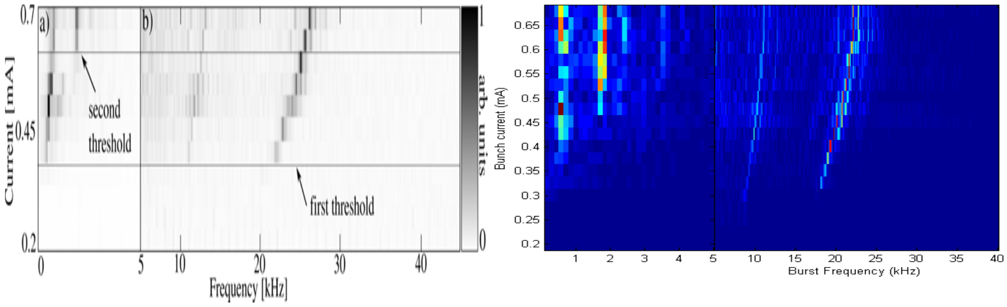

Figure 3.11: Comparison of numerical results investigating the CSR bursting signal at SOLEIL performed by Evain *et al.* (Left) with the bursting pattern generated by sbtrack (Right).

From now on, sbtrack is brought into the numerical investigation of the collective instabilities encountering on the short bunch production regime at Diamond Light Source. The results will be exhibited in chapter 5.

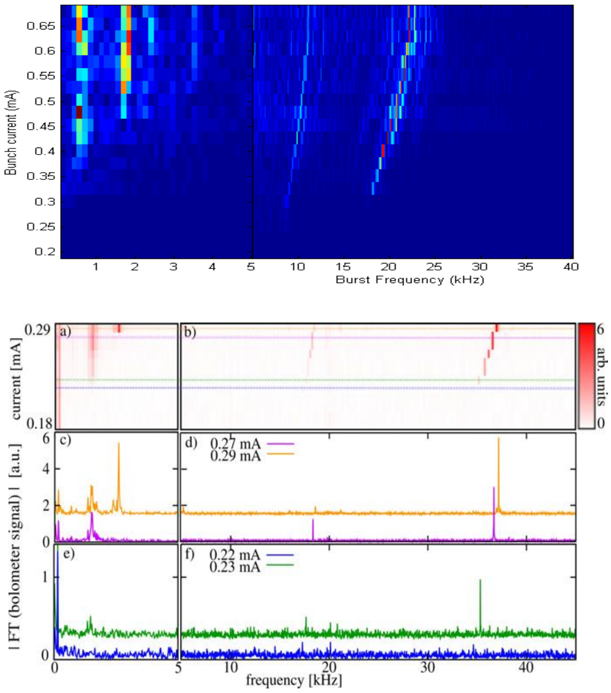

Figure 3.12: Comparison of an experimental result obtained at SOLEIL with a numerical results performed by sbtrack.

Chapter 4

Modelisation of Impedance

The total impedance is often budgeted consistently with the beam intensity requirement. However, the higher beam intensity is pushed, the more beam-induced electromagnetic fields in vacuum chamber generated. Beam dynamics can be significantly influenced by such fields eventually limiting the maximum stored current. This beam-wall interaction is obviously an implication of unavoidable imperfections of accelerator structure. It would not be emerged if the beam environment is perfectly smooth and has no electrical resistance.

An evaluation of total ring impedance is generally complicated and time consuming due to the complexity of accelerator components. Especially in synchrotron light source, storage ring components and parameter setup are often modified in order to improve beam quality and customize suitable radiation for specific needs of beam line experiments. Consequently, these variations always contribute to an alteration on the total ring impedance and collective instabilities.

The usual approach to approximate machine impedance is analytically evaluating the impedance of individual component and sum up altogether to construct the total impedance value [5]. However, such process is apparently impractical.

The idea of identifying an impedance of the ring with simple resonator model permits simplification on further beam dynamics analysis especially an evaluation of wake function. Hence the process of machine impedance characterization is truncated to the construction of impedance model and evaluating its capability to reproduce the intensity dependent effects due to potential well distortion as well as beam instability onset. The comparison between numerical and experimental results is essential to the model adjustment in order to obtain the best arbitrary parameter that provide the most consistent result with machine measurements.

This chapter is proposing the idea of evaluating the impedance model by taking advantage of Haissinski equation [34]. Its solution is generally formulated as an equilibrium bunch distribution profile which can be obtained within considerably short time by numerical calculation. Therefore, the longitudinal distribution of a bunch under corresponding wakefield produced by an arbitrary impedance model can then be depicted really fast. Trial-and-error process of model adjustment could be carried out at shorter time than exploiting a tracking programme. Although the solution is restricted to low bunch current, the effects of potential well distortion such as bunch lengthening and energy spread growth might be sufficiently consistent for benchmarking with measurement. The bunch length and centroid position would be evaluated from this numerical solution profile.

In general, the constructed impedance model needs to be adjusted by benchmarking with the results from machine measurements. A Vlasov-Fokker-Planck (VFP) solver and multiparticle tracking code are usually brought into this task to observe the bunch development with increased current under the collective effects initiated by corresponding impedance model. The model refinement will be carried out by empirically adjusting its arbitrary parameters. Each temporary model is executed with VFP solver or tracking code, observing the bunch deformation and benchmarking with measurement results. The comparison result will indicate further arbitrary parameter adjustment. This process is repeated until a particular model is able to generate well fitted numerical result with experiment. The problem is each model tryout takes considerably long time on tracking procedure.

In contrast, each model tryout can be preliminary tested with Haissinski equation within a few minutes. The curve plots of bunch lengthening and centroid shifting with increasing current can also be generated altogether. These primary results can be benchmarked with experiments and further decision on model refinement can be made within much shorter time.

According to the Haissinski integral equation expressed in equation 2.25, it can also be written in a form

$$\lambda_0(q) = \frac{1}{\kappa}\exp\left[-\frac{q^2}{2} - I\int_q^\infty V_{ind}(q')dq'\right] \tag{4.1}$$

where

$$V_{ind}(q') = -\int_{q'}^\infty \lambda(q')W(q''-q')\,dq'' \tag{4.2}$$

In general, the solution of Haissinski equation can be found analytically in just a few simplified impedance cases, however it can be solved numerically in much faster way using Newton iteration starting with the Gaussian distribution fitting.

A separated MATLAB code is specifically developed for solving the Haissinski integral equation numerically. The code constructs a wake function, $W(q)$, corresponding to an arbitrary impedance model. For the LRC broad-band resonator model (BBR model), the wake function is produced following the equation previously deducted by Oide and Yokoya, Bane *et al*. and Cai *et al*. [36], [85], [87] while the model with serial connecting of purely resistive and purely inductive (R + L) follows the works done by Holtzapple and Heifet [29], [88]. When the wake function of corresponding model is generated, it is passed on to be convoluted with a calculated bunch density distribution (the Gaussian distribution for starting turn). The iteration equation for solving Haissinski equation follows a formula derived by Martin [84].

$$\lambda_{n+1}(q) = \frac{1}{3\kappa}\left\{\exp\left[-\frac{q^2}{2} + I\int_q^\infty V_{ind}(q')dq'\right] + \lambda_n(q) + \lambda_{n-1}(q)\right\} \tag{4.3}$$

where I is the normalized current following equation 2.19 and a constant κ can be obtained from normalization condition shown in formula 2.23. Subscription $n+1$ indicates the next turn, n indicates the recent turn and $n-1$ represents the previous turn. This numerical process will be carried on until the bunch density distribution converged into a stable bunch profile (the discrepancy between λ_{n+1} and λ_n is less than pre-defined convergence tolerance). The final bunch distribution will be measured for a bunch length and bunch centroid shift by calculating its standard deviation and mean position of particles respectively.

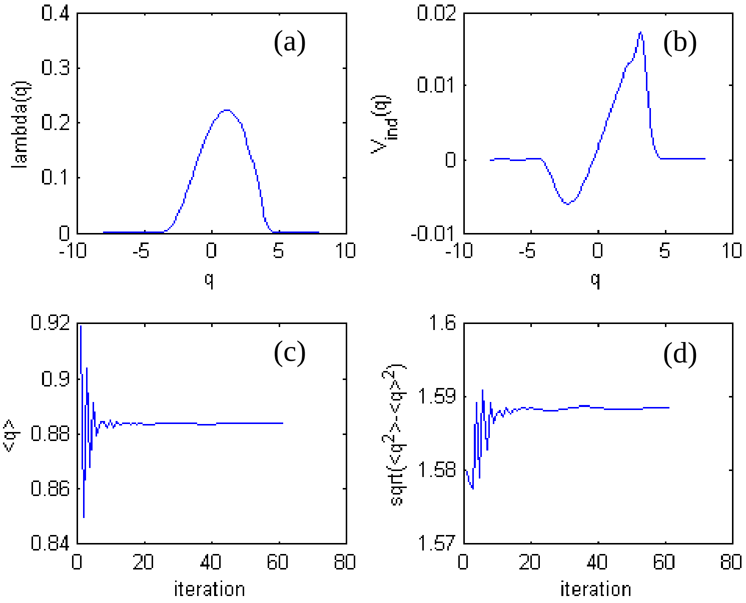

Figure 4.1: (a) A numerical calculated bunch density distribution following Haissinski integral equation. (b) Collective inducing voltage due to corresponding impedance. (c) and (d) Mean position and standard deviation of particles ensemble are converging to particular values.

Figure 4.1(c) and (d) demonstrate that mean position and standard deviation of particles converge into stable values after approximately 20 iterations. Figure 4.2(a) demonstrates that the distortion of bunch profile becomes easily inspected at higher current. This phenomenon depicts the nature of potential well distortion that can be estimated with Haissinski equation within a limit of low current. The calculated bunch density distribution will apparently be broken and the numerical calculation of the bunch distribution with Haissinski equation is invalid when a low current limit is no longer satisfied. Thus the impedance modelisation with

Haissinski equation has to be aware of reaching the broken point. This current limit is usually a few mA. Therefore, the maximum current for impedance modelisation by numerical calculation of Haissinski solution in this thesis is capped at 1 mA.

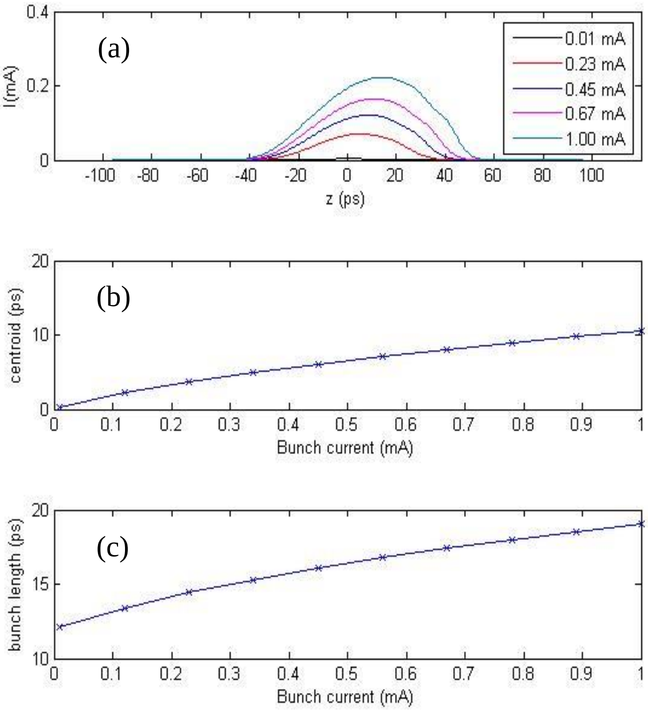

Figure 4.2: (a) Calculated bunch profiles at several currents exhibit an increasing of bunch shape distortion at higher current. Bunch centroid (b) and bunch length (c) growth are exhibited.

The experimental data taken as a benchmark for this study are machine experiment performed in June and September 2012 [89]. According to an expression of synchrotron frequency shown in equation 2.4, there are two parameters that can be experimentally adjusted and play the critical role in the bunch compression regime; the momentum compaction factor, α, and the rf voltage, V_{rf}.

The variation on these operating conditions subsequently differentiate corresponding bunch lengths. The experimental results are plotted in figure 4.3. The bunch length, figure 4.3(a), and bunch centroid shifting, figure 4.3(b), are plotted as function of bunch current. Experiment is also performed with opened insertion devices (IDs) at operating voltages V_{rf} = 2.5 and 3.3 MV because they are nominal operating conditions.

Energy $(\boldsymbol{E_0})$	3.0 GeV
Natural bunch length $(\boldsymbol{\sigma_{\tau 0}})$	12.75 ps
Natural energy spread $(\boldsymbol{\sigma_{\varepsilon 0}})$	9.618×10^{-4}
Longitudinal damping time $(\boldsymbol{\tau_s})$	5.6 ms
Momentum compaction factor $(\boldsymbol{\alpha})$	1.7×10^{-4}
Accelerating voltage $(\boldsymbol{V_{rf}})$	2.0 MV
RF-frequency $(\boldsymbol{\omega_{rf}})$	499.65 × 2π MHz
Circumference $(\boldsymbol{C})$	561.6 m
Revolution time $(\boldsymbol{T_0})$	1.873 μs

Table 4.1: Nominal beam parameter of Diamond Light Source storage ring.

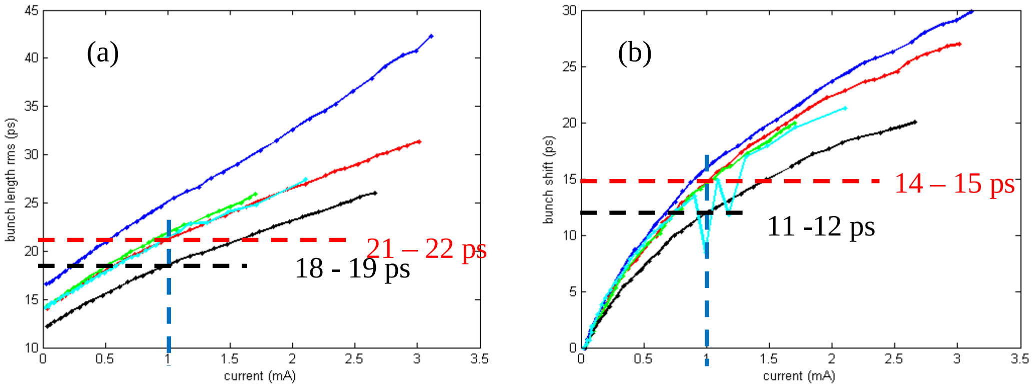

Figure 4.3: Measurement results taken from Diamond storage ring in June and September 2012 show the bunch lengthening (a) and shifting (b) versus bunch currents. The blue line represents V_{rf} = 2.0 MV with opened IDs, the red and green lines indicate V_{rf} = 2.5 MV with opened and closed IDs respectively, the black line represents V_{rf} = 3.3 MV with opened IDs and the cyan indicates V_{rf} = 2.5 MV with opened IDs. The bunch length and centroid shift values are estimated on V_{rf} = 2.5 and 3.3 MV with opened IDs curves at 1 mA and shown with dashed lines.

Due to shortage of precise data taken from experiment, the bunch length and centroid shifting values at 1.0 mA have to be estimated from the plots in figure 4.3. In order to get as most accurate value as possible, the measurement was not decided to estimate the bunch length and centroid shift as exact value but as ranges of value. The experiment shows that at bunch current 1.0 mA, for V_{rf} = 2.5 MV the bunch length is approximately 21 – 22 ps while the bunch centroid shift is approximatly 14 – 15 ps. For V_{rf} = 3.3 MV, the bunch length is approximately 18 – 19 ps while centroid shift is around 11 – 12 ps. The targeting ranges of bunch length and centroid shift at 1.0 mA were arranged from 0.5 ps below the lower bounds to 0.5 ps above the upper bound of approximating ranges estimated from experimental plots.

Thus, the criterions for candidate model are set as the bunch length falling in between 20.5 – 22.5 ps and bunch centroid shift between 13.5 – 15.5 ps on V_{rf} = 2.5 MV, while the bunch length falling in between 17.5 – 19.5 ps and centroid shift between 10.5 – 12.5 ps are also set as the criterions of V_{rf} = 3.3 MV. The candidate model must be able to reproduce the bunch length and centroid shifting developments at 1.0 mA that satisfied these regions of criteria.

4.1 Broad-band resonator (BBR) model

There are three parameters to be estimated for BBR model; resonant frequency ω_r , shunt impedance R_s and quality factor Q. Specifically for broad-band impedance, the quality factor is typically small [5]. Furthermore, broad-band impedance models previously obtained at many circular accelerators were in accordance with $Q = 1$ and yielded the most appropriate results that well agree with experiments. Accordingly, the model refinement would have been decided to set a quality factor at $Q = 1$. Consequently, there are two parameters left to be adjusted.

The model refinement was started at investigating the effect of each parameter on the bunch lengthening and shifting. Additionally, the trending revealed from this process would be beneficial to further empirical adjustment of arbitrary parameters.

The first parameter to be figured out is a shunt impedance R_s. The resonance frequency ω_r was initially set as a constant at 5 GHz while R_s was varied from 0.1 Ω to 35$k\Omega$. Bunch length and its centroid shifting were determined at 1.0 mA by solving Haissinski equation. The curves of bunch length and bunch shift versus R_s are shown in figure 4.4(a).

Next, the R_s was set as a constant at 30 $k\Omega$ then observed the bunch length and centroid shift changing due to variation of ω_r. The resonance frequency was varied from 5 Hz to 20 GHz. The bunch length and its centroid shifting were evaluated at 1.0 mA as well as the previous test and demonstrated in figure 4.4(b). Both numerical evaluations were run with V_{rf} = 3.3 MV.

The plots in figure 4.4 exhibit that bunch length is shortened with an increasing R_s as well as shortened with increasing ω_r. In contrast, the bunch centroid is shifted further with an increasing of both parameters. Increasing rate of centroid shifting is faster than reducing rate of bunch length with respect to both parameters.

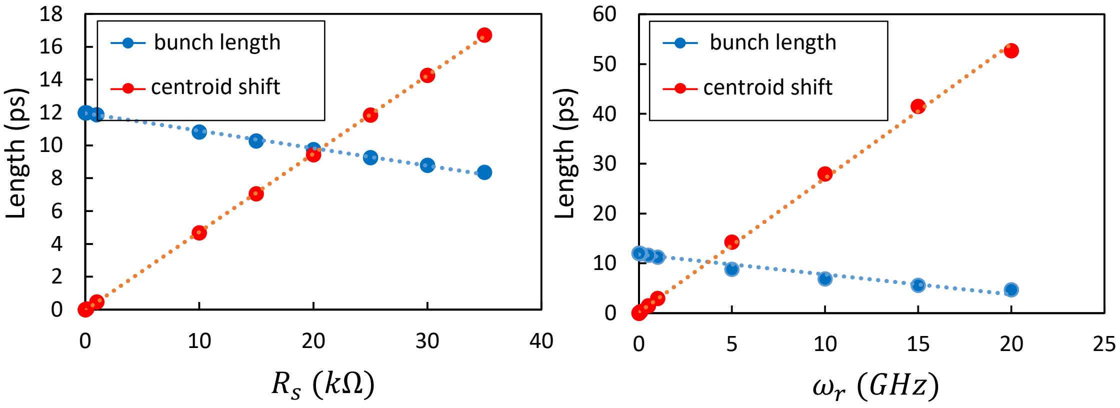

Figure 4.4: The contribution of R_s and ω_r to bunch lengthening and centroid shifting.

Then the study was moved on to the characterization of impedance. The model refinement started with 'old' BBR model; f_{res} = 48 GHz or ω_r = 301.59 GHz, R_s , = 20 $k\Omega$ and Q = 1, which had previously been identified by Bartolini *et al.* [90]. The model was brought into Haissinski equation and run with V_{rf} = 3.3 MV to investigate the bunch distribution profile affected by this impedance model. The calculated bunch profile corresponding to the old model is exhibited in figure 4.5(a).

The calculated bunch profile with old impedance model appears to reach shape broken point at 0.67 mA. However, according to the curve plots of bunch length and position shifting versus current, figure 4.5(b) and (c), it might be approximated that the bunch length and shifting at 1.0 mA due to the old BBR model would actually overestimates experimental result shown in figure 4.3. The experimental plots show that at V_{rf} = 3.3 MV the bunch length is approximately 18 – 19 ps and the shifting is around 11 – 12 ps. Comparing to contribution of R_s and ω_r which have been emphasized in figure 4.4, it can be concluded that in order to reduce the corresponding bunch length both parameters should be increased. In contrast, they should also have to be decreased in order to make the centroid shifting goes down.

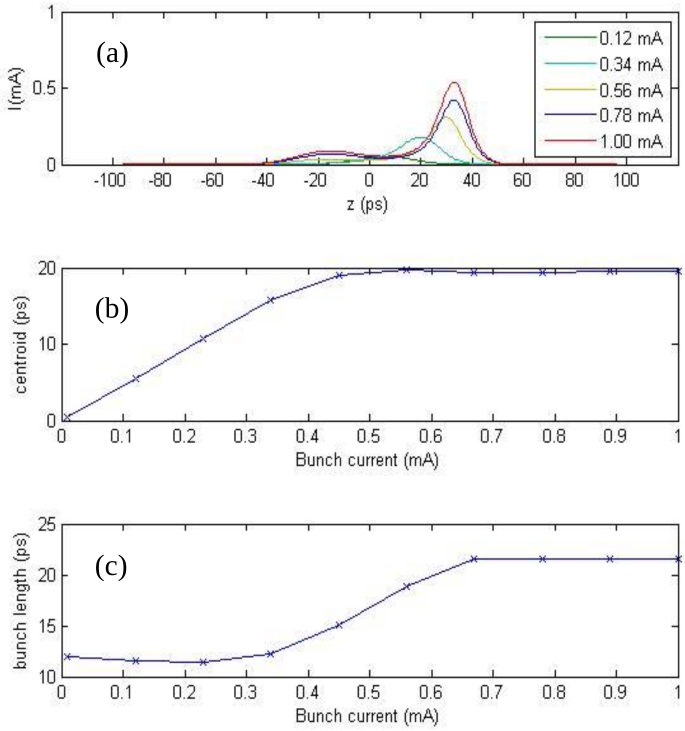

Figure 4.5: (a) Bunch profile influenced by the old impedance model calculated with Haissinski equation. (b) Bunch centroid and (c) bunch length growth are also exhibited.

Accordingly, adjusting both parameters at the same time is complicated and difficult. Nevertheless, the studying in figure 4.4 also implies that empirical tuning up R_s and ω_r should have to be carried out in opposite direction. In other words, if the R_s is increased, ω_r should be decreased accordingly, in contrast, if the R_s is decreased, ω_r should be increased.

$R_s\ (k\Omega)$	$\omega_r\ (GHz)$	$F_{res}\ (GHz)$	**Centroid Shift (ps)**	**Bunch Length (ps)**
32	270	42.97	13.5	20.7
34	260	41.38	13.6	21.1
36	240	38.20	13.5	22.0
36	250	39.79	13.8	21.7
36	260	41.38	14.1	21.5
Selection criteria			13.5 – 15.5	20.5 – 22.5

Table 4.2: Candidate BBR models for V_{rf} = 2.5 MV.

$R_s\ (k\Omega)$	$\omega_r\ (GHz)$	$F_{res}\ (GHz)$	**Centroid Shift (ps)**	**Bunch Length (ps)**
32	290	46.15	10.5	18.0
32	300	47.75	10.8	17.8
34	280	44.56	10.7	18.2
34	290	46.15	11.0	18.1
34	300	47.75	11.3	18.0
36	260	41.38	10.5	18.8
36	270	42.97	10.8	18.7
36	280	44.56	11.0	18.4
36	290	46.15	11.3	18.3
36	300	47.75	11.5	18.5
Selection criteria			10.5 – 12.5	17.5 – 19.5

Table 4.3: Candidate BBR models for V_{rf} = 3.3 MV.

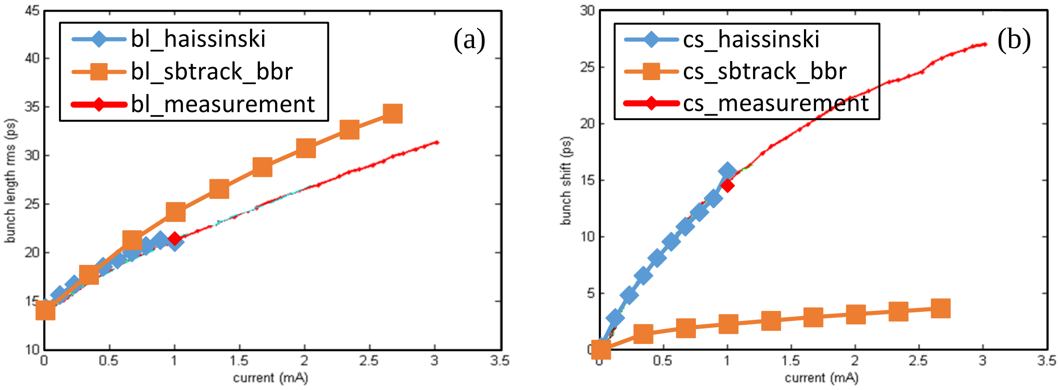

Figure 4.6: Comparison of the simulation results by Haissinski equation and sbtrack with experiment at V_{rf} = 2.5 MV, (a) Plot of bunch length with current, (b) Plot of bunch centroid shift with current.

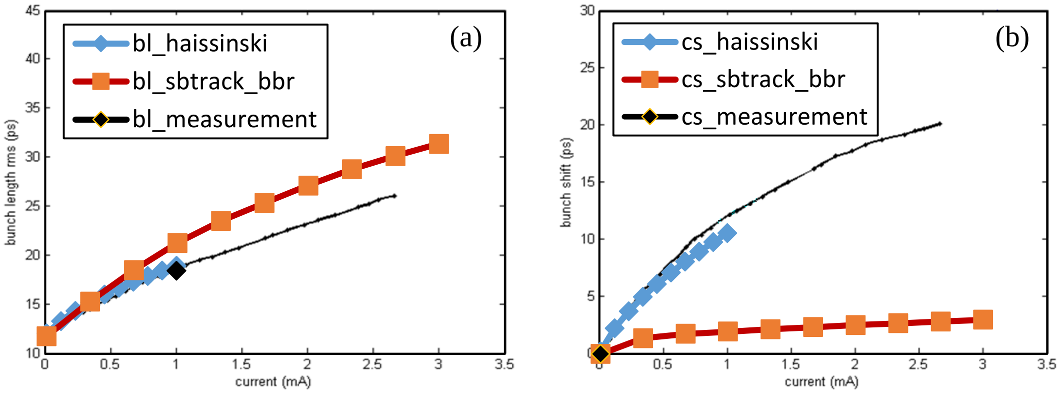

Figure 4.7: Comparison of the simulation results by Haissinski equation and sbtrack with experiment at V_{rf} = 3.3 MV, (a) Plot of bunch length with current, (b) Plot of bunch centroid shift with current.

In conclusion, the decision was made to increase the R_s while decreased the ω_r. These parameters were adjusted until the model was able to reproduce bunch density distribution that matches the selection criteria previously proposed. After solving the numerical calculation of Haissinski integral equation for numerous models, there are several models that met the selection criteria. The candidate models of the case V_{rf} = 2.5 and 3.3 MV are presented in table 4.2 and 4.3 respectively.

The model that simultaneously provides the best reproducing curves that fit with experimental data of both cases of V_{rf} = 2.5 and 3.3 MV was found to be a model with R_s = 36 $k\Omega$, F_{res} = 41.38 GHz and Q = 1 (highlighted on table 4.2 and 4.3).

This new model was brought into further execution by sbtrack in order to examine its quality to reproduce the experimental data. The numerical simulation results are compared in Figure 4.6 and 4.7 with the solution of the Haissinski equation and measurement. They show that the Haissinski calculation with a new BBR model is well describing the bunch lengthening and bunch shifting with current, while the sbtrack result slightly overestimates the bunch length plot. In contrast, the centroid shifting plot shows that sbtrack simulation with this BBR model is not in agreement with Haissinski equation and substantially underestimates the experimental data.

4.2 Purely resistive + purely inductive (R + L) model

Purely resistive and inductive impedance was previously used to characterize the ATF damping ring impedance [35]. Arbitrary parameters of the R + L model that best reproduced the experimental data were also determined from the comparison between numerical results obtained by solving the Haissinski equation corresponds to an impedance of R + L model and experimental data.

The bunch lengthening and centroid shifting curves as function of bunch current generated from solution of the Haissinski equation have to be satisfied with the selection criteria previously proposed. It was then found out that the numerical results that best reproduced the measured data were obtained from an R + L model with a resistance and inductance of 4 $k\Omega$ and 90 nH respectively. This R + L model was also applied to a multiparticle tracking codes, sbtrack, and compared with measurements.

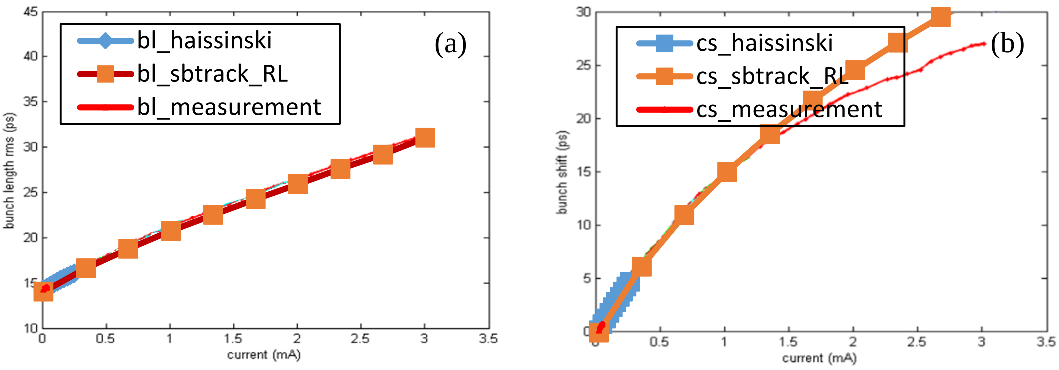

Figure 4.8: Comparison of the simulation results by Haissinski equation and sbtrack with experiment at V_{rf} = 2.5 MV, (a) Plot of bunch length with current, (b) Plot of bunch centroid shift with current.

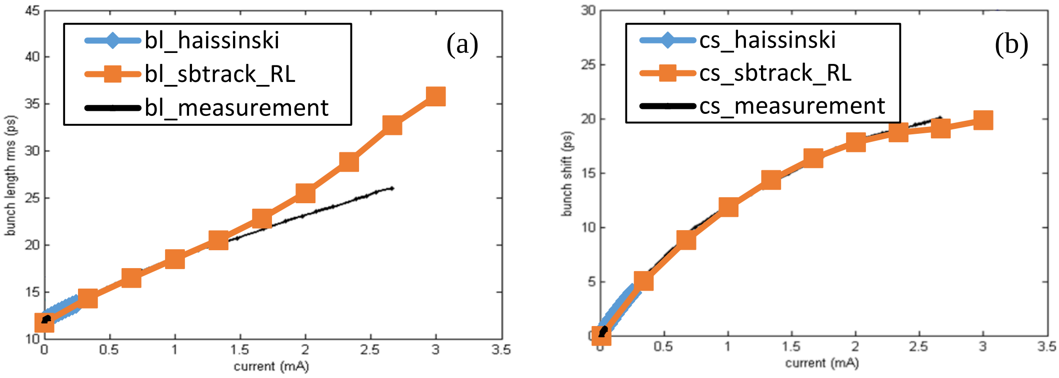

Figure 4.9: Comparison of the simulation results by Haissinski equation and sbtrack with experiment at V_{rf} = 3.3 MV, (a) Plot of bunch length with current, (b) Plot of bunch centroid shift with current.

Figure 4.8 and 4.9 are the plots of bunch length and centroid shift with bunch current comparing among two different simulation methods; sbtrack code and Haissinski equation solver with the measured results.

R + L model simulated with sbtrack exhibits better agreement with Haissinski equation and better describe the measured results of bunch length and centroid shift plots in both V_{rf} than the BBR model.

4.3 Comparison of models

The candidate models, both BBR and R + L, were brought into the sbtrack and executed with potential operating conditions to be applied for THz coherent synchrotron radiation production regime at Diamond Light Source. The plot of simulated bunch lengthening with current as well as the radiation bursting spectrum of two frequency ranges; 60 – 90 GHz and 75 GHz – 1.5 THz, were compared with detected spectrum from experiment. The machine experiment and data collecting were carried out by accelerator physics and beam diagnostic division of Diamond Light Source. The beam was diagnosed with streak camera and Schottky Barrier Diode with detecting frequency 60 – 90 GHz.

The resulting spectra are presented in coloured map of stacking radiation power in frequency domain covering bunch current 1 – 100 μA. The frequency range from 0 to 12000 Hz is represented as horizontal axis in order to investigate significant bursting of synchrotron radiation. It is worth notifying that in some cases machine operation reached the current threshold which accordingly led to beam breaking up. Consequently, the experiments were unable to be carried on with higher current. Their spectrums are consequently depicted with white blank area.

The simulated frequency range 60 – 90 GHz was performed in order to imitate the radiation spectrum detected in experiment. Another detecting range 75 GHz – 1.5 THz was also simulated in order to estimate the radiation in THz frequency range.

In general, the natural bunch length can be analytically calculated from machine parameters following the equation 4.28 of [80]

$$\sigma_z = \sigma_e \sqrt{\frac{\alpha C E}{2\pi U_0} \lambda_{rf} tan\phi_s} \tag{4.4}$$

where

$$\sigma_e = 6.64 \times 10^{-4}\sqrt{\frac{B[T]E[GeV]}{J_s}} \tag{4.5}$$

and

$$\phi_s = arcsin\frac{U_0}{V_{rf}}$$

where σ_e energy spread, C storage ring circumference, α momentum compaction factor, E nominal beam energy, B bending magnet strength, J_s damping partition number, U_0 energy loss per turn, λ_{rf} rf wavelength and ϕ_s synchronous phase. Obviously, it can be concluded that there are two machine parameters governing the bunch length and tuneable in practice; the 1st order momentum compaction factor, α_1 and the rf voltage, V_{rf}.

There are four V_{rf}; 1.5, 2.2, 3.4 and 4.0 MV coupled with six α_1; -0.3 × 10^{-5}, -0.6 × 10^{-5}, -1.0 × 10^{-5}, -1.4 × 10^{-5}, 0.6 × 10^{-5} and 1.0 × 10^{-5} operated in experiment. The simulations were run corresponding to these operating parameters together with other machine condition displayed in table 4.1. Each studying case was tracked turn-by-turn with a number of particle, N_p, at 1.0 × 10^5 and revolving for 15000 turns where the data of the last 1000 turns were collected to be analysed. The simulated bunch current covering 1 – 100 μA was divided into 25 current steps. Each current step was executed until all 25 steps were completed. Then the turn-by-turn 6D tracking data were saved into MATLAB structure `'X'` and passed on to post-processing diagnostic code to generate a bunch lengthening plot and radiation spectrum in two frequency ranges. These simulation conditions are sufficient to exhibit most features of bunch behaviour affected by considering instabilities. They are also the most efficiency and compromising numerical factors with computation resource. All studying cases were run on a Particle Physics cluster which took around 40 hours on average for each running case.

The comparison of experimental and simulation results is able to be categorized into two groups depending on their operated momentum compaction scheme; positive alpha and negative alpha.

4.3.1 Positive alpha

Two values of positive alpha were operated under low alpha scheme; 0.6 × 10^{-5} and 1.0 × 10^{-5}. Incorporated with four values of V_{rf}, eight studying cases were carried out. The comparison of simulated spectrum among two candidate impedance models are demonstrated together with the detected spectra in figure 4.10 and 4.11. Only the cases with V_{rf} = 4.0 MV are exhibited here as examples.

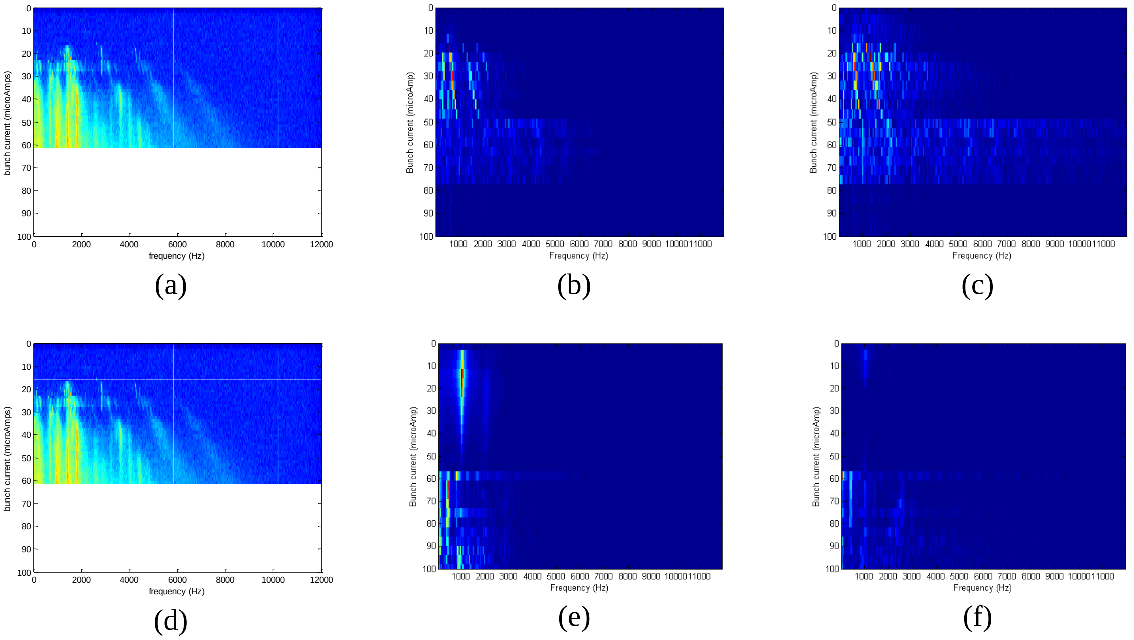

(a) (b) (c)

(d) (e) (f)

Figure 4.10: Comparison of radiation bursting spectrums for α_1 = 0.6 × 10^{-5} with V_{rf} = 4.0 MV. (a) and (d) are experimental detected spectra. (b) and (c) are simulated spectra with BBR model at 60 – 90 GHz and 75 GHz – 1.5 THz ranges respectively. (e) and (f) are simulated spectra with R + L model at 60 – 90 GHz and 75 GHz – 1.5 THz ranges respectively.

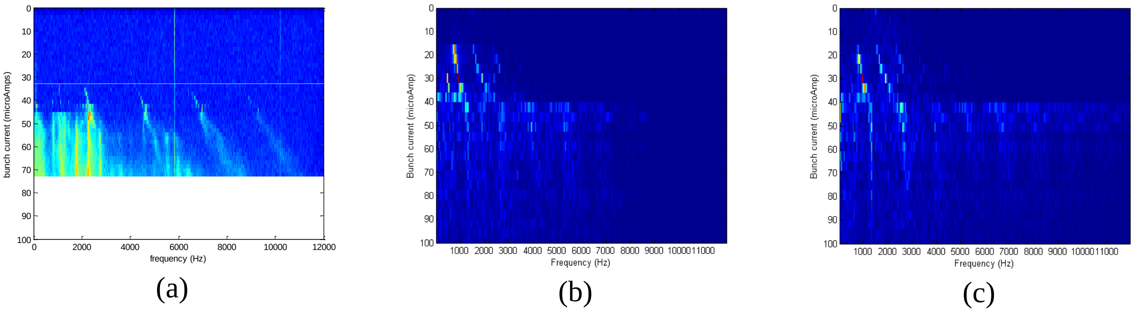

(a) (b) (c)

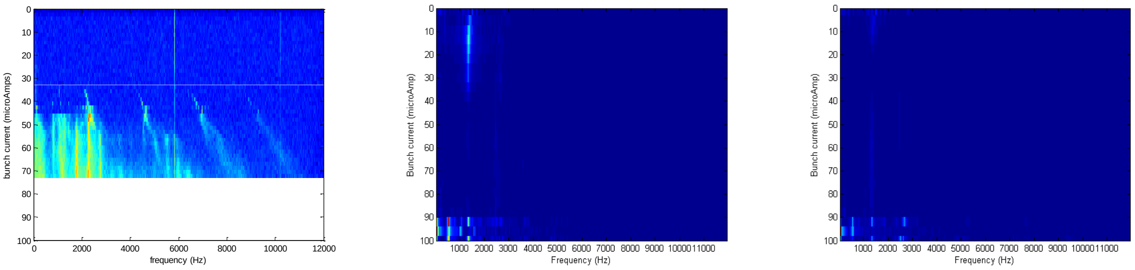

(d) (e) (f)

Figure 4.11: Comparison of radiation bursting spectrums for α_1 = 1.0 × 10^{-5} with V_{rf} = 4.0 MV. (a) and (d) are experimental detected spectra. (b) and (c) are simulated spectra with BBR model at 60 – 90 GHz and 75 GHz – 1.5 THz ranges respectively. (e) and (f) are simulated spectra with R + L model at 60 – 90 GHz and 75 GHz – 1.5 THz ranges respectively.

4.3.2 Negative alpha

Four negative alpha values both nominal and low alpha schemes were operated in machine experiment. These negative alpha are also the candidate values that potentially enable the CSR production in THz frequency range [91]. There are -0.3 × 10^{-5}, -0.6 × 10^{-5}, -1.0 × 10^{-5} and -1.4 × 10^{-5}. The comparison of bunch lengthening and radiation bursting spectra between experimental and numerical results are demonstrated in some cases as examples in figure 4.12 to figure 4.18.

The red line in bunch lengthening comparison represents experimental result while the blue line represents a numerical simulation result. The circles at zero current in the bunch lengthening plots demonstrate the natural bunch length following relation 4.4.

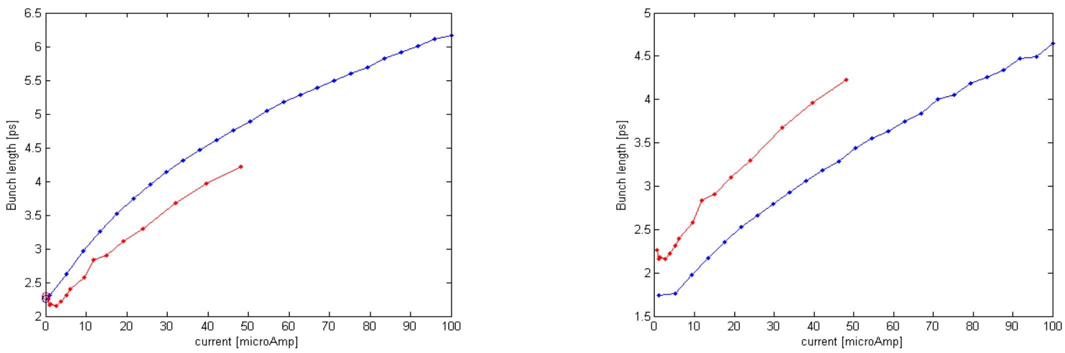

BBR R + L

Figure 4.12: Comparison of bunch lengthening with increasing current of α_1 = -0.6 × 10^{-5} with V_{rf} = 2.2 MV.

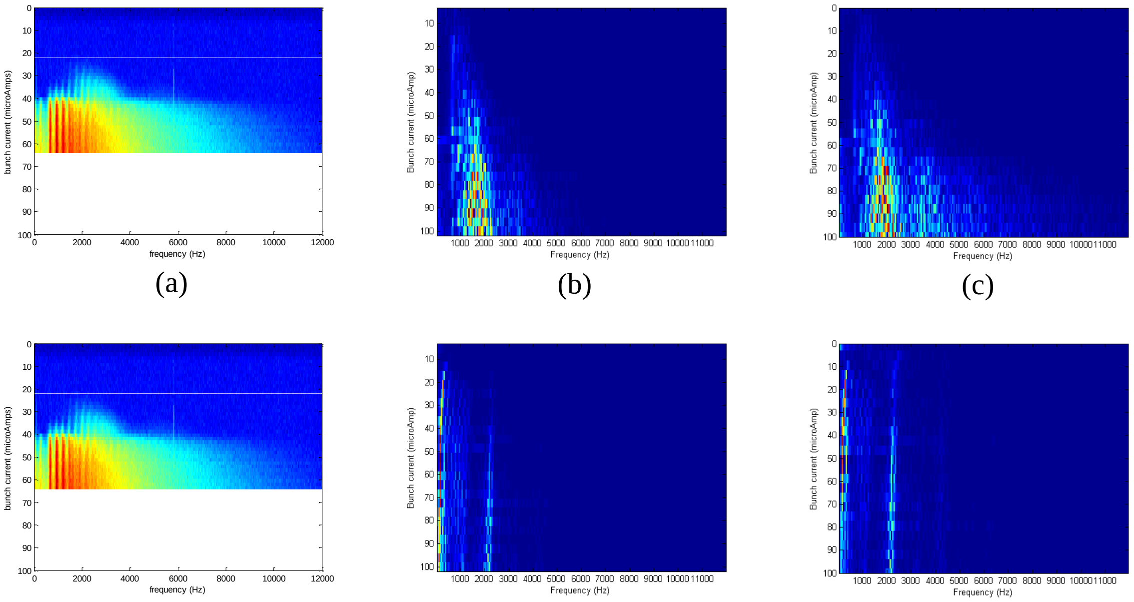

(a) (b) (c)

(d) (e) (f)

Figure 4.13: Comparison of radiation bursting spectrums for α_1 = -0.6 × 10^{-5} with V_{rf} = 2.2 MV. (a) and (d) are experimental detected spectra. (b) and (c) are simulated spectra with BBR model at 60 – 90 GHz and 75 GHz – 1.5 THz ranges respectively. (e) and (f) are simulated spectra with R + L model at 60 – 90 GHz and 75 GHz – 1.5 THz ranges respectively.

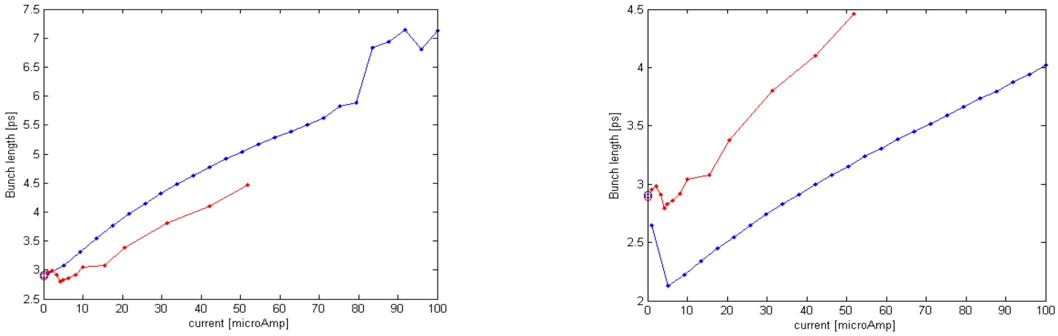

BBR R + L

Figure 4.14: Comparison of bunch lengthening with increasing current of α_1 = -1.0 × 10^{-5} with V_{rf} = 2.2 MV.

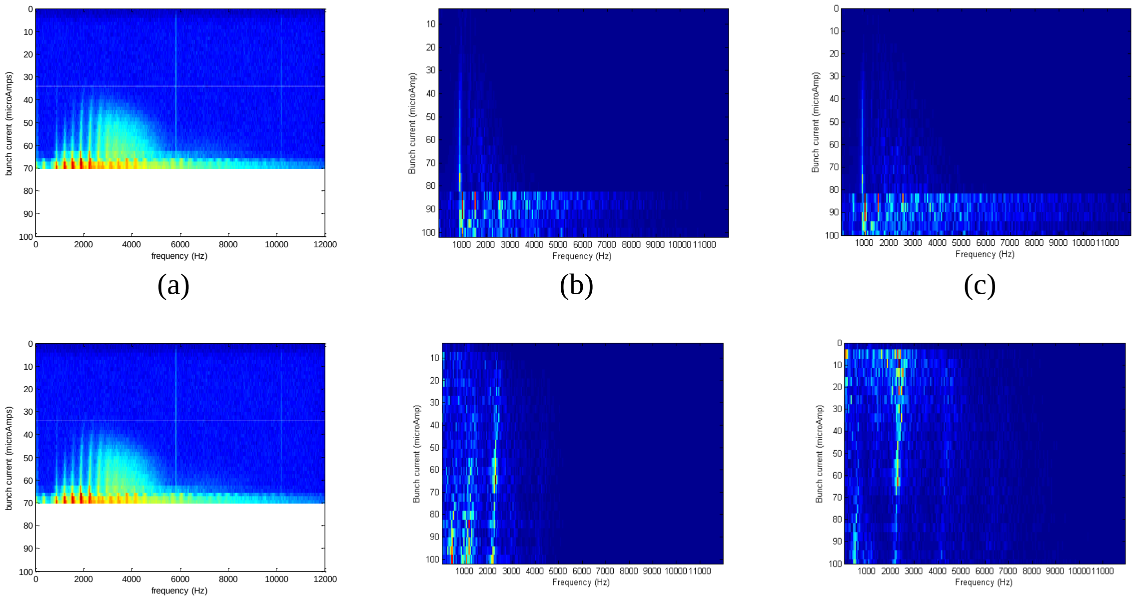

(a) (b) (c)

(d) (e) (f)

Figure 4.15: Comparison of radiation bursting spectrums for α_1 = -1.0 × 10^{-5} with V_{rf} = 2.2 MV. (a) and (d) are experimental detected spectra. (b) and (c) are simulated spectra with BBR model at 60 – 90 GHz and 75 GHz – 1.5 THz ranges respectively. (e) and (f) are simulated spectra with R + L model at 60 – 90 GHz and 75 GHz – 1.5 THz ranges respectively.

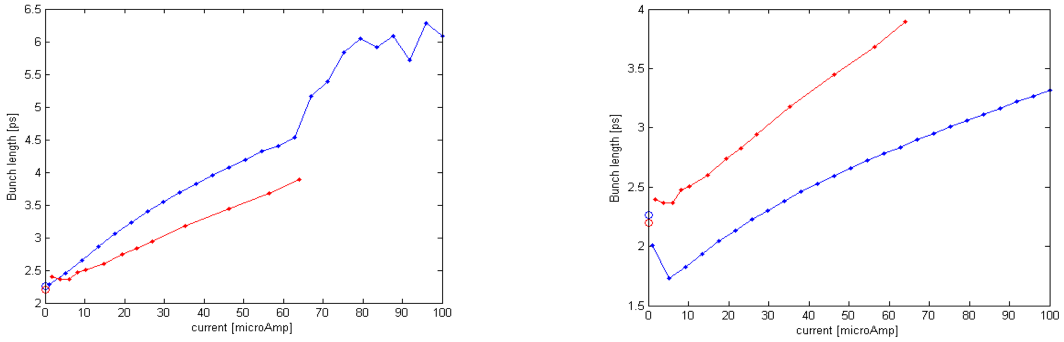

BBR

R + L

Figure 4.16: Comparison of bunch lengthening with increasing current of α_1 = -1.0 × 10^{-5} with V_{rf} = 3.4 MV.

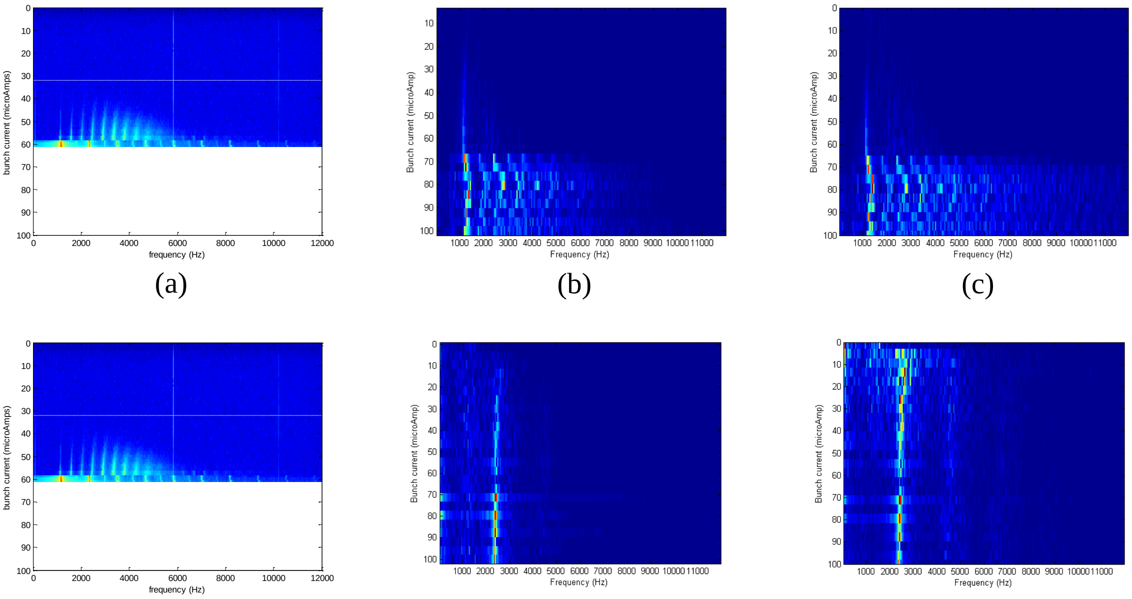

(a)

(b)

(c)

(d)

(e)

(f)

Figure 4.17: Comparison of radiation bursting spectrums for α_1 = -1.0 × 10^{-5} with V_{rf} = 3.4 MV. (a) and (d) are experimental detected spectra. (b) and (c) are simulated spectra with BBR model at 60 – 90 GHz and 75 GHz – 1.5 THz ranges respectively. (e) and (f) are simulated spectra with R + L model at 60 – 90 GHz and 75 GHz – 1.5 THz ranges respectively.

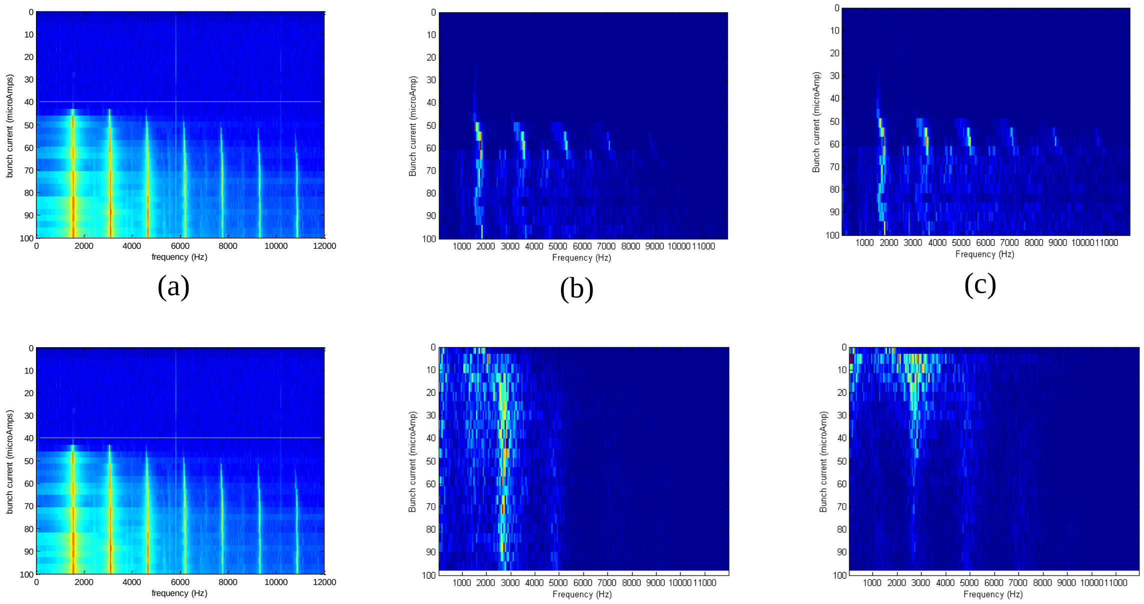

(a) (b) (c)

(d) (e) (f)

Figure 4.18: Comparison of radiation bursting spectrums for α_1 = -1.4 × 10^{-5} with V_{rf} = 4.0 MV. (a) and (d) are experimental detected spectra. (b) and (c) are simulated spectra with BBR model at 60 – 90 GHz and 75 GHz – 1.5 THz ranges respectively. (e) and (f) are simulated spectra with R + L model at 60 – 90 GHz and 75 GHz – 1.5 THz ranges respectively.

4.4 Summary

A dedicated MATLAB code was developed to be used in numerical solving of the Haissinski integral equation in order to figure out the bunch density distribution under particular collective effect. The bunch length and centroid shifting were measured from this equilibrium distribution solution and benchmarked with experimental result to adjust for the most appropriate impedance model for Diamond storage ring. This method considerably reduces the time taken in the process model adjustment by empirical testing of arbitrary parameters.

Two candidate models are found; the broad-band resonator (BBR) impedance model with R_s = 36 $k\Omega$, F_{res} = 41.38 GHz and Q = 1 and the R + L impedance model with R = 4 $k\Omega$ and L = 90 nH. At the process of impedance modelisation, the R + L model demonstrates impressive results on benchmarking with experimental bunch length and centroid shifting growth with current while there is substantial discrepancy on the centroid shift reproduced by the BBR model.

In contrast, the comparison with radiation bursting spectrum expresses completely different outcome. The comparison of all studying cases indicates that the BBR impedance is able to simulate most features of radiation bursting detected in experiment while the R + L model is unable to do so. Furthermore, it is also able to estimate the onset of instability where the bursting signal components become apparent, even though there has still been slightly deviated from experimental detection. In addition, it seems to be capable to imitate the radiation bursting pattern beyond an instability threshold in negative alpha cases (figure 4.15 and 4.17) which obviously indicates that the BBR model might be better accompanying the investigation beyond threshold. This remarkable capability of the BBR impedance model is very promising to be brought into further numerical investigations on the collective instability encountering with longitudinal beam dynamics of short bunch regime.

Chapter 5

Comparison of Simulations And Experiments

In chapter 4, it has demonstrated that the broad-band resonator (BBR) impedance model is able to provide better reproductions of experimental bunch lengthening and radiation bursting spectrum than the R + L impedance model. It is even more impress that the model exhibits remarkable capability to imitate the coherent radiation bursting pattern in the vicinity of the chaotic threshold. This BBR model was brought into multiparticle tracking programme; sbtrack, to perform the numerical simulation with more particles and revolution turns in order to considerately scrutinize the details of bunch behaviour under collective instabilities.

Both coherent synchrotron radiation wake and shielding effect were incorporated into the simulation in order to improve an accuracy of numerical investigation of the beam-wakefield interaction in synchrotron storage ring. In order to investigate the effects of each instability source on the beam dynamic and resulting radiation bursting behaviour, the comparison between measurement and simulation results are distinguished into three categories corresponding to the source of instabilities to be considered. There are the simulations with only radiation wakefield (denoted as CSR wakefield), only broad-band impedance (denoted as BBR wakefield) and a combination of them (denoted as CSR + BBR wakefield). The plots of bunch length, energy spread and bunch centroid shifting versus currents as well as the radiation bursting patterns are illustrated and compared among these simulation schemes.

The variation on machine parameters, particularly the momentum compaction factors and rf voltages were studied. Additionally, some studying cases were investigated into their phase space dynamics due to high possibility to be applied for THz CSR production at Diamond Light Source.

The investigation of bunch fluctuations in transverse plane was also performed by comparing the numerical results with the data collected from experiment in order to supplement an analysis on rigid bunch oscillation mode which is generally unable to be revealed by the resulting bursting pattern alone. Investigation on the bunch oscillation frequency is also brought into analysis of the transition mechanism of instability status.

All simulation cases were performed with the number of particle at 1.0×10^6 and running with 30000 revolution turns in which the last 20000 turns were brought into analysis. The simulated bunch current spans from 1 – 100 μA which were distributed into 25 current steps. Due to large amount of particles and revolution turns, it is almost impossible to track each studying case thoroughly in a single run even on the HPC cluster or supercomputer. A separated UNIX command shell script is developed accordingly to distribute each simulation case into five minor jobs which consisted of five current steps each. Even though these jobs were run independently, the problem on running out of memory had still been persisted in some cases.

An average running time per job of the entire work with these numerical parameters is approximately 50 hours. They were distributed to be run at three main HPC facilities; The Particle Physics cluster - the departmental HPC facility, the Advanced Research Computing cluster ‘ARCUS’ - the central HPC facility of the University of Oxford and the Science and Engineering South cluster ‘IRIDIS’ - the sharing HPC facility among five universities in southern UK situated in the University of Southampton.

The simulated radiation bursting pattern of three different wakefield sources are compared with the experimental detected spectra and illustrated in the section of longitudinal plane together with comparisons of bunch lengthening, energy spreading and bunch centroid shifting versus currents. Especially in some cases, the longitudinal phase space evolution at each stage of instability are demonstrated in order to observe the dynamical development of the bunch under particular collective wakefield.

In the section of transverse plane, the horizontal motion is analyzed to reveal both the rigid-bunch and stationary fluctuation modes during beam instability. The beam dynamics near and beyond the current threshold and the transition from semi-stable bursting fashion to the chaotic behaviour will be numerically evaluated in the last section.

5.1 Longitudinal plane

In chapter 2, it is shown that the synchrotron radiation, especially the coherent one, is strongly related to the time evolution of longitudinal density distribution of individual bunch. In other words, the CSR can be analyzed and monitored with the development of a bunch in longitudinal phase space over time.

It was previously concluded that the bursting of coherent synchrotron radiation can be enhanced by the self-excited radiation wakefield or the so called ‘CSR wakefield’ in the longitudinal plane [67]. However, there is also the self-generated wakefield due to the beam-surrounding interaction, the geometric wakefield, that plays the important role in collective beam instability as well.

This section will scrutinize how these two major wakefields are influencing on the longitudinal dynamics of circulating electron bunch in order to emphasize the time dependent interaction between these instability sources and the bunch profile development.

The simulation has also been attempting to make approximation of the detected bursting spectrum from storage ring. The detecting range of 60 – 90 GHz is specifically simulated to be compared with the results from machine experiment which was carried out with Schottky barrier diode detector with the sensitivity at the same frequency range. Another simulated detecting range, 75 GHz – 1.5 THz, is also set up in order to estimate the bursting of synchrotron radiation in THz range. Various sets of dual parameter, α_1 and V_{rf}, were studied corresponding to the possibility to be applied as operating conditions for THz generation regime at Diamond Light Source.

$\boldsymbol{\alpha_1}$	$\boldsymbol{V_{rf}}$	$\boldsymbol{F_{syn}}$ [Hz]	$\boldsymbol{\sigma_0}$	
			[mm]	[ps]
0.6 x 10^{-5}	4.0	573.33	0.481	1.604
1.0 x 10^{-5}	1.5	396.95	1.157	3.859
-0.6 x 10^{-5}	1.5	307.48	0.897	2.992
-0.6 x 10^{-5}	2.2	407.62	0.676	2.256
-1.0 x 10^{-5}	1.5	396.95	1.157	3.859
-1.4 x 10^{-5}	4.0	875.78	0.734	2.448
-0.6 x 10^{-5}	3.4	525.13	0.525	1.751
1.0 x 10^{-5}	3.4	677.94	0.678	2.261
-1.0 x 10^{-5}	3.4	677.94	0.678	2.261

Table 5.1: Summary of all numerical studying cases and their related parameters.

Four α_1 values were studied; ±0.6 × 10^{-5} and ±1.0 × 10^{-5}, with a special case of -1.4 × 10^{-5}. They were coupled with four V_{rf} values; 1.5, 2.2, 3.4 and 4.0 MV. All studying cases and their related parameters; synchrotron frequency, F_{syn}, and natural bunch length calculated by equation 4.4 are concluded in table 5.1.

Last three cases with following parameters;

- α_1 = -0.6 x 10^{-5} with V_{rf} = 3.4 MV
- α_1 = 1.0 x 10^{-5} with V_{rf} = 3.4 MV
- α_1 = -1.0 x 10^{-5} with V_{rf} = 3.4 MV

were deliberately taken into special investigations because they are of high potential to be exploited in machine experiment for THz CSR generation regime. Their longitudinal beam dynamics were carefully analyzed in order to investigate characteristic contribution of each wakefield to the bunch instability and longitudinal phase space evolution. Longitudinal phase space progressions under each considering instability source are assessed and sequentially illustrated as well as compared among three wakefield schemes.

In all studying cases, the bunch length, energy spread and bunch centroid shifting plotted with bunch currents are illustrated as well as the simulated radiation bursting spectra in two detecting frequency ranges. The bunch lengthening curves and radiation bursting spectrums taken from experiments have also been brought into the comparison. The curves of bunch lengthening deducted from three data sources are demonstrated altogether in the same plotting area and presented with different colours. Red and blue lines represent the curve of experimental and numerical data respectively. The blue line can be further separated into bold and dashed lines which represent the bunch length obtained by calculating with standard deviation of particles and the FWHM of the Gaussian distribution fitted to the bunch distribution respectively. At the same time, on the plots of bunch centroid shifting versus current, bold blue line represents the shifted length of bunch centre obtained by calculating mean value of all particles position and dashed blue line refers to the shifted length obtained by fitting the bunch with Gaussian distribution and measured the deviation of central position from the reference point.

Additionally, there are also white dashed line appeared on the experimental spectrums. These lines indicate the onset of bursting of CSR on each studying case. In other words, it indicates the ‘bursting threshold’ or the ‘instability threshold’ of each considering case. Apart from that, in some cases, the colour diagrams of measured spectra are partially portrayed with white blank area. It indicates the area that an experiment was unable to be carried on because the beam was totally unstable and lost. In general, the current where a white blank area started has been conventionally identified as the ‘current threshold’. Nevertheless, there might be characteristic beam evolution existed beyond this point which is unable to be inspected experimentally. Therefore, it would often be referred to as the ‘chaotic threshold’ throughout this thesis.

The next two sub-sections will present the comparison results between experiments and simulations of positive and negative alpha. Then, the contribution of three different wakefields and the dynamic evolution of a bunch at each stage of instabilities will be revealed and compared in the third sub-section. The development of longitudinal phase space of the bunch is also sequentially demonstrated in order to elucidate the effects of each wakefield to the evolution of bunch deformation.

5.1.1 Positive alpha

There are three studying cases for positive alpha; α_1 = 0.6 × 10^{-5} with V_{rf} = 4.0 MV, α_1 = 1.0 × 10^{-5} with V_{rf} = 1.5 MV and α_1 = 1.0 × 10^{-5} with V_{rf} = 3.4 MV. Only the first case is being presented in this sub-section as an example while the last studying case will be described in detail in section 5.1.3.

In this sub-section, the simulations were performed with two different schemes of wakefield. The CSR and CSR + BBR wake schemes. The plots of bunch length, energy spread and bunch centroid shift with currents were calculated and compared among these schemes. The radiation bursting spectrum in two detecting ranges, 60 – 90 GHz and 75 GHz – 1.5 THz, were also simulated from the post-processing data and compared with the detected radiation bursting taken from experiment.

The result shown in figures 5.1 and 5.2 demonstrate that significant changes have been occurred in the longitudinal bunch profiles after BBR wakefield was implemented to the simulations. In addition, the plots of bunch length, energy spread and bunch centroid shift are smoothly increased with current under CSR wakefield alone. Then the curves become obviously distorted and increased faster with respect to the results of CSR wakefield after BBR wakefield was added.

The simulation with CSR wakefield also demonstrates characteristic features of the coherent synchrotron radiation bursting with observable signals displayed in figure 5.2(b) and (c). The energy spread curve illustrates a broken point where it starts increasing. This point indicates the onset of CSR bursting where the microwave instability starts occurring and leads to an abruptly widening of energy distribution of particle ensemble.

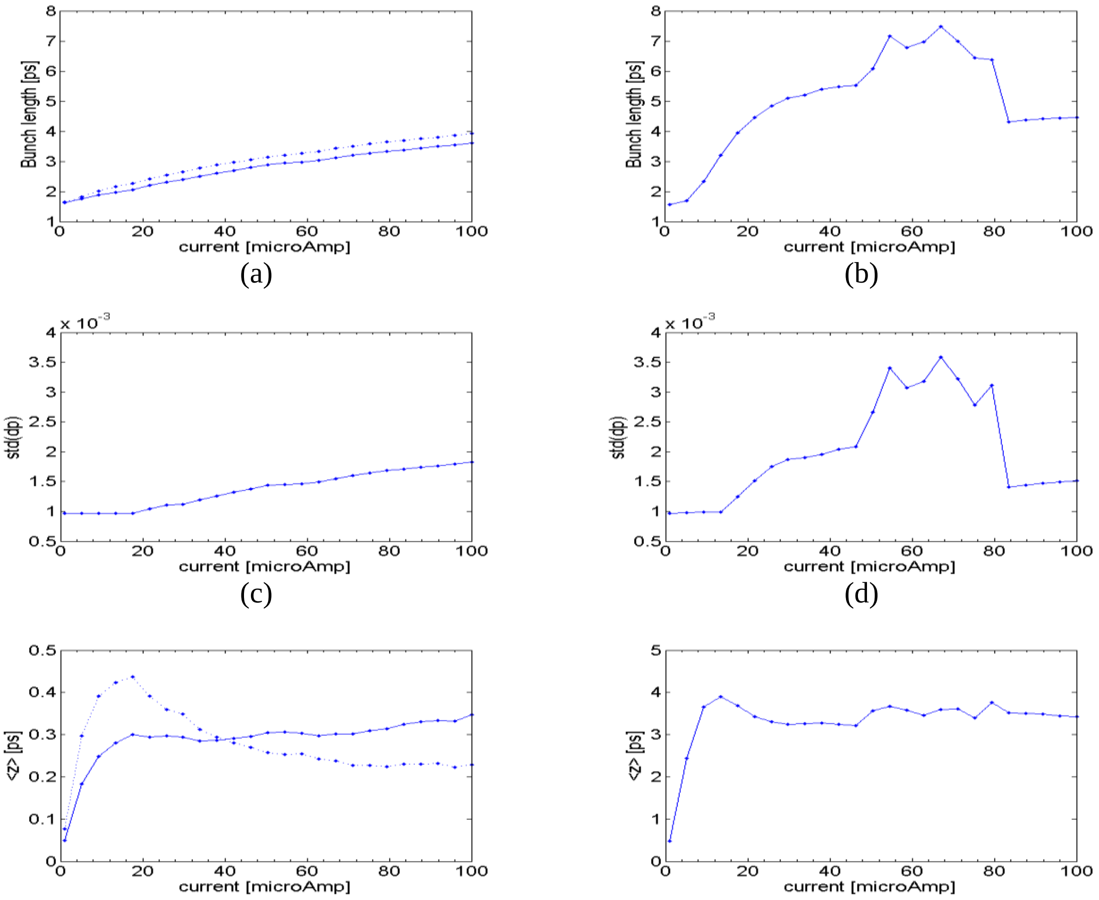

(a) (b) (c) (d) (e) (f)

Figure 5.1: Comparison of bunch profiles for $\alpha_1 = 0.6 \times 10^{-5}$ with V_{rf} = 4.0 MV. (a) and (b) are bunch length vs current. (c) and (d) are energy spread vs current. (e) and (f) are bunch centroid shifting vs current. Left column are the simulations with CSR wakefield and right column are the simulations with CSR + BBR wakefield.

According to the broken point appeared in figure 5.1(c), the bursting threshold is estimated at 17.50 μA. In comparison with the experimental results which exhibit the corresponding CSR bursting threshold are approximately 17 μA, it could be subsequently mentioned that the simulation is able to provide an impressive prediction on the instability threshold of α_1 = 0.6 × 10^{-5} with V_{rf} = 4.0MV.

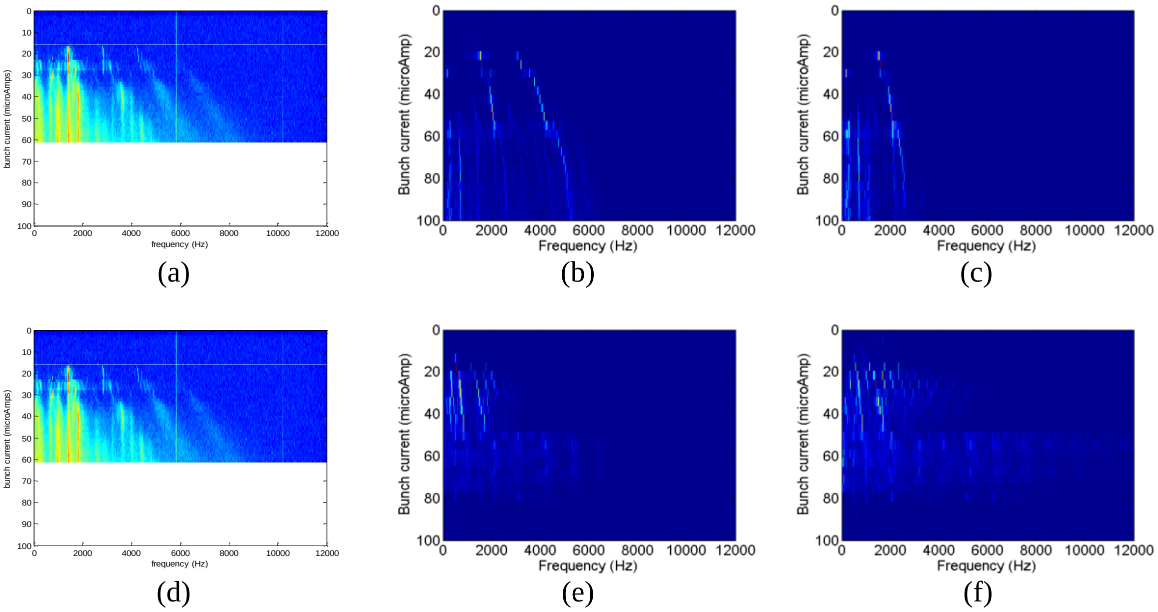

(a) (b) (c)

(d) (e) (f)

Figure 5.2: Comparison of radiation bursting spectrums for α_1 = 0.6 × 10^{-5} with V_{rf} = 4.0 MV. (a) and (d) are the experimental detected spectra. (b) and (c) are simulated spectra with CSR wakefield. (e) and (f) are simulated spectra with CSR + BBR wakefield. (b) and (e) are the simulated spectra with detecting range 60 – 90 GHz and (c) and (f) with detecting range 75 GHz – 1.5 THz.

Additionally, the simulated bursting patterns also illustrate that the CSR bursting threshold are reached at the same currents as predicted by the energy spread curve. The onset of temporal structure of CSR bursting signals are obviously witnessed and shifted toward higher frequencies as the current is increased. According to the bursting patterns in figure 5.2(b), the temporal signals are numerically revealed at 1.47, 3.02 and 4.58 kHz while they are experimentally detected at 1.45, 2.80 and 4.20 kHz. As the synchrotron frequency, f_s, of this case is 573.33 Hz, these frequency components are approximately $2.5f_s$, $5f_s$ and $7.5f_s$.

Furthermore, the numerical simulation is also able to demonstrate its capability to reveal the second CSR bursting structure which was also detected in experiment. These frequency components are exposed with lower amplitude compared to the first signals and situated approximately in the middle between consecutive first bursting frequencies. This double temporal bursting structure was also observed in several synchrotron facilities [13], [24] and has been recognized to be another characteristic feature of coherent synchrotron radiation bursting.

It has been numerically revealed that the second threshold becomes apparent at approximately 40 μA where the bursting signals are exposed at 0.65, 1.30, 1.95 and 2.65 kHz. Meanwhile, the second threshold was also experimentally observed at 35 μA with bursting frequencies 0.65, 0.95, 1.40 and 1.75 kHz. Thus, it could be stated that the numerical result of this case is able to simulate most of the experimental CSR bursting behaviour with acceptable accuracy.

While the chaotic threshold was experimentally revealed at approximately 61 μA, the simulation with CSR wakefield exhibits another broken point on the curves of bunch length and energy spread at 58.75 μA. Moreover, the pattern also depicts broken points on the temporal bursting signals at this current as well.

After the bursting threshold has been exceeded there seems to have initial mode of oscillation dominating over the semi-stable period and resulting on steady emission of CSR. Then, at the chaotic threshold, the bunch fluctuation mode might possibly be transformed to another mode which results another bursting mechanism.

The experimental bursting pattern illustrates the operating current limit at 61 μA. Comparing to the simulation with CSR + BBR wakefield, the energy spread curve shows anomaly strong fluctuation starting at 46.375 μA as well as the broadening of bursting signals. In comparison with the numerical result of CSR wakefield alone, this behaviour is more likely indicating the chaotic threshold. Nevertheless, the current threshold predicted by the simulation has still underestimated the chaotic threshold observed in experiment, the simulation with CSR + BBR wakefield is able to exhibit much clearer indication of the chaotic threshold by exposing strong distortion on the bunch profiles curves as well as broaden bursting pattern.

The CSR bursting signal corresponding to CSR + BBR wake illustrated in figure 5.2 as well as energy spread curve in 5.1 indicate that the instability threshold is reached one current step prior to the previous simulation with only CSR wake. The pattern shows that the instability onset was triggered at 13.375 μA with bursting signals 0.55, 1.12, 1.74 and 2.35 kHz which are almost exactly $1f_s$, $2f_s$, $3f_s$ and $4f_s$ respectively. It should has to be highlighted that these frequency components are impressively in agreement with a theoretical model proposed by Venturini *et al.* [17].

Finally, it has been convinced that the simulation with only CSR wakefield is more favourable to provide CSR bursting features for positive alpha. Numerical simulation with CSR + BBR wakefield seems to make implementations on a clear indication of chaotic behaviour. However, in some cases, simulated radiation bursting patterns illustrate too broadened signals which might be subsequently result on mistaken estimation of the bursting frequencies and instability threshold. This problem could be resolved by simulating with more revolution turns, more particles and finer current step separations. However, these would have to be traded off with considerably longer running time and enormous increasing of system resource requirement.

5.1.2 Negative alpha

There are six cases with negative momentum compaction factor; α_1 = -0.6 × 10^{-5} with V_{rf} = 1.5, 2.2 and 3.4 MV, α_1 = -1.0 × 10^{-5} with V_{rf} = 1.5 and 3.4 MV and α_1 = -1.4 × 10^{-5} with V_{rf} = 4.0 MV. The cases α_1 = -0.6 × 10^{-5} with V_{rf} = 1.5 and 2.2 MV and α_1 = -1.4 × 10^{-5} with V_{rf} = 4.0 MV are simulated with CSR + BBR wakefield scheme. A case α_1 = -1.0 × 10^{-5} with V_{rf} = 1.5 MV is simulated with CSR and CSR + BBR schemes. Lastly, the cases α_1 = -0.6 × 10^{-5} with V_{rf} = 3.4 MV and α_1 = -1.0 × 10^{-5} with V_{rf} = 3.4 MV are simulated with all wakefield schemes; CSR, BBR and CSR + BBR because of their possibility to be applied to machine experiment.

According to the results of the cases with slightly different machine parameters are somewhat deviated. Only the results of α_1 = -1.0 × 10^{-5} with V_{rf} = 1.5 MV and α_1 = -1.4 × 10^{-5} with V_{rf} = 4.0 MV are demonstrated in this sub-section.

The bursting patterns calculated with different numbers of collecting turn; 10000, 15000 and 20000 turns, are also compared for the case α_1 = -1.4 × 10^{-5}. This comparison is performed in order to reveal the deviation of resulting simulated spectrum due to the variation on data collecting turn.

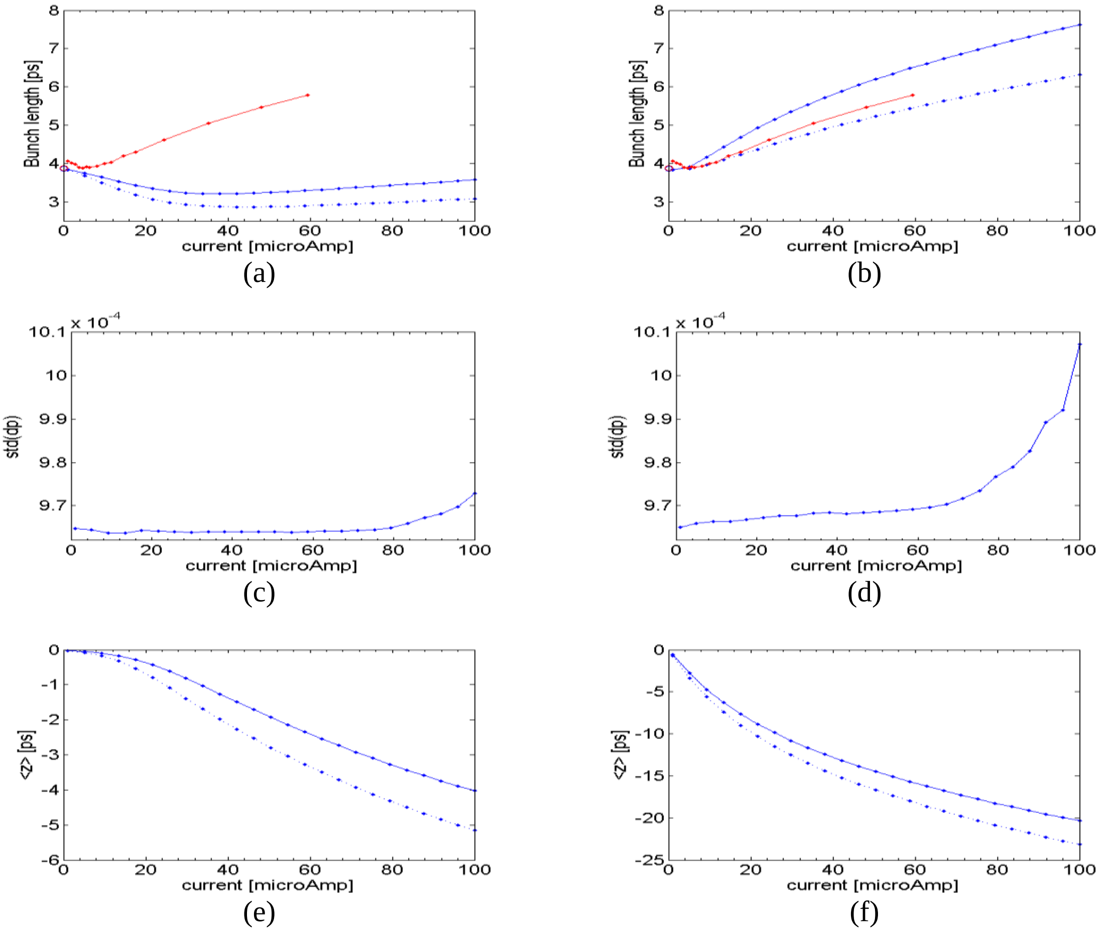

(a) (b)

(c) (d)

(e) (f)

Figure 5.3: Comparison of bunch profiles for α_1 = -1.0 × 10^{-5} with V_{rf} = 1.5 MV. (a) and (b) are bunch length vs current. (c) and (d) are energy spread vs current. (e) and (f) are bunch centroid shifting vs current. Left column is the simulation with CSR wakefield and right column is the simulation with CSR + BBR wakefield.

Plots of bunch length with current in figure 5.3 shows an obvious improvement after BBR wakefield is implemented to the simulation. Numerical result with CSR + BBR wake scheme demonstrates fairly accurate estimation of bunch lengthening. Especially at the current below 20 μA, the calculated bunch length obtained by Gaussian fitting method is able to reconstruct a bunch lengthening curve that closely fitted with the curve obtained from experiment.

Nevertheless, it has still been unable to imitate characteristic bunch contraction at low current due to an effect of space charge mismatch at the transition energy which is regularly detected in experiment with negative alpha [66] either.

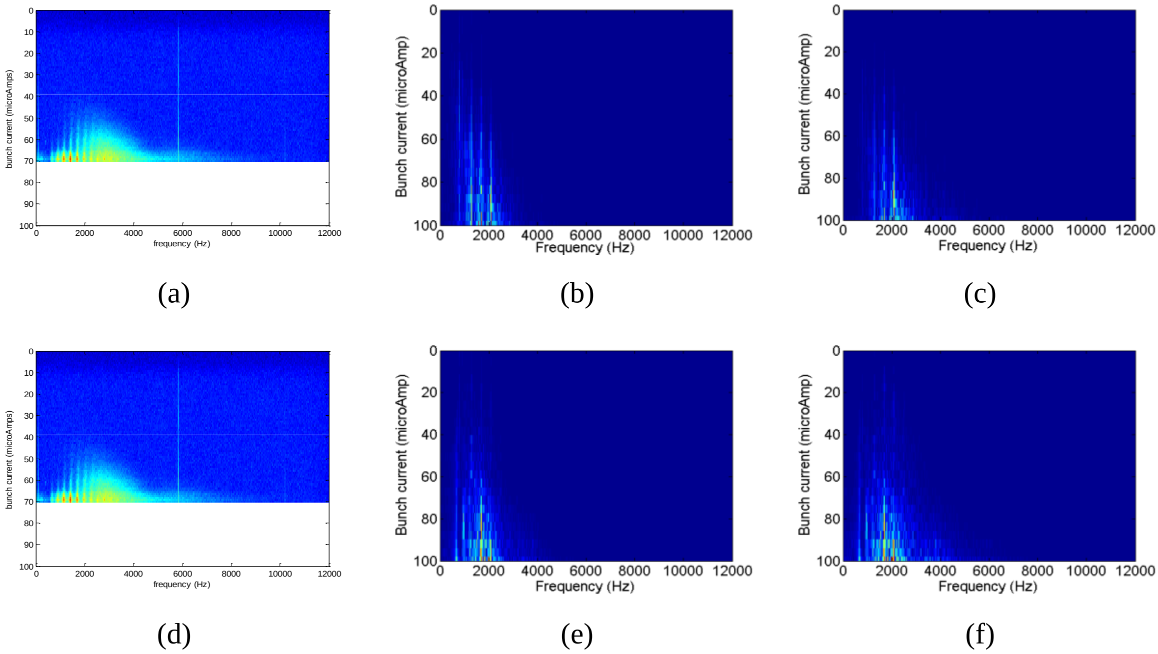

(a) (b) (c)

(d) (e) (f)

Figure 5.4: Comparison of radiation bursting spectrums for α_1 = -1.0 × 10^{-5} with V_{rf} = 1.5 MV. (a) and (d) are experimental detected spectra (b) CSR simulated spectra at 60 – 90 GHz range (c) CSR simulated spectra at 75 GHz – 1.5 THz range (e) CSR + BBR simulated spectra at 60 – 90 GHz range (f) CSR + BBR simulated spectra at 75 GHz – 1.5 THz range.

In term of the investigation of CSR bursting behaviour, the instability threshold predicted by an energy spread curve overestimates the experimental result. While the plot of energy spread indicates that the slope starts gradually increasing at 79.375 μA in the simulation with CSR wakefield and 75.25 μA in CSR + BBR wakefield, the numerical bursting patterns indicate that the coherent bursting start occurring at 25.75 and 9.25 μA for CSR and CSR + BBR simulations respectively. Several frequency components are numerically detected in both simulated patterns of CSR and CSR + BBR schemes. For example, the first five bursting frequencies of the simulation with CSR wakefield are observed at 0.35, 0.78, 1.25, 1.69 and 2.08 kHz which are almost exactly $1f_s$, $2f_s$, $3f_s$, $4f_s$ and $5f_s$ since f_s = 396.95 Hz. After adding BBR wake to the simulation the $1f_s$ component seems to be faded away. Therefore, the first five observable frequency components are 0.78, 1.25, 1.65, 2.05 and 2.45 kHz which are clearly $2f_s$, $3f_s$, $4f_s$, $5f_s$ and $6f_s$.

Comparing to the bursting pattern detected in experiment, the CSR signal starts exposing at approximately 39 μA and the bursting frequencies illustrated in figure 5.4 are 0.38, 0.65, 0.85, 1.10, 1.38 and 1.65 kHz which are approximately $1f_s$, $1.5f_s$, $2f_s$, $2.5f_s$, $3.5f_s$ and $4f_s$. Consequently, it might be concluded that the simulation is only able to reproduce the bursting frequencies at multiplications of the synchrotron frequency whereas unable to estimate the bursting signals at half a synchrotron frequency.

Evidently, the experimental bursting pattern indicates that the bunch microstructures occurred during instability are strong enough to subdue the diffusion due to energy fluctuation induced by synchrotron excitation. The bursting signals are also portrayed with uniform amplitude which evidently implies that the microstructures can be persisted at half a synchrotron oscillation.

Simultaneously, the simulated radiation bursting pattern suggests that the microstructures occurred during instability are not strong enough to be attained at half a synchrotron oscillation. They are repetitively drifted away and diffused to the main bunch every half a synchrotron period. Thus there are only the bursting signals yielded at multiplications of synchrotron frequency in numerical evaluation.

In term of an indication of bursting threshold where an energy spread curve depicts that its slope is gently increased. Comparing to the result of positive alpha, this point generally indicates the onset of microbunching effect. However, in negative alpha, it might probably be an indication of the chaotic threshold instead of the bursting threshold. The simulated patterns show that when current is further increased, the bursting frequency components are broadened and ultimately constitute a lump of high amplitude frequency region where signals become undistinguishable. The predicted threshold at 79.375 and 75.25 μA in CSR and CSR + BBR simulations respectively appear to be the currents that such the crest of high amplitude bursting lump is revealed. Moreover, the bursting pattern has illustrated CSR components since the current is reaching at 25.75 and 9.25 μA for CSR and CSR + BBR simulations respectively. Hence these currents are more likely to be the chaotic threshold than the bursting threshold. Furthermore, they are also numerically revealed somewhat closely to the current threshold measured in experiment which is approximately 70 μA.

The explanation of this misinterpretation might be expressed that the irregular motion of a bunch during the chaotic pattern exhibits too strong bursting elements which are much more intense than that was occurred during self-consistent microbunching effect. Thus the simulation illustrates misconceived colour map according to enormous difference of signal amplitudes throughout the whole range of simulated spectra from 0 to 100 μA.

A studying case α_1 = -1.4 × 10^{-5} with V_{rf} = 4.0 MV exhibits remarkable result on reconstruction of experimental spectra. The plots of bunch length and energy spread versus current give an estimation of the bursting threshold at 46.375 μA which somewhat overestimates the experimental threshold which is approximately 40 μA. Although the numerical simulation has demonstrated its capability to imitate the CSR bursting feature, the simulated frequency components have still been mismatched with the experiment.

The simulation illustrates detectable bursting signals at 1.70, 3.45, 5.20, 6.95 and 8.75 kHz while the experiment shows the coherent bursting occurred at 1.50, 3.05, 4.60, 6.10, 7.70, 9.22 and 10.80 kHz. Since the synchrotron frequency is 875.78 Hz, the frequency components revealed by simulation are almost exactly $2f_s$, $4f_s$, $6f_s$, $8f_s$ and $10f_s$ respectively.

Interestingly, the bursting frequencies exposed in experiment have been revealed really closed to $1\frac{3}{4}f_s$, $3\frac{2}{4}f_s$, $5\frac{1}{4}f_s$, $7f_s$, $8\frac{3}{4}f_s$, $10\frac{2}{4}f_s$ and $12\frac{1}{4}f_s$ or equal to $\frac{7}{4}f_s$, $\frac{14}{4}f_s$, $\frac{21}{4}f_s$, $\frac{28}{4}f_s$, $\frac{35}{4}f_s$, $\frac{42}{4}f_s$ and $\frac{49}{4}f_s$ respectively. These signals are equally spaced at $\frac{7}{4}f_s$ or $1\frac{3}{4}f_s$ or $1.75f_s$ while the simulated bursting signals are equally spaced at $2f_s$.

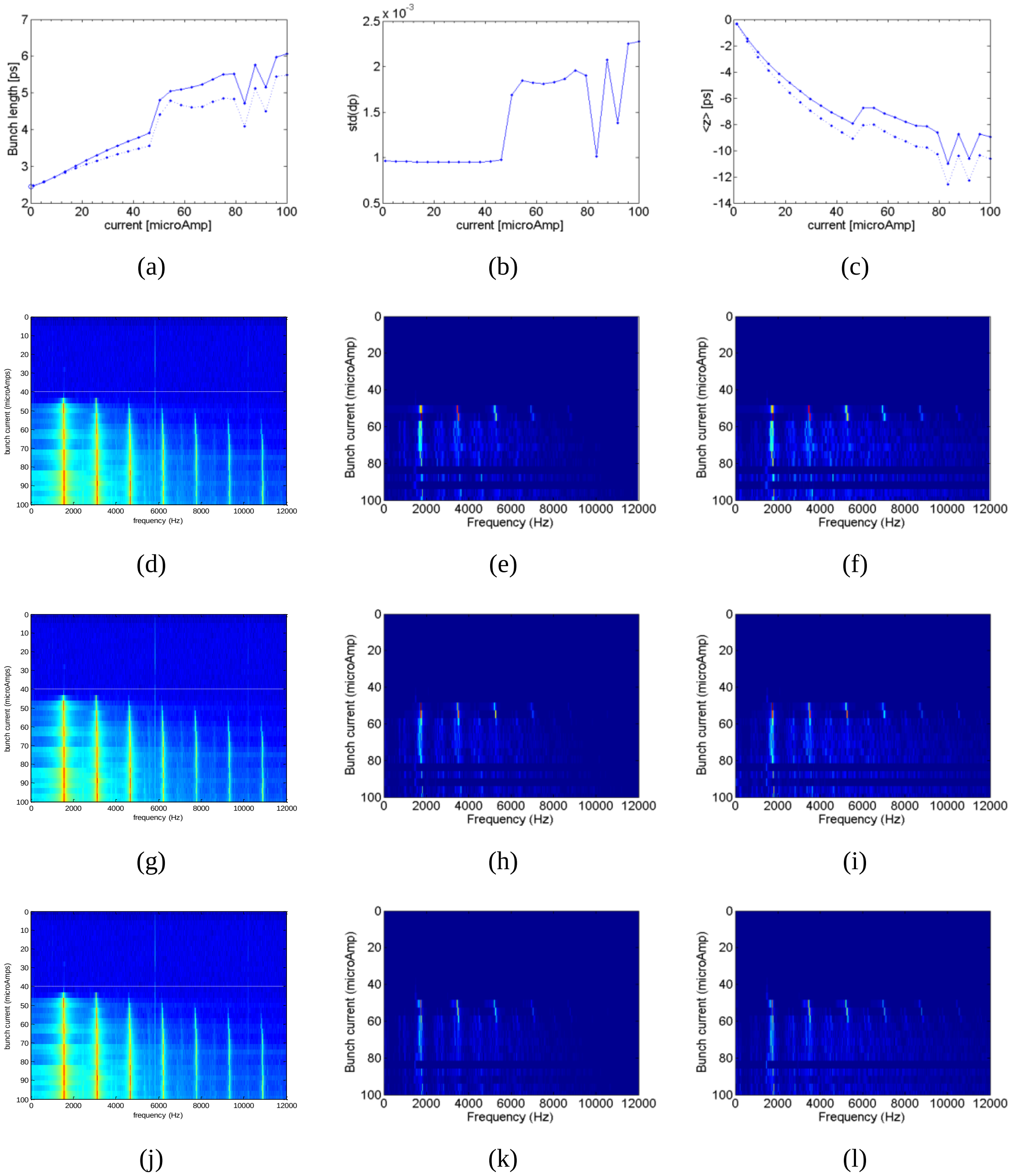

(a) (b) (c)

(d) (e) (f)

(g) (h) (i)

(j) (k) (l)

Figure 5.5: Comparison of bunch profiles and radiation bursting spectrums of α_1 = -1.4 × 10^{-5} with V_{rf} = 4.0 MV. (a) Bunch length vs current (b) Energy spread vs current (c) Centroid shift vs current (d), (g), (j) Experimental detected spectra (e), (h), (k) Simulated spectra at 60 – 90 GHz analyzed with 10000, 15000 and 20000 turns respectively (f), (i), (l) Simulated spectra at 75 GHz – 1.5 THz analyzed with 10000, 15000 and 20000 turns respectively.

Apart from the first bursting signals, there are also several second signals with lower amplitude appeared in experiment similar to that occurred in positive alpha. 3 – 4 thin spectral lines located between successive first series components are exposed. Of these, there are spectral lines with the highest amplitude appears to be revealed in between consecutive first signals. Such a bursting behaviour is another characteristic feature of the coherent synchrotron radiation which has previously been detected in many synchrotron light source such as VUV ring at National Synchrotron Light Source (NSLS) [22], BESSY II [24], SURF II storage ring at the NIST [71], ALS at the Lawrence Berkeley Laboratory [70], Diamond Light Source [57], Metrology Light Source [92] and SOLEIL [93]. Unexpectedly, the numerical simulation is apparently able to exhibit this characteristic feature with acceptable accuracy.

The discrepancy between numerical and experimental frequency spacing of consecutive first bursting signals and the frequency mismatching might be associated with the number of particles exploited in the numerical simulation [86]. Numerical study at SOLEIL [13] also experienced this frequency shift and mismatch due to inadequate particle number. It has been found that the numerical bursting spectra tends to be shifted toward higher frequency with respect to experimental data. Furthermore, it has also been shown that the numerical spectral lines would be shifted back to the experimental reference position when the number of particles is increased [5].

The simulation result of the case α_1 = -1.4 × 10^{-5} with V_{rf} = 4.0 MV also exhibits another interesting behaviour on the bursting of coherent radiation. The plot of bunch length, energy spread, bunch centroid shifting and the bursting pattern are all in agreement that at currents 83.50 and 91.75 μA, the bunch is deliberately rebounded back into the initial state before the bursting signals are revealed. It might also be notified that the radiation bursting pattern seems to be distinguishable into two separated patterns overlay one another. On top of the colour map, there are the ‘major’ higher amplitude coherent bursting signals occurred at $2f_s$, $4f_s$, $6f_s$, $8f_s$ and $10f_s$ as previously described. Meanwhile, there is also supplementary ‘minor’ bursting pattern with lower amplitude initially appeared at approximately 40 μA, just before the instability threshold is reached at 46.375 μA. The bursting signals of the minor pattern are visibly observed and appeared again at 83.50 and 91.75 μA.

In addition, the number of collected revolution turns considerably affects the level of detectability of the minor bursting element. Figure 5.5(e), which was numerically generated with the data collected from last 10000 turns shows only a single minor bursting signal at 1.45 kHz. When the number of collecting turn is increased to 15000, figure 5.5(h), additional signals are detected at 2.00 kHz on the current ranging from 40 to 46.375 μA. Then 2.40 and 2.80 kHz components are later revealed at 83.50 and 91.75 μA. However, additional bursting frequencies observed in figure 5.5(h) are relatively broader and lower amplitude compared to 1.45 kHz signal. They are eventually almost faded out in figure 5.5(k) which was generated from 20000 collecting turns.

Remarkably, bursting signals of the minor series; 1.45, 2.00, 2.40 and 2.80 kHz, are approximately $1\frac{3}{4}f_s$, $2\frac{1}{4}f_s$, $2\frac{3}{4}f_s$ and $3\frac{1}{4}f_s$ respectively which are equally spaced at $\frac{1}{2}f_s$ or $0.5f_s$. These repetitive CSR bursting at half a synchrotron frequency behave very similarly to the coherent radiation bursting due to the microbunching effect.

Comparison of figure 5.5(e), (h) and (k) has further revealed another informative implication. All simulations were originally executed with 30000 revolution turns which is roughly around ten times larger than the longitudinal damping time (τ_s); 5.5959 ms or 2987.2 turns. Data from the last 10000 (turn number 20001 - 30000), 15000 (turn number 15001 - 30000) and 20000 (turn number 10001 - 30000) turns were collected accordingly to generate corresponding bursting pattern. A comparison of figure 5.5(e), (h) and (k) demonstrates that the minor bursting pattern is more favourable to be exposed from the data taken after evolving for several damping time. It would be revealed more obviously when the data collecting is performed during the turns that a bunch has already succeeded into equilibrium. Consequently, it informs that the minor bursting pattern would have definitely been shown in even longer revolutions.

This numerical revelation has subsequently implied that when bunch current is further increased beyond the chaotic threshold, there might possibly be the ‘relaxation gaps’ existed at some point amongst the chaotic pattern. At these gaps, the disordered behaviour seems to be temporarily ‘switched off’ and the bunch turns back into its ‘semi-stable’ state which the coherent synchrotron radiation is able to be steadily emitted again.

Hence there might not be only the ‘spatio-temporal’ bursting of coherent synchrotron radiation that occurred during the microbunching phenomena induced by collective effects but also the ‘temporal-temporal’ bursting of CSR; the spatio-temporal bursting of CSR that temporally occurred according to beam intensity. This temporal chaotic-harmonic behaviour also suggests that the generation of THz coherent radiation at higher current than conventional method is possible at particular controlled beam parameter. However, this behaviour has only been revealed in specific condition especially the negative alpha and has yet detected in experiment. The further study on the beam dynamics of this ‘temporal chaotic behaviour of the temporal CSR bursting’ will be carried out in the next sub-section.

5.1.3 Comparison of wakefield contributions

Three studying cases were specifically simulated with three wakefield schemes; CSR, BBR and CSR + BBR, in order to compare the longitudinal bunch behaviour and phase space dynamics affected by each beam instability source.

The visualization of time evolving beam-wakefield interplay was observed in order to inspect the development of wake potential induced by longitudinal bunch distribution and its resulting effect on the dynamical development of a bunch distribution itself. The evolving bunch distribution in longitudinal phase space is sequentially displayed in order to examine the dynamical development of electron bunch and inspect any noticeable behaviour due to particular wakefield source. These dynamical bunch-wakefield interaction are brought into comparison throughout stability stages especially near and beyond the chaotic threshold where the unique formation of longitudinal dynamic would likely be developed.

Each of three studying cases with V_{rf} = 3.4 MV; α_1 = -0.6 × 10^{-5} and ±1.0 × 10^{-5} also demonstrates the plots of bunch length, energy spread and centroid shifting with current compared among three wakefield simulation schemes as well as their radiation bursting spectra in two detected frequency ranges.

5.1.3.1 α_1 = -0.6 × 10^{-5} with V_{rf} = 3.4 MV

The plots of bunch length with current presented in figure 5.6 clearly demonstrate that the BBR wakefield plays an important role in bunch lengthening replication. The numerical revelation of bunch lengthening with CSR wakefield significantly underestimates the experimental result. After implementing the BBR wakefield, the bunch lengthening curve is obviously lifted up closing to the curve of measurement.

Figure 5.6 also suggests that the BBR is a dominant wakefield over the cooperative wake model of CSR + BBR in this studying case. The plots of bunch length, energy spread and bunch shifting show that the result of CSR + BBR simulation are almost identical to the simulation with only BBR wakefield except huge fluctuation area at high current. However, the bursting patterns illustrated in figure 5.7 display slightly different outcome. The pattern of CSR + BBR wakefield appears more likely to be a combination of both CSR and BBR bursting patterns. Several lumps of high amplitude signals with descending height similar to that of the CSR case are developed in the case of CSR + BBR wake but with thinner shape similar to the BBR pattern. The formation of bursting pattern might be more clearly demonstrated with the intensified spectra generated by the direct colour mapping in figure 5.8.

In term of bunch profiles development, as same as the previous numerical simulations with negative alpha, the plots of bunch length, energy spread and bunch centroid shift with current have neither demonstrated particular point that incisively notifies the onset of microbunching development nor the coherent emission behaviours on the curves. They are smoothly increased with current until reaching a point where the huge fluctuation on the bunch profile curves are obviously revealed. Contrary to the bursting patterns which illustrate that the forked bursting signals are apparently revealed since approximately 20 μA and then dramatically broadened with increasing current eventually become undistinguishable at approximately 60 μA.

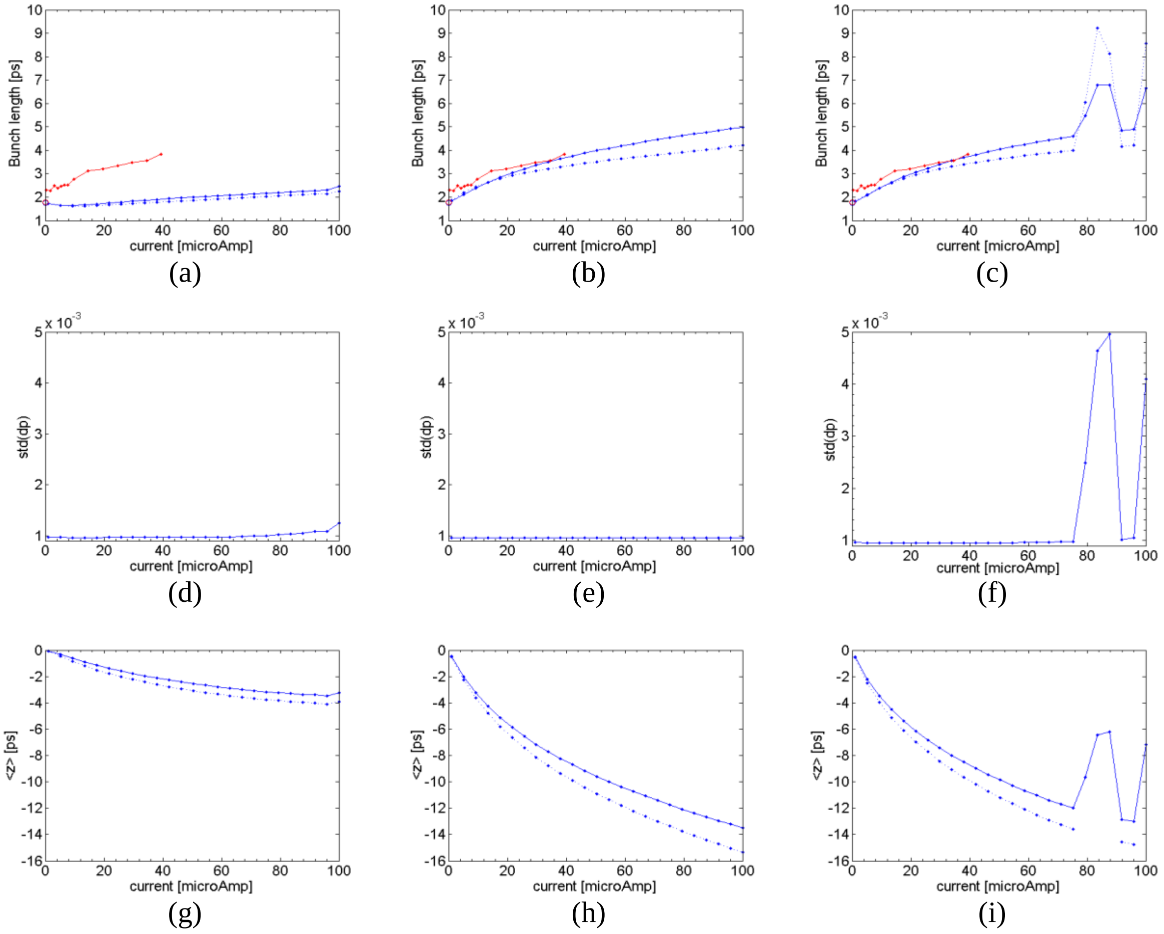

Figure 5.6: Comparison of bunch profiles for $\alpha_1 = -0.6 \times 10^{-5}$ with $V_{rf} = 3.4$ MV. (a), (b) and (c) are plots of bunch length vs current. (d), (e) and (f) are energy spread vs current. (g), (h) and (i) are bunch centroid shifting vs current. (a), (d) and (g) are the simulations with CSR wakefield. (b), (e) and (h) are the simulations with BBR wakefield. (c), (f) and (i) are the simulations with CSR + BBR wakefield.

In figure 5.7, the simulation with CSR + BBR wakefield demonstrates that the current where the branched bursting signals have been developed is well agreed with the instability threshold measured in experiment. Moreover, the current where the bursting signals are appeared undistinguishably is unexpectedly more or less than the chaotic threshold observed in experiment.

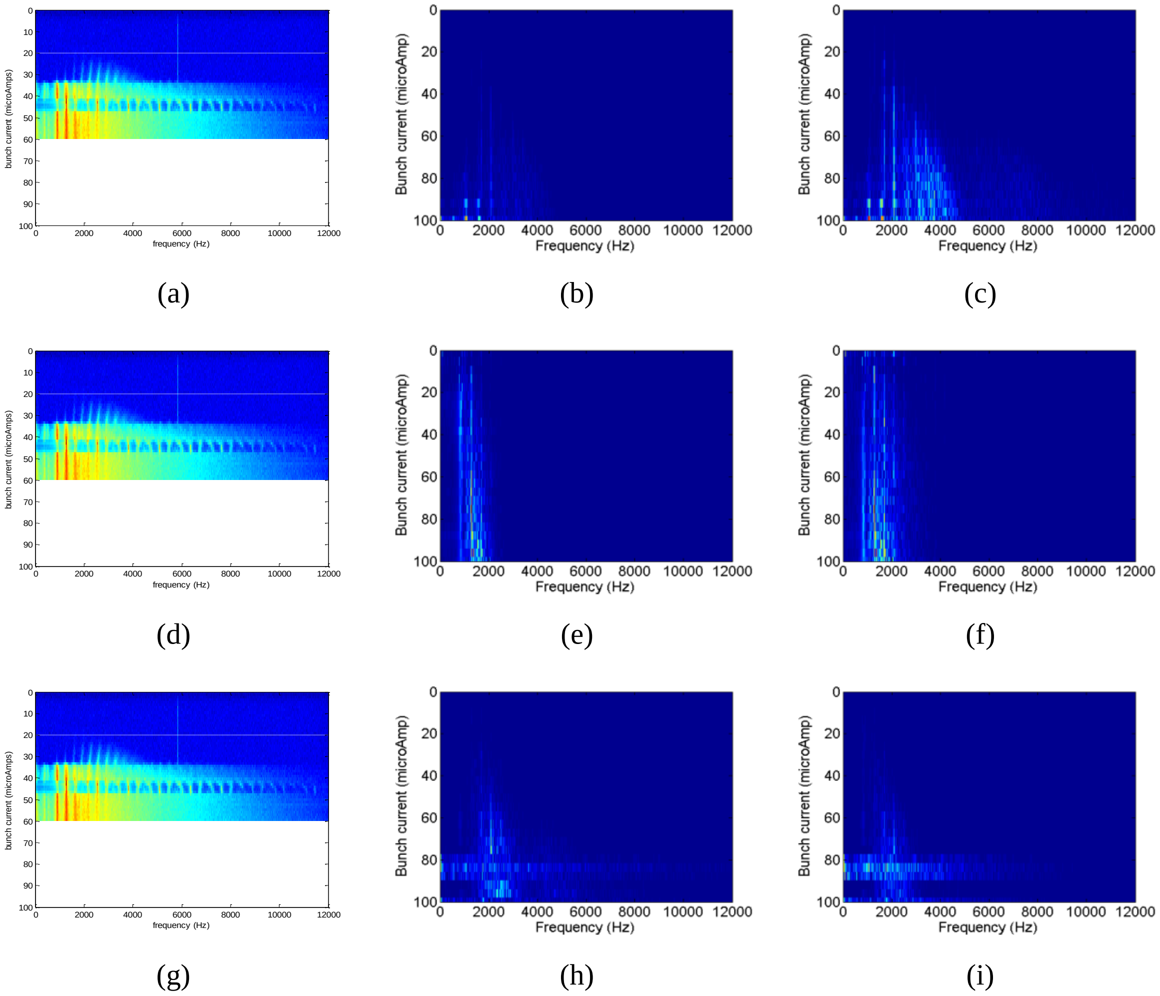

(a) (b) (c)

(d) (e) (f)

(g) (h) (i)

Figure 5.7: Comparison of radiation bursting spectrums for α_1 = -0.6 × 10^{-5} with V_{rf} = 3.4 MV. (a), (d) and (g) are experimental detected spectra. (b), (e) and (h) are simulated spectra at 60 – 90 GHz with CSR, BBR and CSR + BBR wakefields respectively. (c), (f) and (i) are simulated spectra at 75 GHz – 1.5 THz with CSR, BBR and CSR + BBR wakefields respectively.

The plots of bunch profiles and the bursting patterns of the simulation with CSR + BBR wakefield also demonstrate that the double layer bursting structures are also revealed in this case. At 75.25 μA, bunch length, energy spread and bunch shifting curves are suddenly increased altogether, then rebounded back into their initial positions on the trend lines suggested by the previous points before huge fluctuation within the next four current steps and finally lifted up again at 100.00 μA. This behaviour is in agreement with its simulated coherent bursting pattern which displays broad spectral region from 75.25 to 87.62 μA and steps back into its original pattern for 91.75 to 95.87 μA before steps into the broad signal region again at 100.00 μA. This alternating behaviour of the chaotic radiation bursting region is comparable to the temporal occurrence of relaxation gaps appeared in previous simulation for α_1 = -1.4 × 10^{-5} with V_{rf} = 4.0 MV.

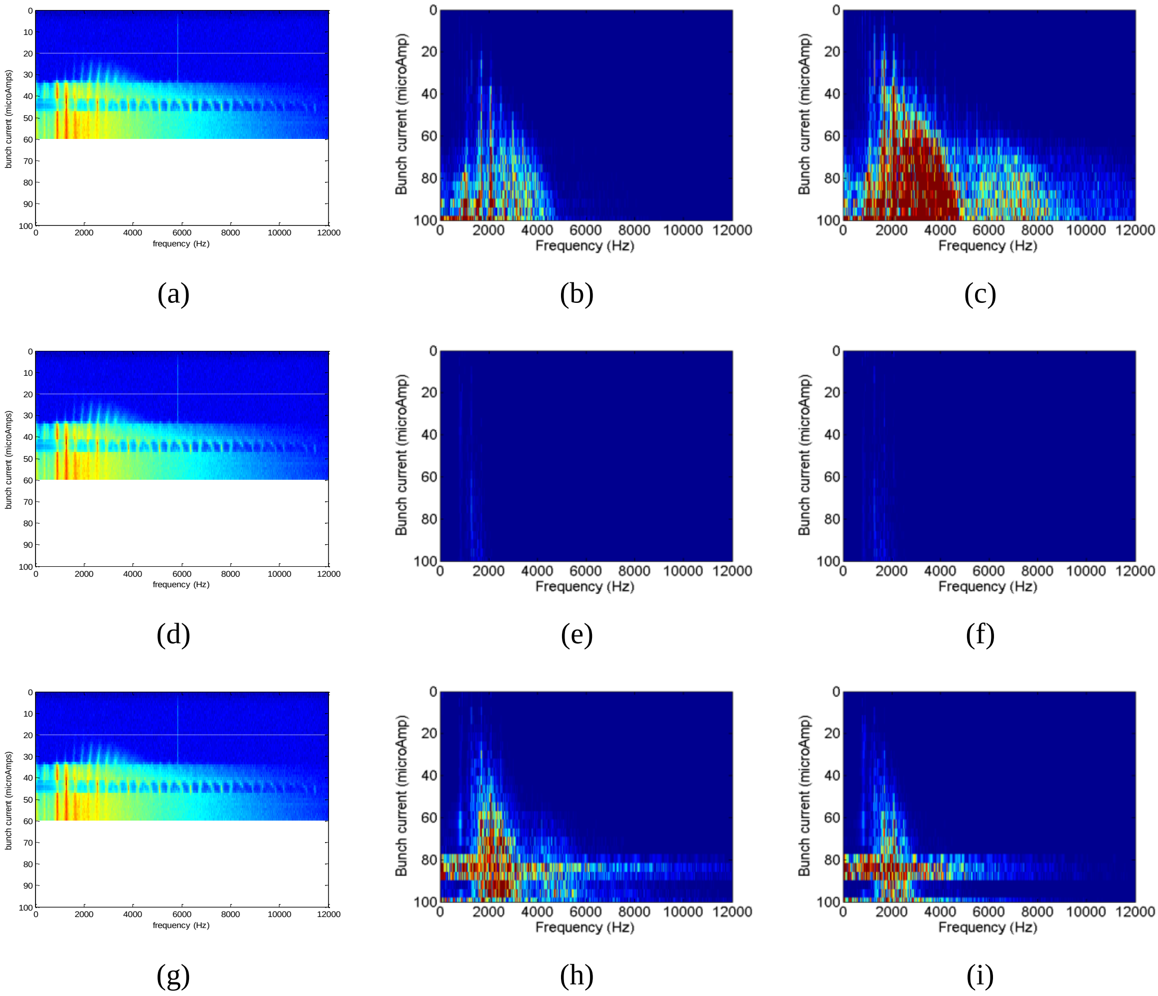

(a) (b) (c)

(d) (e) (f)

(g) (h) (i)

Figure 5.8: Another version of radiation bursting spectrums comparison in direct mapping scale for α_1 = -0.6 × 10^{-5} with V_{rf} = 3.4 MV. All patterns are reconstructed from figure 5.7 with direct mapping interpretation in MATLAB. (a), (d) and (g) are experimental detected spectra. (b), (e) and (h) are simulated spectra at 60 – 90 GHz with CSR, BBR and CSR + BBR respectively. (c), (f) and (i) are simulated spectra at 75 GHz – 1.5 THz with CSR, BBR and CSR + BBR respectively.

In term of the revelation of bursting frequencies, at the instability threshold, the experimental radiation bursting pattern has been revealed at frequencies 0.85, 1.20, 1.55, 1.90, 2.30, 2.65 and 3.00 kHz. Since the synchrotron frequency, f_s, is 525.13 Hz, these frequencies are according to $1\frac{2}{3}f_s$, $2\frac{1}{3}f_s$, $3f_s$, $3\frac{2}{3}f_s$, $4\frac{1}{3}f_s$, $5f_s$ and $5\frac{2}{3}f_s$ respectively. The separation between consecutive frequencies is approximately 0.35 kHz which is almost exactly $\frac{2}{3}f_s$.

Concurrently, the CSR bursting frequencies are numerically observed at 1.70, 2.08, 2.50 and 2.95 kHz in the simulation with CSR wakefield. Some frequency components in this series appear to be revealed in the simulation with BBR wakefield as well with implementing components at the lower frequency range. The bursting frequencies corresponding to the BBR wakefield are 0.85, 1.30, 1.70 and 2.05 kHz.

The numerical bursting frequencies revealed in the simulation with CSR + BBR wakefield seem to be congregated with both the frequency components from CSR and BBR wake models above. There are 0.80, 1.28, 1.70, 2.10 and 2.50 kHz with the separation between consecutive frequencies at approximately 0.40 kHz. This frequency separation slightly overestimates that of the experimental result for 0.05 kHz.

In term of temporal occurrence of the chaotic CSR bursting, figure 5.9 has revealed that the longitudinal phase space evolution of a bunch is well agreed with the temporal chaotic bursting pattern. The longitudinal beam dynamics is able to provide reasonable revelation of the background mechanism that resulting on the temporal branched and broaden bursting signals.

The temporal occurrence of chaotic radiation bursting pattern is also detected in experiment with similar fashion to the numerical simulation. Nevertheless, the simulation is able to provide an impressive estimation of the instability threshold at 20 μA where the bunch starts bursting the CSR, it has still considerably overestimated the onset of the chaotic bunch evolution. The experimental result demonstrates that the bursting pattern reaches the broad spectral region at approximately 34 μA before turning back into relaxation region at 40 μA. Then, it finally rebounds to the broad signal region again at 46 μA.

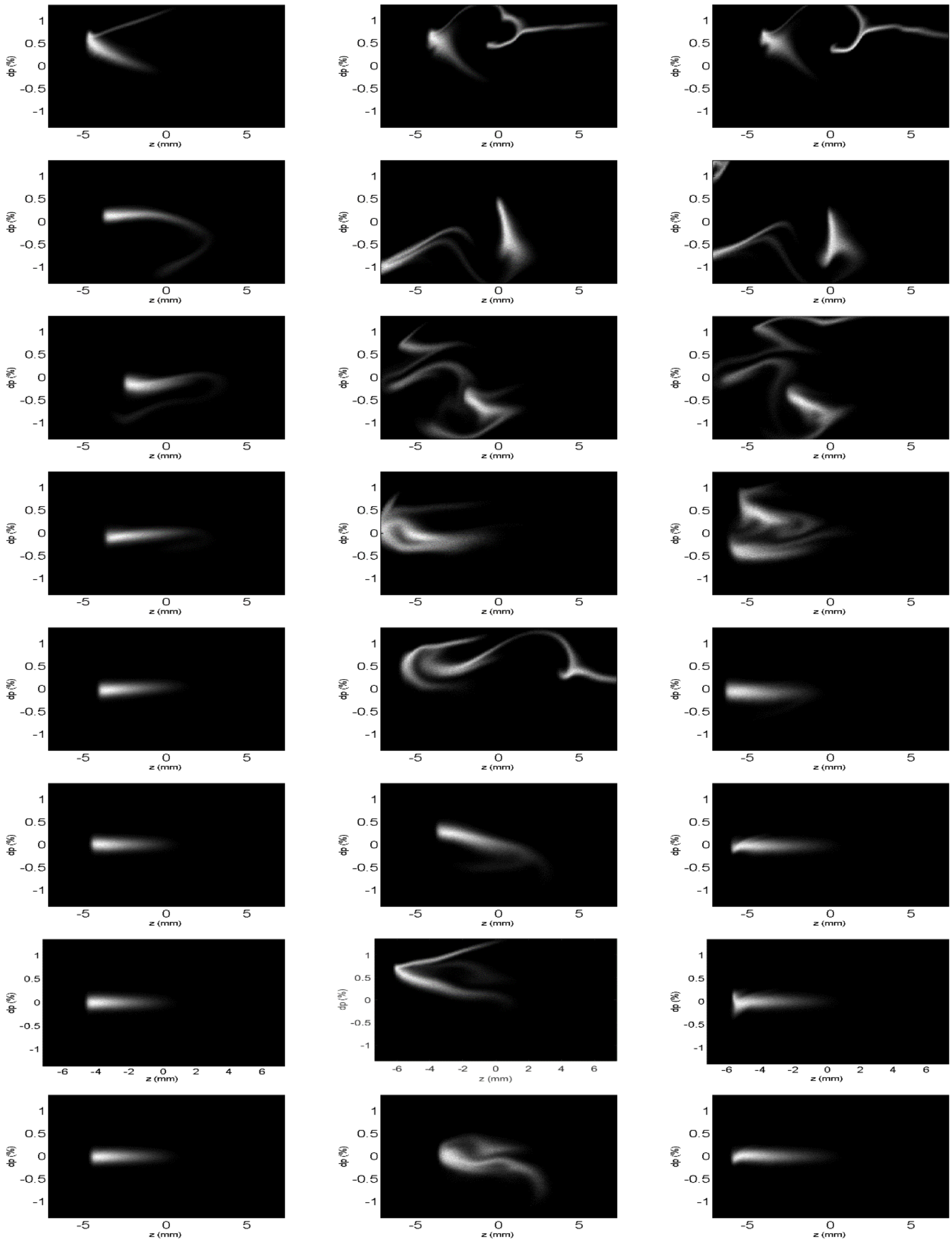

Figure 5.9: The longitudinal phase space evolutions under CSR + BBR wakefield of α_1 = -0.6 × 10^{-5} with V_{rf} = 3.4 MV captured at 0.5T_s, 1T_s, 2T_s, 5T_s, 8T_s, 15T_s, 24T_s and 30T_s for 50.50 μA (left column), 83.50 μA (middle column) and 95.87 μA (right column). Bunch head is to the right.

Conclusively, this behaviour is apparently the characteristic feature of the CSR emission bursting of negative momentum compaction factor which is also detected in other studying cases with negative alpha. Interestingly, this temporal chaotic bursting behaviour is able to be replicated by the numerical simulation with only a single model of broad-band resonator co-operated with the coherent synchrotron radiation wakefield.

The comparison of longitudinal phase space dynamics among numerical results of three simulated wakefields; CSR, BBR and CSR + BBR is able to reveal the details of beam dynamics behind double radiation bursting patterns arrangement. The longitudinal phase space evolution of these simulated wakefields are compared throughout figure 5.11 – 5.13.

In figure 5.9, the numerical simulation of longitudinal phase space dynamics under CSR + BBR wakefield is demonstrated at three bunch currents; 50.50, 83.50 and 95.87 μA. According to figure 5.7, these bunch currents are representatives of the CSR bursting behaviour at each stage of temporal occurrence of branched and broaden frequencies structures. Longitudinal phase space evolution was captured at 500, 1000, 2000, 5000, 8000, 15000, 24000 and 30000 turns which are corresponded to $0.5T_s$, $1T_s$, $2T_s$, $5T_s$, $8T_s$, $15T_s$, $24T_s$ and $30T_s$ where T_s is the synchrotron period which is 1016.55 turns or 1.9043 ms for $\alpha_1 = -0.6 \times 10^{-5}$ with $V_{rf} = 3.4$ MV.

Time sequential illustration of longitudinal phase space dynamics illustrated in figure 5.9 suggest that at 50.50 μA, the collective effect has still been considerably weak and inadequate to induce any significant distortion on the bunch phase space after progressed to the equilibrium except the conventional microbunching effect which may be somewhat hard to be observed from the phase space snapshots. After $5T_s$, the bunch seems to be able to sustain its dynamical equilibrium and steadily bursts the coherent radiation which could be detected as several discrete sharp signals on the bursting pattern in figure 5.7.

Meanwhile, the longitudinal dynamic at 83.50 μA evidently illustrates broad bursting signal which suggests that the chaotic fluctuation might be enhanced at this current. Accordingly, phase space evolution shown in figure 5.9 is in agreement with this broad bursting signal. The bunch seems to be unable to succeed into the confined dynamical equilibrium in longitudinal phase space. According to the bunch-wakefield interplay, the bunch phase space has become severely deformed and fragmented into several distorted pieces since the beginning of simulation. Nevertheless, it seems to be intentionally evolved into periodic reintegration at approximately 5000, 13000, 21000 and 29000 turns, it appears unable to be retained in this status for long and starts deforming again within few hundred turns. This periodic reintegration may also be associated to the repetitive radiated power blow-up at approximately 7000, 16000 and 24000 turns shown in figure 5.10.

At 95.87 μA, the longitudinal phase space is evolving in similar chaotic fashion to the bunch at 83.50 μA until proceeded to approximately 8000 turns. The bunch appears to be able to sustain its semi-stable progression and being confined in a packet similar to phase space evolution at 50.50 μA. Even though the longitudinal phase space evolution of 50.50 and 95.87 μA have shown that their overall bunch evolutions are able to be proceeded into similar semi-chaotic fashion after $8T_s$, the collective beam instability due to higher bunch current has still apparently initiated an interesting movement at the bunch tail of 95.87 μA.

The longitudinal phase space at 95.87 μA exposes the localized condense microstructure at the bunch tail which resembles to a ‘spur’ rotating clockwise and drifting toward the head of the bunch as the time is advanced. This micro-fluctuation is obviously noticeable on figure 5.9 which has also revealed that its effect is not strong enough to completely deform a semi-stable bunch formation in phase space and appears to be able to persist in this state throughout the whole range of simulation.

It is also worth noting that this micro-fluctuation at bunch tail also initiates noticeable modification on the radiation power. According to figure 5.10, the radiated power is somewhat enhanced with respect to the power radiated at 50.50 μA. An assumption is that the coherent synchrotron radiation from the bunch at 95.87 μA is not only generated by the conventional microbunching effect but also the coherent radiation due to the unconventional ‘spur-like’ micro-fluctuation or ‘localized microbunching’ effect at bunch tail.

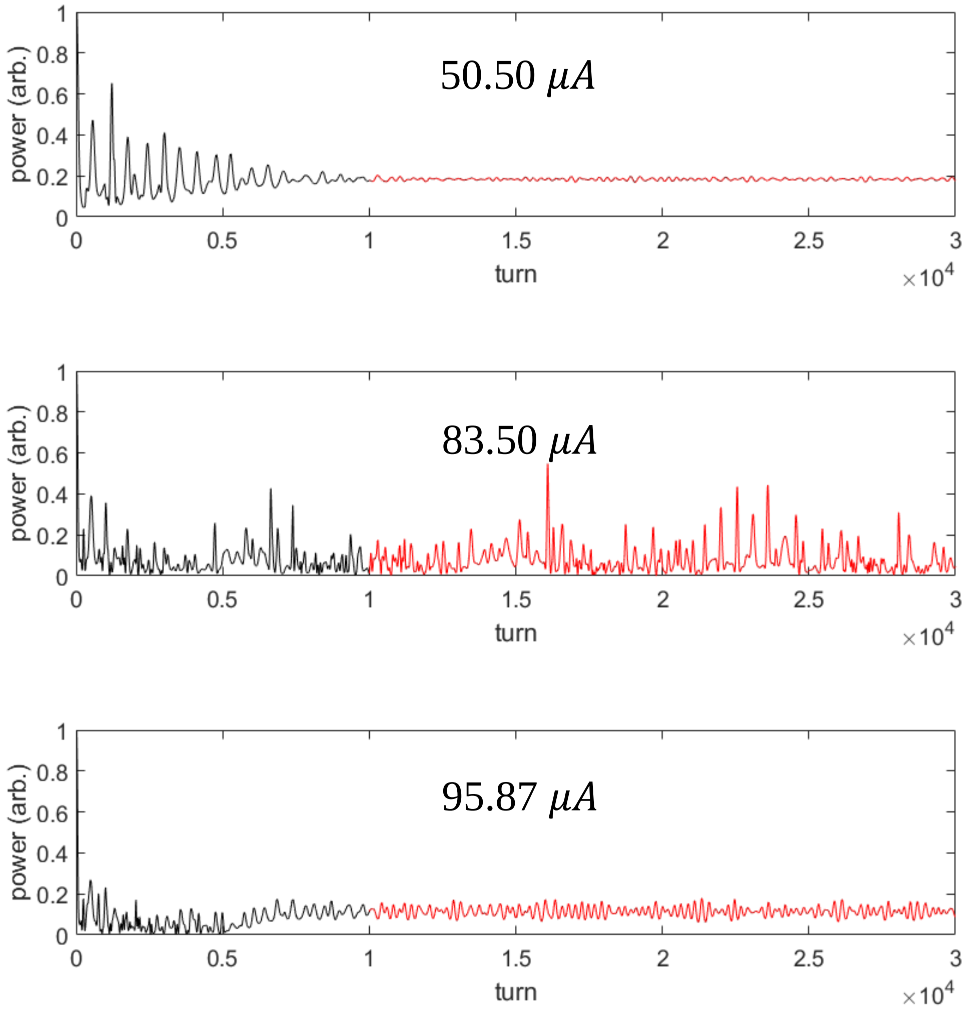

Figure 5.10: The comparison of radiation power bursting in time domain from the numerical simulations with CSR + BBR wakefield for α_1 = -0.6 × 10^{-5} with V_{rf} = 3.4 MV at 50.50 μA (top), 83.50 μA (middle) and 95.87 μA (bottom). Red lines indicate the turns collected for analysis.

Figure 5.10 also conforms to the formation of double bursting behaviour exhibited in figure 5.7. It affirms that the chaotic dynamical evolution is intensified at 83.50 μA but turning out to be suppressed at 95.87 μA just similar to the pre-chaotic stage at 50.50 μA. Both the plots of radiation power at 50.50 and 95.87 μA are exposed with considerably more relaxing and relatively less fluctuating than the radiation power at 83.50 μA. Thus the implication is that the bunch appears to be substantially reconfined again after passing through the more intense chaotic fluctuation region during 75.25 to 87.62 μA. In other words, the numerical simulation suggests that there might be the semi-stable dynamical behaviour existed beyond the conventional chaotic threshold where the bunch is able to be self-reorganized and continues steady bursting the CSR.

In order to elucidate the beam dynamics during beam-wakefield interaction at the background of these dynamic fashions, the clarification on how the bunch is effectively influenced by each wakefield and how geometric and radiation wakefields are negotiating and dominating over each other in the bunch-wakefield interplay is important. Figure 5.11 – 5.13 illustrate the development of a bunch in longitudinal phase space influenced by three modes of wakefield at current 50.50, 83.50 and 95.87 μA respectively. At each current, the bunch longitudinal dynamics simulated with corresponding wakefield is presented and sequentially compared at $0.5T_s$, $1T_s$, $5T_s$ and $30T_s$.

Figure 5.11 shows that, at 50.50 μA, the bunch under CSR wakefield is revealed to be the shortest bunch length while the bunch under BBR and CSR + BBR wakefields are obviously longer. The bunch length of CSR + BBR wake is also comparable to the bunch length of BBR wake which agrees with the result of bunch lengthening indicated by figure 5.6 and radiation bursting pattern in figure 5.7.

Furthermore, figure 5.11, 5.12 and 5.13 have also interestingly remarked that the localized micro-fluctuation at the bunch tail is unarguably induced by the CSR wakefield. According to the comparison among wake models, it is obviously shown that the micro-fluctuation is specifically induced in the simulation with CSR wakefield while there seems to have no significant sign of such a localized fluctuation initiated in the simulation with only BBR wakefield. This localized microbunching is also appeared on the simulation with CSR + BBR wake model with increasing fluctuation strength at 95.87 μA. In figure 5.11, left column illustrates that the 'spur-like' structure has been developed and faded down after passed by $3T_s$ or approximately 3000 revolution turns. It might be described that the beam instability due to

CSR wakefield has still been insufficient to sustain the localized microbunching and might probably be weaker than the effect of radiation damping. Then, when the bunch is proceeding into equilibrium, the micro-fluctuation has apparently been diffused to the main phase space packet and become disappearance.

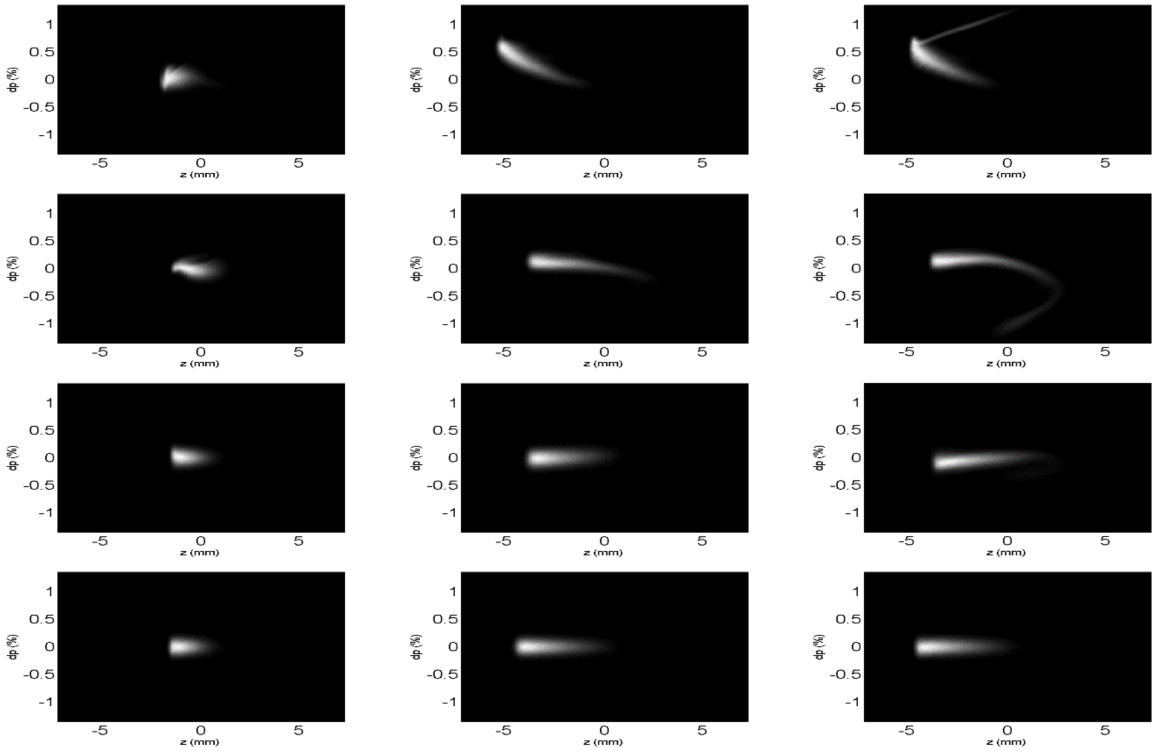

Figure 5.11: The comparison of longitudinal phase space evolutions with bunch currents 50.50 μA of α_1 = -0.6 × 10^{-5} with V_{rf} = 3.4 MV under CSR (left column), BBR (middle column) and CSR + BBR (right column) wakefields captured at $0.5T_s$, $1T_s$, $5T_s$ and $30T_s$. Bunch head is to the right.

The bunch under cooperated wake model; CSR + BBR, at 50.50 μA also appears to be sustainably confined in a packet when it is progressed into the equilibrium. Bunch spreading both in aspects of position and momentum deviation are apparently similar to the dynamic evolution under BBR wakefield. Moreover, the characteristic localized microbunching is too weak to be detected in the bunch phase space. Therefore, it might be implied that the effect of BBR wake is relatively higher than the CSR wakefield at this current.

The longitudinal dynamics illustrated in figure 5.12 and 5.13 evidently affirm that the characteristic micro-fluctuation at the bunch tail is initiated by the CSR wakefield. Figure 5.13 also indicates that this localized microbunching is consistently occurred throughout the whole range of simulation both in the CSR and CSR + BBR cases even when the bunch has already been advanced to equilibrium. This phenomenon also implies that the effect of CSR wakefield is collectively stronger as the current is increased. Its strength is apparently sufficient to compete with excitation induced by BBR wakefield and diffusion effect from radiation damping. Therefore, the localized microbunching is able to be consistently exposed in the longitudinal phase space motion under the cooperated CSR + BBR wakefield in long run.

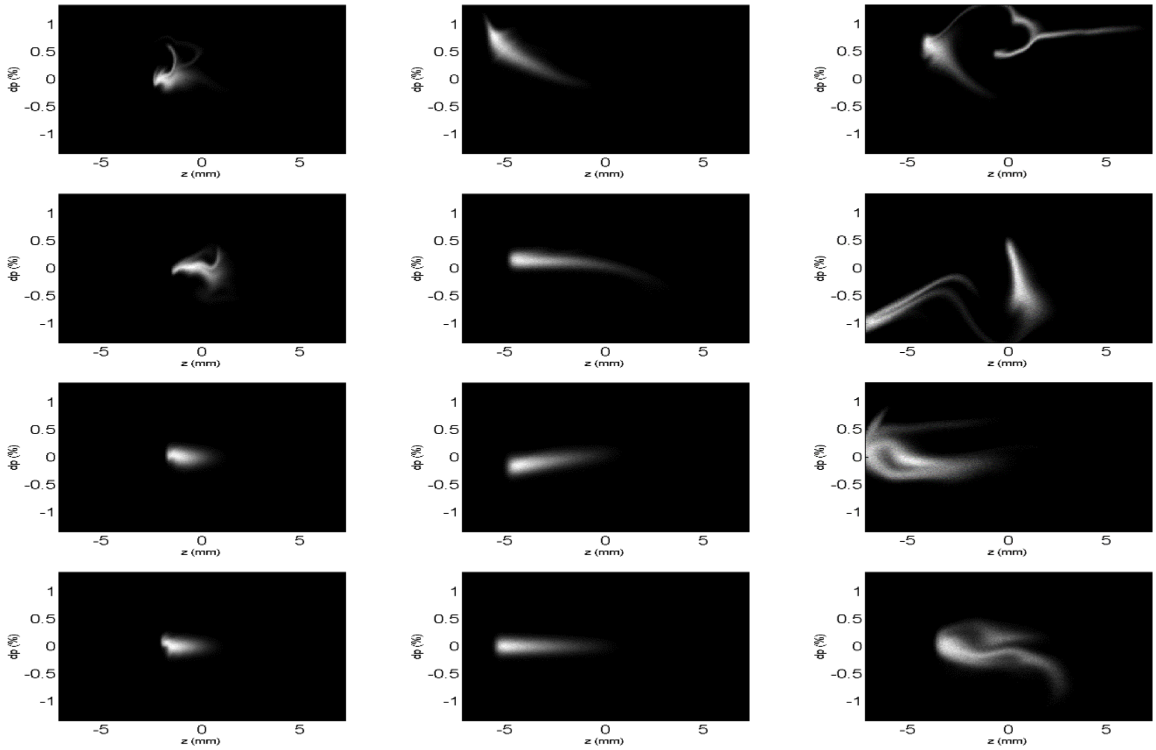

Figure 5.12: The comparison of longitudinal phase space evolutions with bunch currents 83.50 μA of α_1 = -0.6 × 10^{-5} with V_{rf} = 3.4 MV under CSR (left column), BBR (middle column) and CSR + BBR (right column) wakefields captured at $0.5T_s$, $1T_s$, $5T_s$ and $30T_s$. Bunch head is to the right.

Interestingly, at 95.87 μA, the bunch evolution influenced by the cooperated CSR + BBR wake model is unexpectedly suppressed in a confined semi-stable evolution state. The influences of both wakefields seem to be effectually cancel out each other as well as compromising with the radiation damping. The bunch is consequently able to proceed into its overall stabilized confinement after $8T_s$ with attached 'spur-like' fluctuation at the tail. Accordingly, the synchrotron radiation from the bunch at 95.87 μA is coherently emitted due to both the conventional microbunches and unconventional 'spur-like' density fluctuation or localized microbunches which is able to moderately enhance the total radiation power as illustrated in figure 5.10.

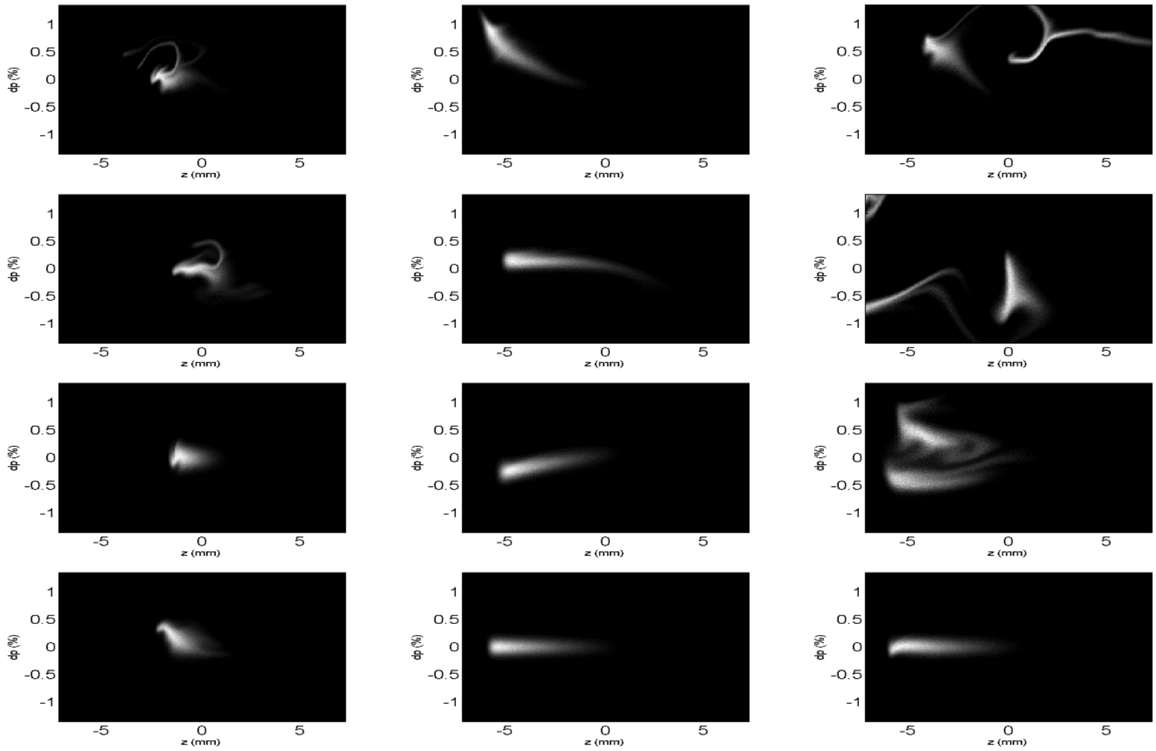

Figure 5.13: The comparison of longitudinal phase space evolutions with bunch currents 95.87 μA of α_1 = -0.6 × 10^{-5} with V_{rf} = 3.4 MV under CSR (left column), BBR (middle column) and CSR + BBR (right column) wakefields captured at $0.5T_s$, $1T_s$, $5T_s$ and $30T_s$. Bunch head is to the right.

Contrary to the bunch at 83.50 μA, figure 5.12 shows totally different bunch evolution behaviour under CSR + BBR wakefield. The cooperation of CSR and BBR wakefields appears unable to maintain the semi-stable state evolution of the bunch. Even though the bunch evolution tends to be periodically confined into a semi-stable packet as previously mentioned, the bunch will always be severely decomposed into broken shape again. Consequently, the synchrotron radiation bursting signals at 83.50 μA are broaden due to this complex fluctuation of longitudinal density distribution of a bunch.

5.1.3.2 $\alpha_1 = 1.0 \times 10^{-5}$ and $V_{rf} = 3.4$ MV

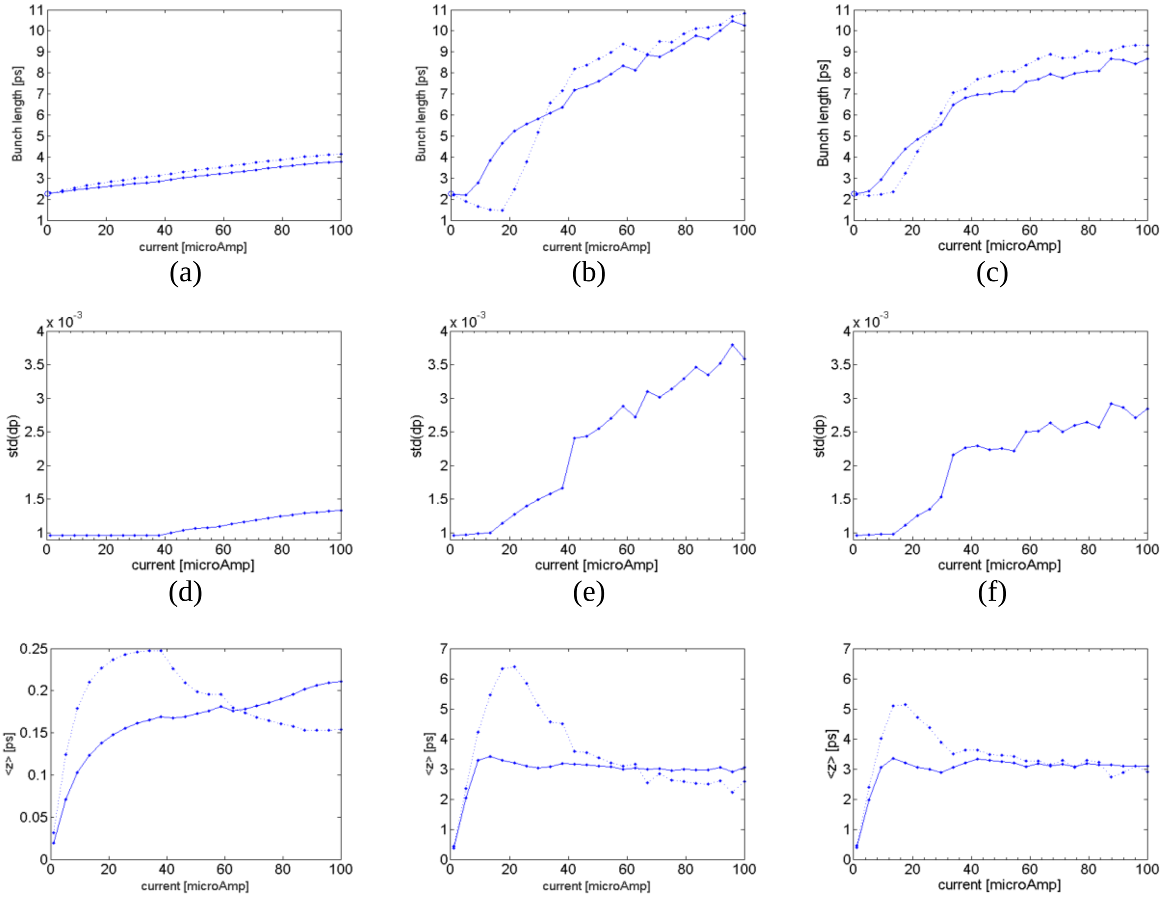

(a) (b) (c)

(d) (e) (f)

(g) (h) (i)

Figure 5.14: Comparison of bunch profiles for $\alpha_1 = 1.0 \times 10^{-5}$ with $V_{rf} = 3.4$ MV. (a), (b) and (c) are plots of bunch length vs current. (d), (e) and (f) are energy spread vs current. (g), (h) and (i) are bunch centroid shifting vs current. (a), (d) and (g) are the simulations with CSR wakefield. (b), (e) and (h) are the simulations with BBR wakefield. (c), (f) and (i) are the simulations with CSR + BBR.

Figure 5.14 and 5.15 demonstrate that the bunch under CSR wakefield exhibits the feature of CSR bursting as same as the previous studies in many synchrotron facilities. The plot of energy spread illustrates an obvious broken point on the curve which indicates the onset of collective instability at 38.125 μA. The radiation bursting pattern influenced by CSR wakefield illustrated in figure 5.15 has also given supportive evident with an illustration of bursting signals start appearing at approximately 40 μA.

In term of the radiation bursting under CSR wakefield, after the instability threshold is revealed at 40 μA the second instability threshold has subsequently been exposed at approximately 70 μA. However, the first and second instability thresholds predicted by the simulation with CSR wakefield have still somewhat overestimated the thresholds detected in experiment. The experimental pattern demonstrates that the bunch reaches the first instability threshold at approximately 30 μA, then, when the current is further increased, the second instability threshold is revealed at approximately 40 μA and later at 60 μA.

The temporal bursting frequencies 2.05, 4.15, 6.40 and 8.55 kHz are exposed at the first threshold detected in experiment. The amplitudes of these signals are dramatically faded with increasing frequency. The second threshold revealed at 40 μA has shown the bursting frequencies at 0.15, 0.95 and 1.65 kHz then appeared again at 60 μA with many bursting frequencies, for examples, 2.50, 2.90, 3.35, 3.65 and 4.10 kHz. Meanwhile the simulation with CSR wakefield reveals the first threshold at 40 μA with bursting frequencies 0.10 and 2.35 kHz in 60 – 90 GHz detecting range and additional signal at 4.75 kHz revealed in 75 GHz – 1.5THz detecting range. The second threshold is numerically revealed at approximately 70 μA with bursting frequencies 0.75, 1.30, 1.60, 2.30, 3.90, 4.75, 5.45 and 7.05 kHz.

Numerical simulation with BBR wakefield provides significantly different results with respect to the result of CSR wakefield. The plot of energy spread indicates that the onset of microbunching effect which principally leads to the first instability threshold is taken place at 13.375 μA. It also expresses that when the current is further increased, the curve meets another broken point at 38.125 μA where the energy spread curve takes substantial leap from 0.16 to 0.24 %. The bursting pattern shown in figure 5.15(e) correspondingly illustrates that the branched bursting signals are firstly appeared at approximately 15 μA then the second bursting pattern subsequently occurred at approximately 40 μA.

In term of bursting frequencies, the numerical revelation of the BBR wakefield illustrates signals of the first instability threshold at 0.63, 1.35 and 2.05 kHz on 60 – 90 GHz detecting range and additional 2.80 kHz on 75 GHz – 1.5 THz range. When entering to the second bursting pattern at 40 μA, the bursting signals are revealed at 0.55, 1.20, 1.83, 2.48, 3.10, 3.70, 4.33, 4.95, 5.60 and 6.23 kHz on 60 – 90 GHz detecting range and 6.85, 7.45, 8.05, 8.70, 9.35, 10.00, 10.70 and 11.25 kHz are later implemented on 75 GHz – 1.5 THz range.

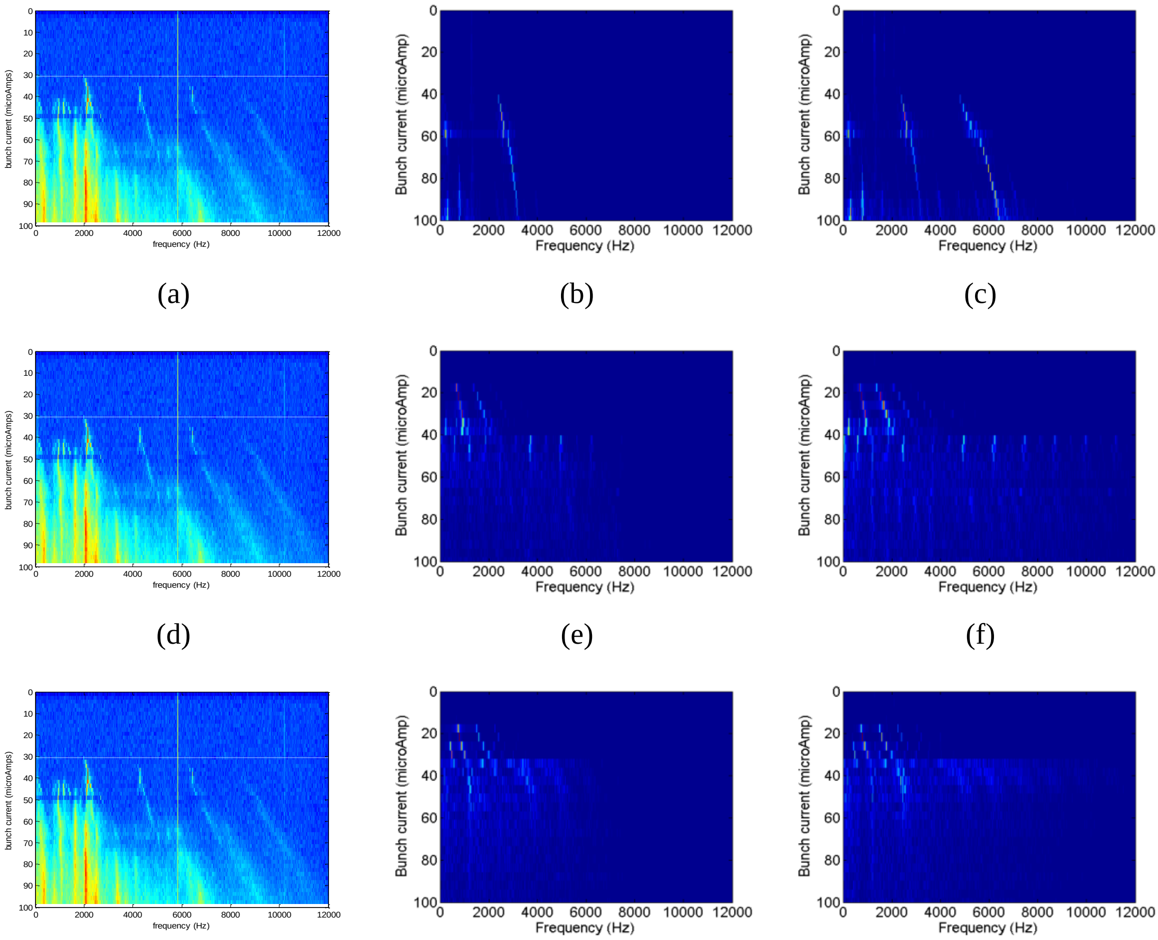

(a) (b) (c)

(d) (e) (f)

(g) (h) (i)

Figure 5.15: Comparison of radiation bursting spectrums for α_1 = 1.0 × 10^{-5} with V_{rf} = 3.4 MV. (a), (d) and (g) are experimental detected spectra. (b), (e) and (h) are simulated spectra at 60 – 90 GHz with CSR, BBR and CSR + BBR respectively. (c), (f) and (i) are simulated spectra at 75 GHz – 1.5 THz with CSR, BBR and CSR + BBR respectively.

The numerical result of CSR + BBR wakefield simulation reveals that the bunch reaches the first instability threshold at the same current as it is indicated by BBR wakefield. However, it reaches the second threshold at lower current than the BBR wake. The energy spread curve and the radiation bursting pattern illustrate that the second instability threshold is revealed at 29.875 μA. The bursting pattern of a bunch due to CSR + BBR wakefield demonstrates the bursting frequency components at first instability threshold with the same series of frequencies occurred on the BBR wakefield. As well as the bursting frequencies at the second instability threshold, the pattern illustrates several intense areas corresponding to the frequency components indicated by the BBR wake simulation. There is a noticeable point that the bursting frequencies on the second bursting pattern due to BBR wake are apparently sharper than the signals due to CSR + BBR wakefield.

After carefully considered the first and second bursting patterns of BBR wakefield in figure 5.15(e) and (f), it is apparent that both patterns are disconnecting. Their bursting signals are revealed at totally different frequency series and has no connection points. In contrast, the connection between both bursting signal series has become apparent in the resulting pattern of CSR + BBR wakefield. At the transition area between two bursting patterns, the first bursting frequencies are obviously bent and rigorously shifted toward higher frequencies with increasing current and connected to the second series.

It would be worth investigating the background longitudinal beam dynamic at this transition region between bursting patterns because it might be able to provide deeper understanding of how the bursting behaviour is transformed or, in other words, what is a mechanism of an emergence of chaotic threshold. Ultimately, it might be able to figure out an effective method to tackle the current limitation due to collective instabilities in accelerator experiment.

In order to comprehend how the transition of bursting patterns is occurred, the longitudinal beam dynamics of the bunch at each stage of radiation bursting is considered. The longitudinal phase space of the bunch at 20.35, 26.80, 30.02, 31.63 and 44.53 μA under the CSR, BBR and

CSR + BBR wakefields will be considerately analysed and compared among each other to reveal how the bunch formation and deformation is periodically developed.

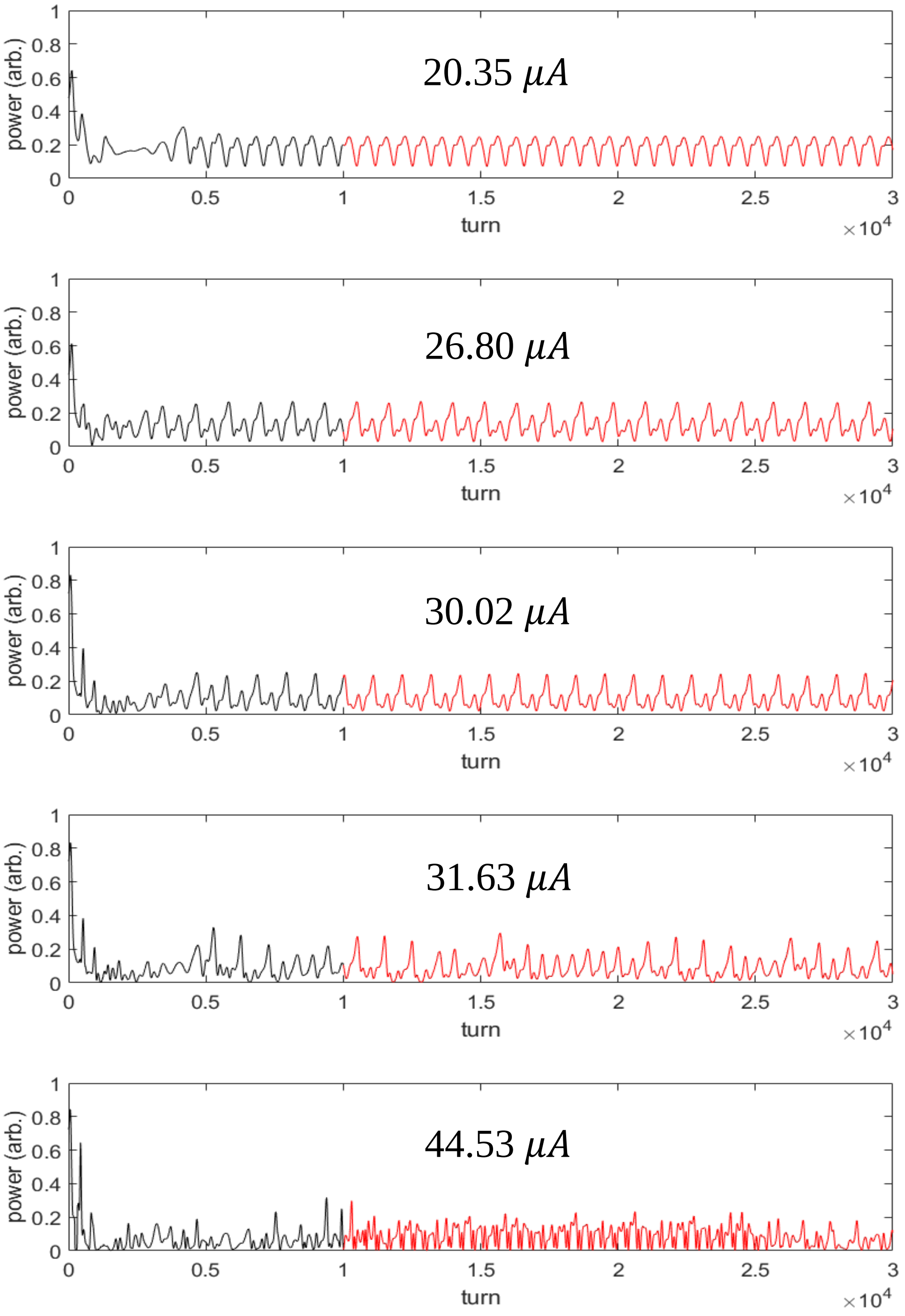

Figure 5.16: The comparison of radiation power bursting in time domain from numerical simulation with CSR + BBR wakefield for α_1 = 1.0 × 10^{-5} with V_{rf} = 3.4 MV at 20.35, 26.80, 30.02, 31.63 and 44.53 μA. Red lines indicate the collecting turns to be analysed.

The bunch currents 20.35, 26.80 and 30.02 μA are chosen to be representatives of beam dynamics during the semi-stable state evolutions where the temporal CSR bursting is taken place and yields the first radiation bursting pattern accordingly. The illustrative development of the dynamical formation of the bunch in longitudinal phase space under particular wake model which is gradually strengthened with increasing current will be depicted. Current 31.63 μA represents beam dynamic near the chaotic threshold where noticeable characteristic bending of the resulting CSR bursting signals is developed.

At these currents, the bursting pattern is changing from the first to the second bursting pattern. The analysis of beam dynamics during this stage is critically mandatory in order to emphasize the background mechanism of stability states transition.

The current 44.53 μA is a representative of beam dynamic beyond the chaotic threshold that yields the second bursting pattern. The consideration at this current is important because it apparently demonstrates that the temporal CSR bursting has still been revealed and exhibited with several sharp spectral lines of high amplitude signals despite it had already been proceeded beyond the chaotic threshold.

It would be worth investigating what is being happened in longitudinal phase space and how the bunch density distribution evolved with time. Furthermore, its temporal CSR bursting evidently confirms that the perturbed phase space evolution has still been able to progress consistently under intense instability. Therefore, it might probably be able to suggest some implications on high current steady CSR bursting operation.

According to the radiation bursting power of the bunch simulated with CSR + BBR wakefield illustrated in figure 5.16, it is obvious that the radiation burst is exhibited with distorted wave form in time domain in accordance with the bunch evolution in longitudinal phase space. It is apparently fluctuated and distorted due to the progression of the bunch deformation which has been induced by particular collective beam instability. These distortions evidently assert that the bunch is not solely revolved as a rigid bunch in phase space. There must be an oscillation modes mixing and some chaotic elements of distribution progressed in a background. The distortion on the radiation burst is also dramatically stronger and getting more complicated with increasing current as obviously demonstrated in figure 5.16. At 20.35 μA, the characteristic radiation bursting due to microbunching effect is exhibited. Then, at 26.80 and 30.02 μA, the distortion become stronger and more complicated which indicates that there are more complex bunch deformations collectively arisen due to higher intensity. The radiation power burst appears even more intricate near the chaotic threshold at 31.63 μA where the systematic periodicity of the radiation bursting seems to be deviated. This bursting behaviour in time domain is strongly correlated to the radiation bursting in frequency domain illustrated in figure 5.15 which demonstrates several broader bursting signals especially at higher frequency band.

Finally, at 44.53 μA, the radiation bursting power is sharply fluctuated with more complicated fashion, nevertheless there seems to be periodically consistent at particular period. The implication of this periodic fluctuation is that the temporal bursting of CSR is transformed to another oscillation mode with higher frequency than the initial one. This characteristic evolution in phase space is much likely to be detected in longitudinal phase space.

The numerical simulation of longitudinal phase space is captured and sequentially illustrated at 800, 4000, 10000, 16000 and 24000 turns. Since the synchrotron period, T_s, of α_1 = 1.0 × 10^{-5} with V_{rf} = 3.4 MV is 1.4750 ms or 787.38 turns, these turn numbers are approximately corresponding to $1T_s$, $5T_s$, $12.5T_s$, $20T_s$ and $30T_s$. Figure 5.17, 5.19, 5.20, 5.21 and 5.23 illustrate the longitudinal phase space evolutions at 20.35, 26.80, 30.02, 31.63 and 44.53 μA respectively. Each figure will compare phase space evolution among three wakefield schemes; CSR, BBR and CSR + BBR in order to inspect the deviation of their effect on the development of longitudinal beam dynamics with increasing beam intensity.

The longitudinal dynamic illustrated in figure 5.17 shows that the CSR wakefield at 20.35 μA seems to be too weak to initiate any apparent fluctuation on the bunch phase space such as the microbunches. The bunch phase space distribution appears almost stationary evolving at an original position. Thus the dipole mode oscillation ($m = 1$) [65] is undetectable.

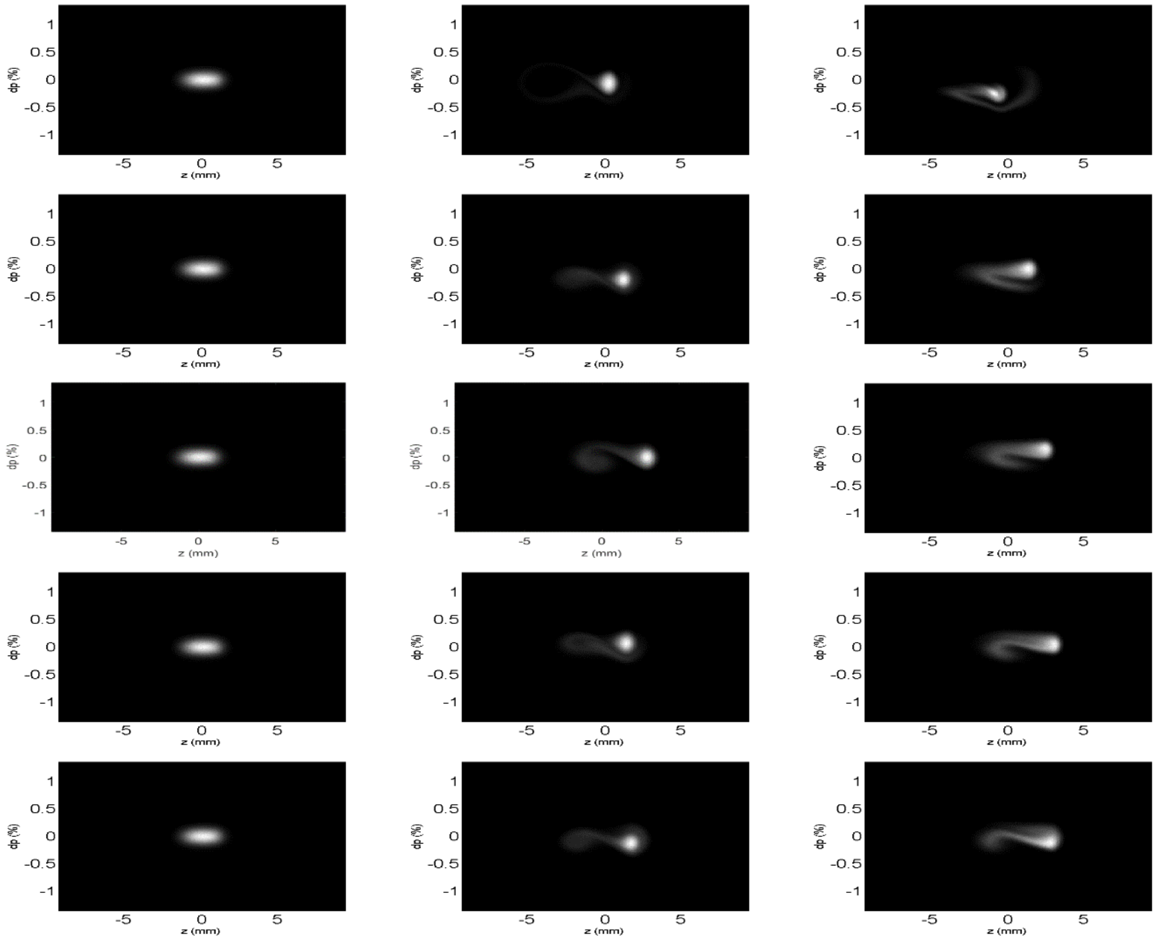

Figure 5.17: The comparison of longitudinal phase space evolutions at 20.35 μA of α_1 = 1.0 × 10^{-5} with V_{rf} = 3.4 MV under CSR (left column), BBR (middle column) and CSR + BBR (right column) wakefield captured at 1T_s, 5T_s, 12.5T_s, 20T_s and 30T_s. Bunch head is to the right.

The radiation bursting in time domain depicted in figure 5.18 has also agreed with the bunch phase space evolution. With CSR wakefield, the bursting power is really low with respect to the bursting power influenced by BBR and CSR + BBR wakefields. It is corresponded to the phase space evolution under CSR wakefield which exhibits a well confined bunch packet filled with homogeneous particle density distribution.

Under BBR wakefield, the bunch behaviour is much more complicated than the bunch influenced by CSR wakefield. Within a few hundred turns after starting, the bunch is vertically sheered due to an inductive part of BBR impedance [66]. Then, it is suddenly elongated which almost all particles are concaved counterclockwise around the stable fixed point at the head that subsequently leads to a formation of densely compact minor bunch. Concurrently, all other particles are diffused toward the bunch tail and assembled the 'filamentation' which curls counterclockwise around another fixed point at the tail. Particles in the outer shell of the minor bunch on the head continue flowing into the filamentation, proceeding to the tail and curled around the tail fixed point.

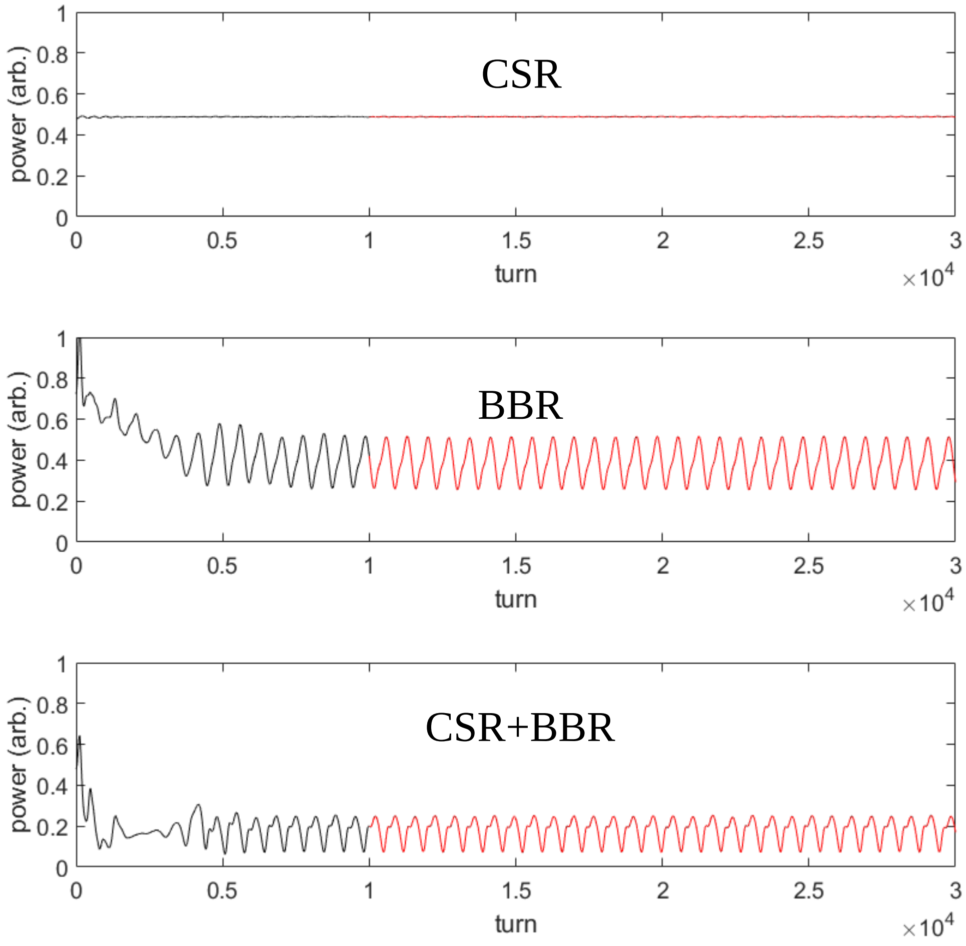

Figure 5.18: The comparison of radiation power bursting in time domain from the numerical simulation with CSR, BBR and CSR + BBR wakefields for α_1 = 1.0 × 10^{-5} with V_{rf} = 3.4 MV at 20.35 μA. Red lines indicate the turns collected for analysis.

Noticeably, these migrated particles are progressively accumulated and formed another minor bunch with toroidal shape around the tail fixed point instead of the solid one as being developed at the head fixed point. At the same time, some amount of particles from this ‘halo’ minor bunch also diffuse back to the head solid minor bunch passing through the filamentation as well.

The flow rate of particles from the head solid bunch to the tail halo bunch is greater than the rate of particles migrating backward from the halo to the solid minor bunch. The particles continue flowing and gradually accumulated at the halo minor bunch until approximately 5000 revolution turns. At this point the particle exchanging rate between sub-bunch seems to be stabilized. It indicates that the system has been evolved into the dynamical equilibrium. Eventually, the minor solid bunch apparently attains much more particles than the minor halo bunch on the tail. The entire ‘binary halo-solid bunch’ system also executes a synchrotron motion by orbiting counterclockwise around a certain point on phase space. This dynamical equilibrium continues consistently evolving throughout the whole range of simulation.

It is also worth noting that, at dynamical equilibrium, the halo bunch is unable to be damped down into a solid bunch. The hypothesis of its mechanism might be given similar to the formation of binary bunch of sawtooth behaviour as described in 2.9.3 but the beam current is not intense enough. Most of particles have still been able to be contained in the main bucket. Moreover, a new bucket created by the wakefield is too small. There is only a portion of particles leak to this new bucket and can be confined. Accordingly, charge density in the new bucket is insufficient to compete with the quantum excitation effect. Thus, a sub-bunch is sustained with toroidal formation unable to evolve into the solid bunch.

After combining the CSR with the BBR wakefield, the bunch under CSR + BBR wake behaves much similar to the bunch under BBR wakefield. However, it appears to have less amount of particles packed in a minor solid bunch than the particle accumulation induced by BBR wakefield. All other particles appear flowing toward the filamentation and curling around the tail fixed point. Particles are apparently diffused from the solid bunch to the tail knot intending to form another minor bunch just like in BBR case. However most of the migrated particles circulate counterclockwise around the outer shell of the tail knot and flowing back through filament and cover the outer shell of the solid bunch on the head again.

At some point, the tail knot is almost entirely diffused back to the solid bunch, nonetheless another portion of particles from the head sub-bunch flow in to fill up the knot again and prevent it to be completely swallowed by the minor solid bunch. Eventually, large amount of particles is circulating around both minor bunches and exchanging through thicker filamentation which connects them together. Hence the overall system appears to be more attached to each other than the binary halo-solid bunch system developed in the bunch-BBR wakefield interplay.

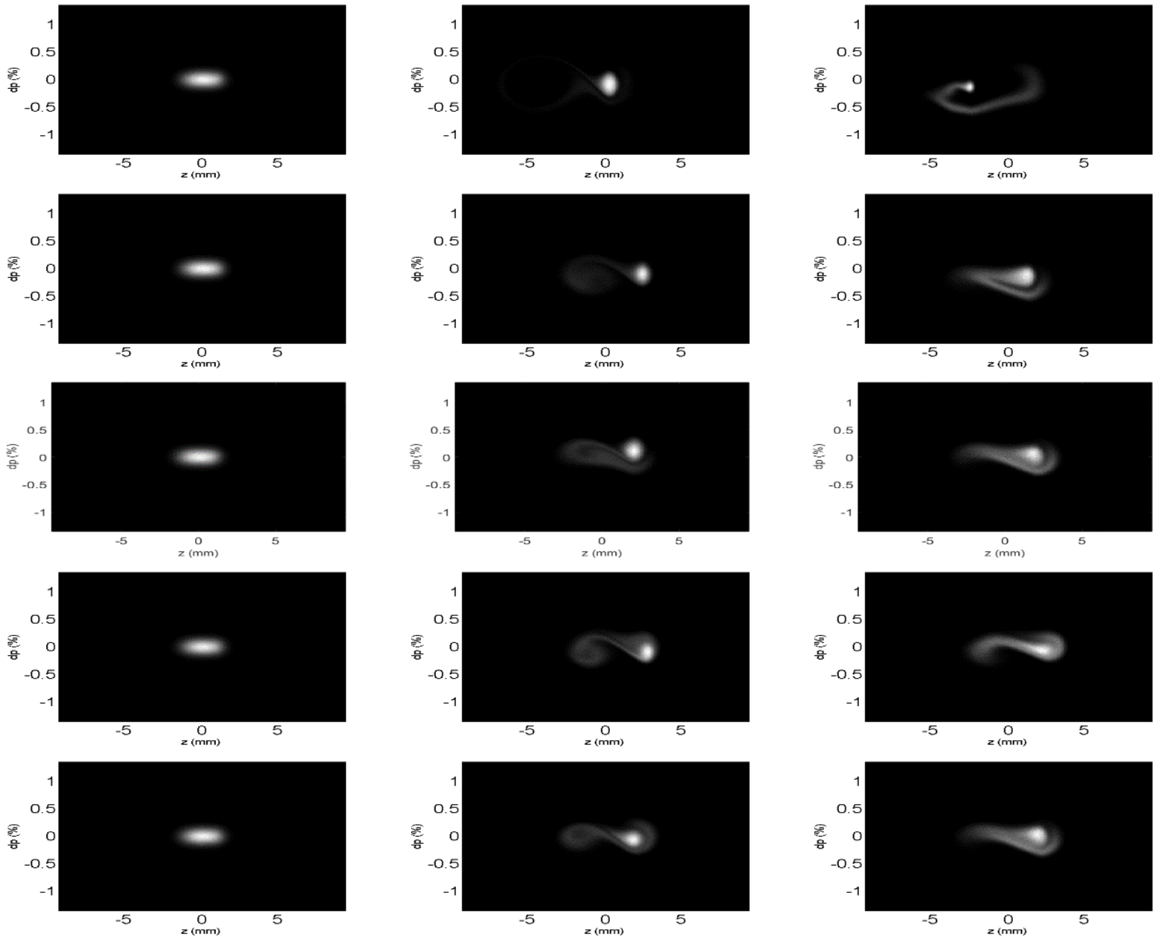

Figure 5.19: The comparison of longitudinal phase space evolutions at 26.80 μA of α_1 = 1.0 × 10^{-5} with V_{rf} = 3.4 MV under CSR (left column), BBR (middle column) and CSR + BBR (right column) wakefield captured at $1T_s$, $5T_s$, $12.5T_s$, $20T_s$ and $30T_s$.Bunch head is to the right.

It seems that the CSR wakefield contributes on promoting the particle circulation across the system. The comparison of the bunch evolution in phase space on figure 5.17 also indicates an implication on the negotiation between CSR and BBR wakefield in the cooperative wake model CSR + BBR as follow. The BBR is apparently a source of bunch elongation or even separation into two identical minor bunches if the wake potential is sufficiently strong while the bunch lengthening effect due to the CSR wake is relatively small.

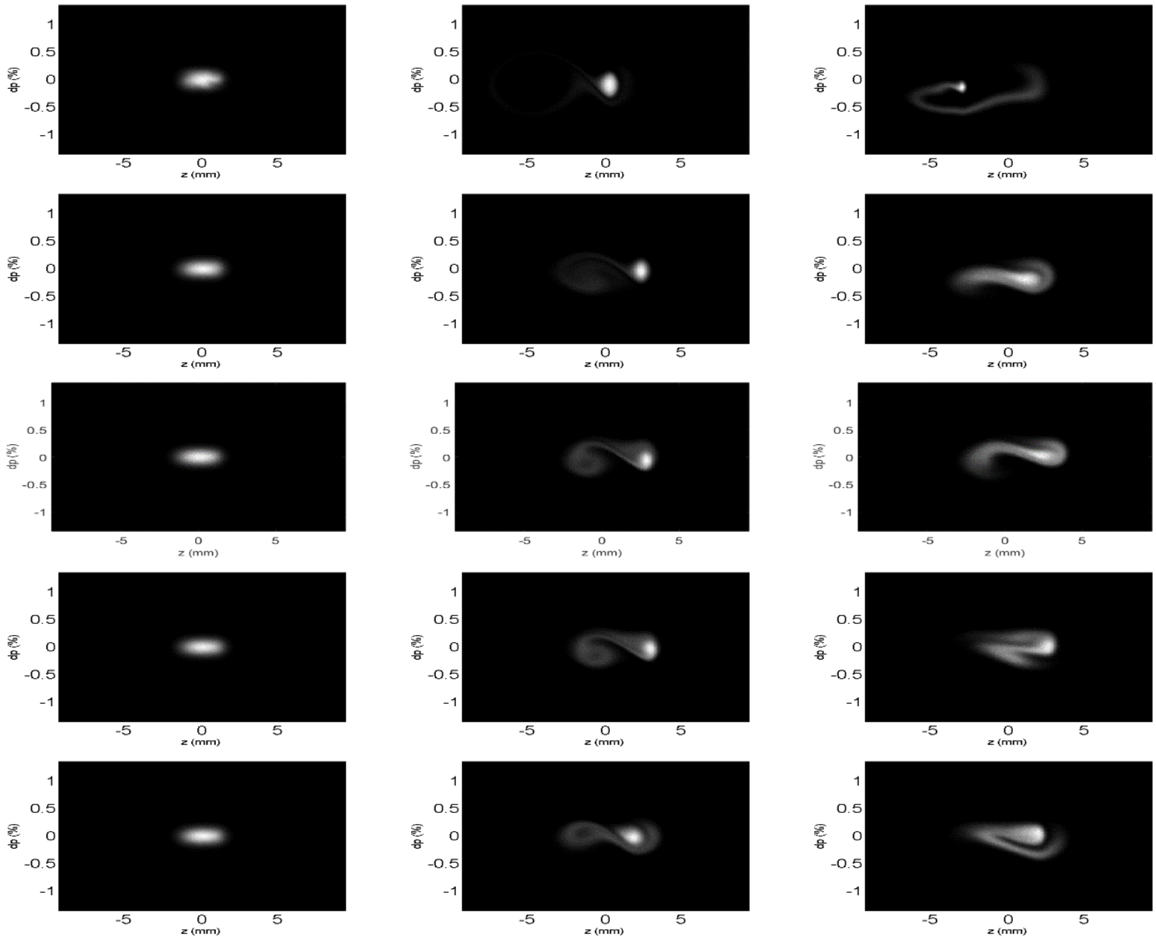

Figure 5.20: The comparison of longitudinal phase space evolutions at 30.02 μA of α_1 = 1.0 × 10^{-5} with V_{rf} = 3.4 MV under CSR (left column), BBR (middle column) and CSR + BBR (right column) wakefield captured at $1T_s$, $5T_s$, $12.5T_s$, $20T_s$ and $30T_s$. Bunch head is to the right.

Bunch evolution in longitudinal phase space depicted in figure 5.19 – 5.21 illustrate that the bunch evolves in similar fashion as it previously happened at 20.35 μA. However, the effects of wakefields are apparently stronger corresponding to higher current. Under CSR wakefield, the bunch lengthening curve in figure 5.14 demonstrates marginal change on the curve compared to BBR and CSR + BBR cases although the microbunching effect is being dramatically initiated and can be seen on the longitudinal phase space evolution at 26.80 μA. At 30.02 μA, severe deformation of a bunch distribution is obviously seen at the early revolution turns. The microbunching 'arms' are clearly exhibited then damped down by the effect of radiation damping in the next several hundred turns. Noticeable density fluctuations at the outer shell of the bunch cluster has been left behind and continue circulating throughout the simulation after the arms was diffused into the cluster.

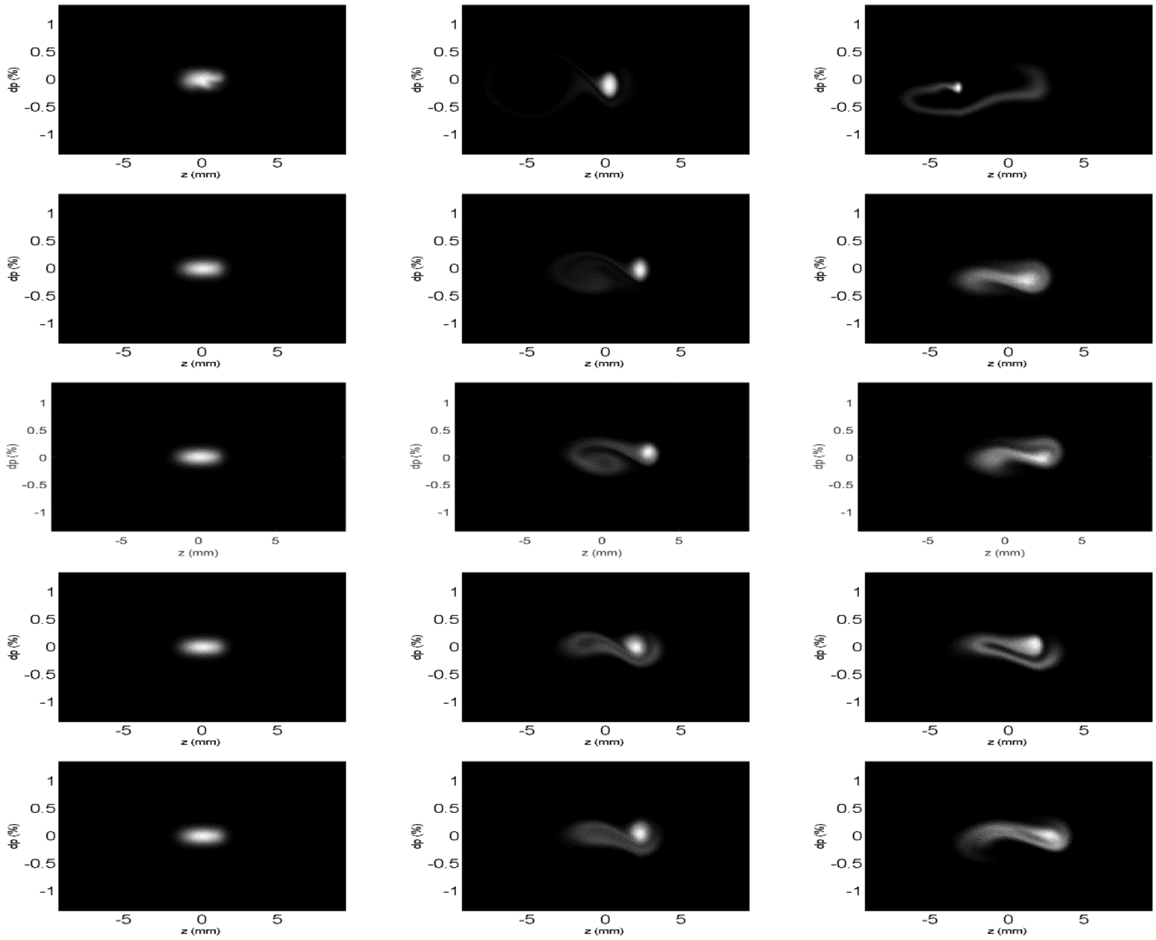

Figure 5.21: The comparison of longitudinal phase space evolutions at 31.63 μA of α_1 = 1.0 × 10^{-5} with V_{rf} = 3.4 MV under CSR (left column), BBR (middle column) and CSR + BBR (right column) wakefield captured at $1T_s$, $5T_s$, $12.5T_s$, $20T_s$ and $30T_s$. Bunch head is to the right.

Longitudinal phase space of a bunch under BBR wakefield evidently reveals that the influence of wakefield is collectively increased with current. The binary halo-solid bunch system is developed in the same way as occurred at 20.35 μA but with higher particle density accumulation. The binary halo-solid bunch system becomes gradually observable due to more intense particle accumulation at higher current. The system is apparently looked like the symbolic representation of ‘Yin-Yang’ which most of the particles are concentrated at the head fixed point while the others are curling around the emptiness at the tail fixed point and continuously exchanging between ‘halo-solid’ binary in meantime.

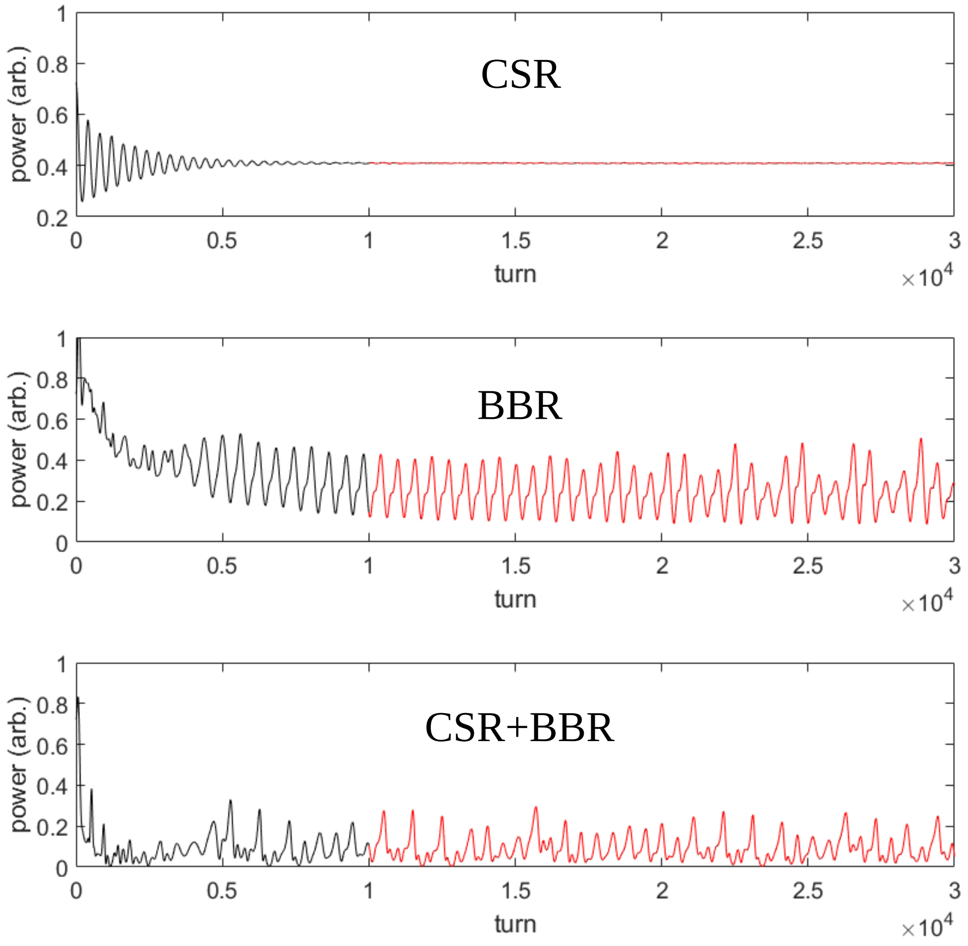

Figure 5.22: The comparison of radiation power bursting in time domain from the numerical simulation with CSR, BBR and CSR + BBR wakefields for α_1 = 1.0 × 10^{-5} with V_{rf} = 3.4 MV at 31.63 μA. Red lines indicate the turns collected for analysis.

A bunch influenced by CSR + BBR wakefield is able to exhibit characteristic evolution features on the bunch phase space due to combining effects of CSR and BBR wakefields. The bunch seems to be intending to progress in the same fashion as it behaved under BBR wakefield. However, due to the particles circulating between binary bunch are much more than occurred at 20.35 μA, thus, when the system has been undergone to the dynamic equilibrium, most of the particles flow back to the minor solid bunch on the head while the minor halo bunch has yet to be developed at the tail. Therefore, the dynamical formation of the entire system is apparently looked more likely the ‘stationary barred spiral galactic evolution’ rather than the ‘Yin-Yang’ dynamical form.

Noticeably, at these currents near the chaotic threshold, with CSR + BBR wakefield the binary system is able to proceed into the dynamic equilibrium much faster than the bunch under BBR wakefield. It has been able to attain particle exchanging equilibrium since approximately 5000 turns while the bunch under BBR wake has still been unable to achieve this dynamical equilibrium state until succeeded into 11000 turns.

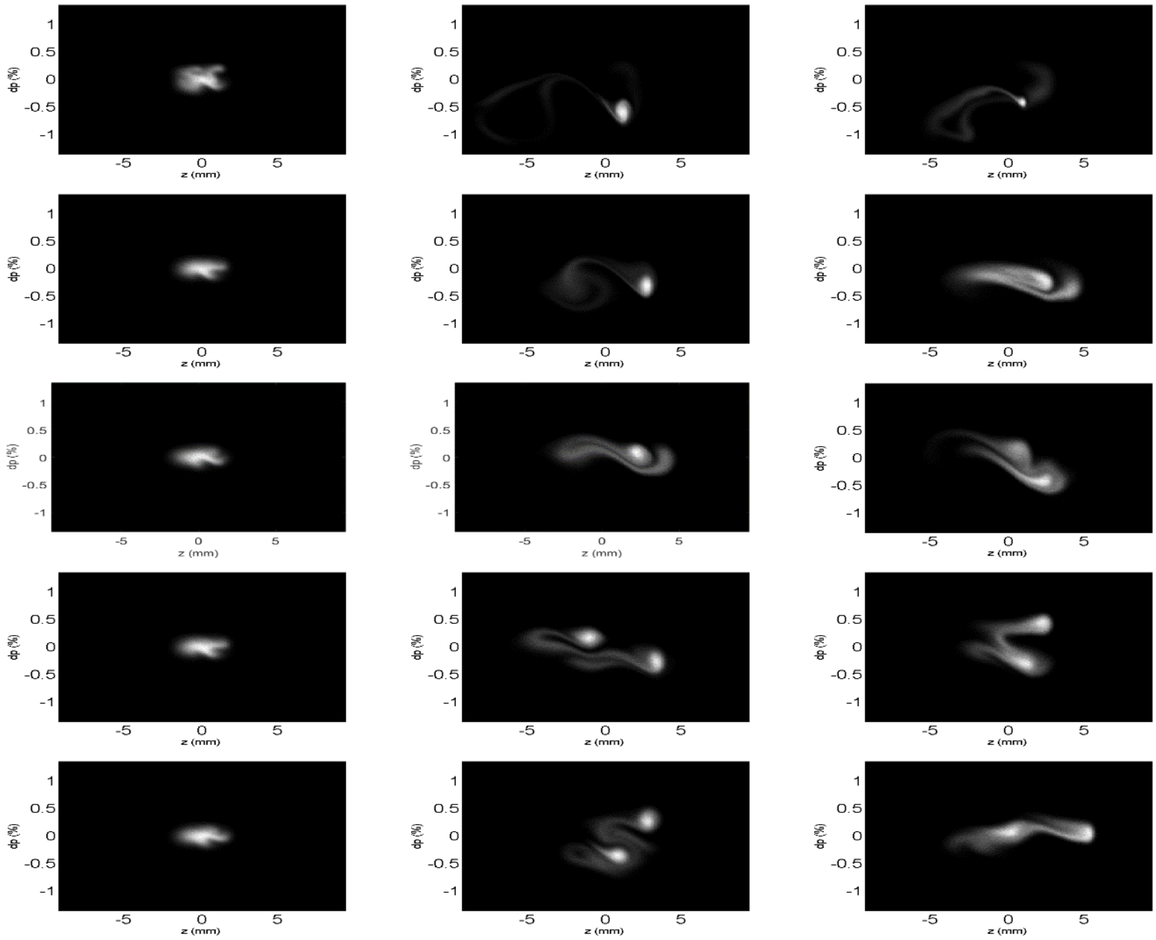

Figure 5.23: The comparison of longitudinal phase space evolutions at 44.53 μA of α_1 = 1.0 × 10^{-5} with V_{rf} = 3.4 MV under CSR (left column), BBR (middle column) and CSR + BBR (right column) wakefield captured at $1T_s$, $5T_s$, $12.5T_s$, $20T_s$ and $30T_s$. Bunch head is to the right.

Beyond the chaotic threshold, at 44.53 μA, the CSR wakefield exhibits its characteristic feature on the bunch deformation again. Left column of figure 5.23 obviously shows that the microbunching is consistently induced and evolving throughout the whole simulation. It has also accordingly resulted on the bursting pattern illustrated on the top row of figure 5.15. Two CSR bursting signals are clearly detected corresponding to this microbunching phenomena.

The 'binary star instability' [78] is unexpectedly discovered on the simulation with BBR wakefield at 44.53 μA. The initial bunch starts elongating and develops the halo-solid bunch formation in the same way as it was occurred in previous simulations at lower current with BBR wakefield. But the particles exchanging between halo and solid bunches as well as the particles confined in both minor bunches are much more condensed than the previous cases due to higher bunch current.

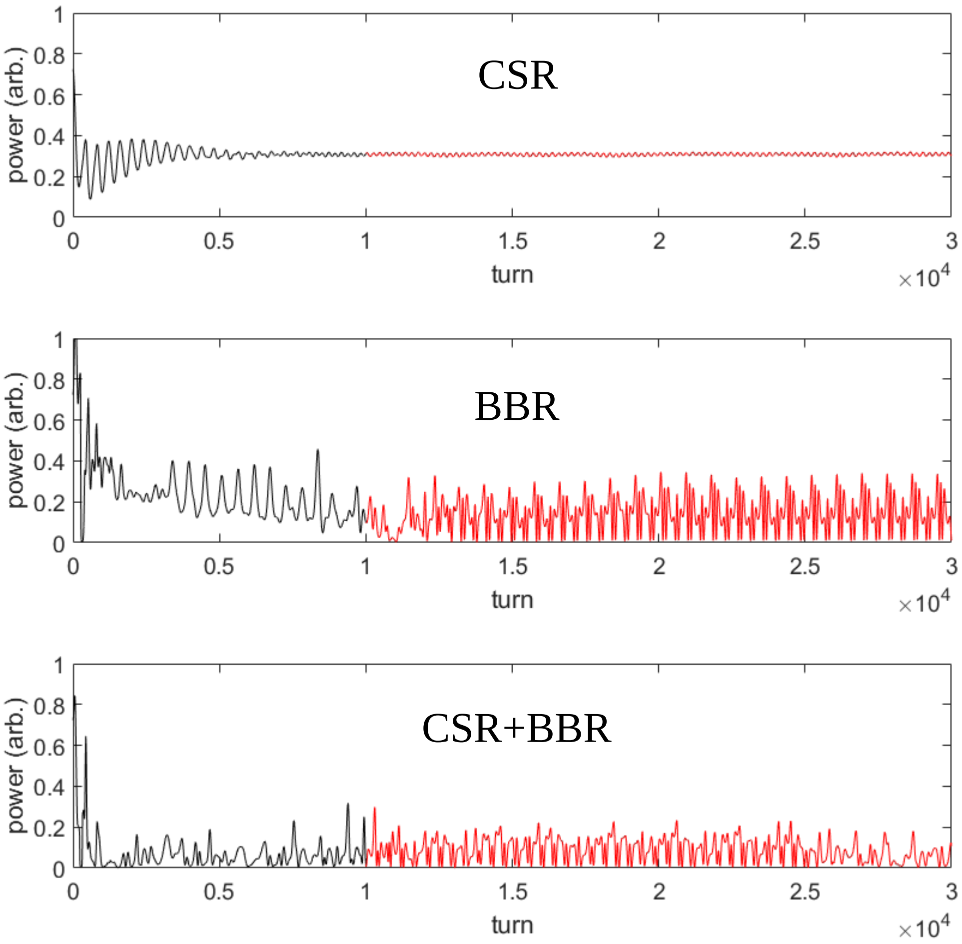

Figure 5.24: The comparison of radiation power bursting in time domain from the numerical simulation with CSR, BBR and CSR + BBR wakefields for α_1 = 1.0 × 10^{-5} with V_{rf} = 3.4 MV at 44.53 μA. Red lines indicate the turns collected for analysis.

The number of particle exchanging has been continuously increasing with revolution turns before the halo-solid bunch relation appears unable to be sustained. Eventually when the bunch is proceeding into approximately 11000 turns, both minor bunches coalesce. Then, the bunch is immediately stretched longitudinally again and separated into two individual solid minor bunches connected together with filamentation. These minor solid bunches orbit about one another like the binary star system with the period equivalent to the synchrotron oscillation. This behaviour has previously been investigated as the ‘sawtooth instability’ [77] which have been reported for the observations in several synchrotron facilities [8], [9].

At early stage of separation, a minor bunch on the head appears acquiring more particle accumulation than the tail bunch. The binary-star-oscillation is carrying on while the net particles migrated to the tail bunch is gradually increased. Until approximately 16000 turns, the particle exchanging rate seems to be stabilized and converging into equilibrium where the particle accumulations in both minor bunches appear to be equal.

The binary bunch system periodically oscillates between diffusion and separation phases throughout the simulation. During the diffusion phase, the binary bunch are not completely collapsed but only passed by each other in similar fashion to the numerical simulations performed by Baartman and D’Yachkov [77][78] while continuously exchanging their particles through the filamentation in meantime. Particle density distribution plotted with longitudinal scale can be illustrated as a big steep ‘hump’ during this diffusion phase which also causes a bursting of CSR as well. Accordingly, the plot of particle density distribution evolving with time appears to consistently oscillating between the single big hump of diffusion phase and double dominated peaks of separation phase with a period equals to half a synchrotron period. This behaviour would consequently cause the bursting of CSR at twice the synchrotron frequency. Second row of figure 5.15 shows a supportive bursting pattern at 44.53 μA which illustrates the highest bursting amplitude at approximately 1.25 kHz that slightly underestimates twice the synchrotron frequency; 2 × 677.944 Hz = 1.356 kHz. Radiation power of a bunch under BBR wakefield at 44.53 μA illustrated in figure 5.24 has also exhibited periodic blow-up of radiated power since approximately 11000 turns where the binary bunch system is developed.

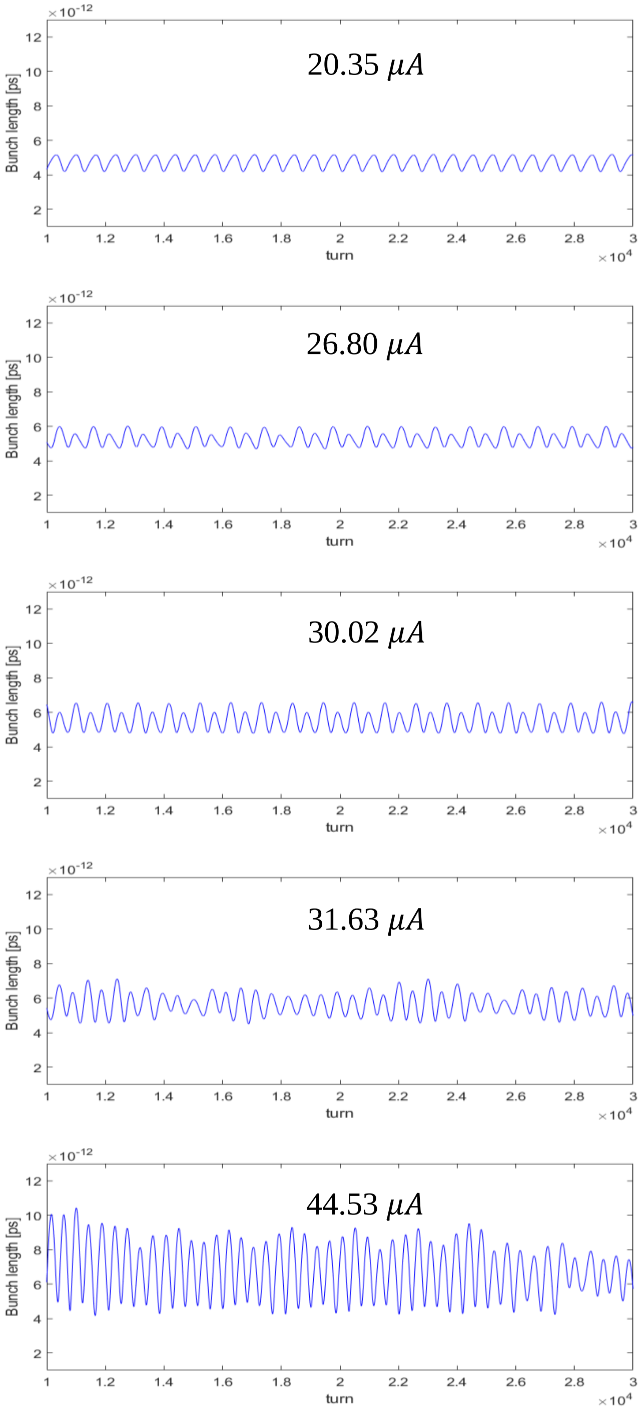

Figure 5.25: The plots of bunch length with revolution turns from numerical simulation with CSR + BBR wakefield for α_1 = 1.0 × 10^{-5} with V_{rf} = 3.4 MV at 20.35, 26.80, 30.02, 31.63 and 44.53 μA. Sawtooth behaviour of bunch length progression is depicted at 44.53 μA.

Figure 5.23 demonstrates that the competition between CSR and BBR wakefields in CSR + BBR wake scheme becomes more intense at high current. The longitudinal phase space of the bunch under CSR + BBR wakefield displays that during early revolutions, the bunch has yet been separated into the binary system but periodically fluctuated between elongation and diffusion states. Until it reaches at approximately 10000 turns, the binary bunch system is developed with thicker filamentation than the binary system generated by BBR wakefield. The binary bunches almost collapse to each other at diffusion phase before they are stretched away again within less than half a synchrotron period. The maximum distance between two minor bunches is seemingly to be shrunk as the system is evolving. The binary bunch system is eventually collapsed together at approximately 26000 turns. An emergence of sawtooth behaviour of bunch length progression over time can be obviously inspected on the bottom plot of figure 5.25.

The bunch evolution after the binary system collapsed is similar to the bunch behaviour during a few thousand turns before the binary system is constituted. Consequently, it would have probably been anticipated that the bunch longitudinal phase space might be alternating between the singular and binary bunch formations. The bunch evolution might periodically evolve in temporal singular-binary bunch manner.

In conclusion, it has been found that the bunch behaviour which plays the critical role in essentially generates different resulting radiation bursting patterns is the formation of binary bunch arrangement. The halo-solid system seems to take responsibility on resulting the first bursting pattern which turns out to be similar to the radiation bursting behaviour of a bunch due to CSR wakefield. The hypothesis is proposed as during the binary halo-solid bunch arrangement, most of the particles are concentrated in a minor solid bunch where its ‘local bunch length’ is short compared to the initial bunch length. Furthermore, the particles stream circulating between minor bunches as well as some elements of density fluctuation appears drifting around both minor bunches are comparable to the microbunching induced by CSR wakefield. Therefore, in macroscopic view point, the bursting of CSR can be apparently occurred in similar fashion to the bunch affected by CSR instability but with stronger power radiated.

The binary solid-solid bunch arrangement appears to play an important role in resulting the second bursting pattern. After proceeding into equilibrium, the initial bunch is separated into two identical minor bunches which orbiting around each other just similar to the binary star system. Both minor bunches are shorter than the initial one, certainly, their bunch length are sufficiently short to emit the coherent radiation as illustrated in figure 5.24. Periodic oscillation of the binary solid bunch system consequently occurred temporal bursting of CSR emission at another frequency. This phenomenon is subsequently illustrated as the second bursting pattern.

Another important contributor that governs the bursting behaviour of the bunch is the particle circulation across the entire binary system. In the simulation at 44.53 μA, the comparison between bursting patterns and longitudinal phase space evolutions due to BBR and CSR + BBR wakefields can be concluded that the particle circulation across the binary bunches and filamentation plays a critical role in bridging both sub-bunches together. Synchrotron radiation bursting due to BBR instability illustrates sharper signals and the bunch evolution in longitudinal phase space correspondingly demonstrates that the binary bunch is almost completely separated into two individual sub-bunches. This dynamic fashion has previously been identified as the sawtooth instability.

The pattern due to CSR + BBR wakefield illustrates somewhat different result. Even though the bursting signals are observed at almost the same frequencies as appeared in BBR simulation, they have been exposed with more broaden spectral lines. The bunch evolution in phase space also shows supportive information by illustrating both minor bunches connecting together with a thick filament acquiring particle density comparable to the minor bunches. Particle stream circulating around the system that makes the binary bunch seems to be more ‘linked’ has also been resulting on the radiation bursting in macroscopic view point. Stream of particle fluctuations within the system also circulate around the entire system at comparable revolution rate to the orbiting rate of the binary bunches. This streaming ‘clouds’ is analogous to the microbunches induced by CSR wakefield.

In terms of the bunch evolution in longitudinal phase space, it can be concluded that the transition between patterns is remarkably associated with the transition of binary bunch arrangements. It has obviously been revealed that the halo-solid system is responsible for the ‘CSR-liked’ first bursting pattern while the solid-solid arrangement is responsible for the second bursting behaviour. Longitudinal phase space evolution of a bunch under CSR + BBR wakefield demonstrates that the bunch is transformed from the singular to the binary bunch distribution profile when the current is crossing the chaotic threshold. Consequently, it might be able to conclude that the chaotic instability threshold in positive alpha is indicated by the maximum current that the bunch distribution can still be remained in a singular shape.

According to the beam dynamic phenomenology, it can be concluded that the BBR wakefield crucially results on the development of binary bunch formation while the CSR wakefield is responsible for regulating the particle circulation all over the entire system including the filamentation. It has also been evidently revealed that the CSR and BBR wake forces are negotiating throughout the simulation range. While the BBR wakefield is intending to separate the bunch into binary arrangement, the CSR wakefield is simultaneously attempting to retain them together by encouraging the circulation of particles all over the system which leads to the inspissation of the bridge between binary bunches.

At low current, collective wakefield has still been weak. An extra potential well induced by BBR wakefield has still been too shallow to contain as much particles to be accumulated into a solid sub-bunch. As well as the effect of CSR wakefield has also been weak and unable to regulate as much particle circulation on the system. Hence the overall system is appeared as most particle concentrated at the solid minor bunch which its length is sufficiently short to radiate the CSR. Therefore, the CSR-like bursting pattern is constituted as the first pattern.

When the current is further increased, the binary separation becomes increasingly perceivable due to an increasing effect of BBR wake which is able to generate deeper extra potential well that particles can be accumulated into a solid sub-bunch. The binary solid-solid system is then established. Due to the length of each minor bunch is sufficiently short, both of them are able to emit the CSR. According to the oscillation frequency of the binary system is approximately twice the synchrotron oscillation. The resulting CSR bursting is consequently exposed at half multiplication of the synchrotron oscillation. This phenomenon establishes the second bursting pattern as depicted in figure 5.15(e) and (f).

However, the presence of CSR wakefield is also encouraging particles circulation over the system. Thus the binary bunch appears more connected. Furthermore, there is also particle stream circulating over the system. Thus the second bursting pattern is revealed with broaden spectral lines due to this fluctuated stream.

Additionally, during the diffusion phase, the longitudinal distribution is appeared as a single steep hump which all particles are concentrated within considerable short length. This single hump appears to be able to radiate coherently. Moreover, the radiation power is unexpectedly higher than the binary system during separation phase. Thus the second bursting pattern is exhibited with a combination of the major series with higher amplitude and the minor series with lower amplitude.

5.1.3.3 α_1 = -1.0 × 10^{-5} and V_{rf} = 3.4 MV

Comparison of bunch length curves illustrated in figure 5.26 obviously demonstrates an impact of BBR wakefield to the bunch lengthening phenomena. It significantly improves the quality of simulation result which is able to better reproduce the bunch lengthening behaviour revealed in experiment. The plot of bunch length with current also shows that the BBR wakefield enormously lengthens the bunch much more than the effect from CSR wakefield. All the plots of bunch length, energy spread and centroid shifting with currents also demonstrate that the BBR wakefield is dominated over the cooperated CSR + BBR wake model. Plots of beam profiles under CSR + BBR wakefield are appeared almost identical to the beam profiles under BBR wake.

Although the BBR wakefield is dominated in the CSR + BBR model, the CSR wakefield has still been able to exhibits its characteristic effect by inducing distinctive fluctuations at higher current. More importantly, these fluctuations imply that at some points the bunch seems to be rebounded back into the initial state before it entered to the chaotic region. This is an indication of temporal occurrence of the chaotic behaviour as it was previously detected in the studies with negative momentum compaction factor.

As same as the previous studies for negative alpha, the energy spread curve seems to illustrate a broken point that more likely indicating the chaotic instability threshold rather than the microbunching instability threshold. The result of CSR + BBR wakefield shows that the presence of CSR wake reduces the chaotic threshold from the revelation with BBR wakefield from 71.125 to 67.00 μA.

All the plots of beam profiles of CSR + BBR simulation are all in agreement that the bunch is rebounded at 91.75 and 100.00 μA into the points on the trend lines drawn from the curves at lower current before entering to the huge fluctuation region. Radiation bursting pattern of the bunch under CSR + BBR wakefield is also agreed with the plots of bunch profiles by revealing an alternation of bursting signals to the first pattern at 91.75 and 100.00 μA. This phenomenon suggests that the temporal occurrence of chaotic bursting pattern is happen to be taken place in this studying case as well.

Experimental bursting pattern indicates the first instability threshold where microbunching effect starts occurring at approximately 31 μA. The bursting signals amplitude become stronger and observable at approximately 45 μA with frequency components 1.10, 1.60, 2.05, 2.50, 2.95, 3.45, 3.90, 4.40 and 4.80 kHz. These frequencies are almost equally spaced at an average 462.50 Hz which is closed to $\frac{2}{3}f_S$. As the synchrotron frequency, f_S, of this case is 677.94 Hz then $\frac{2}{3}f_S$

= 451.96 Hz. This outcome indicates that the sextupole mode of the bunch oscillation [65] might plays the dominated role on the first pattern of longitudinal fluctuation in experiment.

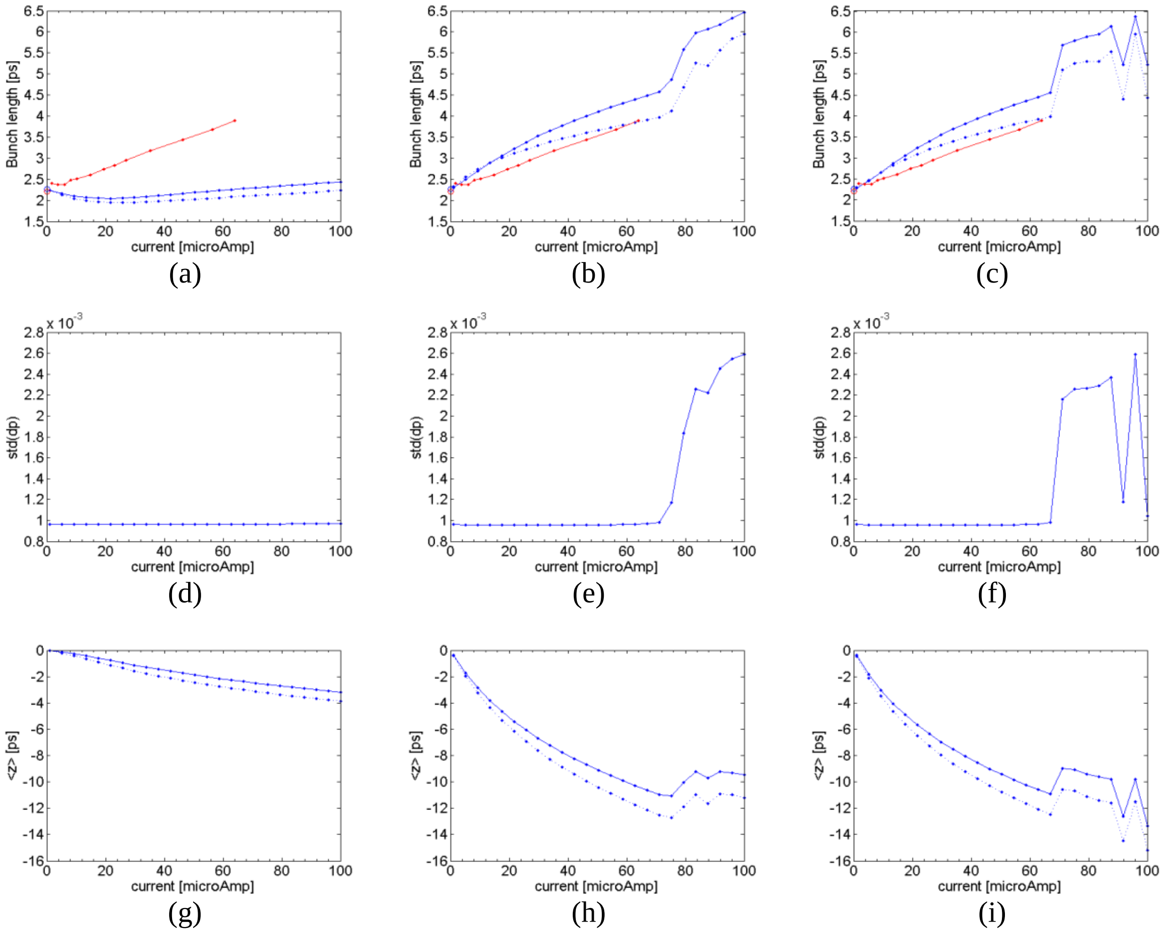

(a) (b) (c)

(d) (e) (f)

(g) (h) (i)

Figure 5.26: Comparison of bunch profiles for α_1 = -1.0 × 10^{-5} with V_{rf} = 3.4 MV. (a), (b) and (c) are plots of bunch length vs current. (d), (e) and (f) are energy spread vs current. (g), (h) and (i) are bunch centroid shifting vs current. (a), (d) and (g) are the simulations with CSR wakefield. (b), (e) and (h) are the simulations with BBR wakefield. (c), (f) and (i) are the simulations with CSR + BBR.

When the current is further increased, experimental bursting pattern exhibits that the chaotic threshold is reached at approximately 59 μA. Nevertheless, it has been revealed that the experiment was unable to be carried on after this threshold, the last achievable operating current left valuable data of the second bursting signals for this case. The second bursting pattern has been revealed that the major bursting frequencies are occurred at 1.13, 2.30, 3.48, 4.63, 5.80, 6.98, 8.15, 9.30 and 10.50 kHz which their signal amplitudes are descended with increasing frequency. The minor bursting signal series have also been disclosed at approximately half frequency between consecutive major signals with lower amplitude than the major series.

Noticeably, the major bursting signals are almost equally spaced at an average 1.1712 kHz which is unexpectedly closed to 5 times multiplication of $\frac{1}{3}$ of the synchrotron frequency. It is $\frac{5}{3}f_s$ which equals to 1.1299 kHz.

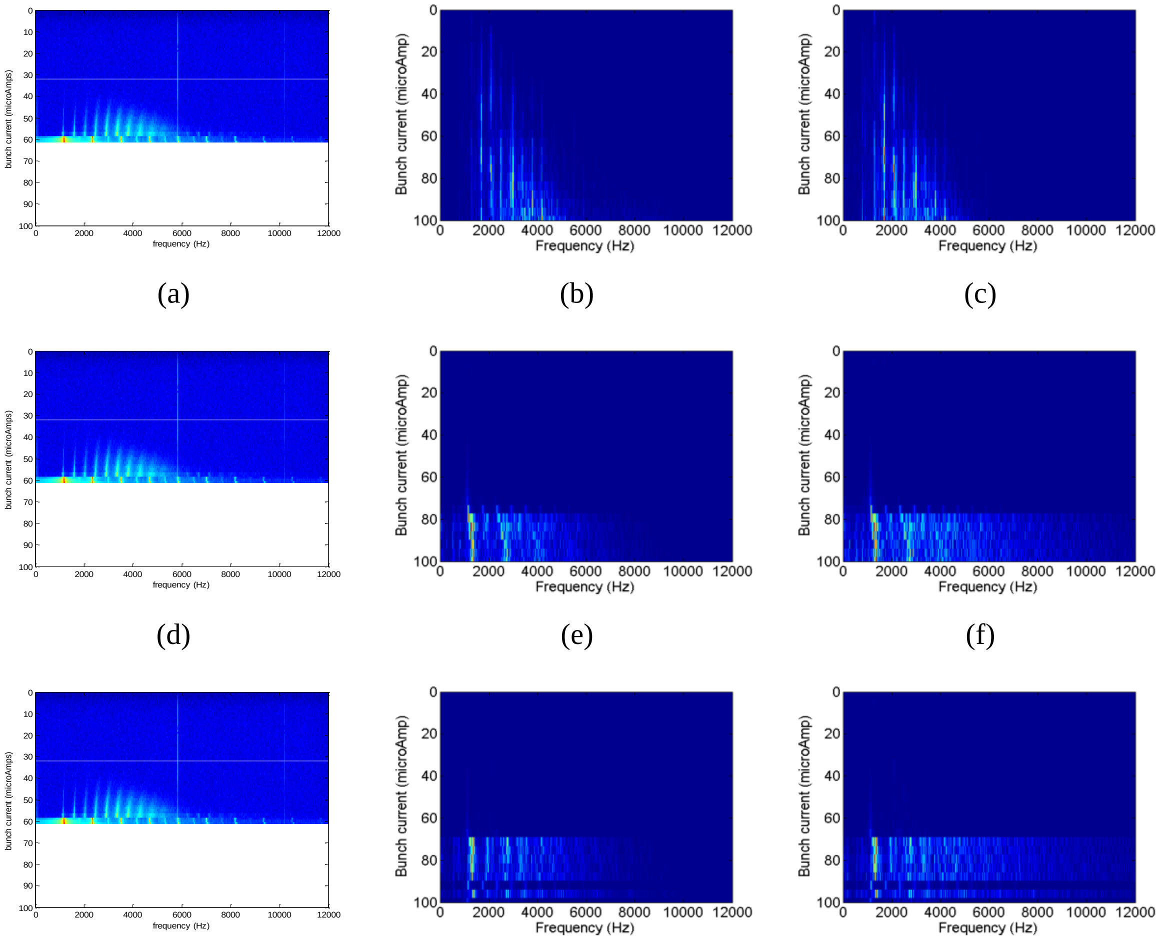

(a) (b) (c)

(d) (e) (f)

(g) (h) (i)

Figure 5.27: Comparison of radiation bursting spectrums for α_1 = -1.0 × 10^{-5} with V_{rf} = 3.4 MV. (a), (d) and (g) are experimental detected spectra. (b), (e) and (h) are simulated spectra at 60 – 90 GHz with CSR, BBR and CSR + BBR respectively. (c), (f) and (i) are simulated spectra at 75 GHz – 1.5 THz with CSR, BBR and CSR + BBR respectively.

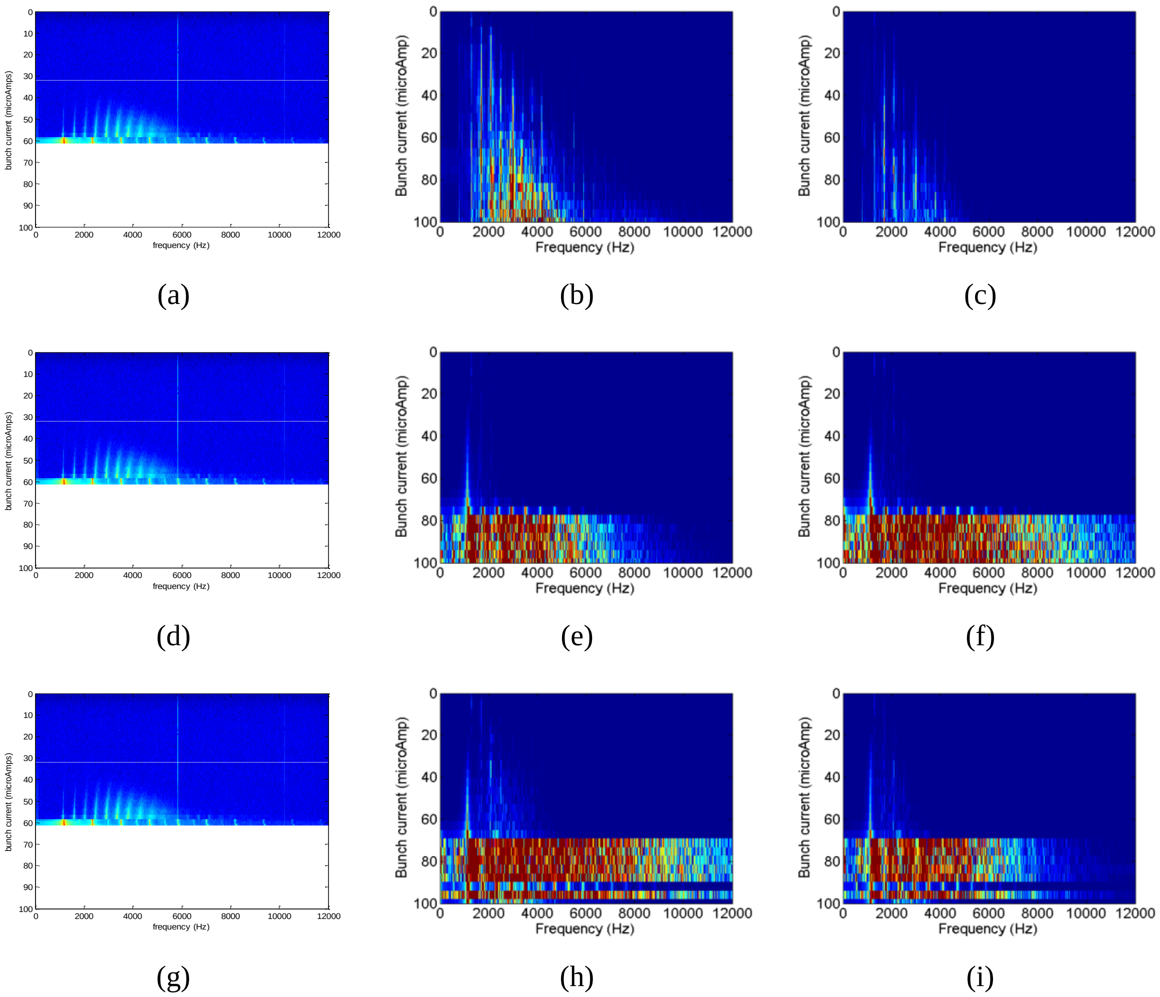

(a) (b) (c)

(d) (e) (f)

(g) (h) (i)

Figure 5.28: Comparison of radiation bursting spectrums in direct mapping scale for α_1 = -1.0 × 10^{-5} with V_{rf} = 3.4 MV. All patterns are reconstructed from figure 5.27. (a), (d) and (g) are experimental detected spectra. (b), (e) and (h) are simulated spectra at 60 – 90 GHz with CSR, BBR and CSR + BBR respectively. (c), (f) and (i) are simulated spectra at 75 GHz – 1.5 THz with CSR, BBR and CSR + BBR respectively.

Characteristic features of the CSR bursting signals induced by CSR wakefield are able to be demonstrated on the simulated pattern under CSR wakefield. Several sharp bursting signals have been clearly observable since approximately 10 μA and portrayed throughout the whole simulation. The bursting signals due to CSR wakefield are revealed at 1.25, 1.69, 2.08, 2.45, 2.95, 3.40, 3.75 and 4.20 kHz. Apparently, all these signals are comparable to the first bursting signals detected in experiment. These bursting signals are almost equally spaced at more or less than 427.78 Hz in average. This number is also very closed to the value 451.96 Hz or $\frac{2}{3}f_s$ as well as experimental result.

Simulated bursting patterns with CSR, BBR and CSR + BBR wake models have suggested interesting investigations. The radiation bursting pattern of a bunch under CSR + BBR wakefield appears to be exposed with a combination of both the patterns of CSR and BBR wakefields. The signature temporal bursting of CSR pattern is illustrated as the first bursting pattern while the broaden bursting signal due to BBR wakefield is appeared as the second pattern. This double bursting feature could be more perceivable by reproducing the bursting patterns in figure 5.27 with the direct mapping function provided in MATLAB. Figure 5.28 illustrates all the reproduced bursting patterns in direct mapping scale which obviously demonstrates the combination feature of CSR and BBR patterns on the CSR + BBR bursting diagram.

According to the direct mapped bursting pattern of CSR + BBR wakefield, it is clearly detected that the first bursting pattern occurred from 0 to approximately 67 μA is similar to the bursting pattern of CSR wakefield. The bursting signals are also revealed at the same frequencies as previously observed in the simulation with only CSR wake with an additional signal at 1.15 kHz. This implementing component is evidently contributed by the BBR wakefield and also being the strongest amplitude in the first bursting pattern. It is also noticeable that this bursting signal is slightly shifted toward lower frequency with an increasing current which is contrary to characteristic feature of the temporal CSR bursting in positive alpha. It is firstly appeared at approximately 38 μA at frequency 1.15 kHz then shifted to 1.05 kHz just before reaching to the chaotic threshold.

The second bursting pattern is unquestionably contributed by the BBR wakefield. It is revealed from 67 to 100 μA and appeared almost identical to the pattern of BBR simulation except the temporal relaxation gaps at 91.75 and 100.00 μA. Major bursting signals are emerged at 1.30, 2.75 and 4.15 kHz with descending amplitude as well as the minor signals that are occurred at half frequency between consecutive major series. These major bursting frequencies somewhat overestimate the major bursting signals revealed in experiment. As stated, the discrepancy between numerical estimations and experimental detections has been previously emphasized by many studies at several accelerator facilities. There has been suggested that the accuracy of numerical investigation can be improved by increasing the number of simulated particles.

These major bursting signals are approximately $2f_s$, $4f_s$ and $6f_s$ which indicate that the stationary distribution of the bunch evolves with linear combination of several discrete modes of oscillation where the quadrupole mode appears to be the strongest one. Moreover, the bursting signals of the second pattern are relatively much broader compared to the first bursting pattern. It suggests that the beam evolution in this region is considerably affected by the collective instability which causes significant fluctuations on the bursting sideband. These evolution elements lead to an extension of bursting signals frequency.

It was already scrutinized in the studying for α_1 = -0.6 × 10^{-5} with V_{rf} = 3.4 MV that the temporal occurrence of chaotic bursting behaviour seems to be potentially occurred at considerably high bunch current for negative alpha. In that case, the bursting pattern starts performing with the first bursting pattern which resembles to the radiation bursting due to CSR wakefield. Then the pattern proceeds into the chaotic bursting region before steps back to the first pattern again at higher current. Apparently, this phenomenon is also occurred in this study for α_1 = -1.0 × 10^{-5} with V_{rf} = 3.4 MV too.

According to the plots of beam profiles and the bursting patterns due to CSR + BBR wakefield, after the semi-stable or CSR-like bursting fashion is vanished, it has been replaced by the second pattern which exhibits another bursting signals both majority and minority series. Then, they illustrate that the bursting behaviour temporally steps down into the gap of another bursting series which is much likely to be the first pattern at 91.75 μA. Afterward, they step up to the second pattern and, finally, steps down again into the gap of the first pattern at 100.00 μA.

The bursting signals occurred at 91.75 and 100.00 μA are revealed at 1.10, 1.71, 2.30, 2.90, 3.50, 4.10, 4.68, 5.25 and 5.85 kHz which are presumable to be the bursting series of the first pattern. These frequency components are anticipated to be the first bursting series that are being shifted toward the higher frequencies with an increasing current. On the other hand, after considerately evaluating the bursting signals, they are revealed at almost equally spaced on an average of 593.75 Hz which is slightly lower than the synchrotron frequency, 677.94 Hz. This value has also been extended from 427.78 Hz which is an average spacing between successive signals of the first bursting pattern. The bunch behaviour might be influenced by more complex wake potential than at the lower current due to increasing collective effect, nevertheless sharp appearance of the bursting signals verifies that the bunch has still been consistently evolving with particular periodic constraint which resulting on the steady temporal bursting of CSR as same as occurred at lower current.

The temporal occurrence of the chaotic-harmonic evolution phenomena has incidentally made an important implication on the generation of terahertz coherent synchrotron radiation. It has been numerically evaluated that the steady temporal bursting of CSR can be occurred at higher current than it was conventionally determined. After the bunch has been proceeded into the chaotic bursting region, it would potentially be able to recover to the semi-stable state again and consistently attained in the steady temporal bursting of CSR fashion at some point in the chaotic region.

It would also be critically important to figure out the beam dynamics at each stage of radiation bursting. Figure 5.29 – 5.32 demonstrate the longitudinal beam dynamics of a bunch at 50.50, 83.50, 91.75 and 95.87 μA respectively. The bunch behaviour due to CSR, BBR and CSR + BBR wakefields are also illustrated and compared at each current.

The beam dynamic at 50.50 μA is illustrated in order to determine the bunch behaviour that causes the radiation bursting series similar to the pattern due to CSR wakefield. At current 83.50 μA, the bunch evolution is inspected for the beam dynamic behind the second bursting pattern that is exposed with more chaotic manner than the first one. Beam evolution at 91.75 μA and

95.87 μA are considerately examined because they are representatives of the temporal occurrence between first and second patterns at high current. It is important to figure out their longitudinal phase space dynamics in order to comprehend the mechanism of chaotic-harmonic beam alteration as well as the contribution of each wakefield source to such temporal behaviour.

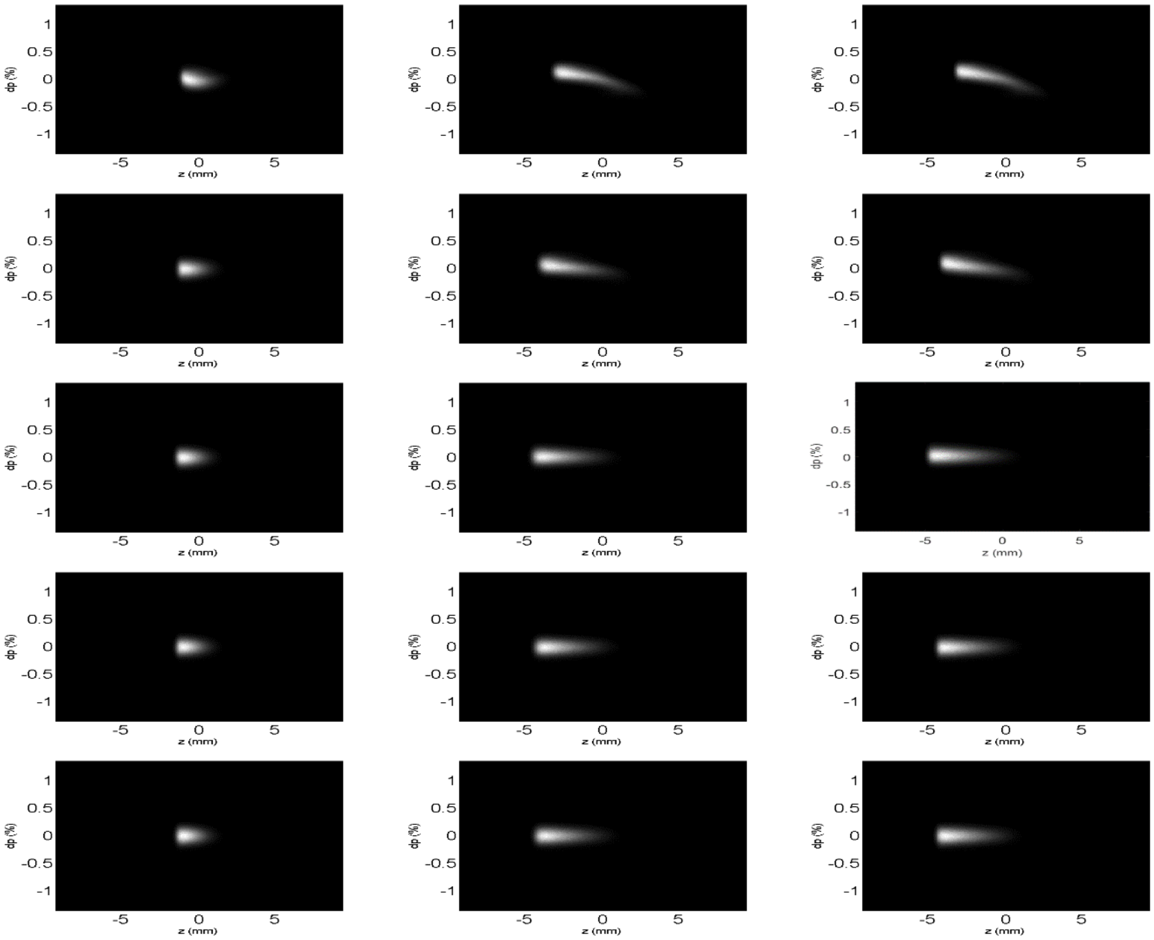

Figure 5.29: The comparison of longitudinal phase space evolutions at 50.50 μA of α_1 = -1.0 × 10^{-5} with V_{rf} = 3.4 MV under CSR(left column), BBR(middle column) and CSR + BBR(right column) wakefield captured at $1T_s$, $5T_s$, $12.5T_s$, $20T_s$ and $30T_s$. Bunch head is to the right.

Longitudinal dynamic of a bunch at 50.50 μA reveals that bunch lengthening effect due to the BBR wakefield is stronger than the CSR wakefield as well as stronger rigid bunch oscillation. At the same time, fluctuated bunch density distribution due to microbunching phenomena is obviously seen and drifting clockwise covering the whole bunch in CSR and CSR + BBR simulations while there are relatively slighter microbunches drifting around the bunch in the BBR wake simulation. The bunch behaviour under CSR + BBR wakefield turns out to be a combination between elongation and rigid-bunch oscillation effects due to BBR wake and microbunching effect induced by CSR wakefield.

The 'spur-like' local fluctuation is obviously detected again in the simulation with CSR wakefield at 83.50 μA. Strong fluctuation at the bunch tail is induced together with the microbunching phenomena drifting clockwise around the bunch. Phase space evolution under BBR wakefield also reveals that the bunch distribution is severely deformed and evolves in chaotic fashion due to an intensive complicated wake potential. However, a longitudinal sharp 'spike' of a longitudinal bunch distribution is periodically developed every half a synchrotron period. This single large spike is much likely to be responsible for the temporal CSR bursting at $2f_s$ as it was previously illustrated in figure 5.27(e) and (f).

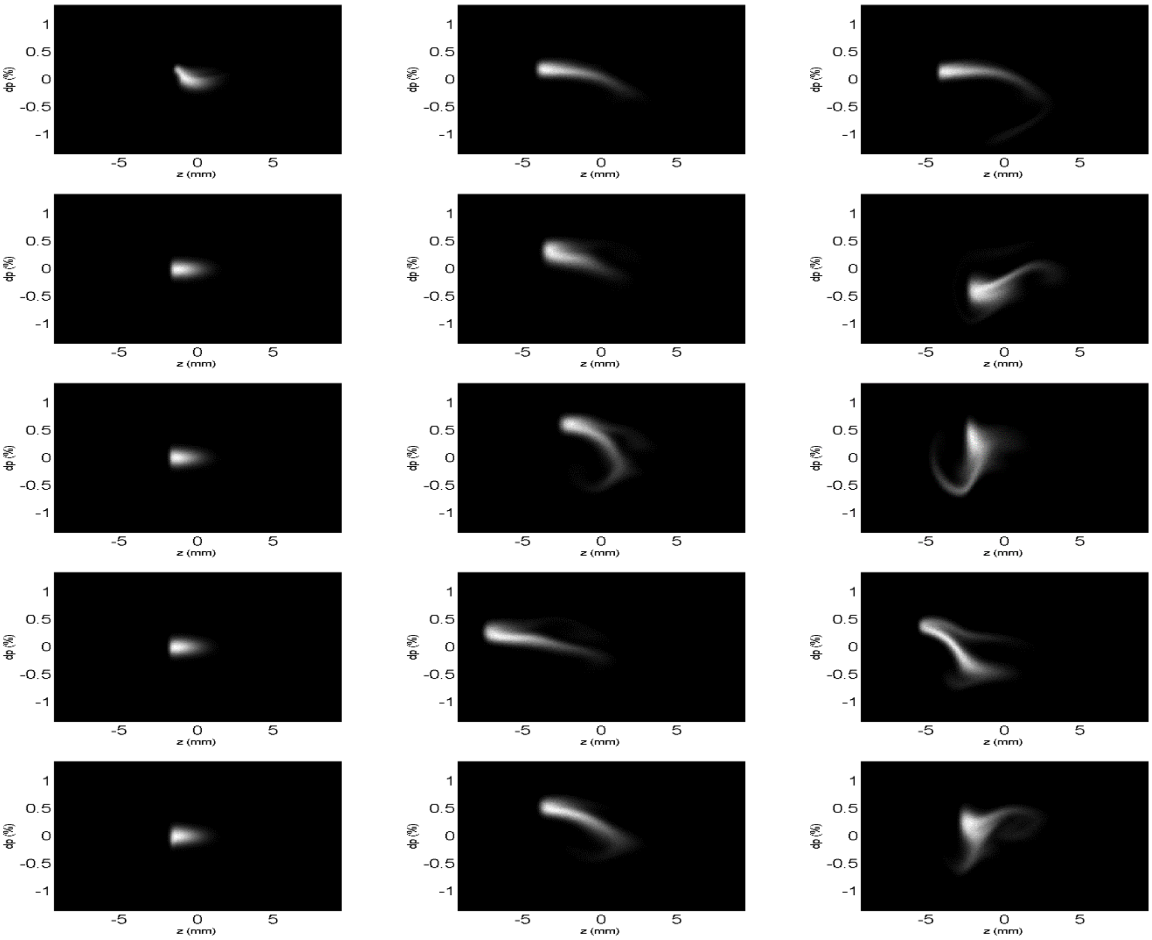

Figure 5.30: The comparison of longitudinal phase space evolutions at 83.50 μA of α_1 = -1.0 × 10^{-5} with V_{rf} = 3.4 MV under CSR(left column), BBR(middle column) and CSR + BBR(right column) wakefield capturd at $1T_s$, $5T_s$, $12.5T_s$, $20T_s$ and $30T_s$. Bunch head is to the right.

During the chaotic stage, the bunch evolution under CSR + BBR wakefield seems to follow the evolution under BBR wakefield while the CSR wake implements the stationary fluctuations on a bunch distribution. This dynamical fluctuation implemented by CSR wake, at some point, superimposes with the original large spike and subsequently evolves into an even larger sharp spike. Plot of radiation power with revolution turns in figure 5.34 obviously exhibits the resulting repetitive burst of radiation power due to periodic development of this enormous spike bunch.

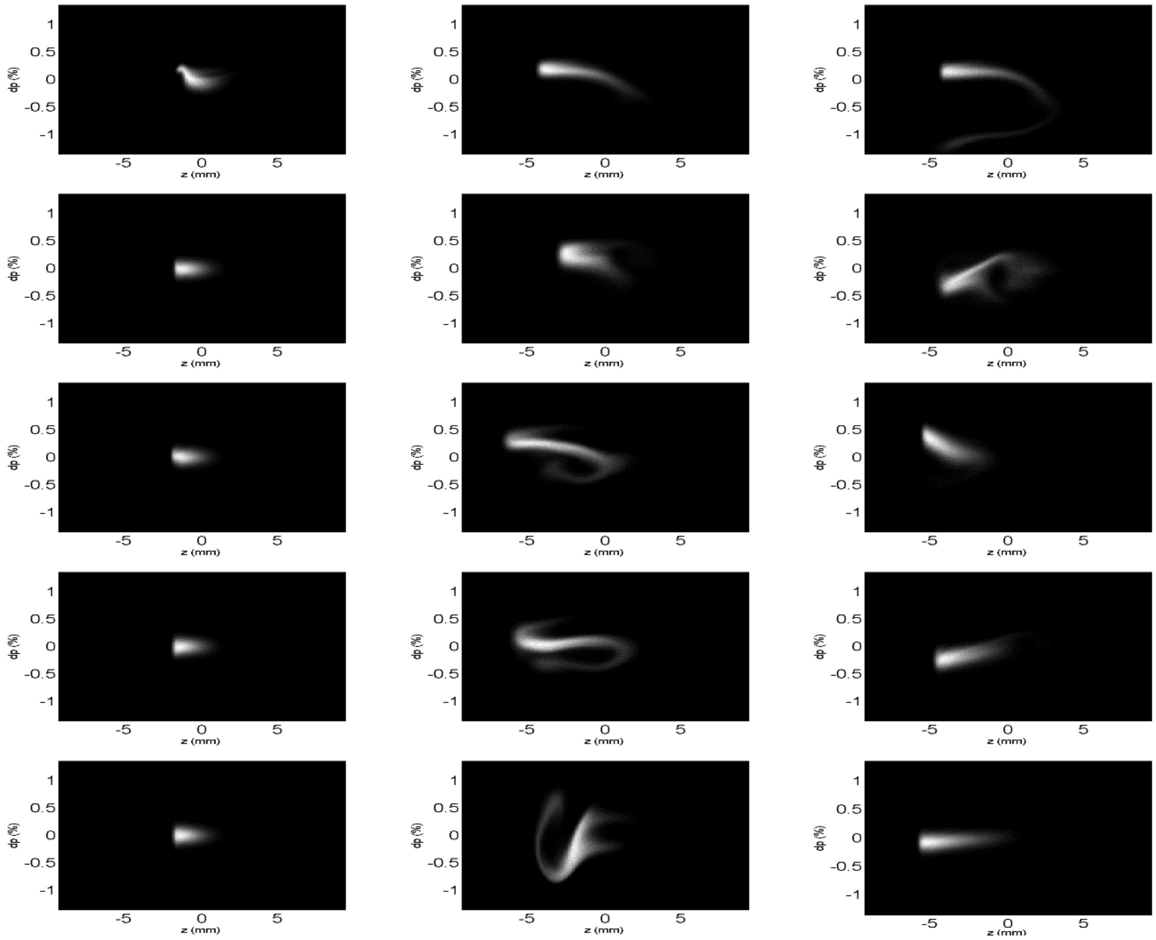

Figure 5.31: The comparison of longitudinal phase space evolutions at 91.75 μA of α_1 = -1.0 × 10^{-5} with V_{rf} = 3.4 MV under CSR(left column), BBR(middle column) and CSR + BBR(right column) wakefield captured at $1T_s$, $5T_s$, $12.5T_s$, $20T_s$ and $30T_s$. Bunch head is to the right.

When current is further increased to 91.75 μA, both the simulations with CSR and BBR wakefields exhibit their characteristic features of the bunch fluctuations in much stronger manner. The spur-like fluctuation has become larger as well as more obvious bunch density oscillation due to the microbunching effect in the simulation with CSR wakefield. In the case of BBR wake simulation, the bunch cluster is elongated and folded up according to stronger wake force, nevertheless the overall evolution is likely a rotating barred spiral galaxy. Such longitudinal dynamic is in accordance with bursting spectrum illustrated in figure 5.27(e) and (f) that exhibits several strong bursting frequencies.

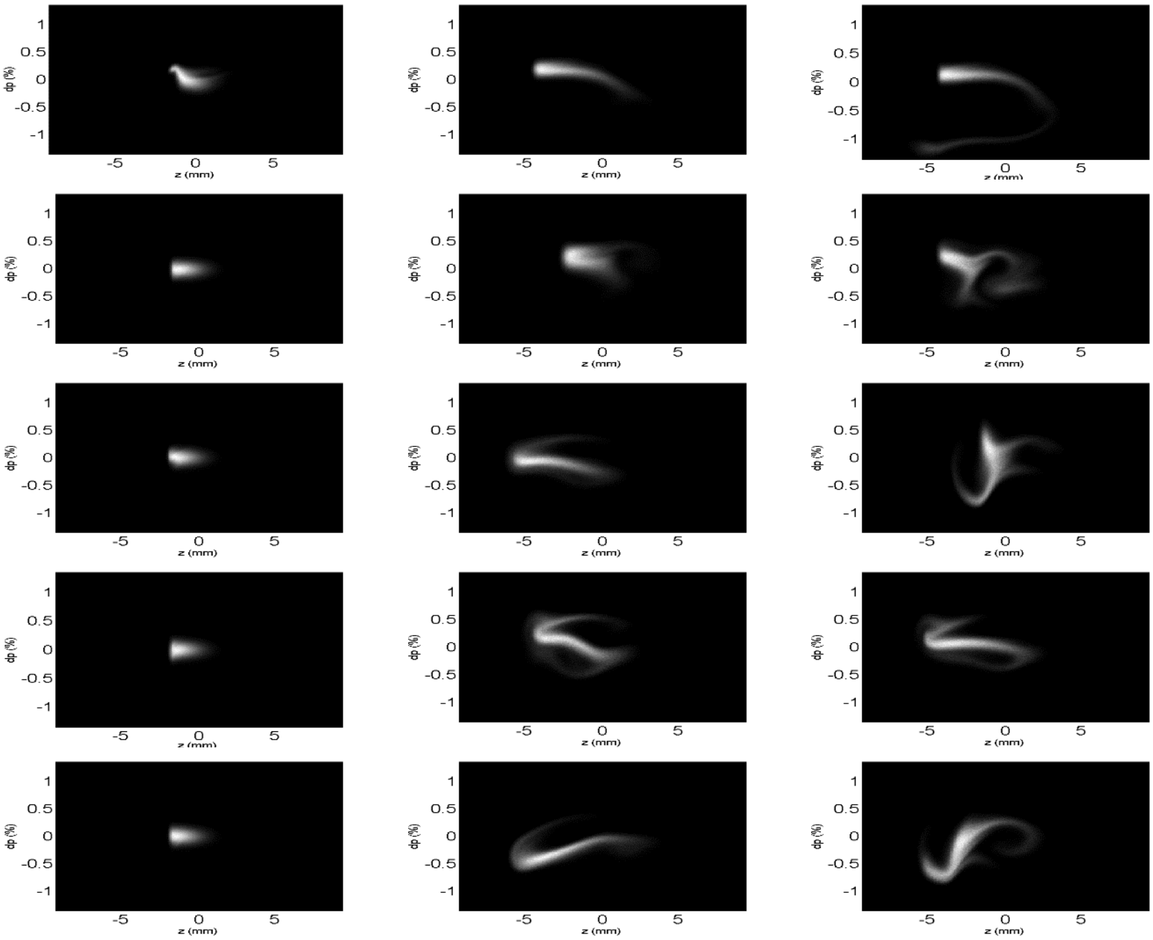

Figure 5.32: The comparison of longitudinal phase space evolutions at 95.87 μA of α_1 = -1.0 × 10^{-5} with V_{rf} = 3.4 MV under CSR(left column), BBR(middle column) and CSR + BBR(right column) wakefield captured at $1T_s$, $5T_s$, $12.5T_s$, $20T_s$ and $30T_s$. Bunch head is to the right.

At early revolution turns, the chaotic bunch fluctuation under CSR + BBR wakefield seems to be stronger while periodically exhibits the development of single spike distribution as same as occurred in the BBR wake. Until it has already been proceeded into approximately 6000 turns, the bunch happens to be confined in a distribution contour similar to that previously revealed under the CSR wakefield alone but with a longer length. Furthermore, its bulblike tail is also wavering up and down until it is damped down at approximately 25000 turns leaving the microbunches drifting around similar to a bunch under CSR wakefield.

Phenomena that the bunch is appeared to be damped down into particular confinement and recovered to its semi-stable state at the current beyond the chaotic threshold has never been experimentally revealed before. According to longitudinal dynamics of the bunch under each source of wakefield, it seems that, just before the bunch confinement, the influences of CSR and BBR wakes coincidentally result the net wake force that bounds the particle distribution within particular restraint.

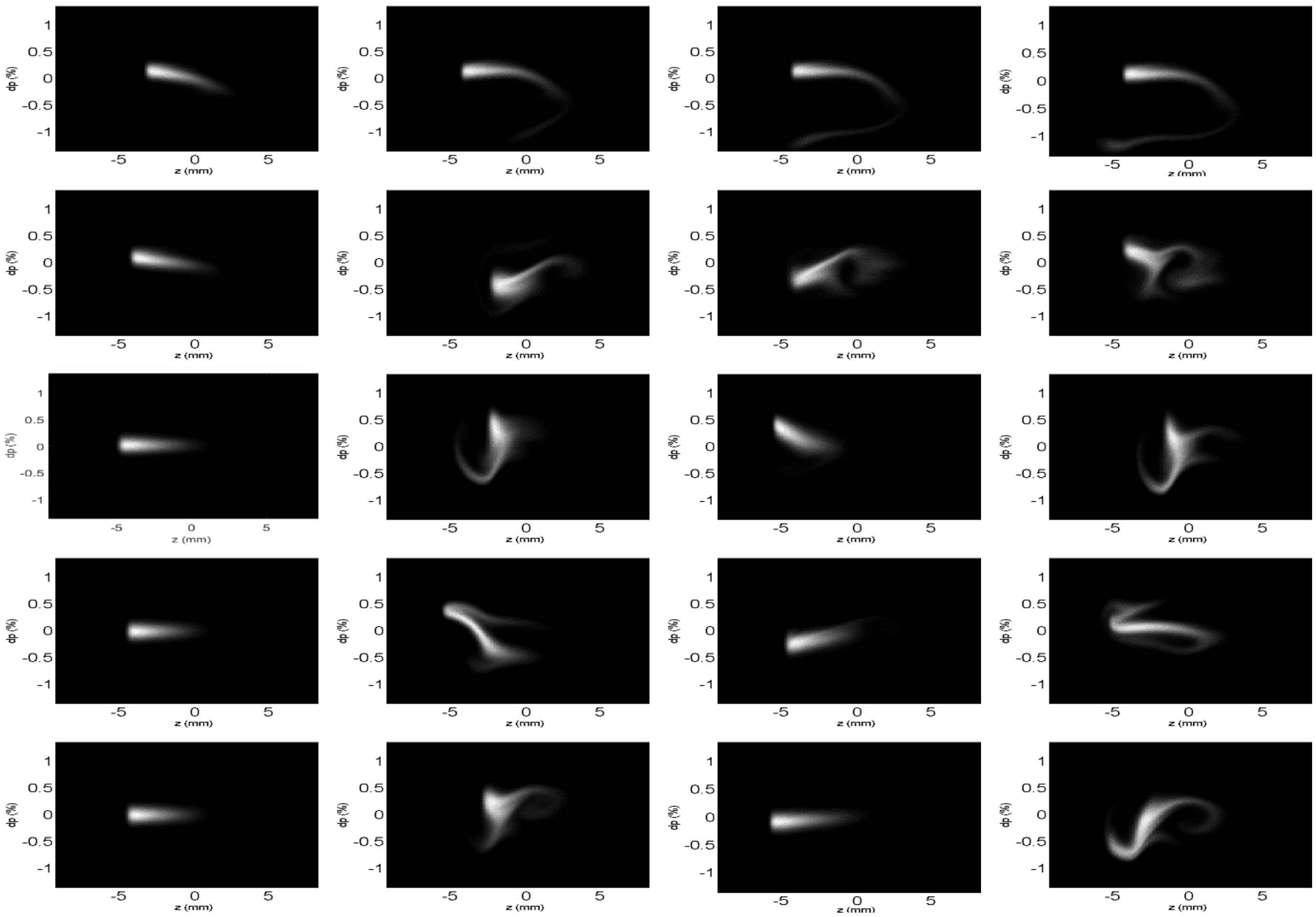

Figure 5.33: The comparison of longitudinal phase space evolutions of α_1 = -1.0 × 10^{-5} with V_{rf} = 3.4 MV under CSR + BBR wakefield at currents (left to right) 50.50, 83.50, 91.75 and 95.87 μA captured at 1T_s, 5T_s, 12.5T_s, 20T_s and 30T_s. Bunch head is to the right.

It has been learned from previous studies that at high current, the influence of CSR wakefield seems to be strong enough to compete with the effect from BBR wakefield. Consequently, more particle circulation across the bunch regulated by CSR wake results in bridging over the entire bunch formation while BBR wake effect is attempting to elongate and deform the bunch distribution in phase space. Specifically at this intensity, the microbunches which is amplified due to collective CSR wakefield appears fluctuating in accordance with the development of the barred galactic shape distribution initiated by BBR wakefield. This coincidence particularly results in a bunch constraint that subsequently confines the bunch longitudinal evolution as demonstrated in figure 5.31 (right column).

Bunch evolution happens to get back into the chaotic evolution again at 95.87 μA. Stronger spur-like fluctuation is obviously exhibited in phase space under CSR wakefield as well as the chaotic motions which are immensely illustrated in phase space under BBR and CSR + BBR wakefields. Periodic occurrence of the single large spike formation is also appeared in both the BBR and CSR + BBR cases. Furthermore, their temporal occurrence is exposed at the same frequencies as occurred at 83.50 μA. According to the plot of power radiation versus revolution turns illustrated in figure 5.34, it has been shown that the temporal bursting of CSR due to the bunch fluctuation at 95.87 μA is quite similar to the bursting behaviour at 83.50 μA.

Bunch evolution under CSR + BBR wakefield of four representatives of each bursting behaviour are demonstrated together in figure 5.33 in order to compare their development through an increasing current at the same turn number throughout the simulation range.

Comparison of the longitudinal phase space evolution in figure 5.33 obviously shows how the alternated double bursting pattern is developed at considering condition. The bunch at 50.50 μA exhibits its confined progression with microbunches that resulting on steady temporal bursting of CSR as illustrated in the first bursting pattern in figure 5.28.

At 83.50 μA, the chaotic bunch evolution is obviously depicted through sequential snapshots of phase space progression as well as its detectable periodic compressed spike development. This complex evolution consequently generates the second bursting pattern. The chaotic beam dynamic fashion has still been carried on at higher current according to the first half of the revolution at 91.75 μA. Unexpectedly, after $10T_s$ the chaotic evolution is restrained and damped down eventually converged to the semi-stable state and steadily bursts the temporal CSR emission as same as occurred in the first bursting pattern. Finally, the bunch is retrieved to the chaotic fashion like at 83.50 μA and periodically develops a large spike on a bunch distribution again at 95.87 μA. The alternating behaviour of the chaotic-harmonic bunch development is also obviously exposed through the bursting of CSR power in time domain illustrated in figure 5.34.

Numerical evaluation of the bunch under CSR + BBR wakefield brings us several remarkable implications of the beam dynamic beyond threshold. First of all, the simulated longitudinal phase space evolution has suggested that the beam dynamic at the threshold is not totally devastating. There is a particular bunch development tending to be repetitively arisen during the chaotic bunch evolution. An intense ‘single spike bunch’ has been found to be periodically developed at finite repetitive rates. Such a development might be compared to the progression of the binary bunch system during the diffusion phase where a huge steep hump of longitudinal distribution is developed. Its periodic development throughout the bunch evolution is responsible for initiation of the second bursting pattern.

Furthermore, the numerical investigation suggests that the chaotic threshold might not be the highest current that the semi-stable bunch evolution and steady CSR bursting can be generated. Beyond the chaotic threshold, there might be the gap of relaxation that allows the beam dynamic to be recovered into the semi-stable evolution and damped down into the particular confinement. Steady temporal bursting of CSR might be able to perform again at this relaxation phase with higher current than conventional estimation. Moreover, the resulting coherent radiation generated on this gap is even much more powerful than the conventional CSR bursting generated at the CSR-like evolution phase before reaching the chaotic threshold.

It might be concluded that this numerical investigation would have probably raised up the promising technique of generating high intensity coherent terahertz radiation from synchrotron based light source.

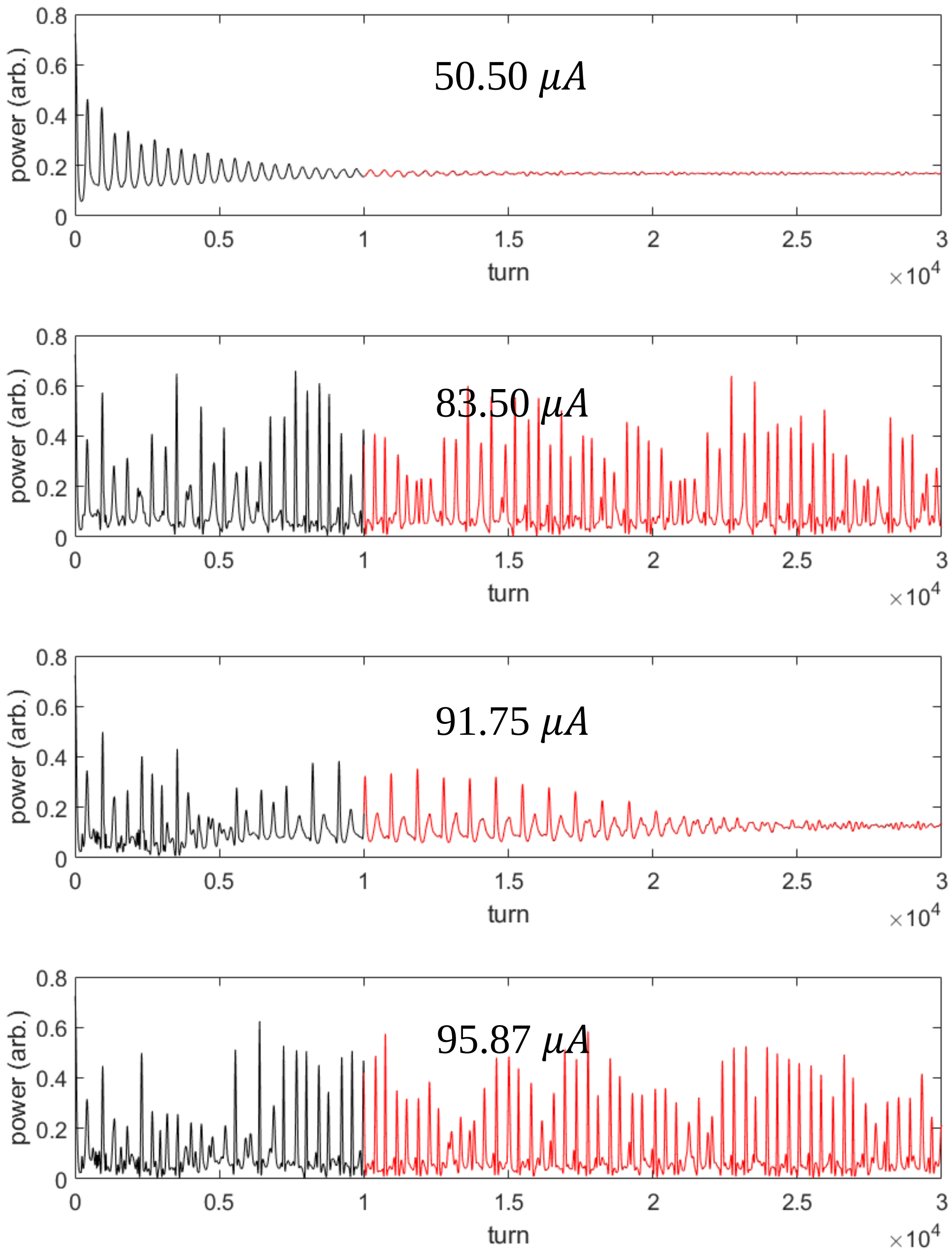

Figure 5.34: The comparison of radiation power bursting in time domain from the numerical simulation with CSR + BBR wakefield of α_1 = -1.0 × 10^{-5} with V_{rf} = 3.4 MV at 50.50, 83.50, 91.75 and 95.87 μA.

5.1.4 Summary

The comparison of simulation and experimental results in longitudinal plane demonstrates remarkable capability of sbtrack in scrutinizing the collective beam instability. The code is able to provide fairly good results on reproducing the bunch lengthening effect due to the collective wakefield as well as the resulting coherent radiation bursting.

Comparison of the beam dynamics influenced by three notable wakefields; CSR, BBR and CSR + BBR, illustrates the details of bunch development behind corresponding radiation bursting behaviour. With positive momentum compaction factor, it has been revealed that the characteristic feature of the bunch evolution in longitudinal phase space beyond the chaotic threshold is the formation of binary bunch system. Its progression plays the central role in governing the radiation bursting behaviour beyond threshold. The existence of halo-solid or solid-solid binary bunch relationship define the bursting behaviour of coherent synchrotron radiation. It also determines whether the bunch will be progressed with only the microbunching effect that constitutes the CSR-like bursting pattern or the sawtooth fashion that executes the second bursting pattern.

In addition, it has also been shown that the bunch dynamic at the conventional current threshold might not always be the total chaotic condition. Periodic development of the single large spike of longitudinal distribution is able to be occurred and resulting on the second bursting pattern. The beam dynamic at current threshold is, in fact, the semi-chaotic evolution. Nevertheless in an actual experiment, the radiated power due to periodic development of this single spike might be too intense and hazardous to accelerator structures.

Alternating occurrence of chaotic-harmonic coherent bursting behaviour has also been revealed by considering the longitudinal phase space dynamic under wakefields. In positive alpha case, the CSR bursting fashion turns out to be ‘irreversible’ progression with respect to the increasing current. When the resulting radiation bursting pattern evolves from first to second pattern, it would have never been retrieved back to the first pattern again. The longitudinal bunch dynamics seems to be permanently evolved to the eternal disordered condition due to superposition of the effects from CSR and BBR wakefields which are collectively increased with current. The CSR wakefield tends to dilute the binary bunch formation introduced by the

BBR wakefield which leads to the bunch distribution broadening and, eventually, chaotic progression in phase space.

In the other hand, negative alpha case appears to progress with ‘reversible’ alternation. The bursting fashion would be able to recover to the previous pattern again even it has already been succeeded into another pattern for ranges of current. This temporal occurrence of the bursting patterns also implies that the conventional current threshold might not be accounted as the current limitation. Because the semi-stable bursting behaviour can probably be recovered at higher current beyond the conventional threshold. The steady temporal bursting of coherent radiation appears to be able to retrieve at the relaxation current slots where the bunch is managed to be confined again.

5.2 Transverse plane

The previous section concentrates on the investigation of longitudinal beam dynamics and resulting CSR bursting behaviour under collective instabilities. The radiation bursting diagrams are brought into analysis according to the fact that this resulting CSR bursting behaviour is a consequence of stationary bunch fluctuation. However, some of the bunch oscillation modes are unable to be exposed through the resulting radiation bursting behaviour, especially the rigid-bunch oscillations that is generally vanished from the bursting spectrum. The consideration of beam dynamics in transverse plane has been brought into analysis to implement this deficiency of the investigation in longitudinal plane.

In general, the transverse beam dynamic is basically related to the longitudinal evolution through the dispersion function which is normally an integral function of longitudinal displacement along the ideal beam trajectory around storage ring. Sbtrack is also able to calculate the transverse bunch motion by handling a set of skew parameters including dispersion function. However, sbtrack is originally developed to be exploited as the numerical tracking tool with turn-by-turn method, the skew parameters including the dispersion function are accordingly reduced into an average form over a revolution turn.

This thesis has been targeting on the investigation of unstable bunch evolution due to the collective effects and its resulting CSR bursting behaviour which are fundamentally depended on the beam dynamics in longitudinal plane. The investigation on the longitudinal plane in section 5.1 suggested that the bunch evolutions at considering conditions are sufficient to be able to exhibit significant dynamical evolution due to collective instability. Moreover, there have been shown that such instability mechanisms are normally developed within fractions of synchrotron period which is in the order of thousand revolution turns for all cases. Therefore, the turn-by-turn averaged skew parameters might also be adequate to provide sensible numerical results in transverse beam dynamics study as well.

The bursting of CSR in terahertz frequency range is governed by the progression of stationary longitudinal distribution of a bunch. Fluctuations on the bunch distribution due to collective effect consequently causes the variations on the CSR bursting behaviour. However, the bunch oscillation in dipole mode $(m = 1)$, rigid-bunch oscillation, where the whole bunch consistently oscillates around the synchronous phase is unable to be extracted through the bursting behaviour of CSR. In contrast, both the dipole mode oscillation and the fluctuations developed on the stationary longitudinal distribution are able to be revealed on the transverse oscillation dynamic [5]. Consequently, the consideration of a bunch motion in transverse plane, particularly, horizontal plane is necessary for evaluating and extracting the effect of collective instabilities on the bunch deformation mechanism behind the CSR bursting behaviour.

The low alpha experiment was conducted at Diamond Light Source as the proposed scheme for steady CSR generation. Experimental results are brought into comparison with the numerical study. Sbtrack is, in general, capable to track the motion of single bunch in both longitudinal and transverse planes simultaneously. This section will investigate how the longitudinal collective instabilities effect the beam behaviour in horizontal plane.

The beam parameters and experimental results [84] are concluded in table 5.2 and figure 5.35. There is only an experiment with parameters α_1 = -1.0 × 10^{-5} and V_{rf} = 3.4 MV performed at bunch current 50 μA being brought into comparison here.

Some of simulation conditions are modified from the previous study in longitudinal plane in order to improve the resolution of Fourier components. It was run with 100,000 revolution turns where the last 80,000 turns were processed. The turn-by-turn horizontal motion of electron bunch was tracked and analysed with the Fast Fourier Transformation (FFT) in order to extract the horizontal oscillation frequencies. Then the resulting Fourier components diagram will be brought into comparison with the corresponding CSR bursting spectrum as well as an experimental result illustrated in figure 5.35(top). A correlation between horizontal oscillations and coherent radiation bursting frequencies will be figured out.

Parameter	Mode 1 (I06)
$\boldsymbol{\alpha_1}$	-1 × 10^{-5}
Number of bunches	400 + 1
Bunch current	50 μA (93 pC)
Lifetime	Typ. 20h
Injection efficiency (IDs open)	Typ. 30 - 40%
$\boldsymbol{V_{rf}}$	3.4 MV
Microbunching instability threshold (SB)	~30 - 35 μA
Bursting threshold (SB)	~55 - 60 μA

Table 5.2: Experimental parameters and results summary. (Courtesy: I.P.S. Martin)

The numerical results were collected in turn-by-turn averaged format which means that the post-processing files contain the data of average bunch horizontal position ($\bar{x}$) and average horizontal momentum deviation ($\overline{x_p}$) of each revolution turn. Then, the turn-by-turn average horizontal position is brought into analysis to evaluate the oscillation frequency components which is corresponded to the rigid-bunch oscillations and the stationary bunch fluctuations.

According to table 5.2, it can be expected that the microbunching effect would has already been induced since 30 - 35 μA. However, the bursting of CSR has yet to be developed either. Of these, the measured horizontal oscillation frequencies illustrated on the top diagram of figure 5.35 demonstrates several sharp spectral lines corresponding to the CSR frequencies produced by microbunching effect.

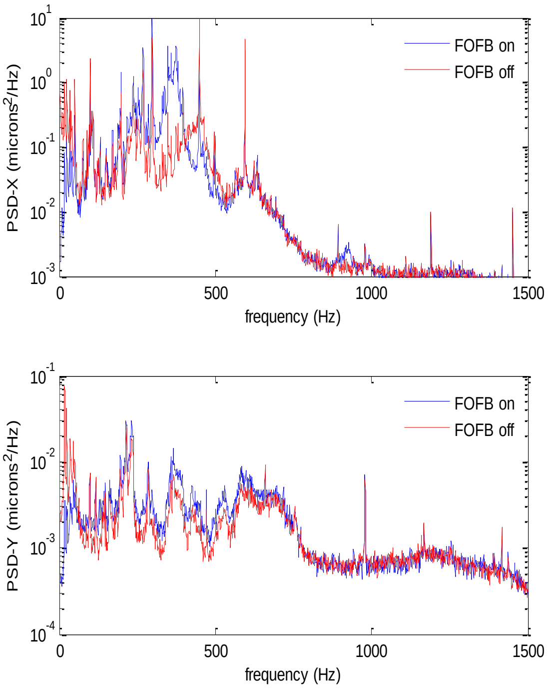

Figure 5.35: Plots of the transverse motion frequencies of α_1 = -1.0 × 10^{-5} with V_{rf} = 3.4 MV at 50 μA with feedback on (blue) and off (red). Top: the horizontal plane. Bottom: the vertical plane. (Courtesy: I.P.S. Martin)

The CSR + BBR wakefield is taken into numerical consideration in this case. Average bunch horizontal positions ($\bar{x}$) and average horizontal momentum deviations ($\overline{x_p}$) of turn number 20,001 - 100,000 are plotted in phase diagram in figure 5.36(top). As well as the turn-by-turn average bunch horizontal position which are also plotted with turn number in figure 5.36(bottom).

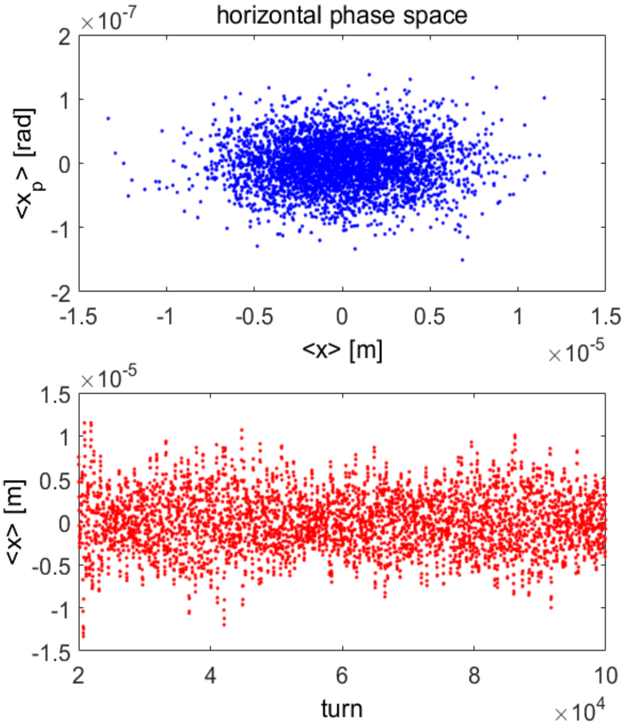

Figure 5.36: Horizontal phase space is plotted on the top diagram. Each blue dot refers to the average horizontal coordinate ($\bar{x}$, $\overline{x_p}$) of each turn. A plot of average horizontal position ($\bar{x}$) of each turn with turn number is shown on the bottom. It represents the rigid-bunch oscillation with respect to an ideal horizontal trajectory.

Comparison of the horizontal oscillations and the CSR bursting frequencies in figure 5.37 and 5.38 obviously shows that the frequencies higher than 5 kHz are seemingly vanished from the CSR bursting plot. It might imply that most of the bunch fluctuations at higher than 5 kHz are mostly the rigid-bunch oscillations while the stationary longitudinal distribution has no significant fluctuation at these frequency range.

The comparison within 0 – 1.5 kHz frequency range in figure 5.39 illustrates that there is no frequency component more or less than the synchrotron frequency, 0.678 kHz, appeared in the CSR bursting pattern. At the same time, there is a couple of frequency components revealed in the horizontal oscillations at 0.654 and 0.701 kHz. The amplitude of 0.654 kHz is higher than the other one. Furthermore, it just slightly underestimates the synchrotron frequency.

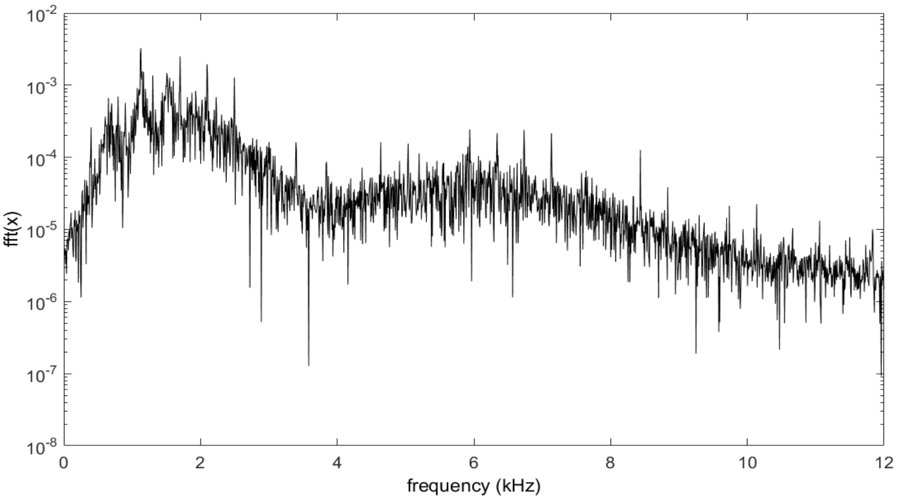

Figure 5.37: The FFT of the horizontal bunch position in log scale.

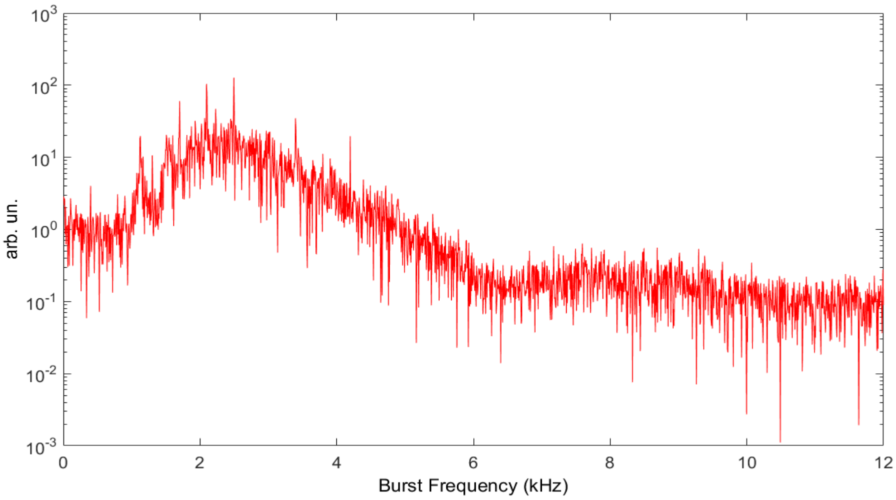

Figure 5.38: The simulated CSR bursting pattern detected with frequency range 60 – 90 GHz at 50 μA.

In term of comparison with experiment, it is observable that most of the frequency components on the plot of horizontal oscillations are able to be coupled with experimental detected peaks. Small peaks at 0.107, 0.167, 0.274, 0.307 and 0.337 kHz, a dominated peak at 0.400 kHz, a peak near the synchrotron frequency at 0.654 kHz and the twin peaks at 0.794 and 0.901 kHz are revealed and able to be matched with the detected frequencies. However, all these simulated frequency components slightly overestimate the detected peaks from experiment.

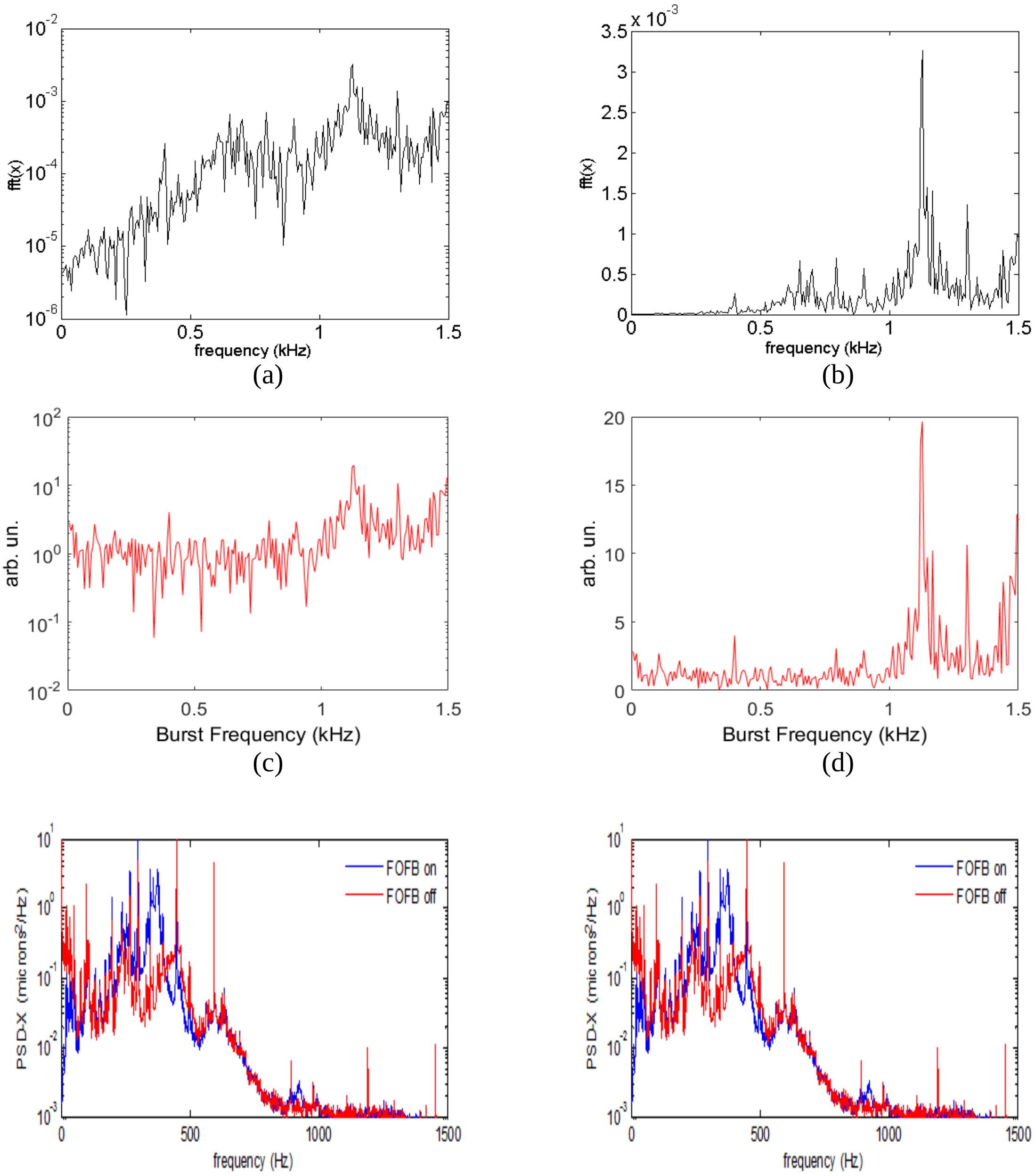

(a) (b)

(c) (d)

(e) (f)

Figure 5.39: Comparison of horizontal oscillations and CSR bursting frequencies with the experimental result. The numerical result of horizontal oscillation frequencies in log scale (a) and linear scale (b). The simulated coherent bursting frequencies detected with frequency range 60 – 90 GHz at 50 μA in log scale (c) and linear scale (d). The experimental result of horizontal oscillation frequencies in log scale (e), (f).

The investigation of collective instability in horizontal plane has demonstrated that it would be able to implement beam dynamics investigation in longitudinal plane. Specifically, the rigid-bunch oscillation mode that is normally vanished from the CSR bursting frequency pattern.

Interestingly, the numerical revelation of microbunching components slightly overestimates the experimental result. This outcome is in agreement with the revelation on longitudinal plane. The numerical CSR bursting pattern before the chaotic threshold exhibited that the series of microbunching signal slightly overestimates the experiment.

The bunch evolution in longitudinal phase space demonstrates that there is not only the stationary bunch fluctuation induced by the collective effect but the whole bunch also oscillates longitudinally. The evaluation of horizontal oscillation frequencies has shown that it could be brought into beam dynamic analysis in order to investigate all possible oscillation mode of the bunch. Due to this crucial advantage, this method would subsequently be brought into the investigation of beam behaviour during the transition of bursting schemes in order to scrutinize any significant alterations of stationary fluctuation and rigid-bunch oscillation that might be arisen.

5.3 Unstable state transition

The investigation of collective beam instability in section 5.1 demonstrates rich phenomenology of longitudinal beam dynamic and resulting CSR bursting behaviour influenced by the wakefields. Especially the revelations of the bunch evolution and bursting behaviour of CSR at each stage of bursting scheme. It has been shown that the bursting behaviour is significantly deviated and can be altered to another dynamic fashion within miniscule increment of bunch current.

The background longitudinal beam dynamics near the current threshold investigated in section 5.1 indicates that, in positive alpha, the alteration of binary bunch formation in longitudinal phase space plays the critical role in governing the CSR bursting behaviour while in negative alpha, the initiations of the localized fluctuation and periodic development of a large spiky single bunch are responsible for the bursting signal series. Moreover, section 5.2 has also implemented an analysis on horizontal fluctuations by investigating the oscillation frequency components which is apparently able to reveal both the fluctuations of stationary distribution and the oscillations of rigid-bunch. Thus, the frequency analysis on horizontal fluctuations of a bunch during the transition of unstable regimes will be carried out in this section to investigate the beam dynamics phenomenology on both the fluctuations of stationary distribution and the oscillations of the rigid-bunch due to collective effects.

It has been evidently shown that the studying case with α_1 = -1.0 × 10^{-5} at V_{rf} = 3.4 MV exhibits the most interesting phenomena on the transition between unstable states. Figure 5.27, 5.33 and 5.34 demonstrate that the CSR bursting pattern is abruptly changed from CSR-like or 'semi-stable bursting' to the 'semi-chaotic bursting' dynamical form within only one current step increment. Furthermore, its temporal occurrence of chaotic pattern or the 'chaotic-harmonic alternation' might indicates a potential approach on the novel technique of high intensity THz CSR generation in synchrotron storage ring. This studying case is, accordingly, concentrated in this section to scrutinize its dynamical fluctuations at the transition region.

The comparison of horizontal beam dynamics before and after the chaotic threshold is firstly surveyed. The turn-by-turn average bunch horizontal position ($\bar{x}$) and average horizontal momentum deviations ($\overline{x_p}$) corresponding to each dynamical stage are illustrated and compared. Bunch currents 50.50 and 83.50 μA are representatives of the 'CSR-like' and the 'semi-chaotic' bursting fashions respectively according to an obvious illustration of the double bursting pattern in figure 5.27.

Additionally, in order to comprehend the mechanism of beam instability that generally limits the performance of accelerators, the operating parameters α_1 = 1.0 × 10^{-5} with V_{rf} = 3.4 MV is also considered because it is also a potential parameter that might be used in low alpha operation mode at Diamond Light Source. Furthermore, it also acquires the same momentum compaction factor with opposite sign to the previous case that is being concentrated. Bunch currents 21.62 and 50.50 μA are the representatives of the ‘steady temporal CSR’ and the ‘chaotic’ bursting fashions respectively according to the illustration of bursting patterns in figure 5.15.

Finally, the last sub-section will inspect the oscillation frequencies during transition between unstable regimes by magnifying the current steps at the transitional region. The bunch currents ranging from 62.27 to 76.78 μA for negative alpha case and 25.18 to 39.69 μA for positive one are redistributed into 10 steps in order to minimize the current step size to be able to observe any significant changes on the oscillation spectrums that would be developed during the transition of instability regimes.

5.3.1 Survey of horizontal oscillation before and after the chaotic threshold

Section 5.1.3.2 and 5.1.3.3 have previously shown that the overall longitudinal phase space dynamics and the resulting bursting behaviour influenced by the CSR + BBR wakefield are similar to the beam dynamics under the BBR wake model. However, they have also indicated that incorporating CSR wakefield to the model results on intensifying the particle exchanging between binary bunches in positive alpha as well as enhancing chaotic behaviour to the bunch evolution in negative alpha due to the local microbunching. In contrast, it has also been apparently demonstrated that the cooperated CSR + BBR model is able to induce the temporal relaxation gaps at high current beyond the conventional threshold in negative alpha. During this relaxation phase, the semi-stable temporal CSR bursting regime happens to be restored again.

This sub-section will briefly investigate the horizontal oscillation frequencies at semi-stable and semi-chaotic stages in order to figure out the detailed difference of signal series according to beam behaviour before and after the chaotic threshold.

5.3.1.1 α_1 = 1.0 × 10^{-5} and V_{rf} = 3.4 MV

In section 5.1.3.2, the bunch progression in phase space under BBR wakefield apparently illustrates the systematic development of binary bunch system which is gradually progressed from the halo-solid arrangement near the chaotic threshold to the solid-solid binary formation just beyond the threshold. Concurrently, particle density within the system seems to be more concentrated at the solid sub-bunch before the threshold then increasingly diffused to fill up the halo sub-bunch when the current is increased.

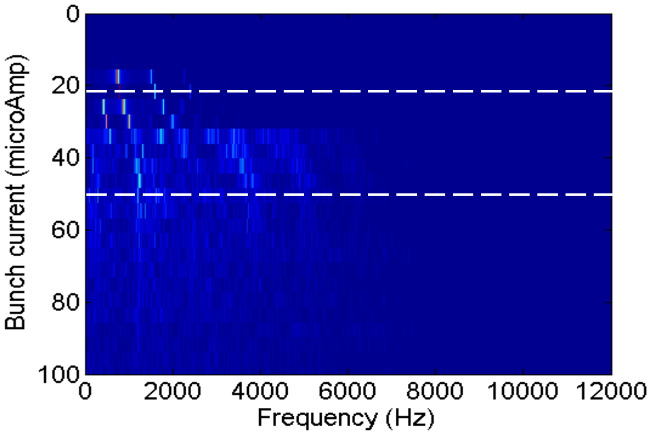

Figure 5.40: Radiation bursting pattern of the simulation with CSR + BBR wakefield in detecting range 60 – 90 GHz.

Contrary to the evolution under CSR + BBR wakefield, during the first bursting pattern, instead of settling with the halo-solid binary bunch system as happened in the simulation with BBR wakefield, the bunch distribution in longitudinal phase space evolves in a confined 'barred-spiral-galactic' packet. This kind of dynamic formation leads to enormous bursting of CSR because of its continuous immense migration of particle between two ends of the packet and an accumulation of particle at the head which appears similarly to a mini-bunch developed on top of the whole bunch.

Consequently, strong radiation bursting is yielded according to this characteristic formation which is exposed on the plot of CSR bursting frequencies illustrated in figure 5.42. Six successive bursting frequencies are obviously revealed at 0.8008, 1.602, 2.402, 3.203, 4.004 and 4.831 kHz which almost equally spaced at averaged of 0.806 kHz.

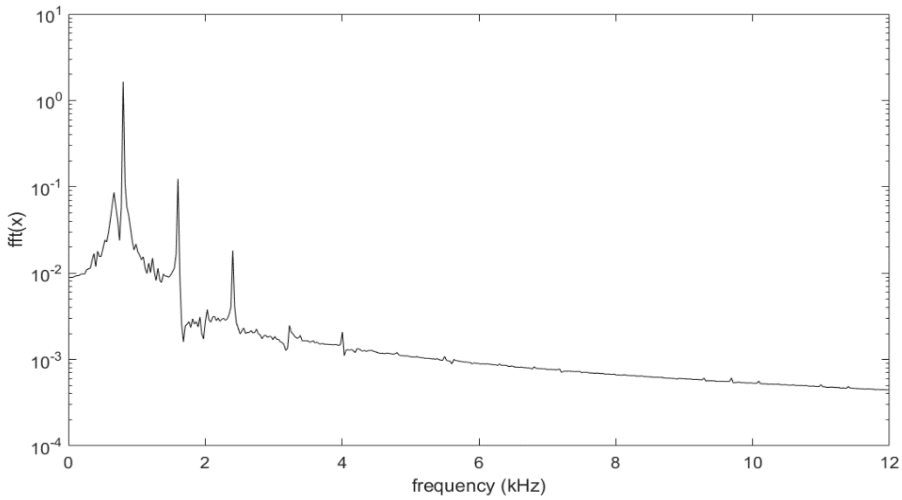

Figure 5.41: The horizontal oscillation frequencies due to CSR + BBR wakefield at 21.62 μA.

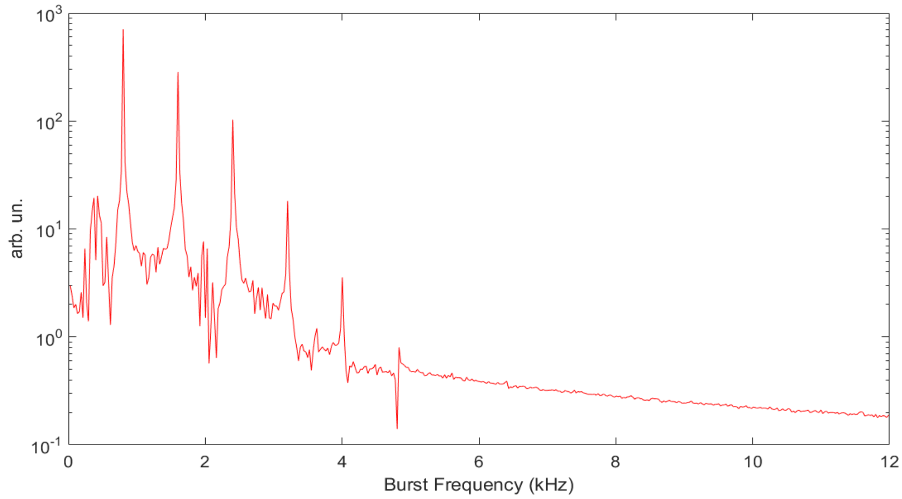

Figure 5.42: The CSR bursting frequencies due to CSR + BBR wakefield detected within frequency range 60 – 90 GHz at 21.62 μA.

Strong horizontal oscillation frequencies are also revealed in accordance with the CSR bursting spectrum. Figure 5.41 illustrates the oscillation frequencies at 0.8008, 1.602, 2.402, 3.230 and 4.004 kHz with an additional frequency at 0.6673 kHz which represents the dipole mode oscillation of the bunch at approximately the synchrotron frequency. The oscillation series are almost all matched to the bursting spectrum in figure 5.42.

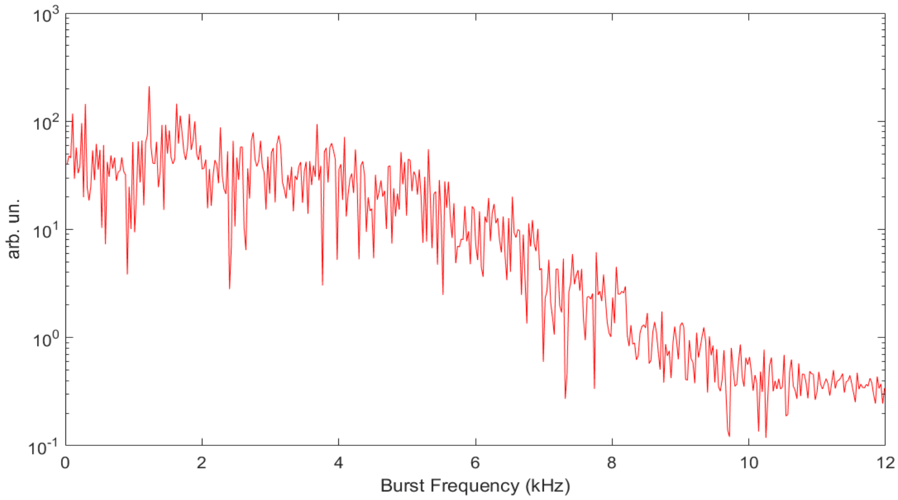

Figure 5.43: The CSR bursting frequencies due to CSR + BBR wakefield detected within frequency range 60 – 90 GHz at 50.50 μA.

On the second bursting scheme, although the CSR bursting spectrum appears to be diluted with other scattered peaks, there are some bursting peaks inspected from the plot in figure 5.43. Bursting elements at 1.228, 1.628, 2.749, 3.684 and 4.911 kHz are observable on the plot. They are arranged with equal spacing at averaged 1.094 kHz.

In term of horizontal oscillation at 50.50 μA, it turned out that the simulation was unable to collect the turn-by-turn average position and momentum deviation at this current due to many of particles were scattered out of the simulation window. The data was declared with a definition 'NaN' or 'not a number' by MATLAB and unable to be brought into further calculation. Nevertheless, this numerical result affirms that there is substantial chaotic evolution at 50.50 μA under the CSR + BBR wakefield.

5.3.1.2 α_1 = -1.0 × 10^{-5} and V_{rf} = 3.4 MV

Section 5.1.3.3 has obviously shown that the complete option of wakefield, CSR + BBR, apparently enhances more complicated fluctuations on the longitudinal phase space evolution. It notices that while the bunch evolution before the chaotic threshold is consistently evolved in confined progression and behaves much alike the bunch evolution influenced by the CSR wakefield alone; ‘CSR-like’ or ‘semi-stable’ phase, the bunch beyond the chaotic threshold is advanced with more chaotic manner but has still exhibited an indication of ‘systematic evolution’ which repetitively occurred with finite frequencies; ‘single-spiky-bunch’ phase. Phase space evolution of a bunch under CSR + BBR wakefield also suggested that while the bunch behaviour before the chaotic threshold seems to be governed by the CSR wakefield, the bunch beyond the threshold is more likely to be governed by the BBR wakefield.

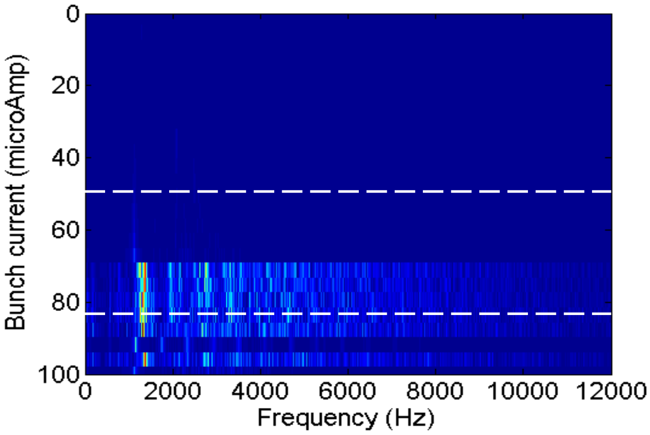

Figure 5.44: Radiation bursting pattern of the simulation with CSR + BBR wakefield in detecting range 60 – 90 GHz.

The oscillation frequencies of 50.50 and 83.50 μA are extracted and plotted in figure 5.45 and 5.47 respectively and compared with the CSR bursting frequencies illustrated in figure 5.46 and 5.48.

The replacement of oscillation frequencies of initial fluctuation regime at 50.50 μA by several minor components when the current is increased to 83.50 μA has been shown. At 50.50 μA, two dominated frequencies are 0.6673 and 1.121 kHz where the higher frequency component is revealed with stronger amplitude than the lower frequency one. The couple are then replaced by two groups of minor components at 83.50 μA. There are 0.694, 0.7741 and 0.8275 kHz which replace the component 0.6673 kHz and 1.281, 1.335 and 1.415 kHz which replace the element 1.121 kHz.

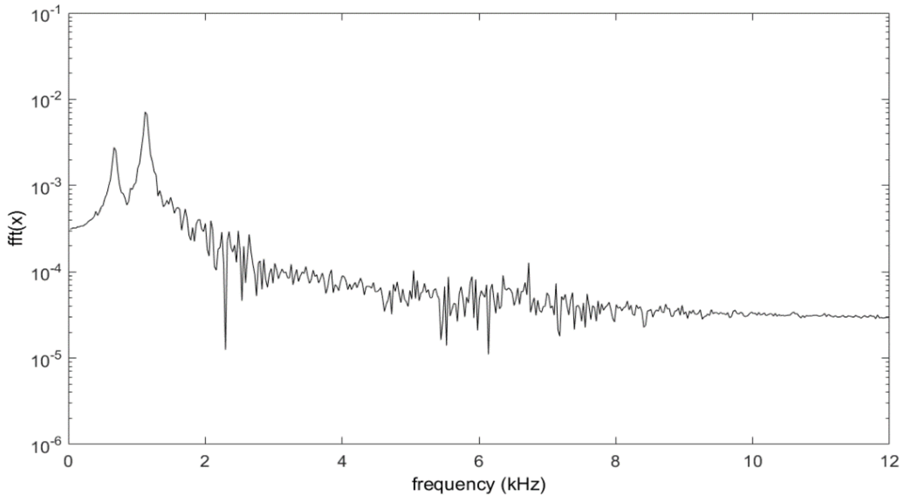

Figure 5.45: The horizontal oscillation frequencies due to CSR + BBR wakefield at 50.50 μA.

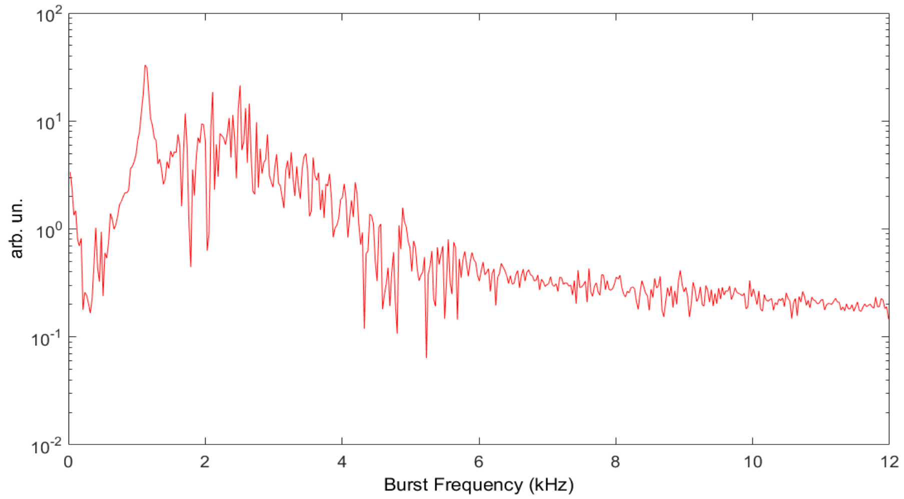

Figure 5.46: The CSR bursting frequencies due to CSR + BBR wakefield detected within frequency range 60 – 90 GHz at 50.50 μA.

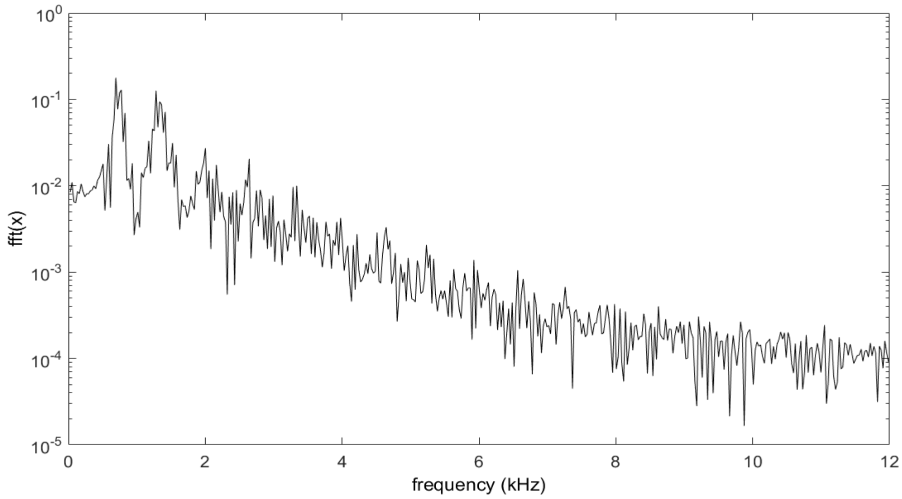

Figure 5.47: The horizontal oscillation frequencies due to CSR + BBR wakefield at 83.50 μA.

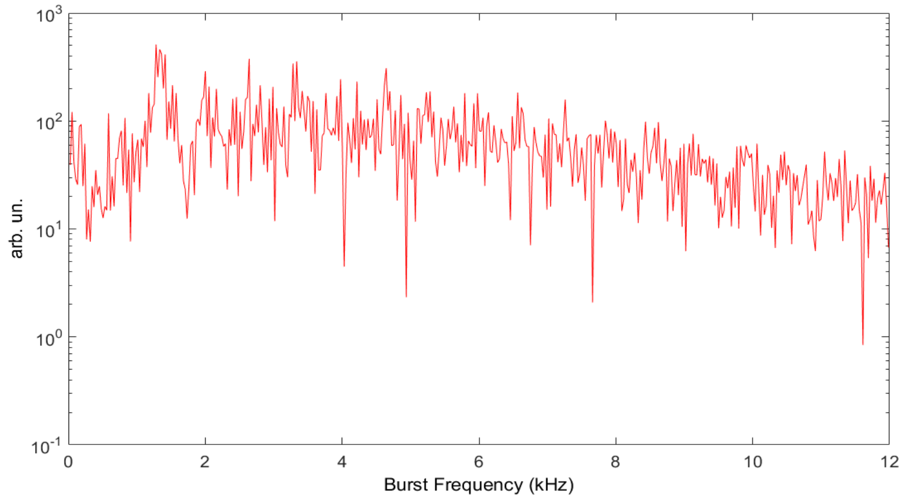

Figure 5.48: The CSR bursting frequencies due to CSR + BBR wakefield detected within frequency range 60 – 90 GHz at 83.50 μA.

The comparison of horizontal oscillations between before and after the chaotic threshold also exhibits that the lower amplitude dominating components in 50.50 μA becomes stronger than the higher one when proceeded to 83.50 μA. It is also noticeable that, at 83.50 μA, the extracted horizontal oscillations illustrated in figure 5.47 suggests that the oscillation components become obvious and are arranged in equal spacing series.

The CSR bursting frequencies at 83.50 μA are also exposed at frequency series in agreement with the horizontal oscillation frequencies. They are almost all matched with the pattern of horizontal oscillation frequencies except the peak within the vicinity of synchrotron frequency.

5.3.2 Enlargement of unstable state transition

Both of the studying cases with α_1 = ±1.0 × 10^{-5}, will be scrutinized with a 'magnified' version of simulation with CSR + BBR wakefield in order to deliberately evaluate the bunch fluctuation frequency and its corresponding bursting spectra during the transition of beam instability regime. The magnified simulations were performed with smaller current separation than all previous investigations in this chapter. The temporal occurrence of chaotic longitudinal dynamics and THz CSR bursting are also revealed according to finer results of colour map generated from this magnifying simulation.

Section 5.1.3 demonstrates the background longitudinal phase space evolutions at each stage of bursting schemes. It has been revealed that at both α_1 = ±1.0 × 10^{-5}, the bunch distribution in longitudinal phase space are arranged in their characteristic confined packet during the first bursting pattern. For positive alpha, the bunch is confined in a 'barred-spiral-galactic' evolution packet while it is restrained in a 'CSR-like' dynamical packet in negative alpha.

After entering to the second bursting scheme, in positive alpha, the bunch is transformed to the rotating binary-star-liked system that orbit around each other while in negative alpha, it advances to more chaotic fashion where the filamentation is developed, extensively stretched, folded up and rotated around the phasal area, nevertheless the systematic formation of spiky bunch tends to be developed. Furthermore, it has also been undoubtedly revealed that the bunch progression of positive alpha seems to evolve with more exquisitely systematic pattern during the early stage of the second bursting scheme.

Although the bunch distribution of negative alpha roughly seems to progress with more disorder fashion, it has still been likely to acquire some explicit recurrent evolutions which is periodically occurred in accordance with the synchrotron period. The ‘single spiky bunch’ is appeared to be repetitively developed right after entering to the second bursting pattern. Therefore, it might be crucial to examine the bunch progression in horizontal plane in order to evaluate the oscillation details of the fluctuation frequencies due to these corresponding semi-chaotic movements. This investigation would be able to scrutinize the alteration of fluctuation details of a bunch during the transformation of unstable schemes which might leads to the fundamental comprehension on how the collective effect induces the chaotic evolution that typically limits the maximum achievable intensity of accelerators as well as how the temporal occurrence of steady temporal CSR bursting at high current is able to be initiated.

This section performs an enlargement of the region where the transition of unstable patterns is taken place by reducing the size of simulated current steps in order to considerately inspect the alterations of oscillation frequencies that gradually changed within miniscule current increment. The current range 0 – 100 μA is separated into 66 pieces which is able to reduce the step size from 4.125 μA to 1.612 μA. Then, all the fluctuation frequencies of five current steps before and after the transition point are extracted by the FFT analysis in order to evaluate all the oscillation frequencies that are developed from both the stationary and rigid-bunch fluctuations and reveal any significant alterations on these frequency components related to the changing of bursting schemes that might have been gradually exposed during the transition.

5.3.2.1 $\boldsymbol{\alpha_1}$ = 1.0 × 10^{-5} and $\boldsymbol{V_{rf}}$ = 3.4 MV

Plot of energy spread with currents illustrated in figure 5.50 shows that the curve is significantly increased at 13.90 μA then suddenly raised up even further at 31.63 μA. By considering the bursting pattern shown in figure 5.49 together, they are in agreement that the microbunching threshold or the first bursting threshold is occurred at the first increasing point, 13.90 μA, while the later point where the energy spread curve is abruptly arisen, 31.63 μA, might indicates the chaotic threshold.

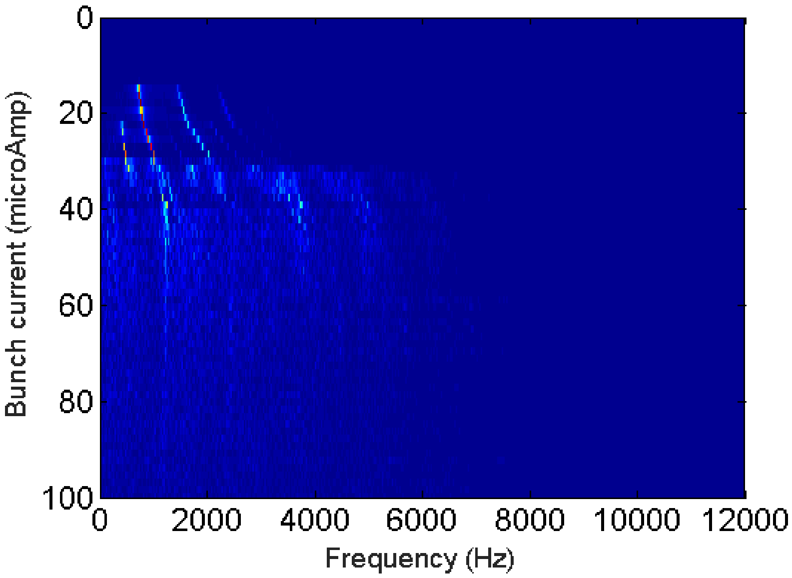

Figure 5.49: Radiation bursting pattern of the simulation with CSR + BBR wakefield for α_1 = 1.0 × 10^{-5} in detecting range 60 – 90 GHz.

Revelation of longitudinal beam dynamics in section 5.1.3.2 suggests that the CSR bursting behaviour of this case is primarily governed by the characteristic formation of the binary halo-solid bunch system. At 20.35 μA while the first bursting pattern is being executed, the bunch is confined in the ‘barred-spiral-galactic’ evolution packet with steady circulating microbunches stream between the two focal points. When the current is further increased, the particle accumulation is gradually strengthened and amplifies the binary system arrangement to become more apparent. Eventually, the barred-spiral-galactic bunch system is completely transformed to the orbiting binary star formation when proceeding into the second bursting pattern.

Figure 5.49 remarkably illustrates that the transformation of bursting schemes is gradually occurred within a range of approximately 10 μA between 30 to 40 μA. This is worth notifying that it is much more smoothly progressed than the case of negative alpha. On the other hand, it also implies that it is more difficult to specify the exact point of the bursting patterns transition in this case. However, the energy spread curve has suggested that there is a point at 31.63 μA where the curve is steeply increased and also situated in the middle of transformation period. Consequently, this current step might be practically defined as the transformation point or the chaotic threshold of this case.

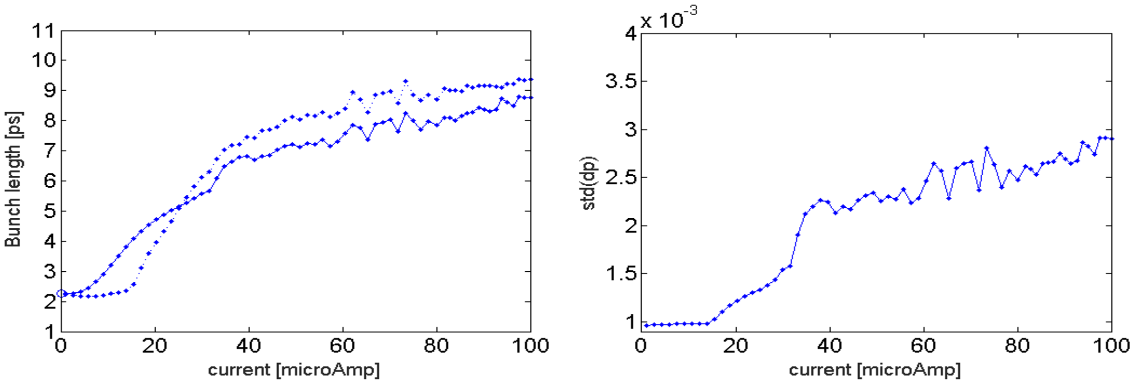

Figure 5.50: Comparison of bunch length and energy spread plotted with currents of the simulation with CSR + BBR wakefield for α_1 = 1.0 × 10^{-5}. The bold line is the data calculated by standard deviation of all particles and dotted line stands for the bunch lengthening calculated by Gaussian fitting method.

Five current steps before and another five steps after this point are brought into consideration. Their CSR bursting spectrums are sequentially demonstrated in figure 5.51 as well as their horizontal oscillation frequencies analysed by the FFT which are also sequentially shown in figure 5.52.

Both the plots of bursting spectrums and oscillation frequencies have been evidenced that their frequency components are exposed in sharp spikes during the first bursting scheme, 25.18 – 30.02 μA. Afterward, several minor frequencies seem to be developed at the shoulder of original peaks when the current reaches 31.63 μA while the amplitude of the original spikes are relatively decreasing in meantime. Furthermore, the frequency components higher than 2 kHz are also relatively diluted at this current. However, when the current progresses one step further to 33.24 μA, both frequency plots appear to be rearranged into several groups of frequency components spreading from 0 to 8 kHz. The rearrangement process is carrying on until 36.47 μA where the frequencies readjustment seems to be settled down into another characteristic formation which is, in other words, the second bursting pattern.

The bursting spectrums and the oscillation frequencies turn out to be exposed with substantially broader frequency band and larger spacing between successive signals in comparison with the first bursting pattern. The transition process appears like the frequency components originated during the first bursting pattern are 'diluted' when the current is crossing the transition point and 'condensed' into the second bursting spectrum when properly proceeded into the second bursting scheme area.

I_b $[\mu A]$	**Horizontal oscillation frequencies [kHz]**							**Average spacing [kHz]**
	1^{st}	2^{nd}	3^{rd}	4^{th}	5^{th}	6^{th}	7^{th}	
25.18	0.4271	0.8808	1.308	1.762	2.189	2.616	3.070	0.4405
26.80	0.4538	0.9075	1.361	1.842	2.296	2.723	3.203	0.4576
28.41	0.4805	0.9609	1.441	1.922	2.402	2.883	3.337	0.4767
30.02	0.5072	1.014	1.521	2.029	2.536	3.043	3.550	0.5071

Table 5.3: The oscillation frequencies at the first bursting pattern and average spacing between consecutive components at each current of α_1 = 1.0 × 10^{-5}.

I_b $[\mu A]$	**Horizontal oscillation frequencies [kHz]**					**Average spacing [kHz]**
	1^{st}	2^{nd}	3^{rd}	4^{th}	5^{th}	
34.86	1.174	2.242	3.417	4.511	5.472	1.074
36.47	1.148	2.269	3.310	4.458	5.579	1.116
38.08	1.148	2.296	3.363	4.538	5.846	1.169
39.69	1.174	2.349	3.523	4.698	6.006	1.201

Table 5.4: The oscillation frequencies at the second bursting pattern and average spacing between consecutive components at each current of α_1 = 1.0 × 10^{-5}.

It would be worth noting that there are some noticeable frequency dynamics inspected in the plots of horizontal fluctuations. Figure 5.51 and 5.52 show that the temporal bursting frequencies are clearly exposed during the first bursting pattern then becoming more distorted on the second bursting pattern. Table 5.3 and 5.4 summarize the bursting frequencies occurred during the first and the second bursting patterns respectively as well as average frequency spacing between successive components at each current. It has already been figured out that when the current is increased, the entire series of bursting spectrum is shifted toward higher frequency. Average frequency spacing between successive exposing frequencies are also increased with current in both bursting patterns. However, the spacing of the second pattern is significantly larger than the first pattern at approximately 2.5 times.

During the first pattern, apart from the CSR bursting components that are being exposed on the plot of horizontal oscillation frequencies, there is also an anomalous peak exposed at 0.6673 kHz. Since the synchrotron frequency, f_s, is 0.6779 kHz, it might be inferred that this peak represents a bunch fluctuation that coincidently revolves with the rotation of longitudinal phase space which is referred to the dipole mode oscillation of a bunch.

In addition, it is always occurred stationary at the same frequency of all currents despite the entire bursting spectrums are shifted toward higher frequency with increasing current. It is even more interesting that the strength of this oscillation component is gradually increased with current but suddenly decreased when the bunch current approaches one step before the chaotic threshold. Then, at 31.63 μA which was previously defined as the transition point, this peak is suddenly fused with the first signal and becomes the most dominated peak throughout the second bursting scheme since then.

Another noticeable dynamical change on the fluctuation frequencies is the bursting frequencies exposed in the second bursting pattern appear to be twin or clustered spike instead of single spike as shown during the first pattern. This behaviour is obviously demonstrated in figure 5.52 at 39.69 μA which is in agreement with the CSR bursting pattern shown in figure 5.51.

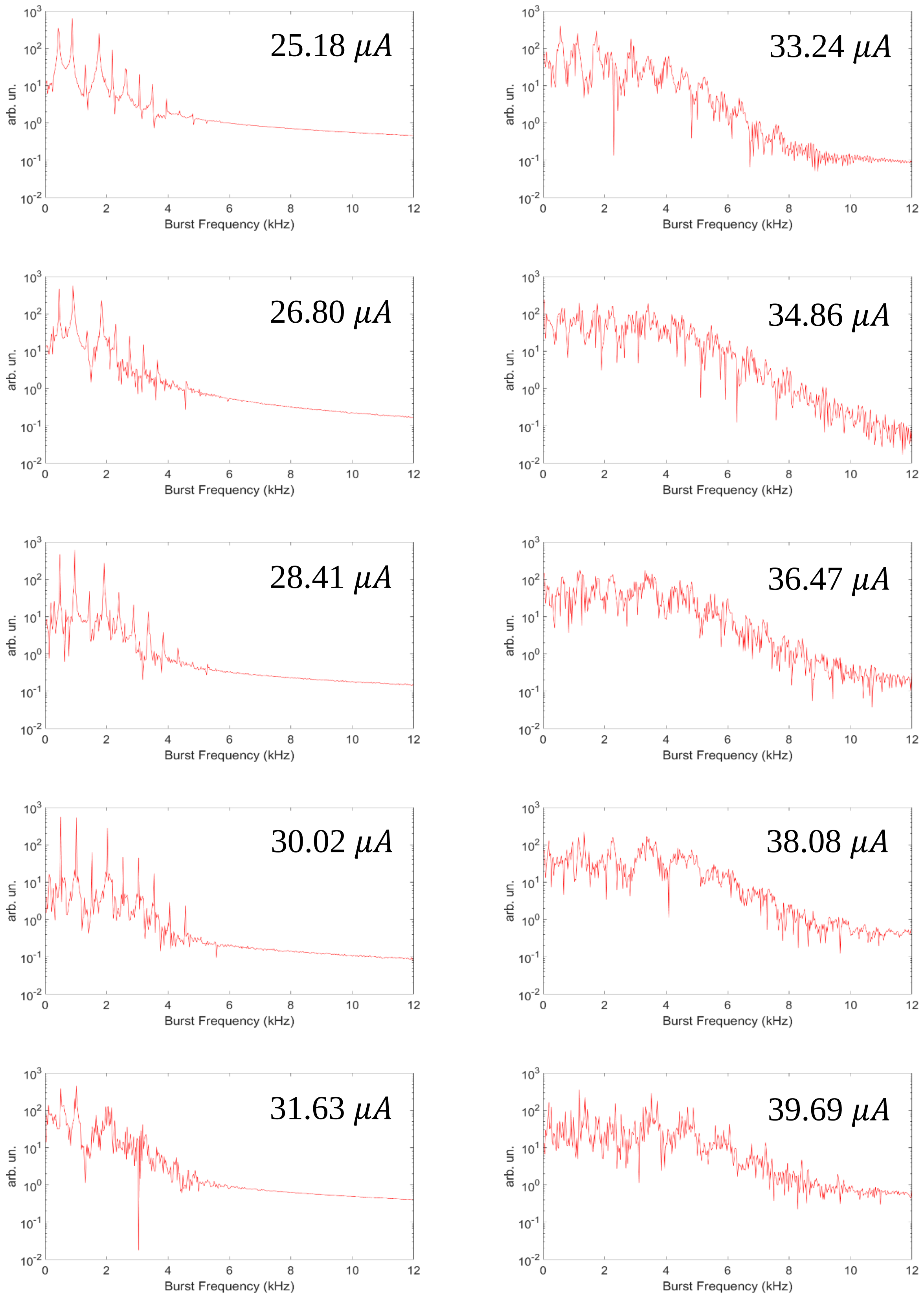

Figure 5.51: The CSR bursting frequencies of α_1 = 1.0 × 10^{-5} detected within frequency range 60 – 90 GHz during the transition of CSR bursting patterns.

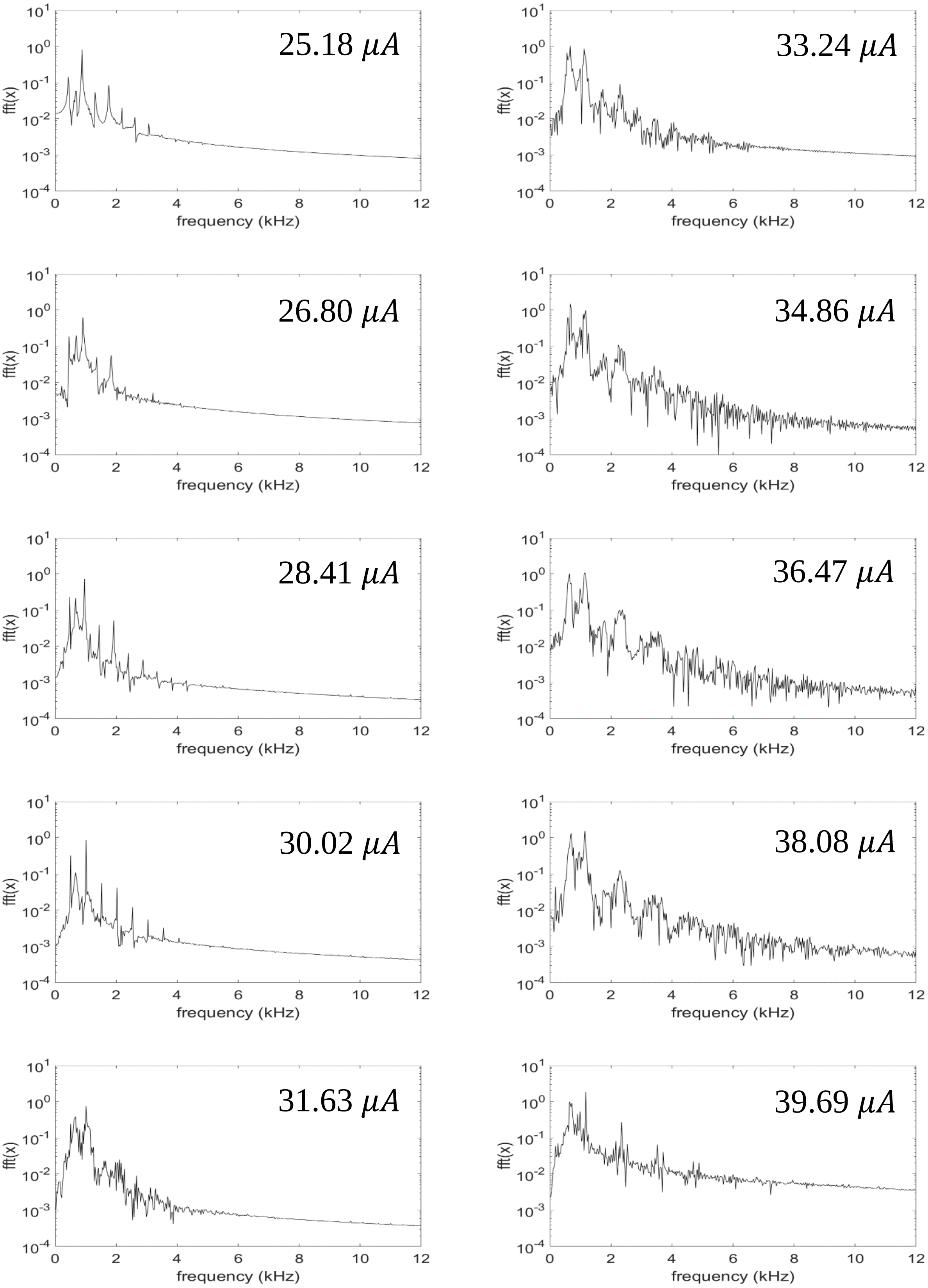

Figure 5.52: The horizontal oscillation frequencies of the bunch during the transition of CSR bursting patterns in $\alpha_1 = 1.0 \times 10^{-5}$.

5.3.2.2 α_1 = -1.0 x 10^{-5} and V_{rf} = 3.4 MV

The plots of oscillation frequencies of ten successive current steps are sequentially plotted in figure 5.56 in order to compare the development of oscillation frequency signals across the transition point.

During the first bursting pattern, 62.27 – 68.71 μA, there are two frequency components obviously revealed at 0.6673 and 1.121 kHz which slightly underestimate the f_s and $2f_s$ respectively (f_s = 0.6779 kHz, $2f_s$ = 1.356 kHz). It also suggests that both components are exhibited in single spike before transformed into clustered spike about the initial frequencies after transformed to the second bursting pattern, 70.33 – 76.78 μA. The horizontal oscillation frequencies of each current on the first pattern are summarized in table 5.5.

Remarkably, the oscillation frequencies during the first pattern also exhibit some significant changes near the threshold. The frequency signal 1.121 kHz almost remains unchanged at the same frequency throughout the first pattern while the other component at 0.6673 kHz is apparently shifted toward the lower frequency. It is shifted to 0.6673, 0.6406, 0.6139 and 0.5872 kHz at 63.88, 65.49, 67.10 and 68.71 μA respectively. Furthermore, the amplitude of the first peak with respect to the second one happens to be gradually decreased when the current is increased but raised up again at the last current step before the transition, 68.71 μA. At this current step, the oscillation frequencies higher than the second dominated peak are apparently rearranged into many groups where several minor peaks are also being developed within. These minor peaks are then grown into existence together with the development of clustered peaks originated from the two dominated ones after the transition.

After transition, the two dominated peaks are broadening and transformed into clustered peaks simultaneously with the minor peaks within each successive groups are turned out to be several spikes. These frequency group arrangements higher than the dominant couple clusters are then gradually diluted at higher currents. The horizontal oscillation frequencies within each cluster for the first eight clusters during the second pattern are summarized in table 5.6.

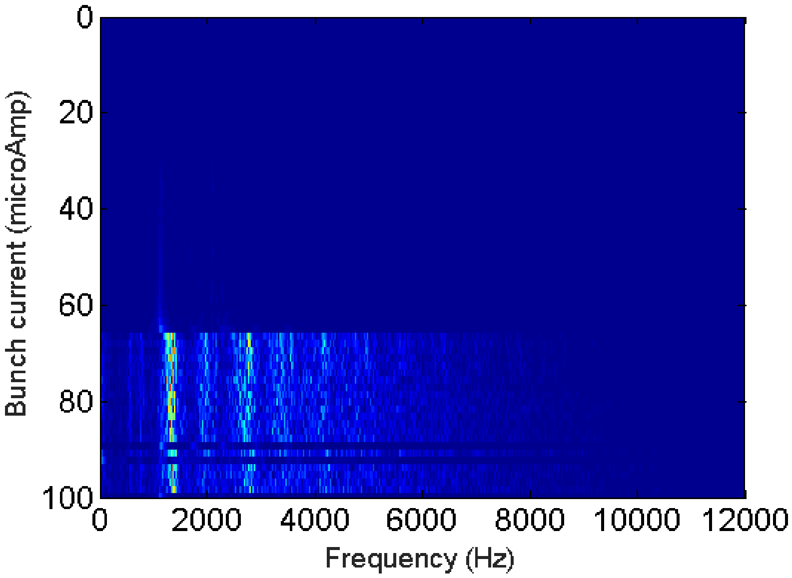

Figure 5.53: Radiation bursting pattern of the simulation with CSR + BBR wakefield for α_1 = -1.0 × 10^{-5} in detecting range 60 – 90 GHz.

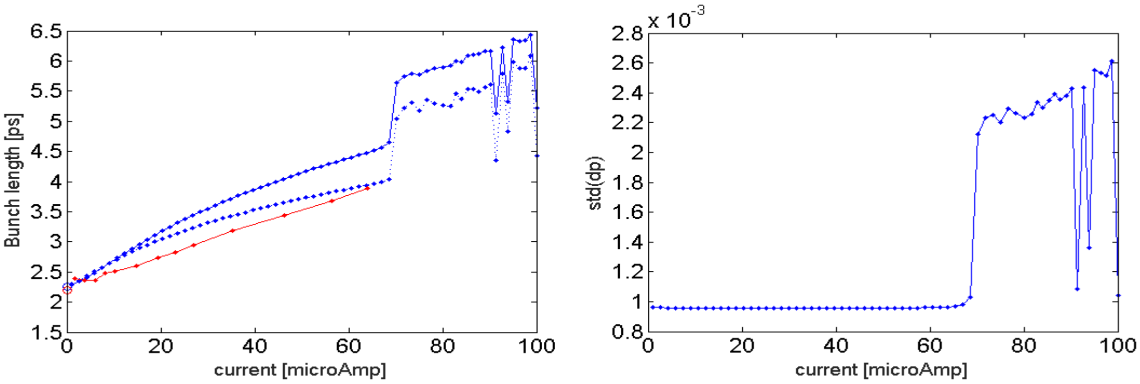

Figure 5.54: Comparison of bunch length and energy spread plotted with currents of the simulation with CSR + BBR wakefield for α_1 = -1.0 × 10^{-5}. Red line is experimental result, blue lines are simulated results where the bold line is bunch lengthening calculated by standard deviation of all particles and dotted line stands for the bunch lengthening calculated by Gaussian fitting.

It is also noticeable that there seems to be an internal dynamical changing within each dominant cluster. After entering to the second bursting region at 70.33 μA, the couple peaks are transformed from single crest into double crests. Then, within each cluster, when the current is further increased, the lower frequency minor peak apparently drifts toward the lower frequency region while the higher frequency one evolves into double crests which its lower frequency sub-peak drifts to the left again.

It has been revealed by the sequential comparison of the oscillation frequencies during the transition that the bunch fluctuation appears to evolves into more complexity when transits the chaotic threshold. A comparison in figure 5.56 evidently shows that the keys background beam dynamics which govern the CSR bursting scheme are the gradually increasing of the prominent fluctuation occurred at approximately the synchrotron frequency and the development of complex fluctuation within the vicinity of f_s and $2f_s$.

The longitudinal phase space evolution illustrated in figure 5.29 (right column) indicates that the bunch is confined in a packet with the rotating microbunches at the outer shell during the first bursting scheme. Then it evolves into more complex evolution fashion when entering to the second bursting scheme as shown in figure 5.30 (right column) where the characteristic single spiky bunch is developed and repetitively occurred every approximately 300 and 700 revolution turns. Due to the fact that the synchrotron period, T_s, is equal to 787.46 turns, it might be able to determine that the two dominated clusters apparently revealed on the second bursting scheme are responsible for this characteristics evolution.

$\boldsymbol{I_b}$ $[\boldsymbol{\mu A}]$	**Horizontal oscillation frequencies [kHz]**							
	1^{st}	2^{nd}	3^{rd}	4^{th}	5^{th}	6^{th}	7^{th}	8^{th}
62.27	0.6673	1.121	-	-	-	-	-	-
63.88	0.6673	1.121	-	-	-	-	-	-
65.49	0.6406	1.121	1.682	2.242	-	-	-	-
67.10	0.6139	1.121	1.708	2.322	-	-	-	-
68.71	0.5872	1.148	1.735	2.296	2.963	3.523	4.111	4.725

Table 5.5: The oscillation frequencies at the first bursting of α_1 = -1.0 × 10^{-5}.

I_b [μA]	Horizontal oscillation cluster frequencies [kHz]							
	1^{st}	2^{nd}	3^{rd}	4^{th}	5^{th}	6^{th}	7^{th}	8^{th}
70.33	0.6673	1.281	1.895	2.509	3.363	4.164	4.778	5.579
	0.7741	1.388	1.975	2.616	3.550	4.217	4.991	5.739
	-	-	2.109	2.776	-	-	-	-
	-	-	2.162	-	-	-	-	-
71.94	0.5872	1.174	1.975	2.509	3.176	4.004	4.778	5.419
	0.6940	1.281	2.029	2.616	3.310	4.084	4.991	5.525
	0.7741	1.335	2.162	2.776	3.363	4.191	5.098	5.605
	-	1.388	-	-	3.577	-	-	-
	-	1.468	-	-	-	-	-	-
73.53	0.5338	1.174	1.922	2.536	3.203	4.164	4.725	5.419
	0.5872	1.255	2.002	2.616	3.310	4.271	4.778	5.579
	0.7207	1.308	2.109	2.749	3.390	-	4.965	5.659
	0.8008	1.388	2.162	2.829	3.577	-	-	-
	-	1.415	2.215	-	-	-	-	-
75.16	0.5605	1.228	1.895	2.562	3.310	4.191	4.805	5.525
	0.6940	1.281	1.975	2.616	3.550	4.271	4.858	5.605
	0.7474	1.335	2.055	2.669	3.603	4.404	4.938	5.739
	0.8808	1.388	2.162	2.776	-	4.458	-	-
	-	1.441	-	2.829	-	-	-	-
76.78	0.5072	1.255	1.868	2.562	3.390	4.164	4.805	5.605
	0.5605	1.308	2.002	2.776	3.577	4.217	4.965	5.685
	0.6139	1.388	2.189	2.829	3.603	4.297	4.991	5.712
	0.6673	1.441	-	-	-	-	-	-
	0.6940	-	-	-	-	-	-	-
	0.7474	-	-	-	-	-	-	-
	0.8008	-	-	-	-	-	-	-
	0.9075	-	-	-	-	-	-	-

Table 5.6: The oscillation frequencies of each clustered peak at the second bursting pattern of α_1 = -1.0 × 10^{-5}.

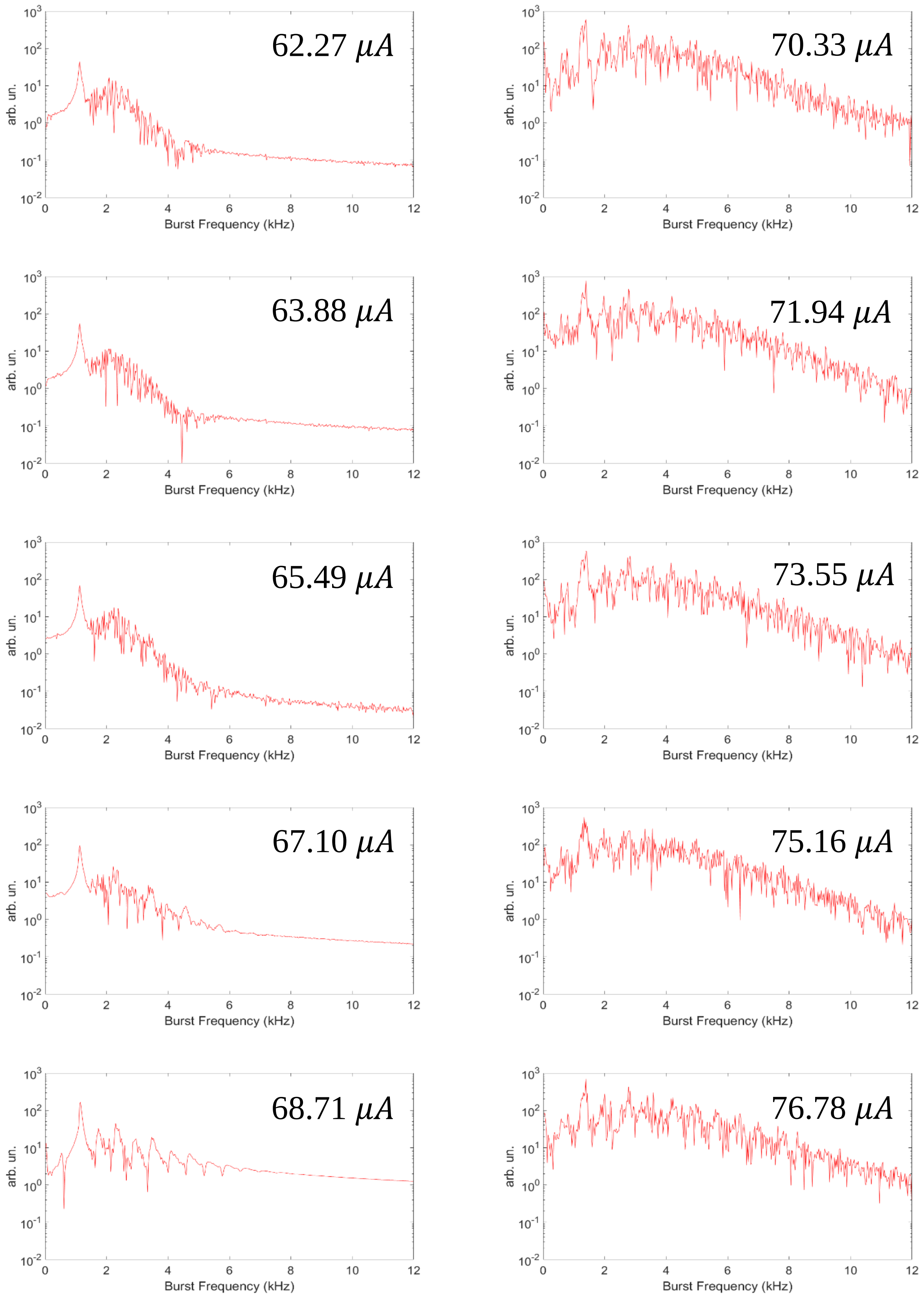

Figure 5.55: The CSR bursting frequencies of α_1 = -1.0 × 10^{-5} detected within frequency range 60 – 90 GHz during the transition of CSR bursting patterns.

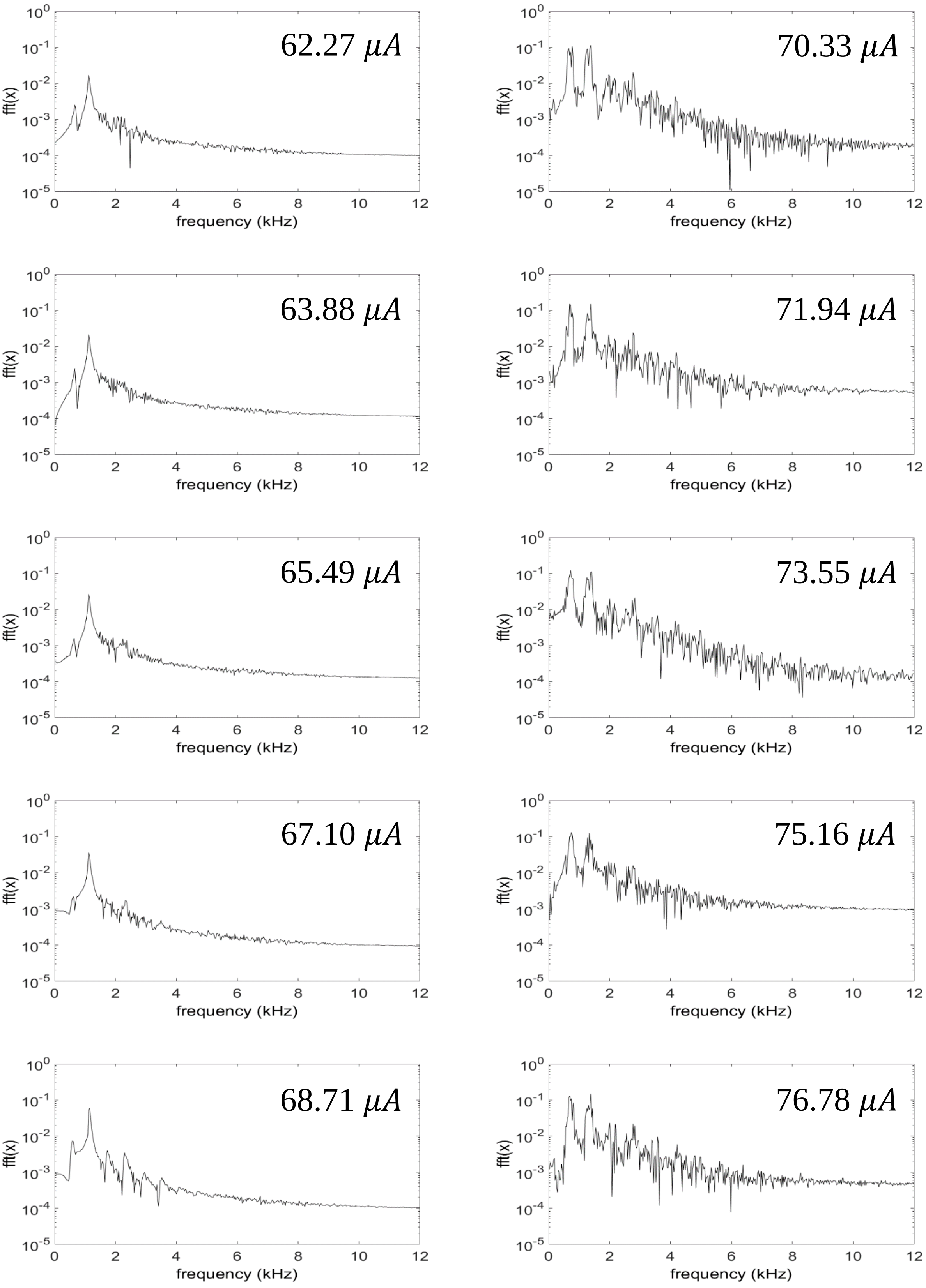

Figure 5.56: The horizontal oscillation frequencies of the bunch during the transition of CSR bursting patterns in α_1 = -1.0 × 10^{-5}.

In addition, the comparison of bunch evolutions in longitudinal phase space between the first and the second bursting patterns has also made an implication that these fluctuations repetitively occurred at f_s and $2f_s$ are developed from the collapse of confined bunch due to the wake potential that collectively increased with current.

The development of several minor peaks within the vicinity of f_s and $2f_s$ might be arisen from the bunch distribution elements that are also developed at the bunch broken point. These elements are created from the particles that left behind the majority distribution then revolved and folded up at comparable rate to f_s and $2f_s$ revolutions. These minor elements are usually slowed down and lagged behind the major group. This behaviour might leads to the shifting of minor peaks to lower frequency region.

5.3.3 Summary

The enlargement of unstable states transition region discloses several key features of the transitional effect in both positive and negative alpha. It has been shown that the dynamical development of oscillation frequency at roughly equivalent to the synchrotron frequency reflects particular evolution that is specifically induced during the transition of bursting schemes. Both the investigations of oscillation frequencies on positive and negative alpha surprisingly demonstrate that this key frequency element is gradually developed in accordance with the domination of the first dominant cluster during the transition stage. Another key feature of transitional effect is the development of minor spikes in the vicinity of original frequencies induced during the first bursting series. It is obviously depicted that these minor spikes are increasingly stimulated at the current near the chaotic threshold. They demonstrate that these elements endorse the dilution of initial bursting series which subsequently rearranging into the second bursting series.

These variations on the oscillation frequencies imply that the bunch evolves in the confined evolution at the first bursting fashion. Then the bunch distribution in phase space becomes more scattered during the transition. Finally, it settles down into another systematic revolution which is the second bursting scheme.

Ultimately, the numerical investigation of horizontal fluctuations has revealed the prominent revelation that the transition of unstable states in both positive and negative alphas is conducted in more or less the same fashion. The only variation is the execution period of the transition that takes larger current range in positive alpha while taking much smaller increment in negative alpha.

5.4 Summary of the comparison of simulations and experiments

The comparison between numerical and experimental results in this chapter indicates that the simulation code is able to exhibit an impressive capability to reproducing the bunch progression with a presence of collective instabilities.

It has been shown that the simulations with completed wake model, CSR + BBR, is able to replicate the bunch lengthening curves in most studying cases both positive and negative alpha. In term of the comparison of resulting radiation bursting, in positive alpha, the numerical simulation is able to exhibit fairly good result on reproducing the bursting pattern as well as the estimation of instability threshold and chaotic threshold. Furthermore, it is also able to reveal the second bursting series detected in several positive alpha experiments.

In negative alpha, the numerical simulation provides exceptional result on the replication of CSR bursting pattern. It is not only able to reproduce the bursting pattern before conventional current threshold but also the region beyond. Additionally, it reveals that the bursting of coherent radiation in negative alpha is comprised of two regimes. The first bursting regime is executed after the microbunching threshold is exceeded where the micro-structure is developed and resulting on the characteristic temporal bursting signals. The numerical simulation is also able to accurately estimate the first bursting pattern in negative alpha cases.

The second regime would subsequently be occurred after the conventional current threshold or the chaotic threshold is exceeded. It has been generally recognised that the beam would not be able to sustain its dynamical stability after this point. However, the experimental bursting result of α_1 = -1.0 × 10^{-5} with V_{rf} = 3.4 MV exhibited a sort of bursting pattern beyond this point even though the beam had become devastated due to chaotic environment within additional increment of beam current. The numerical simulation shows that it is able to replicate this bursting series beyond the current threshold. It suggests that there happens to be a particular periodic development of an instantaneous compressed bunch distribution in phase space existed beyond the conventional current limit. Therefore, such a bunch evolution might probably be redefined as the semi-chaotic fashion because of its semi-disordered dynamic evolution. Additionally, the conventional current threshold might also be able to redefine as the chaotic threshold to be remarked as the onset of the semi-chaotic evolution.

The numerical investigation has also unexpectedly disclosed that the two bursting regimes of negative alpha can be alternated between one another. After the bunch has already been progressed into the semi-chaotic fashion, it would be able to retrieve back to the previous confined state and continues bursting the coherent radiation as same as the first bursting regime. Furthermore, when the current is further increased, it turns out to be restored to its semi-chaotic behaviour again which exposes the characteristic repetitive bursting signals as same as the second regime.

The bunch evolution in longitudinal phase space is also depicted by the numerical simulation which allows dynamical inspection on the bunch progression at particular unstable state. It has been revealed that the characteristic binary bunch formation and the microbunching effect play central role in governing the bursting behaviour in positive alpha. The sawtooth dynamical fashion is also investigated to be initiated by geometric wakefield while the radiation wakefield is responsible for the microbunching effect.

At the same time, the longitudinal phase space evolution also indicates that the microbunching effect is also occurred during the first bursting pattern in negative alpha. The collective effect is considerably strengthened after passing through the chaotic threshold and causes the bunch evolving with more chaotic progression. Nevertheless, repetitive development of the single large spiky bunch is initiated and resulting in the characteristic bursting behaviour of the second pattern scheme.

The evaluation of horizontal oscillation frequencies demonstrates that significant frequency components both the stationary fluctuations and the rigid-bunch oscillations can be revealed. An analysis of horizontal dynamic is able to implement the investigation in longitudinal plane especially the rigid-bunch oscillation frequencies that would not be able to evaluate by the resulting CSR spectrum. This technique was also brought into the investigation of bursting regime transition in order to inspect significant development on frequency domain arisen during unstable state transition.

Surprisingly, it has been found that the transitional effects of the positive and negative alphas are executed in almost the same fashion. In both alpha, a dominated peak at approximately f_s is concurrently developed with the transformation of bursting scheme where the longitudinal phase space is also transforming from the characteristic evolution of the first bursting behaviour to the evolution of second bursting scheme. At the same time, another dominated peak at approximately $2f_s$ is always presented throughout the transition period. Several minor frequencies in the vicinity of the initial frequencies in the first pattern are also developed during the transition then subsequently broaden the initial signals and rearranged into the second bursting series.

The second bursting series of both positive and negative alpha are also unexpectedly exposed with more or less the same fashion. There are a major series exposed together with a minor series in both cases. This might be a consistent development of a single large spike during a fusion state of positive alpha and repetitive development of single spike in negative alpha. While a positive alpha demonstrates that the bursting series is diluted at higher current due to the bunch evolving into chaotic behaviour, a negative alpha is able to consistently expose its bursting series throughout the simulation range.

The dissolution of the first bursting spectrum near the threshold and subsequent condensation into the second bursting pattern when passing through the chaotic threshold implies that the bunch is evolving from an ‘ordered’ state to a ‘disordered’ state. Nevertheless, such notion has already been concluded by many previous studies, the numerical investigation in this work proposes an argument significantly different from the conventional terminology above.

The conventional ‘disordered’ state is, in fact, unlikely to be the state of totally devastation. In contrast, its disorderliness seems to be occurred in ‘ordered’ dynamic manner according to the beam dynamic revelations during the second bursting regime of negative alpha.

Additionally, the alternation between CSR-like or semi-stable and semi-chaotic bursting behaviours disclosed in the negative alpha has proposed the potential technique on the generation of steady temporal bursting of coherent synchrotron radiation at higher current. Furthermore, the retrieving phenomena of a bunch after it has already been progressed into the semi-chaotic behaviour is also a remarkable issue to be emphasized later especially the experimental consideration.

Ultimately, it has been speculated that there might not be only the progression of a single electron bunch with a presence of collective effect that can be described with this alternating chaotic-harmonic evolution regime but it may also be applicable to approach any dynamical system that has a nature of transformation from an ordered to a semi-chaotic state due to an increasing collective effect that consisted of finite frequency component. Further analytical investigation on this phenomenology is interesting to be scrutinized.

Chapter 6

Conclusion and Outlook

The multiparticle tracking tool, sbtrack, has been modified with many essential functions in order to improve the performance to be exploited in numerical investigation of collective instabilities of a single electron bunch and resulting radiation bursting behaviour. It can be concluded that the numerical investigation by a modified sbtrack demonstrates fairly good results. It is able to reproduce characteristic features of THz coherent synchrotron radiation (CSR) bursting on both the reexamination of study at SOLIEL storage ring [13] and the low-alpha experiment at Diamond Light Source.

In order to perform a numerically investigation of beam dynamic under the collective instability, the impedance of storage ring that typically related to the geometric wakefield is needed to be characterized first. The technique of impedance characterization with the Haissinski integral equation has been proposed according to a prominent advantage on numerical solving time. The impedance model can be arbitrarily constructed and passed on to the Haissinski equation to solve for the longitudinal equilibrium distribution at particular current. This solution can be obtained by semi-numerical approach within considerably short time. Thus the empirical adjustment of impedance model can be done within sensible time. Nevertheless, the drawback of this technique is due to the fact that the equilibrium longitudinal distribution generated by Haisinski equation is restricted to low bunch current, the bunch lengthening is presumably adequate for an estimation of bunch profile development with increasing current due to collective effect.

A broad-band impedance model with R_s = 36 $k\Omega$, F_{res} = 41.38 GHz and Q = 1 is able to provide the most sensible simulation results of bunch development with increasing current as well as resulting radiation bursting spectrum. This model is brought into the numerical investigation as a source of geometric wakefield experienced by circulating electron.

Comparison of numerical and experimental results reveals that the radiation wakefield is responsible for initiating the microbunching effect while geometric wakefield appears to instigating the bunch elongation and complexity in longitudinal phase space evolution. The radiation wakefield is capable to top-up local fluctuations on the potential well of particle ensemble however its effect is not strong enough to cause severe beam dynamic comparing to the effect of geometric wakefield at the same intensity. On the other hand, the wake potential due to geometric wakefield substantially interferes with the potential well that subsequently leads to more extreme beam dynamic complexity. The formation of binary bunch system that results the sawtooth behaviour has been demonstrated to be directly initiated from geometric wakefield. Such a bunch behaviour is numerically revealed at 44.53 μA with α_1 = 1.0 x 10^{-5} and V_{rf} = 3.4 MV.

Combining effect of geometric and radiation wakefields contributes to a formation of barred-spiral distribution shape in phase space for positive alpha. The first pattern of CSR bursting behaviour is a result of the fluctuated microbunches induced after the microbunching threshold. The bursting pattern is then gradually transformed to the second series after exceeding the chaotic threshold. At this region, the binary formation becomes stronger and eventually constituting the binary star instability which has also been reported by other study [78]. The binary star formation is affirmed to be responsible for the CSR bursting behaviour of the second pattern. This finding also indicates that the sawtooth fashion is able to radiate coherently as same as the microbunching effect but with different bursting frequency series.

For the beam with negative momentum compaction factor, nevertheless there is no binary formation detected, other characteristics beam dynamic phenomenology have been revealed. While it is responsible for inducing the microbunches in positive alpha, the CSR wakefield has been found to activate a characteristic local micro-fluctuation or ‘spur-like’ instability at the bunch tail in negative alpha.

The first bursting pattern occurred after the microbunching threshold is revealed to be similar to the radiation bursting due to microbunching effect in positive alpha but with different frequency signals according to an implemented spur-like instability. When the current exceeds the chaotic threshold the bursting behaviour is suddenly transformed to the second bursting series. The beam dynamic at this region appears as the semi-chaotic instead of totally devastating manner. The bunch evolution periodically tends to be converged into a particular confined distribution though it unable to be sustained in this restraint for long. Repetitive development of an immense compressed bunch distribution is occurred during this converging phase. This temporal ‘spiky bunch’ progression is responsible for the bursting signals of the second pattern. Unexpectedly, the second bursting signals according to such spiky bunch on negative alpha case are comparable to the signals due to binary star motion of the beam with the same value of alpha in positive sign.

It is even more astonishing that at some point during the semi-chaotic behaviour, the bunch is managed to be confined in a particular stable bunch packet and starts steady CSR bursting exactly the same as occurred in the first bursting region. Then it turns back to the semi-chaotic fashion as the second pattern again when the current is further increased. This temporal occurrence of the confined evolution might has theoretically proposed another promising approach on the generation of steady CSR at high current from synchrotron based light source.

An analysis of the horizontal oscillation frequency is able to provide both stationary and rigid-bunch oscillations to implement the investigation on resulting bursting behaviour. Evaluation of oscillation frequency during the transformation of bursting pattern reveals that development of a bunch motion particularly synchronized with f_s is being emerged with the rearranging of second pattern. During the transition, the oscillation frequency evaluation expresses that the first bursting series is gradually diluted into the background then condensed and rearranged into the second series.

This frequency evaluation is in agreement with the dynamical development of the bunch phase space during the chaotic threshold. In positive alpha, the bunch evolution is progressively evolved from the barred-spiral shape to the connected binary star evolution. The qualitative explanation can be given as follow.

Before the chaotic threshold the bunch is evolving with the barred-spiral shape which most of particles are concentrated in the main packet. The CSR bursting is therefore resulting radiation from the microbunches continuously drifting on the outer shell. When the threshold is occurred, the distribution is elongated and transformed to the connected binary star which most of particles are concentrated in both sub-bunches. The binary bunch orbits about each other at the amplitude larger than characteristic length of sub-bunch and microbunch fluctuation. Hence the radiation bursting behaviour is a result of the orbiting binary system.

In negative alpha, the bunch distribution progresses from microbunching and spur-like fluctuation to the semi-chaotic fashion at chaotic threshold. The longitudinal phase space depicts that at the first pattern, most particles is concentrated in the main confined packet. When the current is progressively increased the spur-like fluctuation becomes stronger and induce vertical wavering of the bunch tail. This fluctuation is getting stronger as the current is increased and superimpose with elongation and deformation of the bunch cluster. Eventually the bunch distribution evolves with more complicated fashion. While the distribution is rotating around the phasal area, it is periodically compressed into a triangular confinement which resulting on the temporal bursting of CSR as well. This behaviour is depicted as the second bursting pattern.

The temporal occurrence of relaxation gap among the semi-chaotic revolution seems to be a stochastic process. A newly developed theoretical dynamic model of phase space evolution that includes both radiation and geometric instabilities is needed and might be able to evaluate the criterion that constitutes such a temporal occurrence. The chaotic theory as well as quantum mechanics might likely to be brought into the development of an analytic expression of this phenomena. These are further interesting tasks to be scrutinized in the future.

Bibliography

[1] C. E. Nielsen and A. M. Sessler, “Longitudinal space charge effects in particle accelerators”, *Rev. Sci. Instrum.*, vol. 30, no. 1959, pp. 80–89, 1959.

[2] B. Richter, M. Sands and A. M. Sessler, “Instabilities in Stored Particle Beams”, *SLAC-49*, 1965.

[3] A. Chao, “Collective Instabilities in Accelerators”, *6th OCPA School*. Beijing, 2010.

[4] H. Wiedemann, *Particle Accelerator Physics*. Germany: Springer-Verlag Berlin And Heidelberg GmbH & Co. K, 2007.

[5] B. Zotter and S. Kheifets, *Impedances and Wakes in High Energy Particle Accelerators and Storage Rings*. River Edge, NJ: World Scientific Publishing Co Pte Ltd, 1998.

[6] M. Venturini and R. L. Warnock, “Bursts of coherent synchrotron radiation in electron storage rings: A dynamical model”, *Phys. Rev. Lett.*, vol. 89, no. 22, pp. 2248021–2248024, 2002.

[7] R. Baartman and M. D'Yachkov, “Computation of longitudinal bunched beam instability thresholds”, *Proc. Int. Conf. Part. Accel.*, 1993.

[8] P. Krejcik, K. Bane, P. Corredoura, F. J. Decker, J. Judkins, T. Limberg, M. Minty, R. H. Siemann and F. Pedersen, “High intensity bunch length instabilities in the SLC damping rings”, *Proc. Int. Conf. Part. Accel.*, pp. 3240–3242, 1993.

[9] G. Rakowsky and L. R. Hughey, “SURF’s up at NBS: A Progress Report”, *IEEE Trans. Nucl. Sci.*, vol. 26, no. 3, pp. 3845–3847, 1979.

[10] A. W. Chao, *Physics of Collective Beam Instabilities in High Energy Accelerators*. New York: Wiley, 1993.

[11] T. Weiland, “On the computation of electromagnetic fields excited by relativistic bunches of charged particles in accelerating structures”, *CERN/ISR-TH/80-07*, 1980.

[12] J. S. Nodvick and D. S. Saxon, “Suppression of coherent radiation by electrons in a synchrotron”, *Phys. Rev.*, vol. 96, no. 1, pp. 180–184, 1954.

[13] C. Evain, J. Barros, A. Loulergue, M. A. Tordeux, R. Nagaoka, M. Labat, L. Cassinari, G. Creff, L. Manceron, J. B. Brubach, P. Roy and M. E. Couprie, “Spatio-temporal dynamics of relativistic electron bunches during the micro-bunching instability in storage rings”, *EPL*, vol. 98, no. 4, p. 40006, 2012.

[14] J. B. Murphy, S. Krinsky and R. L. Gluckstern, “Longitudinal wakefield for an electron moving on a circular orbit”, *Part. Accel.*, vol. 57, 1997.

[15] J. Schwinger, “On the Classical Radiation of Accelerated Electrons”, *Phys. Rev.*, vol. 75, no. 12, pp. 1912–1925, 1949.

[16] R. L. Warnock and P. Morton, “Fields Excited by a Beam in a Smooth Torodial Chamber”, *Part. Accel.*, vol. 25, no. 1, pp. 113–151, 1990.

[17] M. Venturini, R. Warnock, R. Ruth and J. A. Ellison, “Coherent synchrotron radiation and bunch stability in a compact storage ring”, *Phys. Rev. ST Accel. Beams.*, vol. 8, no. 1, pp. 58–72, 2005.

[18] J. Schwinger, “On radiation by electrons in a betatron”, *LBNL-39088*, pp. 1–25, 1945.

[19] F. C. Michel, “Intense Coherent Submillimeter Radiation in Electron Storage Ring”, *Phys. Rev. Lett.*, vol. 48, no. 9, 1982.

[20] T. Nakazato, M. Oyamada, N. Niimura, S. Urasawa, O. Konno, A. Kagaya, R. Kato, T. Kamiyama, Y. Torizuka, T. Nanba, Y. Kondo, Y. Shibata, K. Ishi, T. Ohsaka and M. Ikezawa, “Observation of coherent synchrotron radiation”, *Phys. Rev. Lett.*, vol. 63, no. 12, pp. 1245–1248, 1989.

[21] A. R. Hight Walker, U. Arp, G. T. Fraser, T. B. Lucatorto and J. Wen, “New infrared beamline at the NIST SURF II storage ring”, *SPIE Int. Soc. Opt. Eng.*, 1997, vol. 3153, pp. 42–50, 1997.

[22] G. L. Carr, S. L. Kramer, J. B. Murphy, R. P. S. M. Lobo and D. B. Tanner, “Observation of coherent synchrotron radiation from the NSLS VUV ring”, *Nucl. Instr. Meth. Phys. Res. A.*, vol. 463, no. 1–2, pp. 387–392, 2001.

[23] A. Andersson, M. S. Johnson and B. Nelander, “Coherent synchrotron radiation in the far infrared from a 1-mm electron bunch”, *Opt. Eng.*, vol. 39, no. 12, pp. 3099–3105, 2000.

[24] M. Abo-Bakr, J. Feikes, K. Holldack, G. Wüstefeld and H. W. Hübers, “Steady-state far-infrared coherent synchrotron radiation detected at BESSY II”, *Phys. Rev. Lett.*, vol. 88, no. 25 I, pp. 2548011–2548014, 2002.

[25] A. Zholents and M. Zolotorev, “Femtosecond X-Ray Pulses of Synchrotron Radiation”, *Phys. Rev. Lett.*, vol. 76, no. 6, pp. 912–915, 1996.

[26] A. Zholents, P. Heimann, M. Zolotorev and J. Byrd, “Generation of subpicosecond X-ray pulses using RF orbit deflection”, *Nucl. Instr. Meth. Phys. Res. A.*, vol. 425, no. 1, pp. 385–389, 1999.

[27] C. Pellegrini and D. Robin, “Quasi-isochronous storage ring”, *Nucl. Instr. Meth. Phys. Res. A.*, vol. 301, no. 1, pp. 27–36, 1991.

[28] D. Robin, E. Forest, C. Pellegrini and A. Amiry, “Quasi-isochronous storage rings”, *Phys. Rev. E*, vol. 48, no. 3, pp. 2149–2156, Sep. 1993.

[29] R. L. Holtzapple, “Longitudinal dynamics at the Stanford Linear Collider”, *SLAC-487*, PhD thesis, Stanford University, 1996.

[30] A. W. Chao and M. Tigner, *Handbook Of Accelerator Physics And Engineering*. Singapore: World Scientific Publishing Co Pte Ltd, 1999.

[31] M. Sands, “The Physics of Electron Storage Rings - An Introduction”, *SLAC-121*, vol. 28, 1970.

[32] S. Y. Lee, *Accelerator physics*. Singapore: World Scientific Publishing Co Pte, 2004.

[33] B. W. Montague, E. J. N. Wilson, G. Guignard, A. Verdier, P. J. Bryant, W. Scandale, A. Ropert, F. Willeke, W. Pirkl, A. Hofmann, L. Palumbo, V. G. Vaccaro, M. Zobov, D. Boussard, J. Le Duff, A. Mosnier, E. Keil, L. Z. Rivkin, D. Möhl, J. Bosser, E. Bonderup, R. P. Walker, A. Gaupp, A. Poncet, J. Buon, J. P. Koutchouk, I. Hofmann, M. Weiss, P. Schmüser, S. P. Moller, A. C. Melissinos and G. Kraft, “CERN Accelerator School: Fifth Advanced Accelerator Physics Course”, *CERN 95-06*, 1995.

[34] J. Haissinski, “Exact Longitudinal Equilibrium Distribution of Stored Electrons in the Presence of Self-Fields”, *Nuovo Cim. B*, vol. 18, no. 2, pp. 72–82, 1973.

[35] K. L. F. Bane, T. Naito, T. Okugi, Q. Qin and J. Urakawa, “Impedance Analysis of Bunch Length Measurements at the ATF Damping Ring”, *10th International Symposium on Applied Electromagnetics and Mechanics*, p. 9, 2001.

[36] K. Oide and K. Yokoya, “Longitudinal Single Bunch Instability in Electron Storage Rings”, *KEK preprint 90-10*, 1990.

[37] Y. Cai, “Linear theory of microwave instability in electron storage rings”, *Phys. Rev. ST Accel. Beams.*, vol. 14, no. 6, p. 61002, Jun. 2011.

[38] National Institute of Standards and Technology (NIST), “http://www.nist.gov/pml/div685/grp07/updated-what-is-synchrotron-radiation.cfm”.

[39] D. H. Auston, K. P. Cheung, J. A. Valdmanis and D. A. Kleinman, “Cherenkov Radiation from Femtosecond Optical Pulses in Electro-Optic Media”, *Phys. Rev. Lett.*, vol. 53, no. 16, pp. 1555–1558, Oct. 1984.

[40] B. Ferguson and X. C. Zhang, “Materials for terahertz science and technology”, *Nat Mater.*, vol. 1, no. 1, pp. 26–33, Sep. 2002.

[41] J. B. Murphy, “Coherent Synchrotron Radiation in Storage Rings”, *ICFA Beam Dyn. Newsl.*, no. 35, p. 20, 2004.

[42] R. W. Schoenlein, S. Chattopadhyay, H. H. W. Chong, T. E. Glover, P. A. Heimann, C. V. Shank, A. A. Zholents and M. S. Zolotorev, “Generation of Femtosecond Pulses of Synchrotron Radiation”, *Science.*, vol. 287, no. 5461, pp. 2237–2240, Mar. 2000.

[43] K. Holldack, S. Khan, R. Mitzner and T. Quast, “Femtosecond Terahertz Radiation from Femtoslicing at BESSY”, *Phys. Rev. Lett.*, vol. 96, no. 5, pp. 1–4, 2006.

[44] W. Guo, B. Yang, C. X. Wang, K. Harkay and M. Borland, “Generating picosecond x-ray pulses in synchrotron light sources using dipole kickers”, *Phys. Rev. ST Accel. Beams.*, vol. 10, no. 2, pp. 1–6, 2007.

[45] A. Sessler and V. Vaccaro, “Longitudinal instabilities of azimuthally uniform beams in circular vacuum chambers with walls of arbitrary electrical properties”, *CERN 67-2 ISR-Division*, vol. 17. p. 680, 1967.

[46] A. Novokhatski, M. Timm and T. Weiland, “Transition Dynamics of the Wake Fields of Ultra Short Bunches”, *International Computational Accelerator Physics Conference*, 1998, p. 132.

[47] I. Zagorodnov and T. Weiland, “TE/TM scheme for computation of electromagnetic fields in accelerators”, *J. Comput. Phys.*, vol. 207, pp. 69–91, 2005.

[48] W. Bruns, “GdfidL: a finite difference program with reduced memory and CPU usage”, *Proc. 1997 Part. Accel. Conf. (Cat. No.97CH36167)*, vol. 2, no. 2, pp. 2651–2653, 1997.

[49] M. Clemens, S. Drobny, H. Kruger, P. Pinder, O. Podebrad, B. Schillinger, B. Trapp, T. Weiland, M. Wilke, M. Bartsch, U. Becker and M. Zhang, “The electromagnetic simulation software package MAFIA 4”, *1999 Int. Conf. Comput. Electromagn. its Appl. Proc. (IEEE Cat. No.99EX374)*, pp. 565–568, 1999.

[50] CST Computer Simulation Technology AG, “CST Studio.” Darmstadt.

[51] A. Hofmann, K. Hubner and B. Zotter, “A computer code for the calculation of beam stability in circular electron machines”, *IEEE Trans. Nucl. Sci.*, vol. NS-26, pp. 6–7, 1979.

[52] R. Nagaoka, J. Rowland and R. Bartolini, “Studies of Collective Effects in Soleil and Diamond Using the Multiparticle Tracking Codes Sbtrack and Mbtrack”, *2009 Part. Accel. Conf.*, pp. 4637–4639, 2009.

[53] K. Bane, “Bunch Lengthening in the SLC Damping Rings”, *SLAC-PUB-5177,* 1990.

[54] G. A. Schott, *Electromagnetic Radiation.* Cambridge University Press, Cambridge, 1912.

[55] H. Hama, S. Takano and G. Isoyama, “Control of the bunch length on an electron storage ring”, *Nucl. Inst. Meth. Phys. Res. A*, vol. 329, no. 1–2, pp. 29–36, 1993.

[56] A. Nadji, P. Brunelle, G. Flynn, M. Level, M. Sommer and H. Zyngier, “Experiments With Low And Negative Momentum Compaction Factor With Super-ACO”, *1996 Euro. Part. Accel. Conf.*, pp. 1–3, 1996.

[57] I. P. S. Martin, G. Rehm, C. Thomas and R. Bartolini, “Experience with low-alpha lattices at the Diamond Light Source”, *Phys. Rev. ST Accel. Beams.*, vol. 14, no. 4, p. 40705, Apr. 2011.

[58] K. Y. Ng, “Quasi-isochronous buckets in storage rings”, *Nucl. Instr. Meth. Phys. Res. A.*, vol. 404, no. 2–3, pp. 199–216, Feb. 1998.

[59] J. B. Murphy and S. L. Kramer, “First Observation of Simultaneous Alpha Buckets in a Quasi-Isochronous Storage Ring”, *Phys. Rev. Lett.*, vol. 84, no. 24, pp. 5516–5519, Jun. 2000.

[60] S. X. Fang, K. Oide, K. Yokoya, B. Chen and J. Q. Wang, “Microwave instabilities in electron rings with negative momentum compaction factor”, *Part. Accel.*, vol. 51, pp. 15–28, 1995.

[61] D. Robin, R. Alvis, A. Jackson, R. Holtzapple and B. Podobedov, “Low Alpha Experiments at the ALS”, *LBL-37759*, 1995.

[62] D. Boussard, “Observation of microwave longitudinal instabilities in the CPS”, *LABII/RF/Int./75-2*. 1975.

[63] E. Keil and W. Schnell, “Concerning longitudinal stability in the ISR”, *Preprint CERN/ISR-TH-RF/69*. 1969.

[64] F. J. Sacherer, “Bunch Lengthening and Microwave Instability”, *IEEE Trans. Nucl. Sci.*, vol. 24, no. 3, pp. 1393–1395, 1977.

[65] F. J. Sacherer, “A Longitudinal Stability Criterion for Bunched Beams”, *IEEE Trans. Nucl. Sci.*, vol. 20, no. 3, pp. 825–829, 1973.

[66] K. Y. Ng, *Physics of Intensity Dependent Beam Instabilities*. *FERMILAB-FN-0713*, 2002.

[67] G. Stupakov and S. Heifets, “Beam instability and microbunching due to coherent synchrotron radiation”, *Phys. Rev. ST Accel. Beams*, vol. 5, no. 5, p. 54402, May 2002.

[68] Y. S. Derbenev, J. Rossbach, E. L. Saldin and V. D. Shiltsev, “Microbunch Radiative Tail-Head Interaction”, *TESLA-FEL-Report 1995-05*, pp. 1–12, 1995.

[69] R. L. Warnock, “Shielded Coherent Synchrotron Radiation and Its Effects on Very Short Bunches”, *SLAC-PUB-5375*, 1990.

[70] J. M. Byrd, W. P. Leemans, A. Loftsdottir, B. Marcelis, M. C. Martin, W. R. McKinney, F. Sannibale, T. Scarvie and C. Steier, “Observation of broadband self-amplified spontaneous coherent terahertz synchrotron radiation in a storage ring”, *Phys. Rev. Lett.*, vol. 89, no. 22, pp. 2248011–2248014, 2002.

[71] U. Arp, G. T. Fraser, A. R. Hight Walker, T. B. Lucatorto, K. K. Lehmann, K. Harkay, N. Sereno and K. J. Kim, “Spontaneous coherent microwave emission and the sawtooth

instability in a compact storage ring”, *Phys. Rev. ST Accel. Beams*, vol. 4, no. 5, pp. 28–36, 2001.

[72] E. Roussel, C. Evain, C. Szwaj and S. Bielawski, “Microbunching instability in storage rings: Link between phase-space structure and terahertz coherent synchrotron radiation radio-frequency spectra”, *Phys. Rev. ST Accel. Beams*, vol. 17, no. 1, p. 10701, Jan. 2014.

[73] F. Sannibale, J. M. Byrd, Á. Loftsdóttir, M. Venturini, M. Abo-Bakr, J. Feikes, K. Holldack, P. Kuske, G. Wüstefeld, H. W. Hübers and R. Warnock, “A model describing stable coherent synchrotron radiation in storage rings”, *Phys. Rev. Lett.*, vol. 93, no. 9, pp. 1–4, 2004.

[74] S. Turner, “CERN Accelerator School: Synchrotron radiation and free electron lasers”, *CERN-98-04*. 1996.

[75] K. Bane, S. Krinsky and J. B. Murphy, “Longitudinal potential well distortion due to the synchrotron radiation wakefield”, *AIP Conf. Proc.*, vol. 367, no. 1996, pp. 191–198, 1996.

[76] M. D’Yachkov, “Longitudinal instabilities of bunched beams caused by short-range wake fields”, PhD thesis, University of British Columbia, 1995.

[77] R. Baartman and M. D’Yachkov, “Simulations of sawtooth instability”, *Proc. Part. Accel. Conf.*, vol. 5, pp. 3119–3121, 1995.

[78] M. D’Yachkov and R. Baartman, “Binary star Instability”, *1996 Euro. Part. Accel. Conf.*, pp. 6–8.

[79] J. H. Rowland, R. Bartolini, R. Nagaoka and R. T. Fielder, “Nonlinear Single-Particle Effects in Multiparticle Tracking Codes for the Analysis of Collective Instabilities”, *2010 Int. Part. Accel. Conf.*, vol. 2, pp. 2069–2071, 2010.

[80] A. Streun, “Practical Guidelines for Lattice Design”, Paul Scherrer Institute, Villigen,

Sep. 1999.

[81] P. Kuske, “Investigation of the Temporal Structure of CSR-Bursts At BESSY II”, *2009 Part. Accel. Conf.*, pp. 4682–4684, 2009.

[82] P. Kuske, “Temporal Characteristics of CSR Emitted in Storage Rings - Observations and a Simple Theoretical Model”, *European Synchrotron Light Source Workshop (ESLS XVIII) Topics in Coherent Synchrotron Radiation: Experimental Consequences of Radiation Impedance*, 2010.

[83] J. B. Murphy, S. Krinsky and R. L. Gluckstern, “Longitudinal wakefield for synchrotron radiation”, *Proc. Part. Accel. Conf.*, vol. 5, pp. 2980–2982, 1995.

[84] I. P. S. Martin, private communication.

[85] Y. Cai, J. Flanagan, H. Fukuma, Y. Funakoshi, T. Ieiri, K. Ohmi, K. Oide and Y. Suetsugu, “Measurements, Analysis, and Simulation of Microwave Instability in the Low Energy Ring of KEKB”, *SLAC-PUB-13587*, pp. 1–4, 2009.

[86] K. L. F. Bane, K. Oide and M. Zobov, “Impedance Calculation and Verification in Storage Rings”, *CARE-HHH-APD Workshop on Beam Dynamics in Future Hadron Colliders and Rapidly Cycling High-Intensity Synchrotrons*, 2005.

[87] K. L. F. Bane, Y. Cai and G. Stupakov, “Threshold studies of the microwave instability in electron storage rings”, *Phys. Rev. ST Accel. Beams*, vol. 13, no. 10, pp. 1–6, 2010.

[88] S. Heifets, “Broad band impedance of the B-factory”, *SLAC/AP-93*, 1992.

[89] R. Bartolini and C. Thomas, “Measurement of the longitudinal loss factor for the diamond Storage ring”, *AP-SR-REP-0190*, Diamond Light Source, 2012.

[90] R. Bartolini, C. Christou, R. T. Fielder, M. Jensen, A. Morgan, S. Pande, G. Rehm and C. Thomas, “Analysis of Collective Effects At the Diamond Storage Ring”, *2008 Euro. Part. Accel. Conf.*, pp. 1574–1576, 2008.

[91] I. P. S. Martin, “Short Pulse X-Ray Generation in Synchrotron Radiation Sources”, DPhil thesis, University of Oxford, 2011.

[92] J. Feikes, M. von Hartrott, M. Ries, P. Schmid, G. Wüstefeld, A. Hoehl, R. Klein, R. Müller and G. Ulm, “Metrology Light Source: The first electron storage ring optimized for generating coherent THz radiation”, *Phys. Rev. ST Accel. Beams*, vol. 14, no. 3, p. 30705, Mar. 2011.

[93] C. Evain, J. Barros, A. Loulergue, M. A. Tordeux, R. Nagaoka, M. LabatL, L. Cassinari, G. Creff, L. Manceron, J. B. Brubach, P. Roy and M. E. Couprie, “Microbunching instability studies at SOLEIL”, *2011 Int. Part. Accel. Conf.*, pp. 709–711, 2011.